Functionalized Cellulose Nanocrystals (CNC) for Advanced Applications

by

Juntao Tang

A thesis

presented to the University of Waterloo

in fulfilment of the

thesis requirement for the degree of

Doctor of Philosophy

in

Chemical Engineering

Waterloo, Ontario, Canada, 2016

AUTHOR'S DECLARATION

I hereby declare that I am the sole author of this thesis. This is a true copy of the thesis, including any required final revisions, as accepted by my examiners.

I understand that my thesis may be made electronically available to the public.

Abstract

Cellulose nanocrystals (CNC) are excellent candidates for various potential applications as they possess many attractive characteristics. The unique properties and the abundant, renewable nature of CNC is of great interest in enhancing existing forest sector products as well as in the development of improved products for various industrial sectors. This PhD study is to exploit new potential applications by modifying this sustainable bio-nanomaterial (CNC) with various types of functionalities and taking advantages of their unique properties. At the same time, fundamental understandings necessary for their applications were elucidated, and the knowledge are critical for the design and development of various types of functional CNCs.

Firstly, a weak polyelectrolyte, poly[2-(dimethylamino)ethyl methacrylate] (PDMAEMA), was grafted onto the surface of cellulose nanocrystals. Stable heptane-in-water and toluene-in-water emulsions were prepared with PDMAEMA-*g*-CNC. Various factors, such as polarity of solvents, concentration of particles, electrolytes, and pH on the properties of the emulsions were investigated. Using Nile Red as a florescence probe, the stability of the emulsions as a function of pH and temperature were elucidated. It was deduced that PDMAEMA chains promoted the stability of emulsion droplets and their chain conformation varied with pH and temperature, which was used to trigger the emulsification and demulsification of oil droplets. Interestingly, for heptane systems, the macroscopic colours would change depending on the pH conditions, while the colour of the toluene system remained unchanged.

Following this, binary polymer brushes, consisting of poly(oligoethylene glycol) methacrylate (POEGMA) and poly(methacrylic acid) (PMAA), were grafted onto the cellulose nanocrystals (CNC-BPB). The physical properties of the CNC-BPB can be controlled by external triggers, such as temperature and pH, which can be utilized to stabilize and destabilize oil/water

emulsions. By virtue of the modifications, these bi-functionalized CNCs diffused to the oil-water interface and stabilized the oil droplets at high pHs. When the pH was lowered to 2, strong hydrogen bonds between POEGMA and PMAA chains grafted on the CNC induced the coalescence of the emulsion droplets, resulting in the phase separation of oil and water. This study demonstrates that functional sustainable nanomaterials can be used for small scale oil-water separations, particularly for oil droplet transportation and harvesting of lipophilic compounds.

The coating of the cellulose nanocrystal with conjugated polymer, polyrhodanine was conducted and explored. The core-shell nanoparticles displayed reversible colour change in response to pH, confirming their utility as an optical pH indicator. This property was retained when the nanoparticles were transformed into other geometries, such as 2-D films or 3-D hydrogel beads. The core-shell nanoparticles also exhibited promising antimicrobial properties, making it a potential candidate for antimicrobial applications, such as food-packaging, antimicrobial additives and antimicrobial surfaces or coatings.

In addition, a green and bio-inspired approach was developed to anchor silver nanoparticles (AgNPs) onto the surface of cellulose nanocrystals using a thin coating of polydopamine on the surface of CNC. The nanocatalyst displayed superior dispersability over pristine AgNPs and was six times more efficient in catalysing the reduction of 4-nitrophenol. In the presence of β-cyclodextrin, host-guest interactions were enhanced, and the catalytic performance of the CNC hybrids was accelerated.

This doctoral thesis research contributes to the basic research on cellulose nanocrystals, which will be beneficial to the academic and industrial laboratories. It also advances the fundamental understanding of the behaviour of cellulose nanocrystals, offering novel value-added applications that are beyond the traditional application of cellulosic materials.

Acknowledgement

Table of Contents

List of Figures

List of Tables

Chapter 1   Introduction

With a growing interest in nanoscience and nanotechnology, the synthesis and modification of nanomaterials with well-defined structure and specific functionalities has become one of the most versatile and challenging topics. Recent advances in nanomaterials have streamlined the development of functionalized nanoparticles, which are believed to hold promise to revolutionize applications in the fields of medicine, electronics, biomaterials and energy production[1,2]. However, a large proportion of the chemicals used to synthesis such nanomaterials are derived from petroleum-based resources and the processes involve the use of toxic reagents that are harmful to the environment. Because of the concerns on global warming and sustainable development, there is an urgent need to replace conventional resources with materials derived from nature or renewable resources. Furthermore, the ability to take a cheap and abundant material and generate products with value-added properties is desirable and worthy of exploration.

From the current perspective, cellulose is the most common organic polymer derived from nature. It represents about 1.5×10^{12} tons of total annual biomass production and is considered an inexhaustible source of raw material supply to meet the increasing demand for environmentally friendly and biocompatible products. Cellulose nanocrystal (CNC) derived from the acid hydrolysis of cellulose-based material has mostly been used to reinforce composites and polymers because it has remarkable strength that rivals carbon nanotubes.[3,4] In the past few years, CNC has also been given other nomenclatures, such as cellulose nanowhiskers, nanocrystalline cellulose, and rod-like cellulose microcrystals. It was not until 2011 that TAPPI's International

Nanotechnology Division proposed and recommended the general designation of "cellulose nanocrystals" for this nanomaterial derived from acid hydrolysis process. Since then, CNC has become a "hot" and topical subject and many researchers have dedicated their efforts to the study of this wonderful material, which is illustrated by the growing number of publications and citations as summarized in Figure 1.1 (The data is summarized according to ISI Web of Knowledge system).
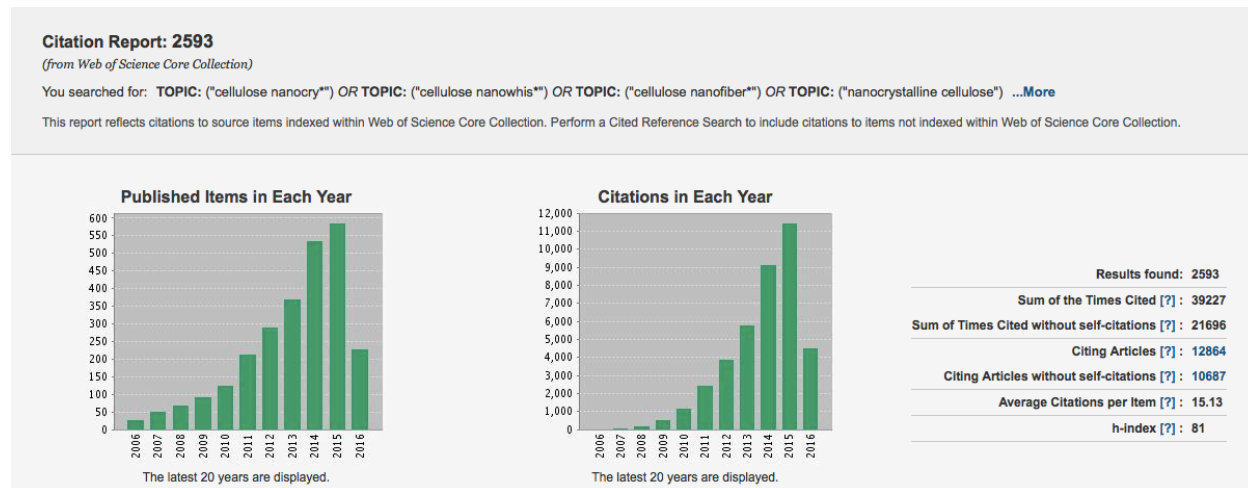
Figure 1.1 Evolution of the number of research publications and citations on cellulose nanocrystals during the past ten years (2006-2016) according to ISI Web of Knowledge system.

Cellulose nanocrystals are proven to be excellent candidates for many applications since they possess attractive characteristics, such as sustainability, biocompatibility, biodegradability, non-toxicity and especially easy surface modification due to the abundant surface primary hydroxyl groups. Thus, functionalizing CNC with alterative functional groups will provide a platform for the exploration of advanced functional nanomaterials[5–9]. Aside from the properties brought by nano size effect, CNC has an additional, less explored property: they organize into a chiral nematic (historically referred to as cholesteric) liquid crystal in water. When dried into a thin film, they retain the helicoidal chiral nematic order and assemble into a layered structure where the CNCs nanorods are aligned within each layer and their orientation rotates with a characteristic pitch

(repeating distance). The structure brought by this property has generated a platform for the use of CNC in templating new materials (carbon material or inorganic materials) with chiral nematic structures. Recently, the field of forest nanotechnology is growing and a number of CNC production facilities are being developed in Canada. The unique properties and the abundant nature of CNC will enhance existing forest sector products, as well as developing improved products for other industrial and commercial sectors.
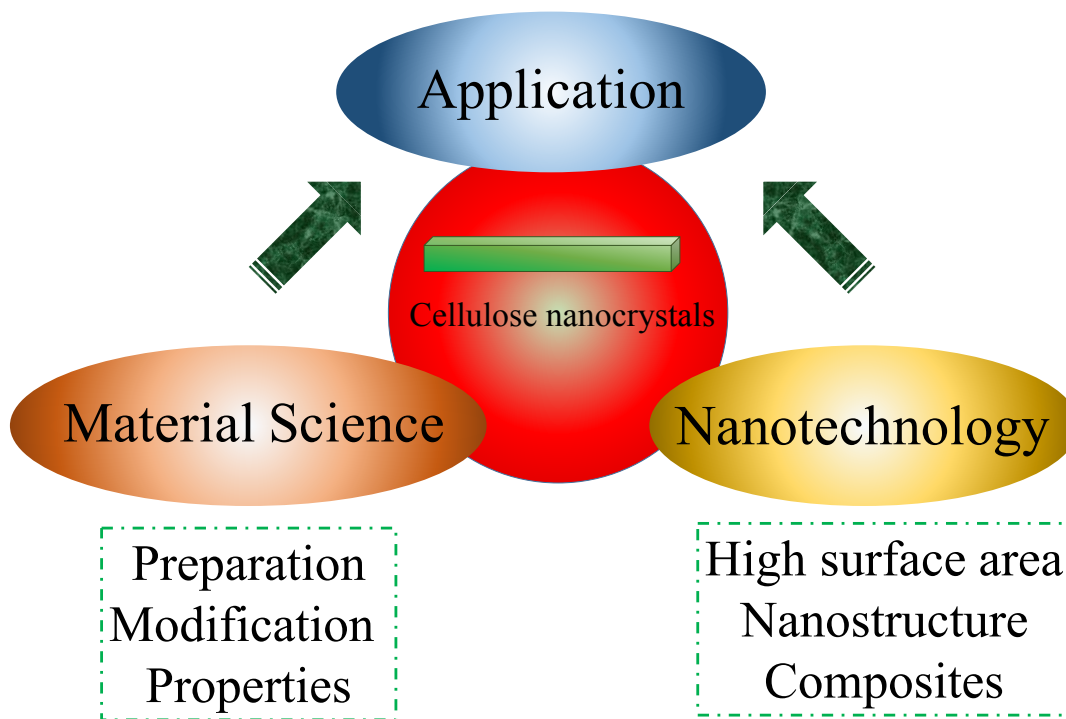
Figure 1.2 Summary of research topics on cellulose nanocrystals.

Research of cellulose nanocrystals that combines nanotechnology and materials science can be divided into different fields, including preparation, properties and modifications as illustrated in Figure 1.2. The purpose of surface modification is to regulate and control of the physical and chemical properties that contribute to novel functions of hybrid nanosystems. However, all these efforts should be driven by applications, more specifically, preparation and modification need to serve the purpose of applications. Nanotechnology and material science are the fundamentals that

provide a platform to select the right material, perform meaningful modifications and design specific nanostructures.

1.1   Objectives

Replacing petroleum-based synthetic materials with green and sustainable materials is desirable in many industrial sectors, ranging from energy to biomedical applications. Cellulose nanocrystals (CNC), derived from acid hydrolysis of cellulose-based material, have mostly been investigated for the reinforcement of composites and polymers due to their remarkable strength rivalling carbon nanotubes. CNCs are excellent candidates as they possess many attractive characteristics, such as sustainability, biocompatibility, biodegradability, non-toxicity and especially easy surface modification due to the abundant surface primary hydroxyl groups. Thus, modifying the CNC with different functional groups will provide a platform for the exploration of advanced functional nanomaterials. To achieve the goal of exploring new ideas, the overall objective of the PhD study is to exploit new applications by modifying this sustainable nanomaterial (CNC) with various functionalities and transforming its properties to meet the desired specifications. At the same time, fundamental knowledge on the the physical and chemical properties of the functionalized CNCs that is relevant to a specific application will be developed. The specific goals of the work are summarized below:

(1) To elucidate the physical and chemical properties of functionalized CNCs by grafting stimuli-responsive polymer chains onto CNC surface, such as in the control of the stability of oil-water emulsions. Through this study, a better understanding on the control of interactions between nanoparticles at the oil-water interface can be achieved. The results will pave the way for the

4

development of controllable Pickering emulsions stabilized by functional cellulose nanocrystals, leading to interesting potential new applications.

(2) To explore the potential of using CNC as carrier or substrate to formulate multi-functional composite materials, especially for functional materials with poor water solubility. The results may provide industries with general design concepts to achieve useful multi-dimension products or composites.

1.2 Thesis outlines

Generally, the thesis comprises of eight chapters as follows (see Figure 1.3).
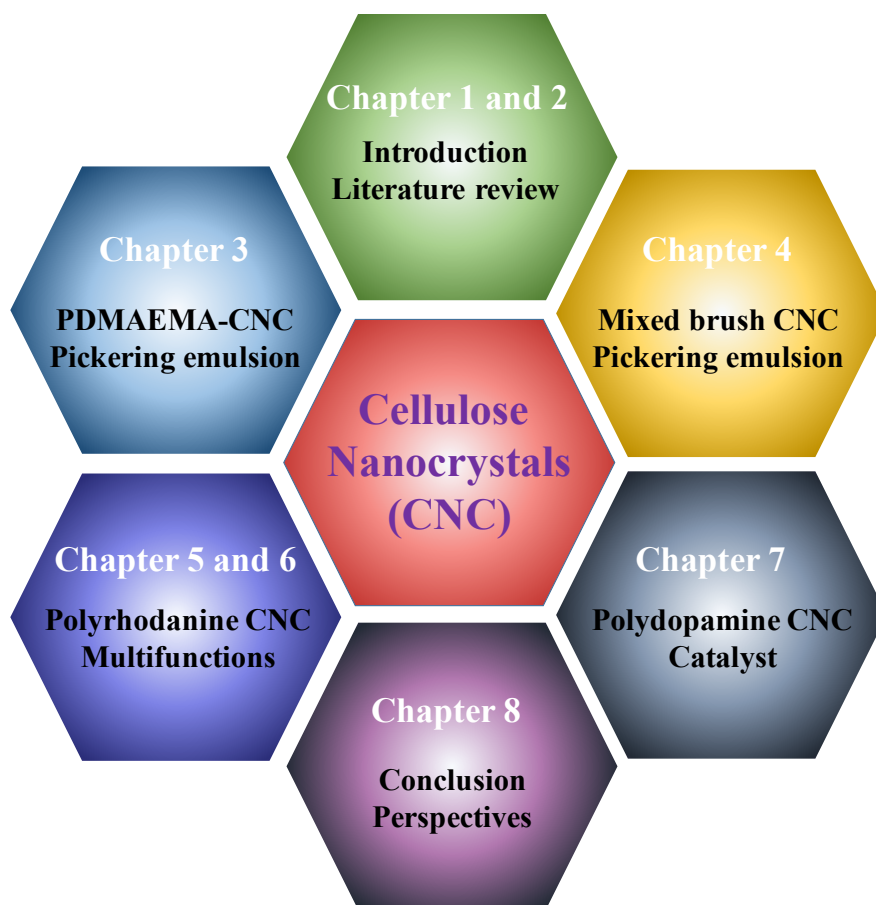
Figure 1.3 Structure and organization of this thesis

Chapter 1 and 2: *Introduction*. This chapter presents a thorough background of the research, research objectives and literature review respectively.

Chapter 3: *Dual responsive Pickering emulsion stabilized by poly [2-(dimethylamino) ethyl methacrylate] grafted cellulose nanocrystals*. This chapter reports on the Pickering emulsions systems stabilized by weak polyelectrolyte (PDMAEMA) grafted cellulose nanocrystals. Various factors, such as polarity of solvents, concentration of particles, electrolytes, and pH, were investigated. Using Nile red as a fluorescence probe, the stability of the emulsions as a function of pH and temperature was elucidated.

Chapter 4: *Stimuli-responsive cellulose nanocrystals for surfactant-free oil harvesting*. This chapter examines the preparation of Pickering emulsions with switchable properties stabilized by binary polymer brush [poly(oligoethylene glycol) methacrylate (POEGMA) and poly(methacrylic acid) (PMAA)] grafted cellulose nanocrystals. The switchable interactions between grafted polymer chains at the oil-water interface were used to manipulate and control the stability of the emulsions. The surface chemistry and interfacial properties at oil-water interface were investigated and discussed.

Chapter 5: *Polyrhodanine coated cellulose nanocrystals for optical pH sensing applications*. This chapter discusses the preparation of a multi-functional nanomaterial by coating cellulose nanocrystals with a conjugated polymer, polyrhodanine. pH optical indicator application was demonstrated and investigated.

Chapter 6: *Polyrhodanine coated cellulose nanocrystals for antimicrobial applications.* This chapter investigates the coating conditions for fabricating CNC-polyrhodanine hybrid materials. The hybrid material with improved coating characteristics was used to quantify the bacterial inhibition properties. Antimicrobial tests were performed using *Escherichia coli* (Gram negative)

and *Bacillus subtilis* (Gram positive) as model bacteria and the minimum inhibitory concentrations were determined by plate colony counting methods.

Chapter 7: *Polydopamine coated cellulose nanocrystals as catalyst substrate for improved catalysis*. This chapter describes a green and bioinspired approach to anchor silver nanoparticles onto the surface of cellulose nanocrystals coated with polydopamine. The nanocatalyst displayed superior dispersability over pristine silver nanoparticles (AgNPs) and was six times more efficient in catalysing the reduction of 4-nitrophenol. By associating the CNC hybrid with β-cyclodextrin to promote host–guest interactions, the catalytic process was accelerated. The associated physicochemical parameters associated with the catalytic process were investigated and compared.

Chapter 8: *Conclusion remarks*. The thesis closes with concluding remarks and the recommendation for further studies.

.

Chapter 2   Literature review and Background information

2.1   Cellulose and Nanocellulose

As early as 1838, Payen established a unique chemical structure named cellulose that can be found in the fibrous component of all higher plant cells.[10] Since then, this abundant material has been developed and applied to many industrial and academic applications. Cellulose is a high molecular weight polysaccharide composed of anhydroglucose units where the repeating segments are connected via the β-1, 4-glycosidic linkages. Cellobiose is the dimer of cellulose and the repeating units of the cellulose polymer chain, which is shown in Figure 2.1.

"non-reducing end"   **"reducing end"**
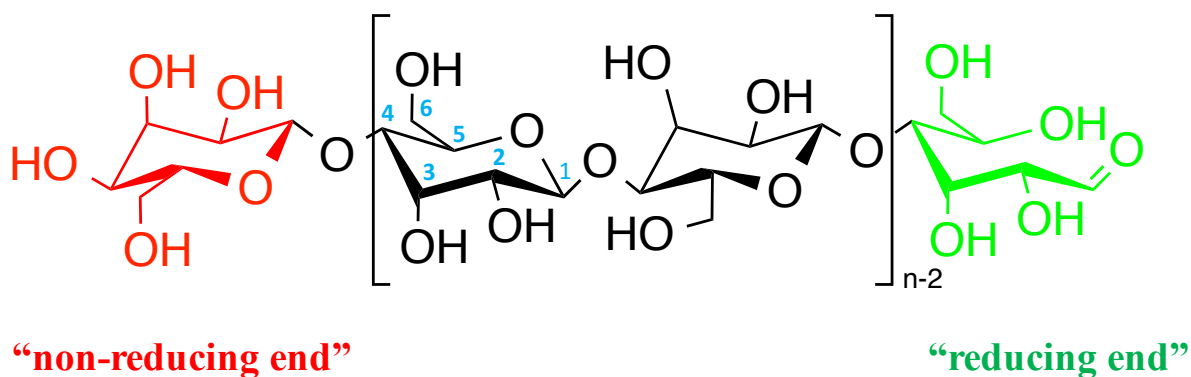
Figure 2.1 Molecular structure of cellulose. (n=DP, degree of polymerization)

Cellulose is a straight chain polymer, and unlike some polysaccharides, e.g. starch, no coiling or branching occurs. The molecule possesses an extended and fairly stiff rod-like conformation, aided by the equatorial conformation of glucose residues. In nature, cellulose chains associate through van de Waals forces, as well as inter- and intra-molecular hydrogen bonds to form hierarchical assemblies. This inter- and intra-molecular hydrogen bonding are formed by the interaction

between hydroxyl groups from one single chain with oxygen atoms on the same or on a neighbouring chain. Thus, individual chains associate and assemble to form larger units called elementary fibrils, which further aggregate into microfibrils and finally to cellulose fibers, as shown in Figure 2.2.[11] Cellulose fibers consist of alternating highly ordered crystalline regions, where cellulose chains are tightly packed and stabilized by hydrogen bonds, and less ordered amorphous regions. However, due to the complex interactions and conformations, the supramolecular structure of cellulose has been the topic of debate for decades. Several types of crystalline cellulose structures are known (cellulose I, II, III, and IV), corresponding to the location of hydrogen bonds between and within the strands. Since cellulose can be extracted from different sources or via biosynthetic processes, the crystal structure and distribution of fully crystalline regions and amorphous domains may vary.
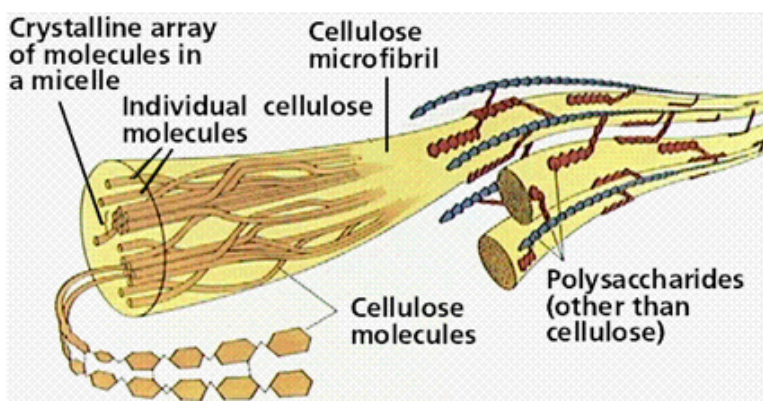
Figure 2.2 Illustration to show the structural level of cellulose[11].

Currently, much interest is directed to the isolation, characterization and modification of novel form of cellulose, ranging from whiskers, nanocrystals, nanofibrils to nanofibers.[12] The method of producing these kinds of materials consists of either top-down or bottom-up approaches. For example, using enzymatic/physical/chemical methods to isolate them from wood or agricultural

residues (top-down), as well as utilizing bacteria to produce cellulose nanofibrils from glucose (bottom-up). The cellulosic materials with one dimension in the nanometer range are generally called nanocellulose. Undoubtedly, these nanocelluloses possess various cellulose properties (versatile fiber morphology, hydrophilicity, and easy surface modification) and specific nanomaterial features (large surface area and high aspect ratio). Depending on their dimensions, sources and processing conditions, nanocelluloses can be divided into three main categories (Table 2.1). A comparison describing the typical structures of three different kinds of nanocellulose is shown in Figure 2.3.
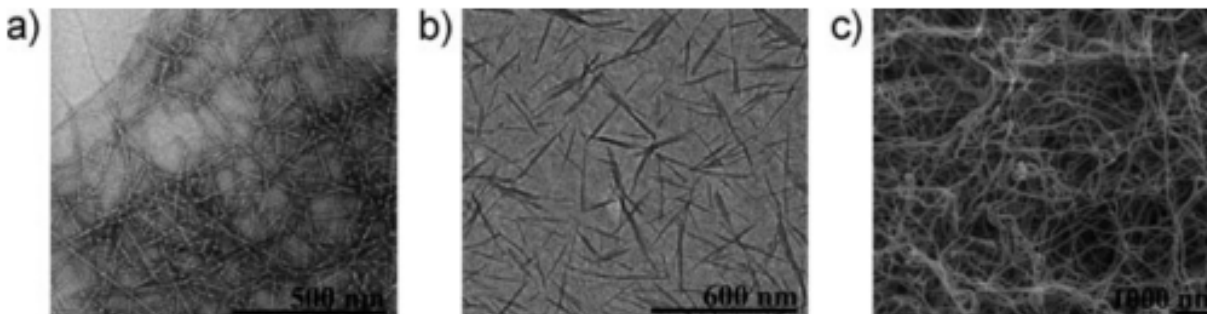
Figure 2.3 Transmission electron micrographs (TEM) of a) MFC and b) CNC; c) Scanning electron micrograph (SEM) of BNC[12].

Table 2.1 The family of nanocellulose materials

Type of Nanocellulose	Typical Source	Typical Size Range	Typical Aspect Ratio	Degree of Polymerization
Microfibrillated cellulose(MFC)	wood, sugar beet, potato tuber, hemp, flax	10-100 nm wide, 1-100 µm long	up to 100	up to 1000
Nanofibrillated cellulose(NFC)	wood, sugar beet, potato tuber, hemp, flax	4-30 nm wide, 70 nm-5 µm long	up to 100	up to 900
Cellulose nanocrystals (CNC) or whiskers	wood, cotton, hemp, flax, wheat straw, ramie, tunicin, cellulose from algae and bacteria	3-5 nm wide, up to 300 nm long	~20	up to 300

2.2   Cellulose nanocrystals

Cellulose nanocrystals (CNC) are one type of nanomaterials derived from cellulosic biomass.[13] Figure 2.4 shows the important milestones of cellulose nanocrystals research. The first attempt in isolating cellulose nanofibers from cellulose sources and imaging them by electron microscopy were performed by Nikerson & Habrle[14] and Ranby & Ribi[15], respectively. Ten years later, Marchessault et al. observed the birefringent crystal structure of CNC colloidal dispersion., and it was not until 1992 that Revol et al. reported the formation of colloidal liquid crystalline phases in CNC suspensions[16]. In the past fifteen years, research on cellulose nanocrystals expanded dramatically driven by the promise of using them as reinforcing nanofillers in polymer composites. These breakthroughs were followed by other important research, such as (i) the modification of CNC surface with florescent functional groups[17], (ii) using cellulose nanocrystal as chiral nematic template to fabricate optical material[18], (iii) the stabilization of the oil-in-water Pickering emulsions[19] and (iv) the announcement of the opening of the first demonstration plant for the production of cellulose nanocrystals by CelluForce Inc. (Quebec, Canada). Recent achievements suggest that this sustainable nanomaterial has potentials for many applications, such as Pickering emulsifier[9,20,21], catalyst and drug carrier[6], nanofiller for the nanocomposites[22,23] as well as templates for mesoporous materials.[24–31]
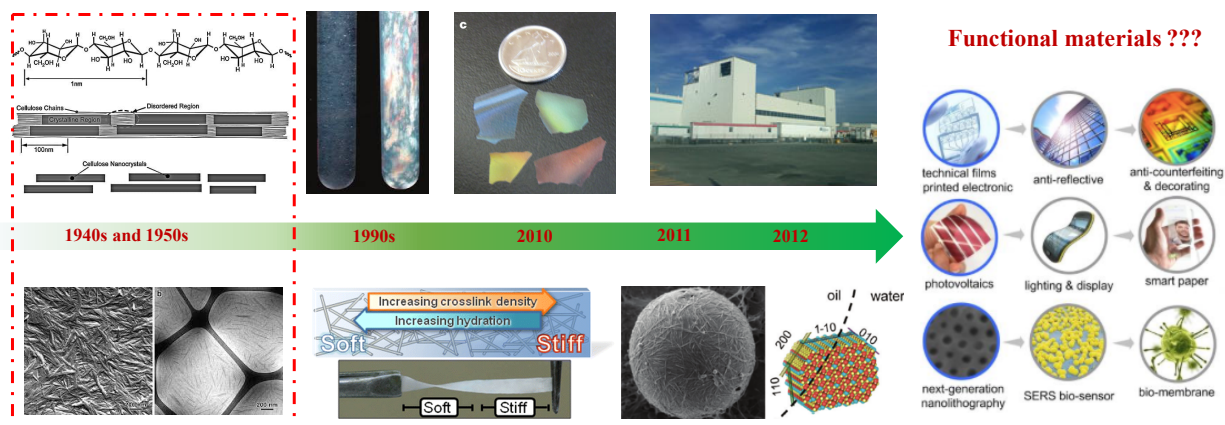
Figure 2.4 Time line and some milestones of cellulose nanocrystals based research and applications.

2.2.1   Preparation of cellulose nanocrystals

The preparation of cellulose nanocrystals includes a chemical hydrolysis process to dissociate the amorphous regions and the release of crystalline domains from the cellulose fibers. This could be achieved by either a small scale lab extraction or a large scale of pilot or commercial production. For lab scale extractions, there were several examples on using enzymatic hydrolysis to produce CNC, however the most popular and common method to isolate CNC from natural sources is by acid hydrolysis. Disordered or paracrystalline regions of cellulose are disrupted, whereas crystalline regions with a higher resistance to acid treatment remain intact. Typical procedures for producing CNC are summarized in Figure 2.5. Cellulose fibres are subjected to strong acid treatment under controlled conditions of temperature, agitation and time. Then the resulting suspension is diluted with water, washed and centrifuged several times. The suspension is then dialyzed against distilled water to remove unreacted chemicals. Additional steps such as differential centrifugation, filtration, spray drying or freeze drying are used to prepare the final dry CNC product. Sulfuric and hydrochloric acids are the most common acids used in the hydrolysis

process, but other strong acids, such as phosphoric and hydrobromic acid have also been used. However, the type of acids used is extremely important for the preparation of CNC. Different acids may lead to significant differences in the dispersity and colloidal stability of CNC. For instance, CNC derived from sulfuric acid hydrolysis disperses readily in water due to the abundance of negatively charged sulfate ester groups on the CNC surface, while aqueous solution of CNC produced from hydrochloric acid hydrolysis displayed poor colloidal stability. They also exhibit significant difference in the thermal stability and rheological behaviour. Furthermore, with the combination of sodium hypochlorite and TEMPO, the hydroxyl groups on the CNC surface can be converted into carboxyl groups, which provide opportunities for further modifications. Ammonium persulfate (APS) has also been reported to oxidize the cellulose materials to yield carboxylate cellulose nanocrystals[32]. Other derivatives of cellulose nanocrystals, such as hydrophobic acetyl functionalized CNC were obtained by hydrolysis in an acid mixture composed of hydrochloric acid and acetic acid in a one single-step process[33].
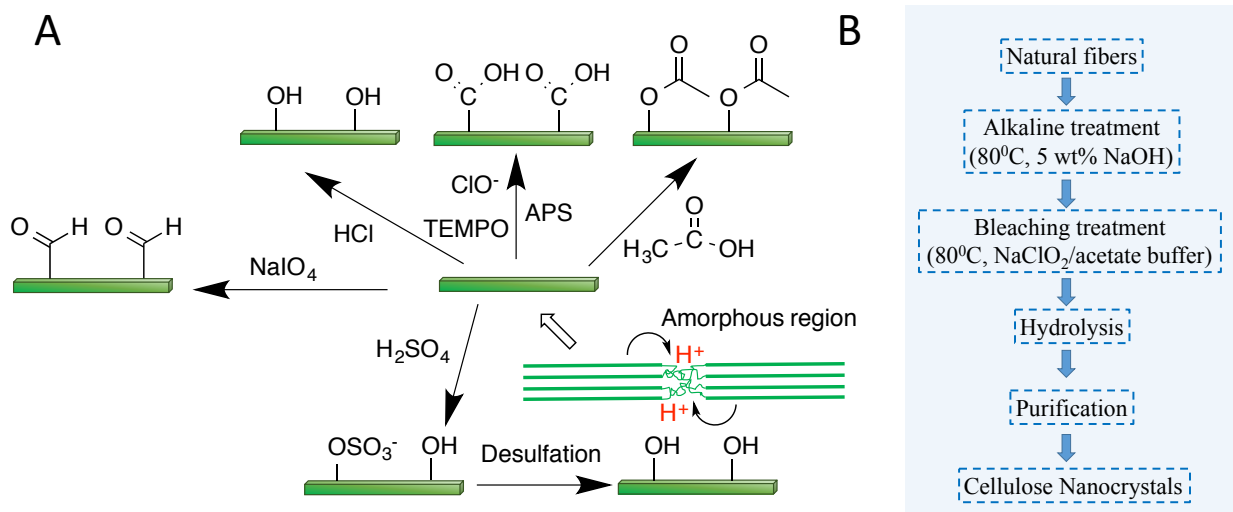
Figure 2.5 (A) Various cellulose nanocrystals with distinctive surface chemistry extracted by different processes; (B) General procedures to prepare cellulose nanocrystals by acid hydrolysis.
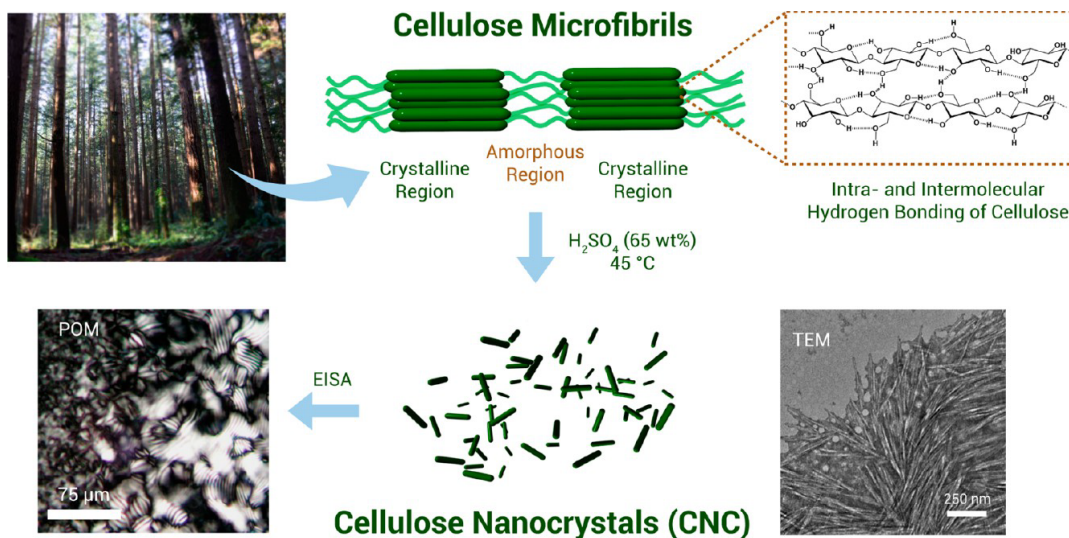
Figure 2.6 Acid hydrolysis of bulk cellulose material to produce cellulose nanocrystals[25].

The production of cellulose nanocrystals in a commercialized scale is being developed. Table 2.2 provides a summary on the manufacturing facilities that have or are being built in many parts of the world. Domtar Corp. and FPInnovations set up a joint venture company (CelluForce Inc.) to construct and operate a demonstration plant that produces 1000kg/day of dried CNC. The company started the first CNC production in 2012 (the first in the world) and it is the world leader in the commercial development of NCC[TM]. US forest service forest products laboratory have also developed a pilot production facility that deliver 35-50 kg/day of CNCs. As the industrial production of CNC is continuing, the development of CNC continues to face many challenges. First is the standardization of CNC productions, which is being developed by the TAPPI standards committee. Second, we need to develop practical applicable CNC-based materials, despite the fact that the potential applications of cellulose nanocrystals have been demonstrated or identified in several research laboratories. Last but not the least, it is likely that many companies are interested in using CNC to improve the quality of their products, and cost and sustainability of supply are

major points of consideration. Bringing the CNC to the commercial market still has a long way to go.

Table 2.2 Industrial production of cellulose nanocrystals (CNC) or carboxylated CNC

Producer	Country	Product	Production capacity in 2015
FPInnovations	Canada	CNC	10 kg/week (pilot production)
Alberta Innovates-Technology Futures	Canada	CNC	100 kg/week (pilot production)
Bio Vision Technology	Canada	Carboxylated CNC	4 tons/year (commercial production)
CelluForce	Canada	CNC	1 ton/day (commercial production)
US Forest Service Forest Products Laboratory	USA	CNC Carboxylated CNC	35-50 kg/day (pilot production)
Melodea	Israel	CNC	unknown
Research on Cotton Technology (CIRCOT)	India	CNC/NFC	unknown

2.2.2 Properties of cellulose nanocrystals
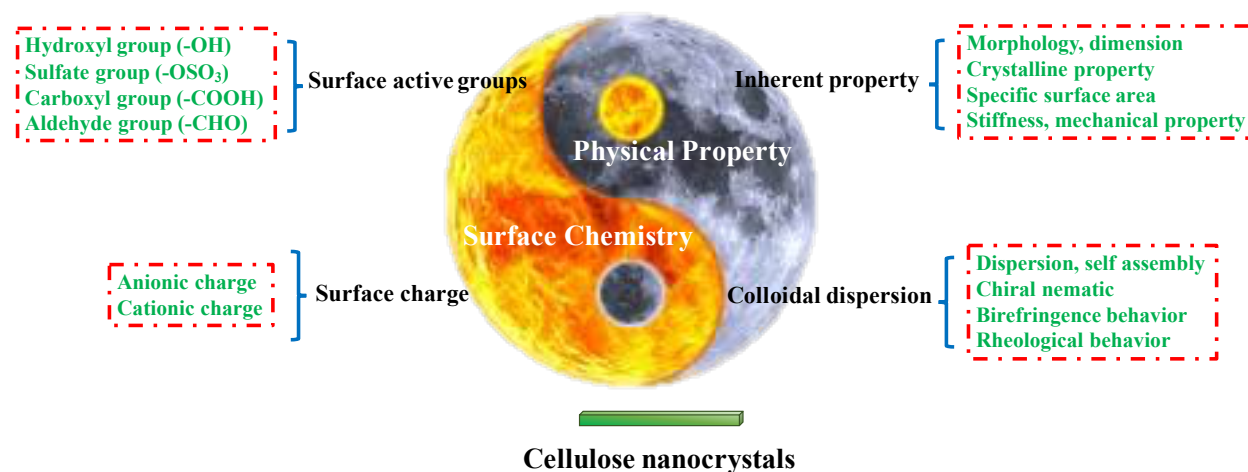
Figure 2.7 A summary of the physical and chemical properties of cellulose nanocrystals.

Cellulose nanocrystals are rigid, rod-like particles with several nanometers in width and up to hundreds of nanometers in length. The diverse properties of cellulose nanocrystals can be

classified into two main categories: Physical properties and surface chemistry properties, which are summaries in Figure 2.7.

2.2.2.1 Physical properties

(a) Inherent properties

As CNC is a specific rigid nanoparticle, the morphology and dimension could be directly captured by microscopic techniques, such as transmission electron microscopy, (TEM), atomic force microscopy (AFM) or scanning electron microscopy (SEM). Other techniques, such as dynamic light scattering could also be used to characterize the dimension of the nanoparticle. The parameters of physical dimension for cellulose nanocrystals include the length (L), diameter (D) and aspect ratio (L/D), which are determined by several factors, such as the source of cellulose or hydrolysis conditions (acid type, reaction time and temperature). It was reported that CNC derived from wood and cotton are usually shorter than those obtained from tunicate and bacterial cellulose as tunicate and bacterial cellulose are highly crystalline. Lower fractions of amorphous regions make them more resistant to the chemical effects of acid hydrolysis, from which the larger rod structures are produced. Usually, the aspect ratio ranges from 10-30 for CNC derived from cotton and up to approximately 70 from tunicate. Other factors that may influence the properties of CNC will not be discussed here, however, detailed descriptions can be found in literatures[1,3,4]

The van der Waals force and intermolecular hydrogen bonding promote the parallel stacking of cellulose chains, which imparts the crystalline structure to cellulose nanocrystals. Theoretically, the degree of crystallinity (mass of crystalline domain to the total mass of CNC) for CNC can approach up to 100%, however, incomplete removal of the disordered region may affect the

crystallinity. It is usually accepted that the degree of crystallinity generally lies in the range of 54 to 90%, depending on the source and extraction conditions. The crystalline structure and degree of crystallinity can be characterized by various techniques, including X-ray diffraction (XRD), solid state ^{13}C NMR and Raman spectroscopy. XRD is the most widely used and direct method to estimate the degree of crystallinity, which is reflected by the intensity ratio between diffraction angle of 18° and 22.5°. Solid state ^{13}C NMR spectrum can also provide the information of crystallinity index as the peak at 84 and 89 ppm are assigned to the C4 atom for disordered and ordered cellulose, respectively[34]. Similarly, in Raman spectroscopy, the crystallinity can be evaluated by the relative intensity ratio of the Raman peak I_{1481cm} and I_{1462cm}, which applies to the crystalline and amorphous regions of cellulose I[35].

The thermal stability of cellulose nanocrystal is a very important parameter for material processing and its practical use. When comparing to pristine cellulose, cellulose nanocrystals display a lower degradation temperature due to the introduction of sulphate ester groups onto the CNC surface. The typical thermal degradation profile is described by a two-step process, with a low temperature region (T_1) of between 150 and 300 °C and a high temperature region (T_2) between 300 and 450 °C, respectively. T_1 can be associated to the decomposition process of most accessible amorphous regions that are highly sulphated, while T_2 corresponds to the degradation of less accessible crystalline domains[36]. In order to increase the thermal stability of CNC, desulfation of the nanoparticle using dilute sodium hydroxide solution can be performed. It is reported that an increment of around 50 to 100 °C was achieved with desulfation.[37]

Excepted for all the properties discussed above, cellulose nanocrystal also possesses some attractive properties: large surface area (250~500 m^2/g), improved mechanical strength (tensile

strength 7500 MPa and Young's modulus of 100~140 GPa).[12] The extremely high Young's modulus is an attractive feature in nanocomposite materials.

(b) Properties of colloidal dispersions

The dispersion or self-aggregation state of cellulose nanocrystals has a significant impact on their physical properties and applications. As HCl-hydrolysed CNC possesses a high surface area and numerous hydroxyl groups, strong hydrogen bonding between the nanoparticles induces the aggregation of the nanoparticles. Several solvents (especially organic solvents) could weaken the inter-chain bonding in cellulose, (e.g. in DMF, the N atoms facilitate the formation of new hydrogen bonds (O-H---N)), however, these solvents are not environmental friendly. Hence, diverse surface treatment is necessary to weaken the inter-particle hydrogen bonding by altering the surface properties. Performing the hydrolysis process in sulphuric acid could be one solution to enhance the dispersibility of CNC in water since the negatively charged sulphate ester groups (OSO_3^-) introduced to the surface lead to strong electrostatic repulsion between the nanoparticles. Similarly, carboxylated CNC can also be dispersed in water due to the electrostatic repulsions brought by carboxylate groups (COO^-). However, due to the hydrophilic nature of CNC, it is hard to disperse the nanoparticles in many organic solvents, hence surface modification is required to improve the compatibility between the nanoparticle and matrix materials, and this will be discussed in detail in Section 2.2.3.

Asymmetric rod-like particle is known to exhibit liquid crystalline behavior in non-flocculating suspensions and this was also observed for cellulose nanocrystals. An investigation into the colloidal CNCs revealed that in the dilute solution regime, CNC are randomly oriented as an isotropic phase. Using polarized optical microscopy, CNC appeared as spheroids or ovaloids and

the initial domains are similar to tactoids. These tactoids may coalesce to form an anisotropic phase at higher concentrations leading to a nematic liquid crystalline alignment that transforms onto a chiral nematic order phase when the critical concentration is exceeded. Above this concentration, CNCs dispersion display shear birefringence, and they can spontaneously phase separate into an upper isotropic and a lower anisotropic phase. The chiral nematic or cholesteric structure in the anisotropic phase possesses a helical twist along the main axis, with the orientation of each stack planes rotated about the perpendicular axis. The parallel alignment of CNC is attribute to the well-known entropically driven self-orientation phenomenon and the helix of cellulose nanocrystal is left-handed, reflecting the intrinsic chirality of crystalline cellulose[38]. However, the pitch distance between different planes varies significantly, ranging from less than 1 to 50 nm and beyond (Figure 2.8), which does not depend on concentration of CNC, but it is a function of temperature, sonication time and ionic strength of the suspension. More interestingly, the chiral nematic structure of the suspension is preserved with slow and complete evaporation of the water phase yielding a iridescent color film. The spectacular iridescent color originates from the refection of light by the chiral nematic phases in a Bragg-type manner. As the reflected colour of the films can be changed by varying the pitch of the helical structure, these iridescent materials are of great interest in coatings, security features, and sensors. The functional materials based on chiral nematic behavior of CNC will be further discussed in section 2.2.4.
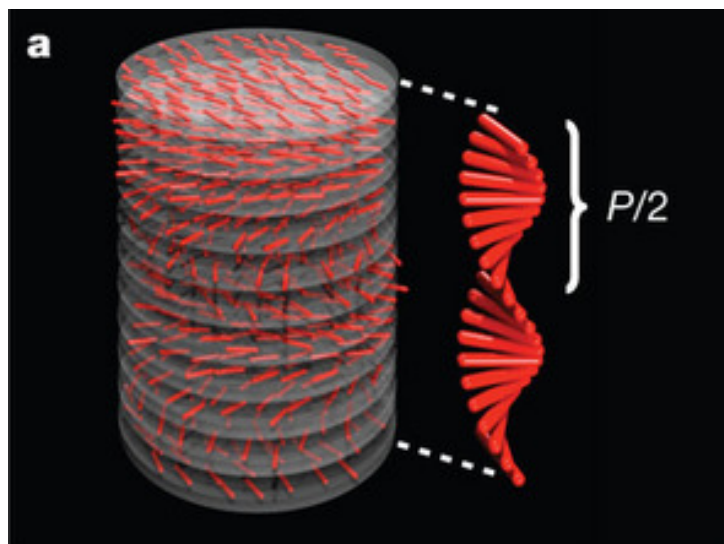
Figure 2.8 Schematic of the chiral nematic ordering present in CNC, along with an illustration of the half-helical pitch P/2.[18]

Rheological property of cellulose nanocrystals suspensions is closely related to the experimental conditions (concentration of suspension, shear rate, temperature, etc) as well as the intrinsic properties of cellulose nanocrystals[39]. In dilute CNC dispersions, shear thinning behavior is observed over a wide range of shear rates. While increasing the concentrations (over 4.0 wt%), the flow curves exhibit three distinct regions, which typifies the rheological behavior of lyotropic liquid crystalline polymers. At low shear rates, the viscosity curve shows a shear thinning behavior due to the alignment of the chiral nematic liquid crystalline domains. With increasing shear rates to the intermediate region, shear thinning gradually decreases to an almost Newtonian regime as the domains have all been oriented along the shear direction. After that, another shear thinning behavior appears in the high shear rate region, which is attributed to the high stress that disrupts the liquid crystalline domains where the individual rods are orientated along the shear flow direction. The aspect ratio of the cellulose nanocrystals is another key parameter. It was found that larger aspect ratio may significantly enhance the viscosity of the CNC suspensions[39]. Very recently,

research also proved that the degree of sulfation of CNC has a significant impact on the transition concentrations of isotropic to liquid crystal and gel.[40]

2.2.2.2 Surface chemistry properties

As the main chemical component of cellulose nanocrystal is cellulose polymer chains, all the classical chemistry on cellulose or polysaccharide can be applied to cellulose nanocrystals. However, CNC is thought to be less reactive when compared to amorphous cellulose chains because most of the polymer chains are buried inside the crystalline regions. The monomeric glucose unit of cellulose chain possesses three hydroxyl groups, which offer the reactive platforms for easy chemical modifications. The reactivity of these three hydroxyl groups are quite different: the hydroxyl groups in the 2nd and 3rd positions that are directly link to the alkyl groups on anhydrous glucose unit experience steric effect brought by the supramolecular structure of cellulose. However, the 6th position hydroxyl group only attaches to the alkyl group on the edge of the glucose ring, functioning as a primary alcohol that can react ten times faster than the other hydroxyl groups. Furthermore, the reaction conditions, including solvents or reactants, may also impact the reactivity of different hydroxyl groups. Take etherification as an example, the reactivity towards electrophile compound follows the order of OH-C6 > OH-C2 = OH-C3. It is generally accepted that only 1/3 of the surface hydroxyl groups can participate in chemical modifications.

Except for abundant hydroxyl groups, CNC surface may also contain other types of functional groups that are directly related to the processes and process conditions. The common functional groups are sulfate groups ($-OSO_3^-$), carboxyl groups ($-COO^-$) and acetyl groups ($-COCH_3$). With

additional mild post-hydrolysis reactions, aldehyde groups (-CHO), amino groups (-NH$_2$) or thiol groups (-SH) may also be introduced onto the CNC surface. Depending on the specific functional groups on the surface, CNC nanoparticles exhibit different charge properties. CNC bearing sulfate or carboxylate groups on the surface are negative charged over a wide range of pH conditions (higher than pK$_a$), while the amino groups are positive charged below the pK$_a$ values of the weak base. Modifying the cellulose nanocrystals with quaternary ammonium groups will render the surface with permanent positive charges.

2.2.3   Chemical modification of cellulose nanocrystals

The dispersibility of nanoparticles in solvents or continuous matrices are critical when processing them into final products that determine their physical or mechanical properties. Owning to the highly hydrophilic nature of CNC, it is difficult to obtain well dispersed systems in many non-polar solvents and polymeric matrices. The hydrogen bonding will lead to rapid aggregation or flocculation of the nanoparticles in hydrophobic media. Thus modifying the surface of CNC by either non-covalent or covalent approaches have explored to address these challenges. By modifying the surface, the physical or chemical properties of the nanoparticles can be adjusted, but the integrity of the crystal is retained.

2.2.3.1 Non-covalent surface modification

Non-covalent surface modification of cellulose nanocrystals is usually achieved through the adsorption of surfactants, oppositely charged polyelectrolytes or polymers. Therefore, the types of

interactions between the modifiers and cellulose nanocrystals comprised of electrostatic attraction, hydrogen bonding, or Van der Walls forces. Heux et al.[41] described the use of surfactant to modify CNC to promote their stability and dispersion in nonpolar solvents. The surfactant used is the Beycostat NA, which is a phosphoric ester of polyoxyethylene nonylphenyl ether. The surfactant molecules can form a thin layer of up to 15 Angstroms on the surface of CNC, thereby promoting their incorporation into the hydrophobic polymeric matrix, such as isotactic polypropylene (isoPP). Several other types of surfactants, such as nonionic surfactants, have also been used to modify the CNC and improve their hydrophobicity for incorporation into polystyrene matrices as reported by Kim et al.[42] and Rojas et al.[43]. Salajková et al.[44] used electrostatic interaction to adsorb a series of positively charged quaternary ammonium salts bearing long alkyl, phenyl, glycidyl, and diallyl groups onto the negatively charged TEMPO-oxidized CNC surface. Other interesting systems that can be used are saccharide based copolymers or dendrimers. Zhou and coworkers showed that by mimicking natural lignin-carbohydrate copolymers, xyloglucan oligosaccharide-poly (ethylene glycol)-polystyrene triblock copolymer could absorb on the surface of CNCs, imparting excellent dispersion stability of CNC in nonpolar solvents[45]. More recently, Nikolay and Olli lkkala[46] synthesized a novel supra-colloidal system by combining CNCs with dendronized polymers (DenPols) containing maltose-based sugar groups on the periphery of lysine dendrons and poly(ethylene-alt-maleimide) polymer backbone. They found that the interactions depended on the dendron generation suggesting multivalent interactions. In addition, the complexation of the third generation DenPol with CNCs enhanced the aqueous colloidal stability, due to the wrapping of the DenPol units around CNCs as visualized by cryo high-resolution transmission electron microscopy and electron tomography (Figure 2.9).
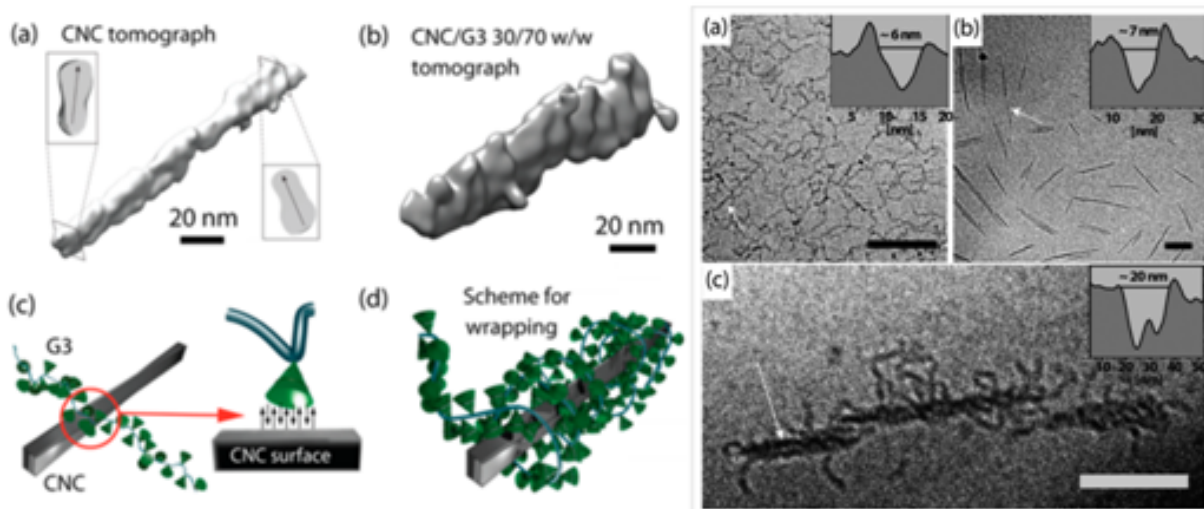
Figure 2.9 (Left) ET image of (a) pristine CNC and (b) CNC/G_3 30/70 w/w). (c) Schematics of the proposed multivalent interactions between G_3 peripheral dendritic units and the CNC surface glucose groups. (d) Schematics for irregular wrapping of G_3 on CNC. (Right) Cryo HR-TEM images from (a) G_3, (b) CNCs, and (c) CNC/G_3 30/70 w/w. The arrows mark the loci for the cross section analysis shown as insets. Scale bars are 100 nm[46].

2.2.3.2 Covalent surface modification

The surface covalent modifications of cellulose nanocrystals have been reviewed extensively[1,3,4,12], and they can be categorized into 3 distinct groups (also see Figure 2.10):

(1) Substitution of surface hydroxyl groups with small molecules (carboxylation, esterification, silylation, ureathanization, amidation, click chemistry, etc);

(2) Polymer surface modification based on the "graft onto" strategy with different coupling agents;

(3) Polymer surface modification based on the "graft from" strategy with the radical polymerization of ring opening polymerization (ROP), atom transfer radical polymerization (ATRP) and single-electron transfer living radical polymerization (SET-LP)
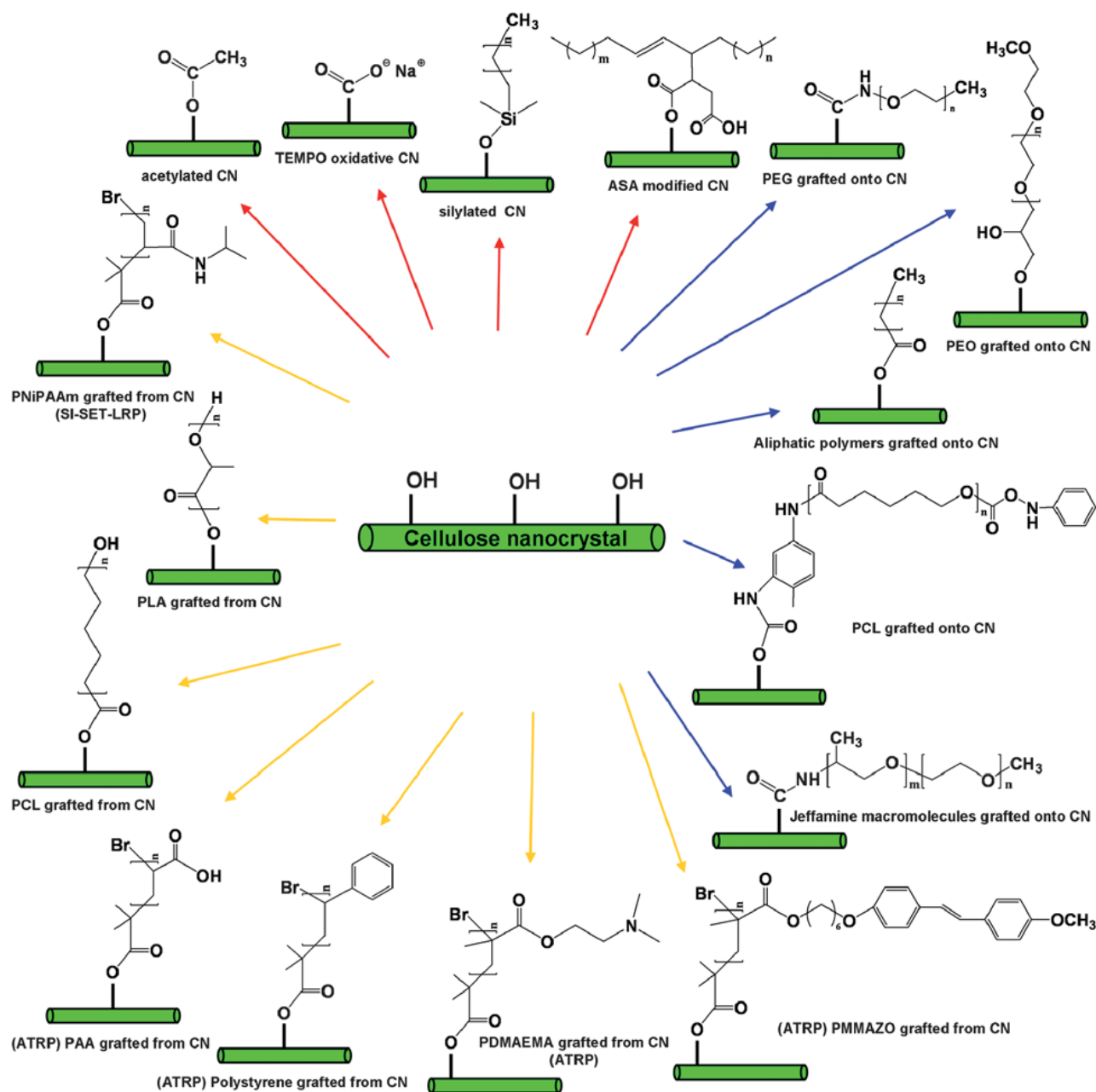
Figure 2.10 Common chemical modifications of cellulose nanocrystals (CNCs)[2,4,47] [PEG: poly(ethylene glycol); PEO: poly(ethylene oxide); PLA: poly(lactic acid); PAA: poly(acrylic acid); PNiPAAm: poly(N-isopropylacrylamide); and PDMAEMA: poly(N,N-dimethylaminoethyl methacrylate)]

2.2.3.3 Grafting of stimuli-responsive polymers to CNC

As discussed earlier, the most popular way to graft stimuli-responsive polymer on to CNC are through "grafting-to" and "grafting-from" techniques. Eyley et al. developed a CO_2 responsive system by grafting the CNC surface with imidazole functionalities through a one-pot functionalization strategy. The modified nanoparticles were tested for the flocculation of Chlorella vulgaris using CO_2 to protonate the functional motif and the flocculation efficiency can approach 90% with a 200 mg/L dosage.[48] For grafting to method, the most feasible and simple approach is through peptidic coupling, which is a reaction between amine-functionalized molecules and TEMPO-oxidized CNCs. Azzam et al.[49] reported a system using this method to graft thermo-sensitive amine-terminated statistical copolymers of ethylene oxide (EO) and propylene oxide (PO) (Jeffamines) onto the CNC surface. The modification can lead to unusual properties in CNC suspension, such as high resistance to ionic strength, surface activity and thermo-reversible aggregation. Very recently, they further investigated into the aggregation and viscoelastic properties of this system and found that a higher grafting ratio can lead to a reversible temperature-triggered liquid-to-gel transition.[50] Peng et al.[7] also use the same method to graft low molecular weight Jeffamine copolymers onto CNC and investigate the interactions between modified CNC and 3 different types of surfactants (cationic, anionic and nonionic) by isothermal titration calorimetry (ITC). Strong electrostatic interaction was only observed between grafted CNC and cationic surfactant, due to the binding of opposite charges. Hydrophobic interaction may be present for the grafted CNC/anionic surfactant system, and negligible interaction between grafted CNC and nonionic surfactant was observed.

For the grafting from method, poly(2-(diethylamino)ethyl methacrylate) (PDMAEMA), poly(4-vinyl pyridine) (P4VP) and poly(N-isopropylacrylamide) (PNIPAM) are the typically examples that have been reported. Those polymers were introduced onto the surface either by controlled living radical polymerization, where the molecular weight is controlled or surface initial polymerization by Ce^{4+}, but the degree of polymerization is not well-defined. In 2008 by Yi and coworkers reported a study on the temperature induced chiral nematic phase behavior of suspensions of PDMAEMA-grafted CNC[51]. Justin et al.[52] described a surface-initiated single-electron transfer living radical polymerization to graft PNIPAM onto CNC surface. The thermo responsive and aggregation behavior of PNIPAM grafted CNCs were investigated by light scattering, rheometry as well as atomic force microscopy. They further incorporated the responsive nanoparticle into Pickering emulsion to study the properties in response to temperature changes. The emulsions stabilized by poly(NIPAM)-g-CNCs dissociated after heating to a temperature above the LCST of poly(NIPAM). Kevin et al.[53] were the first one to report the use of a pH-responsive polymer (P4VP) grafted from CNCs. A reversible flocculation and sedimentation of CNCs from the suspension was observed, which is visible by the eyes at extremely low concentrations. The controlled properties offer new potentials to achieve a uniform dispersion of CNCs in hydrophobic matrices and offer a range of biomedical and industrial separation opportunities for pH-responsive CNC-based materials. Wu et al. introduced fluorescent and thermos-responsive (PNIPAM) brushes onto the surface of cellulose nanocrystals using ATRP and the modified nanoparticle displayed thermos-enhanced fluorescence due to the increment of fluorescence quantum efficiency.[54]

2.2.4   Advanced applications based on CNC and modified CNC

Based on the specific functional groups or materials introduced onto cellulose nanocrystals, we may render the nanoparticles with the desired applications. This section will provide a comprehensive discussion on various emerging applications, such as emulsion stabilizer, catalyst carrier, antimicrobial agents, template for chiral nematic materials and reinforcing fillers for composites.

2.2.4.1 Emulsion stabilizer

Currently there is a strong market trend toward the formulation of products that can maintain the consumer perception of being natural and "green". This has motivated the generation or isolation of biomass-based particles for the formulation of Pickering emulsions (detailed discussion in section 2.3) in food and cosmetic industries. Cellulose nanocrystal is one of the examples that has been proven to be an effective Pickering emulsifier[19]. It can stabilize monodispersed oil (hexadecane) droplets of around 4 μm in water phase against coalescence for 4 months . Further research has shown that cellulose nanocrystals with a charge density greater than 0.03 e/nm^2 were not able to efficiently stabilize oil droplets due to the strong electrostatic repulsions between the nanoparticles located at the oil-water interface. The neutral CNC extracted by HCl hydrolysis performed better than sulphated CNCs at the oil/water interface. Kalashnikova and Capron also investigated the influence of aspect ratio, which was shown to have a direct impact on the interfacial coverage ratio, where low aspect ratio resulted in a dense organization of short nanocrystals at the oil-water interface.[55] Due to the colloidal network structure that forms at the

interface, oil-in-water high internal phase emulsion systems as well as water-in-water emulsions could be stabilized. Very recently, Justin et al.[56] attempted to graft thermo-responsive PNIPAM onto the CNC surface and compared the different nanoparticles for stabilizing the emulsion systems. They found that modified cellulose nanocrystals could stabilize the emulsions for a period of 4 months compared to unmodified CNC nanoparticles. Pelton et al. studied the effects of surfactant or water soluble polymers (hydroxyethyl cellulose or methyl cellulose) on the properties of Pickering emulsions stabilized by cellulose nanocrystals. They found that by adsorbing the polymers, CNC nanoparticles produced emulsions with smaller droplet sizes, and the emulsions could resist coalescence when subjected to multiple cycles of heating and cooling.[57] Very recently, they further coated the emulsified corn oil in water emulsions with tannic acid, which can be transformed into solid dry emulsions via freeze-drying.[58] This work has extended the use of surfactant free emulsions for food, cosmetic and pharmaceutical applications.

2.2.4.2 Antimicrobial agents

Infections by pathogenic microorganisms, especially bacterial, are of great concern in many fields, particularly in medical devices, health care products, water purification systems, food packaging and storage. There is in urgent need to develop antimicrobial agents that can effectively kill or inhibit the growth of pathogenic microorganisms. Cellulose nanocrystal is known to be one of the most abundant natural biopolymers on earth and could be used to fabricate antimicrobial agents due to their biocompatibility and biodegradability. Also by virtue of their high surface area, antimicrobial agents based on cellulose nanocrystals could be implemented in formulations at a relatively lower concentration.

The strategies for fabricating antimicrobial agents is to modify the surface with antimicrobial functional groups, such as silver or zinc oxide nanoparticles, cationic charged polymers, etc. Drogat et al.[59] reported an approach to deposit silver nanoparticles onto the aldehyde functionalized cellulose nanocrystals in which the aldehyde groups could be used to reduce the Ag^+ to Ag^0 in mild conditions. The silver nanoparticles were in the range of 20 to 45 nm and the composite exhibited strong antimicrobial properties. Feese et al.[60] described a cationic porphyrin modified CNC system through "click reactions" between the azide groups on CNC surface and alkyl groups on porphyrin molecules. After the modification, the composite exhibits long lasting photobactericidal properties and could be incorporate into paper, fabrics and plastics, creating novel materials that capable of sterilizing bacteria with high efficiency.

2.2.4.3 Catalyst carrier

The deposition of nanoparticles on the surface of cellulose nanocrystal can generate new hybrid materials suitable for use as heterogeneous catalyst in engineering applications.[61] The use of cellulose nanocrystal in the design of recyclable catalysts is appealing due to the following reasons: (1) high surface area and thermal stability making them as ideal supports; (2) the cellulose chemistry could play important role in reducing the metal species and their chiral properties may enhance selective reactions; (3) the stable colloidal suspension in water can contribute to the stability of the catalyst in aqueous medium; (4) cellulose materials are renewable and relatively cheap.

In summary, using rod-like cellulose nanocrystals as substrate, various kinds catalysts have been prepared, including silver (Ag) nanoparticles[62], gold nanoparticles[63], nickel nanocrystals[64],

palladium nanoparticles[65], TiO_2 nanocubes[66], semiconductor nanoparticles[67] and alloy nanoparticles[68]. They have been widely used in chemical reductions (4-nitrophenol to 4-aminophenol; oxygen reduction reaction; hydrogenation of C-C and C-O multiple bonds), oxidations (benzyl alcohol to benzaldehyde), coupling reactions (Mizoroki-Heck coupling reaction) and photo degradations (methylene blue or methyl orange).[61]

2.2.4.4 Functional materials using cellulose nanocrystals as templates

Hard templating using preformed mesoporous materials (also termed "nanocasting") has emerged as a versatile technique to prepare materials that cannot be accessed through conventional lyotropic template synthesis (e.g., due to hydrolytic instability of precursors). Cellulose nanocrystal dispersion can exhibit lyotropic chiral nematic behavior at a relatively low concentration (e.g., 1-7 wt%), have lower viscosities and form overall shorter time scales when compared to several other cellulose derivatives. This has generated a strong interest in using evaporation-induced self-assembly features to prepare functional mesoporous materials with chiral nematical order. In the templating approach, successive loadings of precursors are infiltrated into a stable mesoporous support, often followed by calcination to construct an interconnected network to produce the desired product. The remaining active components can either be templating materials (CNC) or functional materials introduced into the synthetic steps. Many kinds of ordered mesoporous materials (e.g., carbon, metal oxides, and polymers) can be prepared through hard templating approaches. A summary on the different functional materials is summarized in Table 2.7.

Table 2.3 Summary regarding to functional materials using CNC as templates

Literature	Precursors	Method	Properties or application
Nature, **2010** , 468 , 422-425	TEOS or TMOS	Thermal treatment to remove CNC	Mesoporous Silica film
J. Am. Chem. Soc. **2011**, 133 , 3728-3731	TEOS or TMOS	Remove CNC +Ag NPs filled	Ag assembled in chiral nematic Silica film
Angew. Chem. Int. Ed.**2011**, 50, 10991-10995	TEOS or TMOS	Pyrolysis -remove SiO_2	Mesoporous Carbon
Angew. Chem. Int. Ed. **2012**, 51, 6886-6890	TMOS and $TiCl_4$	Mesoporous silica+$TiCl_4$ infiltration + silica etching	Mesoporous TiO_2
J. Am. Chem. Soc., **2012**, 134, 867–870	Ethylene-bridged organosilica precursors	Remove CNC	Improving mechanical properties and flexibility compared to pure silica
Langmuir **2012**, 28, 17256-17262	TMOS	Remove CNC	Ionic strength for color changing
Angew. Chem. Int. Ed. **2013**, 52, 8912-8916	PAAm hydrogel precursors	EISA (evaporate induced self-assembly)	Hydrogel sensor
Angew. Chem. Int. Ed. **2013,** 52, 8921-8924	Phenol formaldehyde	Remove CNC	Chiral mesoporous photonic resin
Adv. Opt. Mater. **2013**, 1, 295-299	TMOS	Remove CNC	Adding Polyols such as glucose to eliminate the crack
Adv. Funct. Mater. **2014**, 24, 327-338.	TMOS	Remove CNC	Detailed investigation on the conditions for film (pH and ratio)
Adv. Mater. **2014**, 26, 2323-2328.	Phenol formaldehyde	Remove CNC	Chiral nematic Structures and Actuator Properties
Adv. Funct. Mater. **2014**, 24, 777-783	TMOS PVA to reduce the crack	Remove CNC+ CdS QDs	Mesoporous, chiral nematic order and luminescence
Angew. Chem. Int. Ed. **2014**, 53, 8880-8888	Urea formaldehyde	Alkaline treatment to remove UF resin	Mesoporous chiral cellulose material displaying dynamic photonic properties
Anal. Chem., **2014**, 86, 9595–9602	TMOS	Remove CNC	Chiral nematic SiO_2 for Gas Chromatographic separation
J. Am. Chem. Soc., **2014**, 136, 5930–5937	TEOT (Ti)	Remove CNC	Mesoporous TiO_2 film for solar cell

2.2.4.5 Composites reinforced with cellulose nanocrystals

(a) Plastics reinforced with CNC

Nanomaterials like cellulose nanocrystals have been extensively studied for use as reinforcing fillers for numerous polymer matrices to improve their mechanical properties.[13,69] Generally, the cellulose nanocrystal reinforced plastic systems can be divided into two main categories: biodegradable and non-biodegradable as summarized in Figure 2.11. Biodegradable polymers include natural polymers (chitosan, starch, gum arabic, natural rubber etc.) or commonly used biopolymers (PLA, PCL etc.), while polymers from petrochemical sources (PE, PP, PS etc.) contribute to the main part of non-biodegradable polymers. As pristine cellulose nanocrystals are hydrophilic, it is usually straight forward to incorporate them into the hydrophilic systems. However, in order to prevent the agglomeration and adhesion to enhance the composite properties, the introduction of CNC into hydrophobic systems often requires solvent exchange process or surface modifications. Solvent exchange procedure is performed to transform the well dispersed CNC from water to acetone to form organogel, and then introduced the nanoparticles to the desired organic polymer matrices solution. The surface modification of cellulose nanocrystal has discussed in detail in section 2.2.3. The well dispersed mixture of nanoparticle and polymer in organic solvent can be processed in various ways, including solution casting, melting extrusion, elctrospinning and layer-by-layer assembly with improvement in mechanical stiffness, corresponding to an increase of strength and young's modulus.

(b) Hydrogel reinforced with CNC

Polymer hydrogels, bearing some similarities to biological tissues, are soft materials that can absorb up to three orders of magnitude of their dry weight in water. With hydrated and porous characteristics, hydrogels are excellent platforms for various applications, ranging from
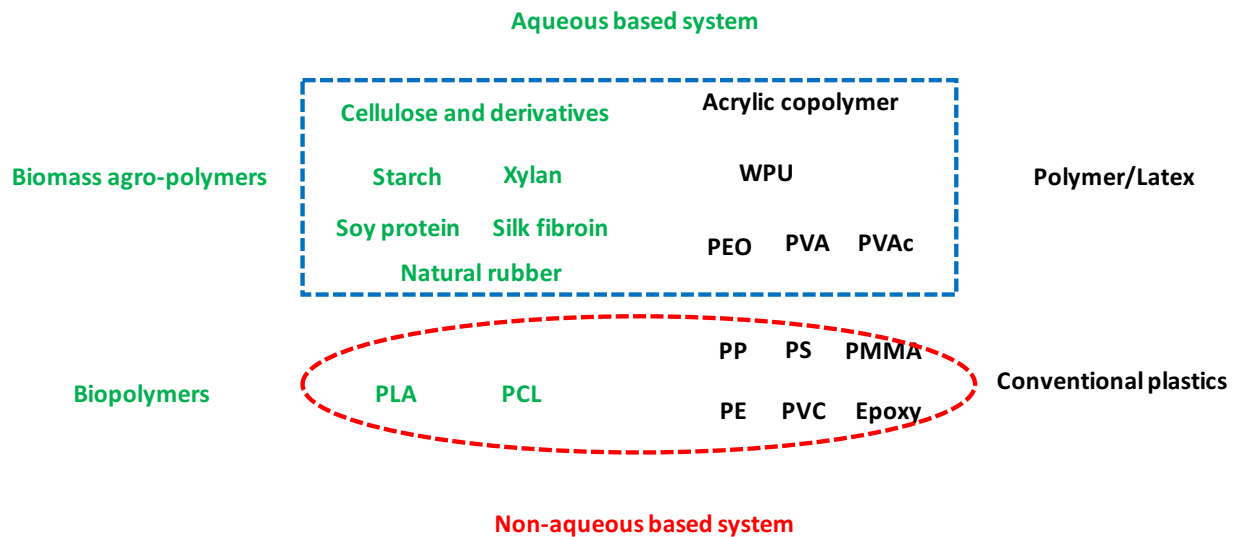
Figure 2.11 Various polymeric matrices used for preparation of CNC reinforced composites. (WPU: waterborne polyurethane; PEO: polyoxyethylene; PVA: poly(vinyl alcohol); PP: polypropylene; PS: polystyrene; PMMA: poly(methyl methacrylate); PE: polyethylene; PVC: poly(vinyl chloride); PLA: poly(lactic acid); PCL: polycaprolactone)

wastewater treatment, tissue scaffold, drug delivery carrier, biosensor and actuators. Due to wet state, their poor mechanical strength and toughness also shortened their life cycle in specific applications. There exists a wide variety of cellulose nanocrystals reinforced hydrogel systems described throughout the literatures, which generally result in improved mechanical properties. Via physical interactions (without no covalent attachment to the hydrogel), CNC has been incorporated into polymer hydrogels based on poly(vinyl alcohol)[70], α-cyclodextrin[71], poly(N-isopropylacrylamide)[72] (PNIPAM), and carboxymethyl cellulose/hydroxyethyl cellulose[73],

poly[oligo(ethylene glycol) methyl ether methacrylate] (POEGMA)[74], poly (N-vinylcaprolactam)[75].

Introducing the nanoparticle into the hydrogel systems through covalent attachment requires the modification of the CNC surface with reactive groups. Yang et al.[76] developed a simple and versatile platform to synthesis composite hydrogels by modifying the CNC surface with silane agent A-174 and subsequently using the exposed vinyl groups to initiate the polymerization. The same methods were applied to different polymer matrices, including polyacrylic acid, polyacrylamide and poly(N,N-dimethylacrylamide)[76–78]. Yang et al. demonstrated a strategy to incorporate CNC nanoparticles into injectable hydrogel system by first functionalizing the CNC surface with aldehyde functional groups and in situ cross-linking the carboxymethyl cellulose matrix by Schiff-base chemistry[79]. The polysaccharide hydrogels are of potential interest in biomedical application, especially in tissue engineering. Very recently, the same chemistry was introduced to POEGMA hydrogel system[80]. By controlling the compositions and conditions necessary in freeze-casting, different hydrogel morphologies were obtained, including fibrillar, columnar and lamellar, which render the hydrogel with anisotropic properties that ca be used to tune the mechanical strength of the hydrogels.

(c) Stimuli-responsive nanocomposites reinforced with CNC

In addition to rendering CNC particles with stimuli-responsive properties, another way of combining these two areas is by incorporating pristine CNC particles into stimuli-responsive matrices. This method can take advantages of high stiffness (an axial Young's modulus ~ 143 GPa[81]) and nanometer dimensions of CNC nanoparticles. Since the first example of using CNCs

as a reinforcing agent for poly(styrene-co-butyl acrylate) reported by Favier et al.[82], it has been introduced to a wide range of polymer matrices, ranging from thermosetting polymers like epoxy resin[83] to thermoplastic polymers such as polyureathane[84]. Due to the sulfate ester groups on the surface, CNCs could be used as stimuli-responsive fillers to produce mechanically or environmentally adaptive polymer nanocomposites, whose stiffness could be manipulated when exposed to different environments. A schematic representation of the reversible mechanism based on a rubbery ethylene oxide-epichlorohydrin 1:1 copolymer (EO-EPI), where a rigid cellulose nanofiber network was incorporated (Figure 2.12).[85] The switching mechanism can be illustrated by changes between "off" and "on" states, which can be regarded as crystal-crystal interactions moderated by sulfate ester groups. The balance of attractive and repulsive interactions is the key factor determining these states. In the "off" state, the nanocomposite is exposed to an aqueous environment and the self-interactions of CNC are "switched off", competitive interactions with solvent molecules dominate. With the evaporation of the solvent, the self- interactions of CNCs are "switched on" and the CNCs transform into a rigid, percolating network. This maximizes the stress transfer within the nanocomposite and increases the overall modulus of the nanocomposite. The same behavior has also been observed in poly(vinyl acetate)[86], poly(butyl methacrylate)[87] and poly(styrene-butadiene)[88] matrices. Furthermore, other than sulfated CNCs, pH-responsive CNCs were incorporated into poly(vinyl acetate) matrices to yield pH-responsive nanocomposite films (Way et al.)[89]. The mechanical properties of these nanocomposites are also influenced in both dry and water swollen states by changes in pH.
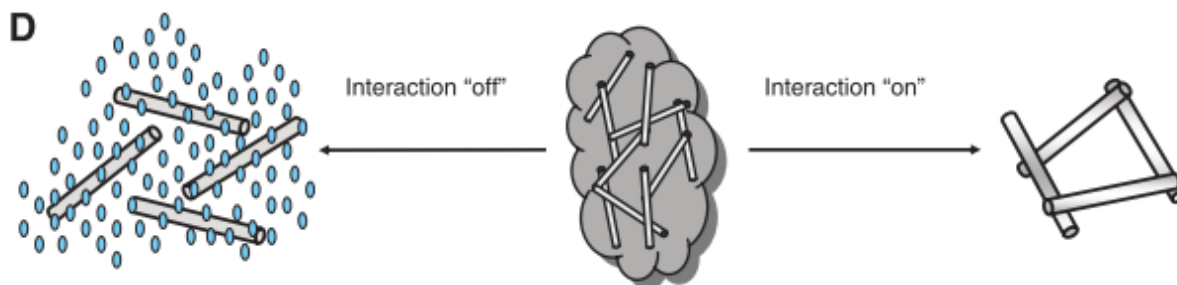
Figure 2.12 Schematic representations of the architecture and switching mechanism in the artificial nanocomposites with dynamic mechanical properties [85]

Unmodified CNCs were used to reinforce a thermally healable supramolecular polymer formed via π-π interactions between an oligomer terminated at both ends with π-electron rich pyrenyl moieties and a chain-folding oligomer containing pairs of π-electron deficient naphthalene-diimide units.[22] It was found that all CNC reinforced nanocomposites could be repaired after damage when exposed to elevated temperatures, where the mechanical properties were greatly enhanced with CNCs. Light-healable, supramolecular nanocomposites reinforced with CNCs have also been reported based on a telechelic poly(ethylene-co-butylene) functionalized with hydrogen-bonding ureidopyrimidone (UPy) and CNCs functionalized with the same binding motif. [90] The reinforced nanocomposites displayed improved mechanical properties, and when they were exposed to ultraviolent radiation, the UPy motifs caused a temporary disengagement of the hydrogen-bonding motifs resulting in a reversible reduction in the molecular weight and viscosity of the supramolecular polymers. More recently, Souleymane et al.[23] reported on the preparation and characterization of light-healable nanocomposites based on cellulose nanocrystals (CNCs) and a metallosupramolecular polymer (MSP) assembled from a telechelic poly(ethylene-co-butylene) that was end-functionalized with 2,6-bis(1'-methyl-benzimidazolyl) pyridine (Mebip) ligands and $Zn(NTf_2)_2$ (see Figure 2.13). The introduction of CNCs into the MSP matrix leads to a significant

37

increase of the stiffness and strength, from 52 and 1.7 MPa for the neat polymer to 135 and 5.6 MPa upon the introduction of 10% w/w CNCs.
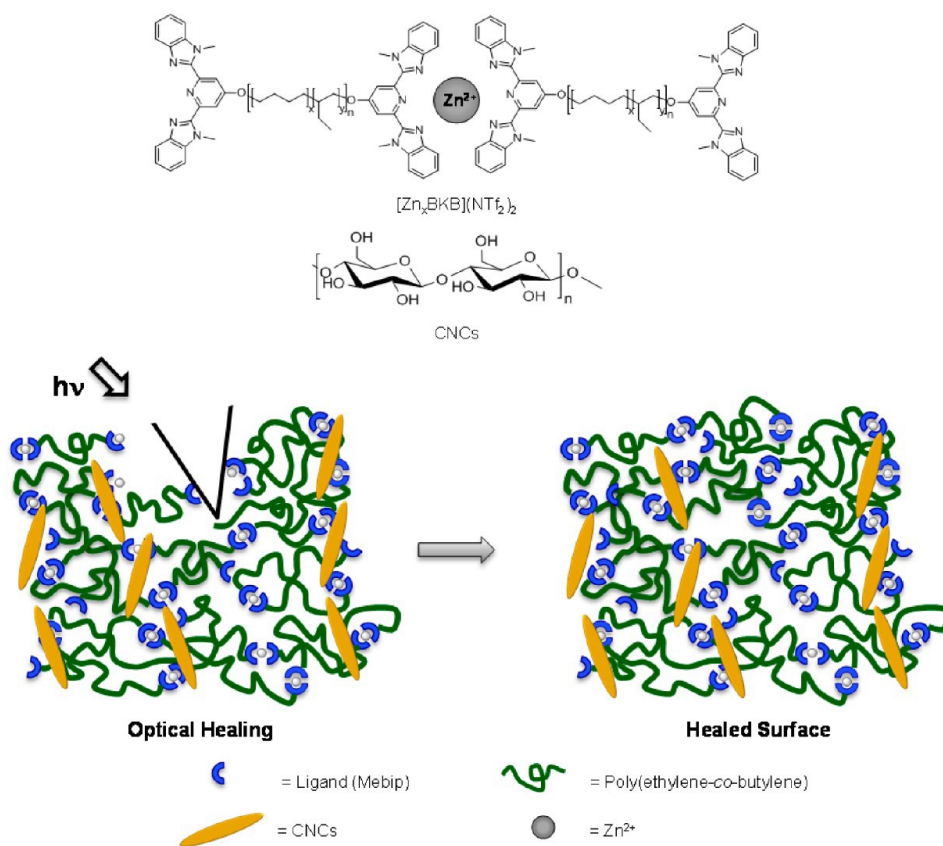
Figure 2.13 Chemical structure of the metallopolymers $[Zn_xBKB](NTf_2)_{2x}$ and the CNCs and a schematic representation of the metallosupramolecular nanocomposites [23].

2.3   Pickering emulsions

2.3.1   General concept

Emulsions play an important role in a number of industrial processes and commercial products where immiscible liquid phases coexist. Conventionally, emulsions are stabilized by the addition of molecular surfactants or amphiphilic polymers, which adsorb at the oil/water interface and impede the coalescence of emulsified droplets by introducing electrostatic and steric repulsive forces. However, the cost of surfactants is typically high and, in most circumstances, their recovery is not practical[91]. Additionally, it is well known that some surfactants induce tissue irritation and even cell damage, making their use in biomedical applications a major concern[92,93]. In the late nineteenth and early twentieth centuries, Haynes, Bessel, Ramsden and Pickering reported on a new classification of emulsions, presently termed Pickering emulsions, wherein solid colloidal particles were observed to adsorb at the oil/water interface and provide emulsion stability[93–98]. Because Pickering emulsions retain several of the basic properties of conventional emulsions, they can, in many cases, be substituted for surfactants. This makes them an attractive alternative in a number of industries seeking to avoid the use of surfactants[92,98–100]. They also open the door for new techniques to prepare functional nanomaterials. Throughout the past century, a considerable amount of interest and effort have been devoted to advancing our understanding and development on this interesting system[92,97,98,101].

The preparation of a Pickering emulsion involves the dispersion of solid particles into the continuous phase of an emulsion, and based on their partial wettability in each of the two immiscible phases, they adsorb at the oil/water interface to form an effective steric and electrostatic

protective shield for the emulsified droplets. Pioneering work in the field revealed that the type of emulsion formed, i.e. oil-in-water (o/w) or water-in-oil (w/o) could be predicted based on the preferential wettability of the emulsifier. For particles more easily wetted by the water phase, it was observed that they would reduce their contact with the oil phase, causing the interface to curve and form spherical oil droplets. The opposite would occur for more lipophilic particles. While the size of droplets in traditional surfactant stabilized emulsion systems is typically submicrometer, droplets in Pickering emulsions are frequently on the order of micrometers[102]. Analogous to the hydrophilic-lipophilic balance (HLB) parameter used to describe the preferential wettability of a surfactant molecule at an oil/water interface, the three-phase contact angle of a solid particle situated at an oil/water interface may also be used[91]. The contact angle measured at the water phase, θ_w, is given by the Young's equation shown below (Eq. 2.1):

$$\cos\theta_w = \frac{\gamma_{s/o} - \gamma_{s/w}}{\gamma_{o/w}} \qquad\qquad \text{Equation 2.1}$$

where $\gamma_{s/o}$, $\gamma_{s/w}$, and $\gamma_{o/w}$ are the solid/oil, solid/water, and oil/water interfacial energies, respectively. For more hydrophilic particles, θ_w is typically less than 90º and the majority of the particle is wetted by the water phase. For more lipophilic particles, θ_w is typically greater than 90º and more of the particle surface is wetted by the oil phase. Particles equally wetted by both phases result in θ_w being equal to 90º. In such a case, the oil/water interface is effectively planar (Figure 2.14). Complete wetting of the particle in either phase results in particle instability at the interface. In this case, the particles become completely dispersed in a single phase, and stable emulsions cannot be achieved[91]. In general, more hydrophilic particles, such as metal oxides and silica, can stabilize o/w emulsions, and more lipophilic particles, such as carbon black, can stabilize w/o emulsions[19,20,103–108]. Optimum stability in a Pickering emulsion system may be obtained when the contact angle approaches 90º, but retains some degree of preferential wettability for one phase

over the other. In fact, studies by Kaptay[109] suggested that the optimum θ_w for stabilizing o/w emulsions is 70-86° and 94-110° for stabilizing w/o emulsions.
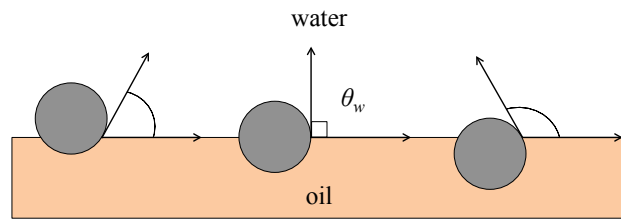
Figure 2.14 Position of a small spherical particle at an oil/water interface with a contact angle measured into the water phase of < 90° (left, hydrophilic), equal to 90° (center, equally hydrophilic and lipophilic), > 90° (right, lipophilic).

Binks[91] showed that for small particles (less than 2 µm), gravitational effects may be neglected, such that the amount of energy ΔE required to remove a solid spherical particle of radius r from the oil/water interface is (Eq. 2.2):

$$\Delta E = \pi r^2 \gamma_{o/w} (1 \pm \cos \theta_w)^2 \qquad \text{Equation 2.2}$$

where $\gamma_{o/w}$ is the oil/water interfacial tension and θ_w is the three-phase contact angle measured into the water phase. The sign preceding $\cos \theta_w$ is negative for particle removal to the water phase and positive for particle removal to the oil phase. From this equation, it may be concluded that the energy of adsorption of a particle at an interface is always greater than the particle's thermal energy, even in the case of very small solid particles. For example, the amount of energy required to remove a 10 nm solid spherical particle from a hydrocarbon/water interface ($\gamma_{o/w}$ = 50 mN·m^{-1}, θ_w = 90°) is ΔE = 1.6 × 10^{-17} J, which is orders of magnitude greater than kT (4.1 × 10^{-21} J at 293 K). Thus, solid particles, once attached to the oil/water interface, can be thought of as irreversibly adsorbed. This is in contrast to surfactant molecules, which adsorb and desorb on a relatively fast timescale[91]. Pickering emulsion stability is influenced by a number of factors,

including θ_w, particle concentration, particle size and shape, the ratio of oil to water phase, and ionic strength[91].

There exists a wide variety of Pickering emulsion systems described throughout the literature, spanning inorganic, organic, and hybrid nanoparticles, the details of which are briefly summarized in Table 2.4. Since the types of Pickering emulsifiers have been reported previously[92,99], several notable examples are presented here.

2.3.2 Stimuli-responsive Pickering emulsion

For some applications, for example bitumen emulsification or food storage, long-term emulsion stability is critical. However, in other cases, such as oil recovery[110], liquid phase heterogeneous catalysis[111], and emulsion polymerization[112], only temporary stability is desired. In these instances, additional physical and/or chemical disruption mechanisms must be introduced into the system to destabilize the emulsion, which demand increased capital and operating costs. In an effort to simplify the demulsification process, much research has been devoted to the development of Pickering emulsifiers that activate and deactivate in response to external stimuli. In many cases, the surface properties of the solid particles undergo some physical or chemical transformation in response to environmental triggers that, in turn, alter the wettability of the particles. This enables the remote control of the emulsion characteristics from the bulk of the system. It also allows for the recovery and reuse of emulsifiers, which helps to achieve a more sustainable operation. In this section, a concise, but comprehensive review of stimuli-responsive Pickering emulsion systems recently reported in the literature is presented.

Table 2.4 A brief summary of Pickering emulsifiers

Particle type		Particles	Emulsion Type	References
Inorganic	Silica	Fumed silica	o/w or w/o	91,108
	Metal oxide	Carbonyl iron particles	o/w	102
		Fe$_3$O$_4$ nanoparticles	w/o	103,113
		TiO$_2$	o/w	114
		CuO	o/w	115
	Clay	Montmorillonite (MMT)	o/w	107,116
		Laponite RD	o/w	117
		Layered double hydroxide (LDH)	o/w	118
	Carbon	Carbon nanotube (CNT)	w/o	119
		Graphene oxide (GO)	o/w	120
		Carbon black (CB)	w/o	105,106
Organic	Protein	Bovine serum albumin coupled with PNIPAM	o/w	121
	Polysaccharide nanocrystals	Cellulose nanocrystals	o/w	19,20,55
		Chitin nanocrystals	o/w	122
		Starch nanocrystals	o/w	123
	Polymeric	Poly(divinylbenzene-methacrylic acid) (P(DVB-MAA)) particles	w/o	124
		Polystyrene (PS) or poly(methyl methacrylate) (PMMA) nanoparticles	w/o	125
		Poly{(styrene-alt-maleic acid)-co-[styrene - (N-3,4-dihydroxyphenylethyl-maleamic acid)]} (P(SMA-Dopa))	o/w	126
Composite/ hybrid		Ag$_3$PO$_4$/MWNT nanohybrid	w/o	127
		Lightly crosslinked Poly(4-vinylpyridine) (P4VP)-Silica Nanocomposite Microgels	o/w	128

2.3.2.1 pH-responsive systems

Special attention has been devoted to the development of pH-responsive Pickering emulsions, as they are one of the simplest and most readily implementable stimuli-responsive systems (Table 2.5). A particle is considered pH-responsive when its surface chemistry undergoes some type of

43

modification in response to changes in proton concentration[129], which then alters the way the material interacts with its surroundings. A wide array of materials has been explored as pH-responsive Pickering emulsifiers, including unmodified organic[126,130,131] and inorganic[132,133] nanoparticles, non-covalent[118,134–139] and covalent[140,141] surface functionalized nanoparticles, and self-assembled particles and micelles[96,142–146].

A number of unmodified nanoparticles possess pH-responsive behavior. For instance, graphene oxide (GO) particles were recently proposed as pH-responsive Pickering emulsifiers by Kim and coworkers[120] (Figure 2.15). As a result of the carboxylate moieties located on the perimeter of the particles and the overall lipophilicity of their basal plane, GO particles possess amphiphilic properties. The authors reported on the size dependent amphiphilicity of GO, concluding that small sheets (≤ 1 µm) were hydrophilic enough to stabilize o/w emulsions for extended periods of time, i.e. months, in neutral pH. Acidification of the aqueous phase reportedly resulted in protonation of the edge-bound carboxylates on GO. This caused the particles to be ejected from the interface into the oil phase, resulting in emulsion destabilization and macrophase separation. Similarly, the addition of strong base caused the GO to become more hydrophilic and for pH > 10, the particles were observed to migrate to the aqueous phase, again resulting in droplet coalescence. Liu and coworkers[131] investigated the use of chitosan nanoparticles to stabilize a variety of o/w emulsions, e.g. liquid paraffin, n-hexane, toluene, and dichloromethane. The authors observed that for neutral and basic conditions, i.e. pH > 6, the particles were able to provide emulsion stability for greater than two months. Acidification, however, resulted in particle removal to the aqueous phase resulting in rapid demulsification. The pH-responsive behavior of the particles was attributed to the protonation and deporotonation of the primary amine groups on deacetylated chitosan monomers under acidic and mildly basic conditions, respectively.

Table 2.5 pH-responsive Pickering emulsion systems

Particles	Modifiers	References
Layered double hydroxide (LDH)		118
Graphene Oxide		120
P(SMA-Dopa) random copolymer		126
P4VP-SiO$_2$ composites		128
Colloidal particles from the water-insoluble protein zein		130
Chitosan NPs		131
Montmorillonite	γ-methacryloxy propyl trimethoxysilane	133
Hydroxyapatite NPs		132
Alumina-coated silica NPs (Ludox CL)	Potassium hydrogen phthalate (KHP)	134
PS latex	PMMA-PDMA as stabilizer	135
PS latex	PMMA-PDMA as stabilizer *	136
Silica NPs	8-hydroxyquinoline (8-HQ)	137,139
Alumina or silica colloids	Poly(methacrylic acid sodium salt) & poly(allylamine hydrochloride)	138
Silica NPs	Mixed organosilanes	140
Silica NPs	P(St-b-2VP-b-EO)	141
P(tert-butylaminoethyl methacrylate) latex		142
P(2-(tert-butylamino) ethyl methacrylate) (PTBAEMA) microgel		143
Self-assembled micelle	P(EO-b-GMA-b-DEA)	144
Self-assembled particles	PU-g-PDEM	145
PS-PAA Janus particles		146
Colloidal silica particles	Sulfonated poly(styrenesulfonate)	147
Opposite charged microgel P(NIPAM-MAA) and P(NIPAM-AEM)		148
Alkaline lignin		149
Partially hydrophobic silica NPs		150
Mg(OH)$_2$ NPs		151
P(St-alt-MAn)-co-P(VM-alt-MAn) *	Self-assembled and crosslinked particle	152
Fe$_3$O$_4$ NPs	Coated with olelic acid	153
Alginate	Chitosan	154
Silica NPs	Mixed brush	155

* PMMA-PDMA: Poly(Methyl methacrylate)-poly(2-(dimethylamino)ethyl methacrylate); P(St-alt-MAn)-co-P(VM-alt-MAn): Poly-(styrene-alt-maleic anhydride)-co-poly (7-(4vinylbenzyloxyl)-4-methylcoumarin-alt-maleic anhydride); NPs- nanoparticles
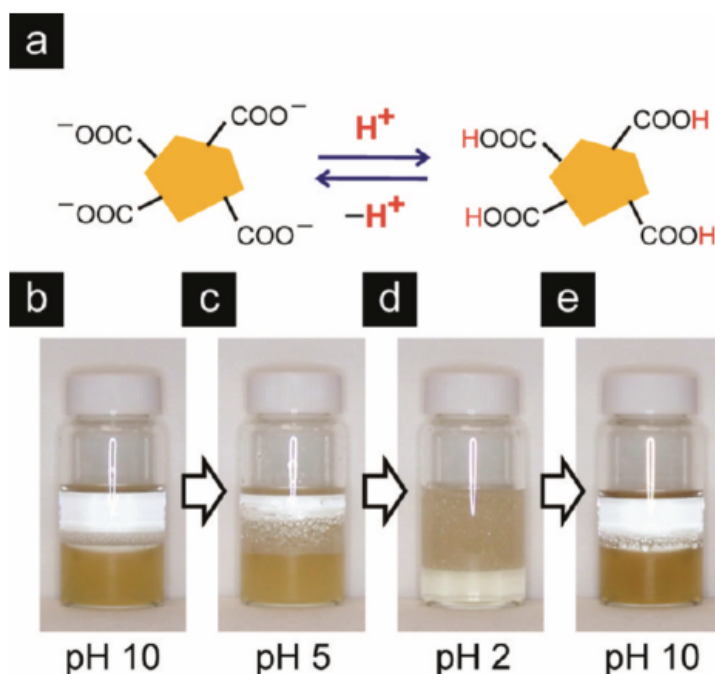
Figure 2.15 (a) Schematic illustration demonstrating the pH-responsive amphiphilicity of GO resulting from protonation and deprotonation of edge-bound carboxylate moieties; (b-e) Digital photographs demonstrating the pH-responsiveness of a toluene-in-water emulsion stabilized by GO[120].

While some nanoparticles alone, such as those discussed above, possess pH-responsive surface behavior, surface functionalization is one way of rendering non-responsive particles with a broad range of pH-responsive properties. The modification of nanoparticles may be achieved through non-covalent, i.e. electrostatic interactions, hydrogen bonding, and van der Waals forces, or covalent bonding. Li and Stöver[134] (Figure 2.16) described a simple and reversible emulsifier based on the interaction between commercially available alumina-coated silica nanoparticles (Ludox CL) and the small molecule potassium hydrogen phthalate (KHP). Under mildly acidic conditions, i.e. $3.5 \leq pH \leq 5.5$, the negatively charged KHP bound reversibly with the positively charged nanoparticle surface, rendering the particles partially hydrophobic. Under strongly acidic conditions, the KHP was primarily present in its protonated form and the electrostatic driving force

for binding was eliminated. Similarly, under neutral and basic conditions, the deprotonation of the nanoparticles diminished the nanoparticle-KHP binding. In the absence of KHP binding, the nanoparticle surface was observed to be strongly hydrophilic and was no longer stable at the oil/water interface. Amalvy et al.[135,136] successfully synthesized well-defined tertiary amine methacrylate-based block copolymers that adsorbed onto polystyrene latex nanoparticles, with the hydrophobic block bound on the particle surface and hydrophilic segment directed outward to provide steric stabilization. The prepared functionalized latexes were employed as Pickering emulsifiers for stabilizing o/w emulsions. They attributed the pH-responsive functionality to the presence of the steric stabilizer, which, under neutral conditions, possessed an affinity for the oil phase. Acidification of the system resulted in the desorption of the particles from the interface, resulting in droplet coalescence. Haase et al.[139] (Figure 2.17) also reported on a pH-responsive Pickering emulsion system that could stabilize o/w emulsions within a narrow pH window ($4.5 \leq$ pH ≤ 5.5). The stabilization of oil droplets was achieved by increasing the hydrophobicity of silica particles (Lumox TMA) through electrostatically driven adsorption of 8-hydroxyquinoline (8-HQ) onto the particle surface. However, when the pH was increased beyond 5.5, insufficient adsorption of 8-HQ resulted in unstable emulsions. Lowering the pH to 4.4 caused the formation of an 8-HQ bilayer on the particle surface, resulting in rehydrophilization and emulsion destabilization. The authors also reported a size dependency of the emulsion droplets as a function of pH. For pH > 5.5, a monomodal size distribution was observed, with the droplets on the order of 12 μm in diameter. Reduction in pH resulted in the presence of smaller droplets on the order of 4 μm in diameter. This bimodal distribution existed for $4.5 \leq$ pH ≤ 5.5. For pH < 4.5, a monomodal size distribution was observed, with only the smaller droplets present. These changes in droplet size reflect the observed changes in the emulsifier particle surface as a function of pH. In another work,

Haase et al.[138] modified alumina and silica particles with the weak polyelectrolytes poly(methacrylic acid sodium salt) and poly(allylamine hydrochloride). The affinity of modified particles to the oil/water interface was influenced by the dissociation and thickness of the adsorbed polyelectrolyte layer. The authors claimed that the dependence of the droplet size on pH and the thickness of coating layer could be explained by particle aggregation, particle wetting, and oil phase polarity.
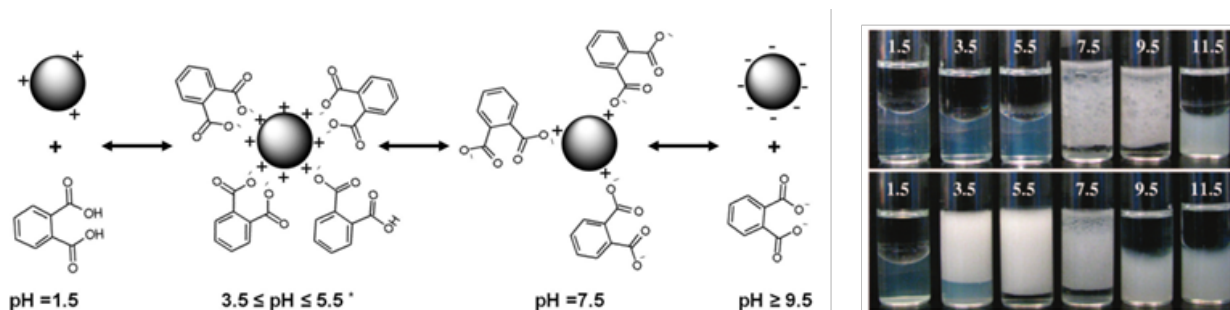
Figure 2.16 (Left) Schematic illustration demonstrating the pH-responsive interaction between Ludox CL nanoparticles and KHP. (Right) Digital photographs demonstrating the pH-responsiveness of xylene-in-water emulsions stabilized by Ludox CL nanoparticles in the absence (upper row) and presence (lower row) of KHP[134].
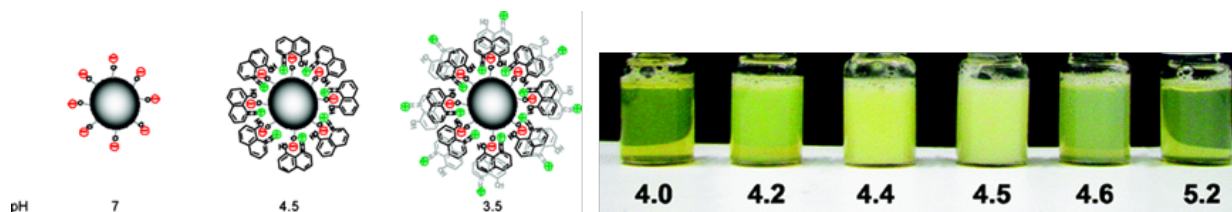
Figure 2.17 (Left) Schematic illustration demonstrating the pH-responsive interaction between Ludox TMA nanoparticles and 8-HQ. (Right) Digital photographs demonstrating the pH-responsive stability of Ludox TMA solutions in the presence of 8-HQ.[139]

Yang et al.[140] investigated the covalent surface functionalization of silica microspheres with organosilanes for use as heterogeneous solid catalysts that could repeatedly be separated and

recycled by phase transfer (Figure 2.18). Both the hydrophobic $(MeO)_3Si(CH_2)_7CH_3$ and the relatively hydrophilic and pH-responsive $(MeO)_3SiCH_2CH_2CH_2(NHCH_2CH_2)_2NH_2$ were surface grafted onto the particles. By varying the molar ratio of hydrophilic and hydrophobic organosilane brushes, the authors obtained the desired surface chemistry for in-situ separation and recycling of submicrometer-sized solid catalysts simply by tuning the emulsion pH. The emulsion catalysis system displayed good reversibility in response to pH and a high yield for hydrogenation of styrene after 36 reaction cycles. Motornov et al.[141] also reported a brush-grafted nanoparticle system (Figure 2.19). Silica nanoparticles were surface grafted with the multifunctional triblock copolymer, poly(styrene-block-2-vinly-pyridine-block-ethylene oxide) (P(S-b-2VP-b-EO)). The emulsions could undergo o/w to w/o transitions in response to pH changes, allowing for direct control over the emulsion stability. Under acidic conditions, i.e. pH < 3, o/w emulsion could be stabilized as a result of the protonation of the P2VP block, making the particle surface more hydrophilic. Adjusting the pH to more neutral and basic conditions, i.e. pH > 4, caused deprotonation of the P2VP block, which resulted in a more lipophilic particle surface, causing the observed o/w to w/o phase inversion.
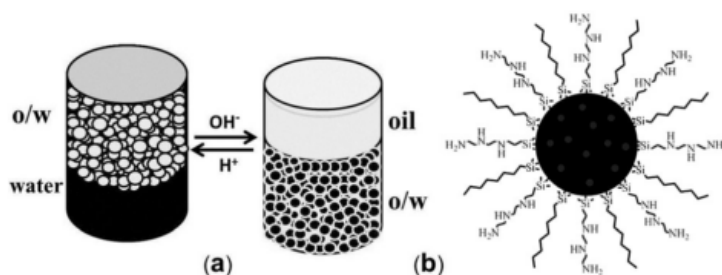
Figure 2.18 (a) Schematic illustration demonstrating the pH-responsive phase inversion of emulsions stabilized by organosilane-functionalized silica microspheres; (b) Combinatory organosilane grafting strategy using $(MeO)_3Si(CH_2)_7CH_3$ and $(MeO)_3SiCH_2CH_2CH_2(NHCH_2CH_2)_2NH_2$ [140].
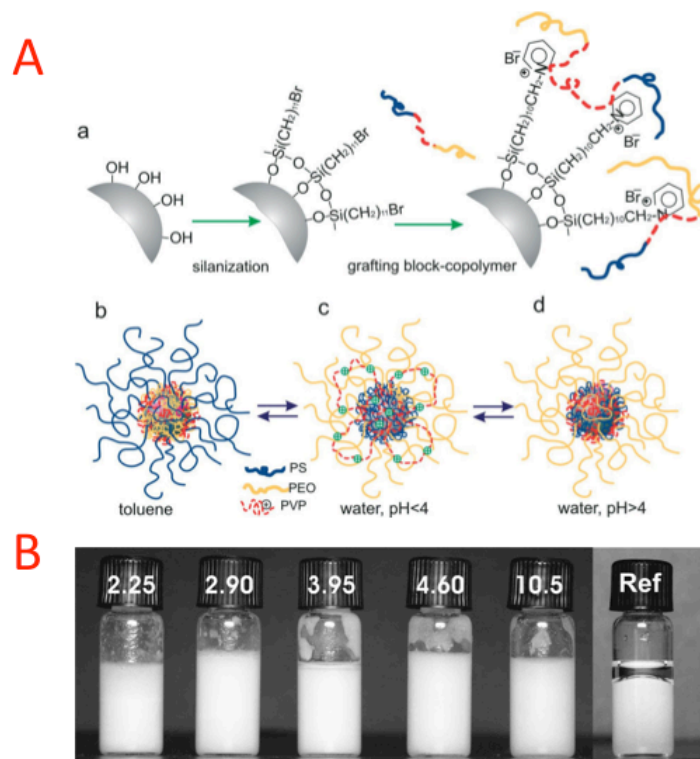
Figure 2.19 (A) (a) Strategy used to graft copolymers onto the surface of silica nanoparticles; (b-d) schematic illustration demonstrating the solvent and pH-responsiveness of the copolymer-functionalized nanoparticles. (B) Digital photographs of toluene-in-water emulsions stabilized by P(S-b-2VP-b-EO) surface grafted silica nanoparticles over a range of pH values[141].

Pickering emulsifiers derived from self-assembled structures or crosslinked microgels have also shown the ability to stabilize and destabilize emulsions in response to pH changes[96,142–146]. Fujii et al.[144] successfully synthesized a poly[(ethylene oxide)-block-glycerol monomethacrylate-block-2-(diethylamino)ethyl methacrylate] (P(EO-b-GMA-b-DEA)) triblock copolymer using ATRP, which was observed to self-assemble into micelles in aqueous solution (Figure 2.20). Crosslinking the shell (PGMA block) of the micelle via amidation reaction with succinic anhydride (SA) yielded core-shell nanoparticles, with the hydrophobic PDEA blocks located within the core of the micelle. PSAGMA and PEO blocks composed the inner and outer coronas of the particle, respectively. These shell crosslinked (SCL) micelles were used to stabilize o/w emulsions at pH 8-9.

50

Acidification of the system caused the emulsion to rapidly coalesce. The authors attributed the demulsification behavior to the protonation of the PDEA core, which caused the particles to swell into cationic nanogels, resulting in the detachment of SCL from the oil/water interface. Ma et al.[145] reported on the design and use of an amphiphilic polyurethane-graft-poly[2-(dimethylamino)ethyl methacrylate] (PU-g-PDEM) copolymer that self-assembled in water to form core-shell nanoparticles, with the hydrophobic PU blocks bound within the core and the hydrophilic PDEM blocks radially directed outward (Figure 2.21). The PDEM side chains on the shell were observed to undergo conformational changes into a collapsed state in response to increasing pH. This inhibited the adsorption of nanoparticles onto the interface due to changes in the wettability, inducing demulsification. Thus, w/o emulsions with average droplet size of 10 µm can be found for pH 8-9, while o/w emulsions with average droplet size of 30-40 µm may be observed for pH > 9 or pH < 5. At pH 7, coalescence occurred after 24 hours. Tu and Lee[146] fabricated amphiphilic polymeric Janus particles, with one side predominantly comprised of hydrophobic styrene and the other consisting of the hydrophilic, pH-responsive acrylic acid. The authors demonstrated that the Janus particles could alter their aggregation and dispersion behaviors in response to changes in pH. Under acidic conditions, the acidic surface of the particles is protonated, allowing the particles to be more easily wetted by the oil phase resulting in the stabilization of w/o emulsions. Under basic conditions, the acrylic acid undergoes deprotonation, which stabilizes o/w emulsions. It was observed that the droplet size for the o/w emulsion was much greater than those observed in the w/o emulsions. The authors attributed this phenomenon to the strong electrostatic charge repulsion between Janus particles in alkaline conditions.
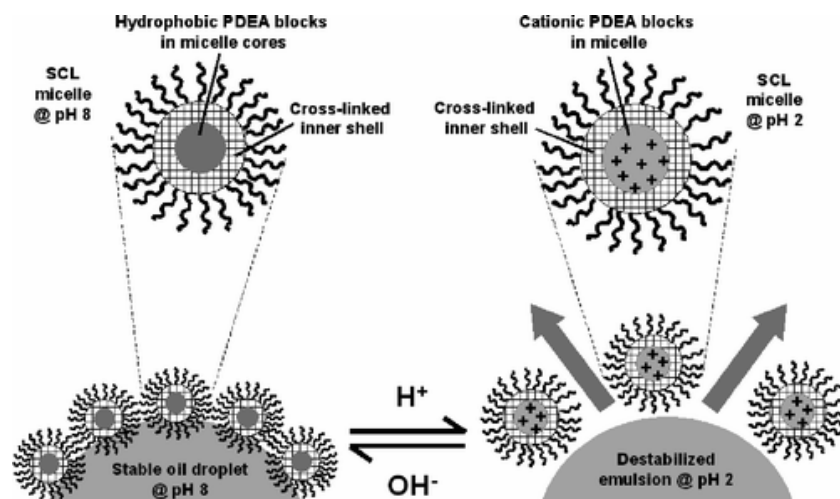
Figure 2.20 Schematic illustration of the pH dependence of 1-undecanol-in-water emulsions stabilized by shell crosslinked micelles[144].
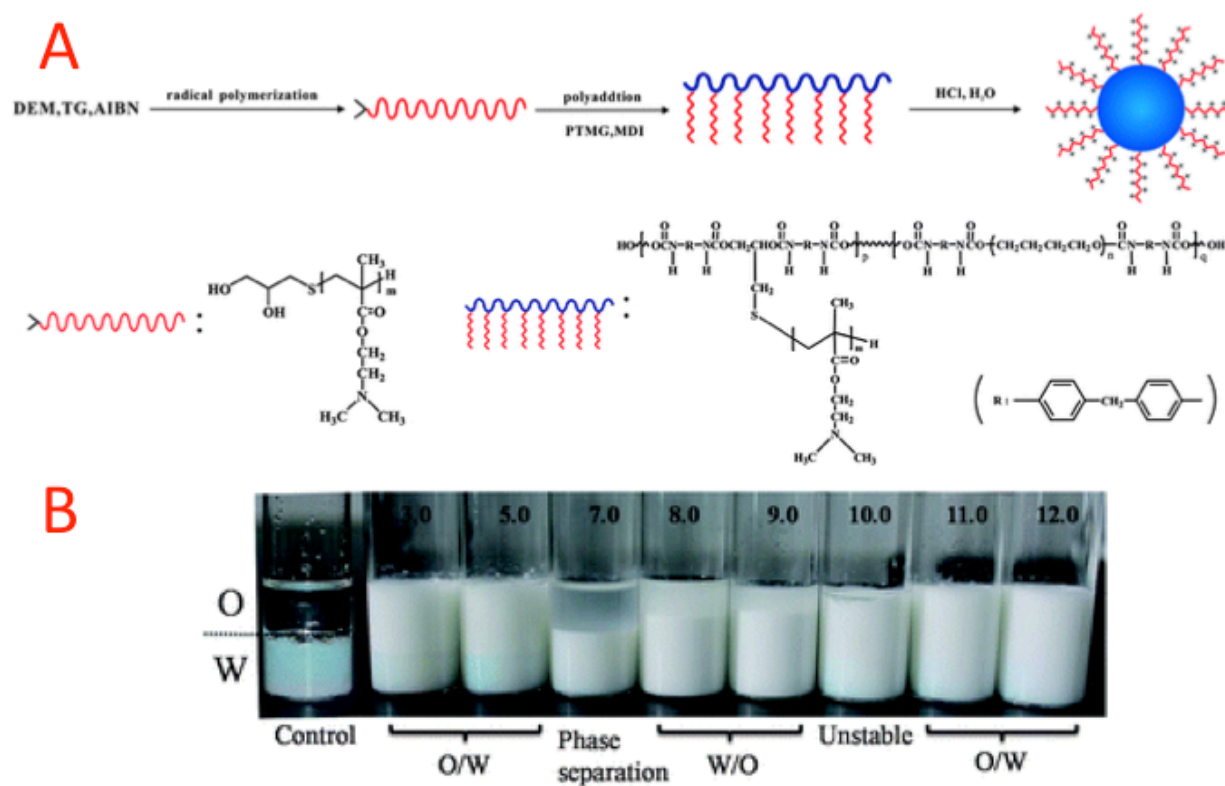
Figure 2.21 (A) Strategy used to prepare self-assembled PU-g-PDEM nanoparticles in water. (B) pH-responsive phase inversion of styrene-water emulsions stabilized by self-assembled PU-g-PDEM nanoparticles[145].

In general, pH-responsive Pickering emulsion systems benefit from their simplicity and the breadth of well-reported materials available for use. In all cases, simply tuning the pH of the system results in some change in the surface behavior of the particles caused by the protonation or deprotonation of pH-responsive functional groups present in the system. Non-functionalized pH-responsive nanoparticles, such as GO[120] and chitosan[131], may be prepared with relative ease and minimal cost. This opens the door for their use in a range of industrial applications, where high quantities of emulsifier would be required. Further, because these emulsifier systems do not rely on complexation with small molecules or polymers to elicit pH-responsiveness, their stability and usable lifetime are likely greater, lending to more sustainable emulsifier recyclability. Composite emulsifiers, such as surface-functionalized nanoparticles[140,141] and self-assembly systems[96,142–146], often require more intensive procedures for preparation. Ultimately, it is expected that this would result in a higher material cost, perhaps limiting their application. However, they also have the potential to be tailored for specific situations, wherein precise control or a narrow transition range is desired. For certain high-value applications, the ability to prepare tailored emulsifier particles may warrant their use.

While pH-responsive systems are simple, well studied, and diverse, most face a number of limitations with respect to their applicability. For instance, it is likely for the cyclability of these systems to be limited to some finite value due to inherent increases in the ionic strength of the solution that results from repeated additions of acid and base. The increased addition of free ions in colloidal systems above a critical concentration often results in a phenomenon known as "salting out", wherein the electrostatic repulsion that stabilizes dissolved colloidal particles in solution is shielded and no longer remains effective[134]. This triggers aggregation of the particles, causing them to lose their functionality as emulsifiers. Another limitation that pH-responsive systems face

is their inability to be applied in sensitive environments, such as biological systems[130,131]. Further, the addition of acid or base to control the properties of emulsions alters the total volume of the system, diluting the chemical species already present. In many cases, this may be undesirable for the operator. While this would likely remain insignificant for high-volume systems, it may be appreciable for systems of lower volume.

2.3.2.2 Thermo-responsive systems

Temperature is another commonly investigated stimulus used to control Pickering emulsion stability. While pH adjustment requires the direct addition of acid or base to an emulsion, temperature adjustments may be easily applied without directly affecting the chemical composition of the system. This is an attractive approach for systems sensitive to pH or ionic strength. Some of the strategies used to design pH-responsive systems can similarly be applied to thermo-responsive systems. Thermo-responsiveness is commonly achieved by surface grafting with polymers that exhibit well-documented thermo-responsive properties, such as poly[2-(dimethylamino)ethyl methacrylate], poly(N-isopropylacrylamide), and poly(oligo-ethylenenoxide) methacrylates (Table 2.6).

Table 2.6 Thermo-responsive Pickering emulsions

Particles	Modifiers	References
PS latex	PMMA-PDMA	156
PNIPAM microgel	PDMAEMA	157
Silica nanoparticles	PDMAEMA	158
PS latex	PNIPAM	159
PNIPAM and P(NIPAM-MAA) microgels		160
PNIPAM microgel		161
Cellulose nanocrystal (CNC)	PNIPAM	56

Binks et al.[156] were among the first to describe a system that used temperature as a trigger to modulate Pickering emulsion stability. They reported on polystyrene (PS) latex particles sterically stabilized by a monodisperse diblock copolymer, poly[2-(dimethylamino)ethyl methacrylate-block-methyl methacrylate] (PDMAEMA-b-PMMA). The hydrophobic PMMA block was anchored onto the surface of the latex particles by physical adsorption and the free PDMAEMA block was used to tune the surface properties of the particle. PDMAEMA homopolymer exhibits a lower critical solution temperature (LCST) between 32 to 46 °C, above which the polymer becomes immiscible in aqueous solution[162]. By increasing the temperature, the polymer-coated particles were observed to increase in hydrophobicity, causing emulsion inversion from o/w to w/o. The average size of the particles was observed to increase from 76 to 113 μm as the temperature of the system increased from 25 to 50 °C, the temperature in which emulsion inversion was observed. For temperatures greater than 50 °C, the w/o droplets were observed to be smaller than the o/w droplets observed below the LSCT. Saigal et al.[158] reported on similar studies, wherein o/w emulsions were stabilized by PDMAEMA surface grafted SiO_2 nanoparticles. ATRP was used to polymerize PDMAEMA brushes from the nanoparticle surface. The authors observed a critical flocculation temperature (CFT) of approximately 50°C, which resulted in the rapid destabilization of emulsions at elevated temperatures. A variety of environmental factors, such as grafting density, pH, ionic strength, and oil phase composition, were observed to influence the stability of the emulsions. Due to its biocompatibility and sharp temperature-induced phase transition, PNIPAM is another thermo-responsive polymer that has been explored as a surface modifier of nanoparticles for Pickering emulsion systems. The amide groups present on PNIPAM make it water-soluble when the solution temperature is below 32 °C, but insoluble above this temperature. The driving force for precipitation at high temperature is the entropy gained by the release of water molecules

that are partially immobilized by the isopropyl moieties of PNIPAM. Tsuji et al.[159] investigated the surface initiated graft polymerization of PNIPAM from polystyrene (PS) nanoparticles to produce thermo-responsive Pickering emulsifiers. The particles reportedly were able to stabilize a variety of o/w emulsions for more than three months at room temperature. However, microscopic phase separation was observed to occur immediately when the temperature was increased to 40 ºC, at which point the surface grafted PNIPAM would undergo a coil-to-globule transition, leading to particle instability at the interface. In a study by Zoppe et al.[56], PNIPAM was grafted to the surface of cellulose nanocrystals (CNC) via surface-initiated single-electron transfer living radical polymerization (SI-SET-LRP). The resulting particles were found to be extremely stable at the oil/water interface, maintaining emulsion stability for up to four months at room temperature. Again, the emulsions were observed to rapidly destabilize at temperatures above the LCST of PNIPAM.

Thermo-responsive systems generally benefit from the fact that temperature is an intensive variable. The temperature of the system may be easily changed without altering its volume or composition. This is particularly useful when a high degree of cycling is required. Emulsions may be stabilized, destabilized, and inverted, all without changing the pH and chemical makeup of the system. Biphasic emulsion-stabilized catalysis, wherein the contents of the system undergo repeated cycling, is one application where non-invasive stimuli, such as temperature, would be of particular interest. An apparent limitation to thermo-responsive systems, however, is the energy requirements for controlling the temperature of the system. For systems of greater volume, the amount of energy required for heating and cooling becomes much more appreciable. However, many thermo-responsive Pickering emulsifier systems may be tailored to have relatively low

temperature transitions close to ambient conditions, potentially reducing the energy requirements of the system.

Table 2.7 CO_2-responsive Pickering emulsions

Particles	Modifiers	References
Silica nanoparticles	N'-dodecyl-N,N-dimethylacetamidine	[163]
Silica nanoparticles	N, N-dimethylacetamine dmiethylacetal	[164]
Lignin nanoparticles	PDEAEMA	[165]
PDEAEMA latex	PEGMA	[166]
Crosslinked polymer particles	PDEAEMA	[167]

2.3.2.3 CO_2-responsive Pickering emulsion systems

CO_2 is a unique stimulus for emulsion control in that it is typically low cost, widely available, benign, biocompatible, and simple to implement. When sparged into solution, CO_2 exists as a dissolved gas in equilibrium with carbonic acid. The increase in acidity, similar to the pH-responsive systems previously described, allows for certain chemical moieties on the surface of particles to undergo some type of ionic or conformational change, altering the wettability of the particles. The CO_2 can just as easily be removed by sparging another gas into the system, such as air or N_2, which helps to strip the dissolved CO_2 from the solution[112,168]. In contrast to pH adjustment, the addition and removal of CO_2 is a non-accumulative process. Therefore, acidification-neutralization cycling may be completed without observing any significant increase in the ionic strength of the system. Table 2.7 outlines a number of CO_2-responsive Pickering emulsion systems reported recently in the literature.

Jiang and coworkers[163] investigated the stabilization of o/w emulsions using silica nanoparticles surface decorated with N'-dodecyl-N, N-dimethylacetamidinium bicarbonate, a CO_2-responsive surfactant. At low CO_2 concentrations, the surfactant was present in its neutral form, N'-dodecyl-

N, N-dimethylacetamidine and the negatively charged silica nanoparticles unable to stabilize o/w emulsions due to their excessive hydrophilicity (Figure 2.22). Upon the addition of CO_2 to the system at 0-5 ^oC, the surfactants were observed to transform from their neutral amidine form to their positively charged amidinium form. This resulted in the electrostatic adsorption of the surfactants on the surface of silica nanoparticles, quenching their negative surface charge and allowing for the particle-surfactant complexes to adsorb at the oil/water interface and stabilize the emulsion. Sparging N_2 or air into the system at 65 ^oC caused the surfactants to revert back into their neutral amidine form, eliminating the electrostatic attraction binding them to silica. This resulted in the desorption of the surfactant from the particles, destabilization of the particles at the interface, and, ultimately, demulsification and macrophase separation. Liang et al.[164] reported on two CO_2-responsive system systems, one of which was composed of N, N-dimethylacetamine dimethyl acetal (DMADMA) grafted silica particles and the other DMADMA and phenyl co-grafted silica particles. The first, due to the high DMADMA content, possessed a more hydrophilic surface and were able to stabilize o/w emulsions under neutral conditions. Addition of CO_2 resulted in rapid demulsification, as the particles were ejected to the aqueous phase. The observed particle instability was attributed to DMADMA protonation. The second and more hydrophobic particles were able to stabilize w/o emulsions. Destabilization was also observed for this system upon CO_2 addition. In both cases, sparging with air of N_2 reversed the effects observed under CO_2 addition and stable o/w and w/o emulsions could again be achieved. Zeta potential was used to confirm the role of particle surface charge in dictating their surface activity. Qian and coworkers[165] used ATRP to graft PDEAEMA onto the surface of water insoluble lignin nanoparticles. Stable o/w Pickering emulsions were obtained by homogenizing decane in water, in the presence of the PDEAEMA grafted lignin nanoparticles. Within 10 minutes of CO_2 sparging, the droplets were observed to

coalesce. In similar fashion to the previously described system, acidification by CO_2 addition resulted in DEAEMA protonation, making the particles more hydrophilic and, thus, unstable at the interface.
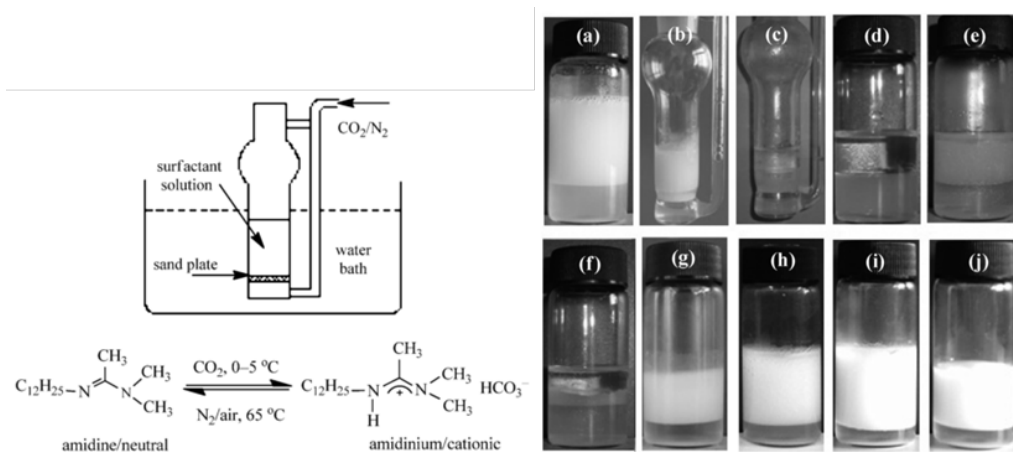
Figure 2.22 (Top-left) Schematic illustration of a temperature controlled gas bubbling device. (Bottom-left) Schematic demonstrating the CO_2/N_2-responsive conversion between N'-dodecyl-N,N-dimethylacetamidine and N'-dodecyl-N,N-dimethylacetamidinium. (Right) Digital photographs demonstrating the CO_2/N_2-responsiveness of n-octane-in-water emulsions stabilized by silica nanoparticles and either N'-dodecyl-N,N-dimethylacetamidinium (a-h) or cetyltrimethylammonium bromide (CTAB) (i, j); (a) Amindinium stabilized emulsion; (b-d) Before, during, and after N_2 bubbling; (e, f) Directly and one week after homogenization; (g, h) Directly and 24 h after CO_2 bubbling; (i, j) CTAB stabilized emulsion before and after N_2 bubbling[163].

Sterically stabilized poly(ethylene glycol) methacrylate-co-poly(2-(diethylamino)ethyl methacrylate) (PEGMA-PDEAEMA) latex particles were synthesized by Morse and coworkers via emulsion copolymerization (Figure 2.23)[166]. The latex particles were observed to behave as pH-responsive Pickering emulsifiers. Similar to previously discussed CO_2-responsive systems, the authors observed that the emulsion could be demulsifed by sparging with CO_2. The acidification that resulted from CO_2 addition induced the protonation of DEAEMA blocks, causing the latex

particles to transform into swollen microgels. These swollen particles were observed to desorb from the oil/water interface, causing the emulsion droplets to coalesce and eventual phase separate. However, subsequent sparging of N_2 caused the microgels to revert back into their denser, more hydrophobic morphology. Interestingly, the authors were unable to observe the restoration of the Pickering emulsion after homogenizing the mixture. They attributed the non-reversibility of the system to the insufficient pH increase by N_2 sparging alone. Liu and coworkers[167] synthesized crosslinked polymer particles via surfactant-free emulsion copolymerization of 2-(diethylamino)ethyl methacrylate (DEAEMA) and sodium methacrylate (SMA) using N,N'-methylenebis(acrylamide) (MBA) as a crosslinker. The zwitterionic particles with a unique isoelectric point in the pH range of 7.5-8.0 were introduced into a mixture of dodecane and water (Figure 2.24). Stable emulsions were prepared under neutral conditions. The emulsions displayed switchable behaviour in respond to CO_2/N_2 sparging. Rapid demulsification was observed during CO_2 addition and efficient re-emulsification was observed upon CO_2 removal with N_2 purging. The simple reversibility and stability during cycling, along with the ability to avoid ion accumulation, demonstrate the attractiveness of CO_2-responsive Pickering emulsion systems across a wide range of industries.
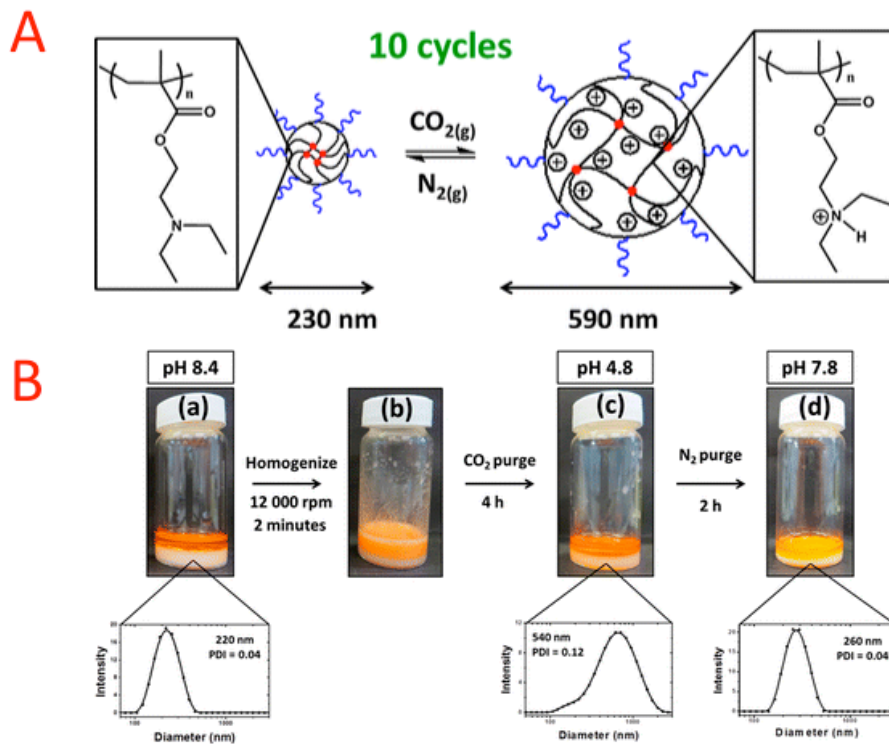
Figure 2.23 (A) Schematic illustration representing the CO_2/N_2-responsiveness of PEGMA-PDEAEMA latex particles. (B) (a-d) Digital photographs demonstrating the CO_2/N_2 tunable stability of isopropyl myristate-in-water emulsions stabilized PEGMA-PDEAEMA latex particles, with insets indicating the DLS particle size distribution[166].
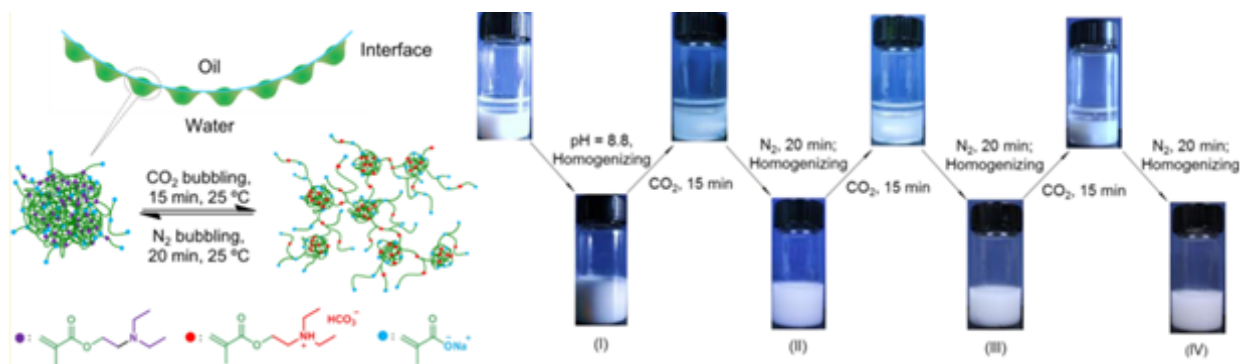
Figure 2.24 (Left) Schematic illustration demonstrating the CO_2/N_2-responsive structural modifications observed for crosslinked P(DMAEMA-co-SMA) particles. (Right) Digital photographs demonstrating the CO_2/N_2-responsiveness for n-dodecane-in-water emulsions stabilized by crosslinked P(DMAEMA-co-SMA) particles[167].

Table 2.8 Alternative stimuli-responsive Pickering emulsion systems

Stimulus	Particles	Modifiers	References
Magnetic	Carbonyl iron particles		102
Magnetic	Fe_3O_4 nanoparticles		103
Magnetic	Fe_3O_4 nanoparticle	Grafting of bromoesterified ethyl cellulose (EC-Br) onto the surface of amino-functionalized magnetite (Fe_3O_4) nanoparticles	169
Magnetic	$CNC/CoFe_2O_4$		170
Ca^{2+}	Poly (4-styrenesulfonic acid-co-maleic acid)		171
ClO^{4-}	SiO_2 nanoparticles	PMETAC brushes	172
Light	SiO_2 nanoparticles	Piropyran decorated UCNP	173

2.3.2.4 Alternative responsive Pickering emulsion systems

A number of other stimuli, such as magnetic field, salt concentration, and light intensity have also been investigated for the control of Pickering emulsion stability[102,103,169–173]. Peng and coworkers[169] studied the use of interfacial active polymer coated magnetic nanoparticles to stabilize and separate w/o emulsions. They first coated Fe_3O_4 nanoparticles with a thin layer of silica, followed by reaction with 3-aminopropyltriethoxysilane (3-APTES) to render the particle surface amine functionalized (Figure 2.25). They then grafted bromoesterified ethyl cellulose (EC) onto the particles to introduce interfacial activity. Stable w/o emulsions were prepared and droplet coalescence was initiated after the introduction of a magnetic field, resulting in macrophase separation. Removal of the magnetic field allowed the oil phase to be stably redispersed within the water phase. Unmodified Fe_3O_4 nanoparticle stabilized o/w Pickering emulsions were the subject of work recently reported by Zhou et al.[103]. Dodecane/water and PDMS (low viscosity)/water emulsion systems were prepared and remained stable for up to six months. More polar oils, such as butyl butyrate and decanol, could not be stabilized by the relatively hydrophilic Fe_3O_4 nanoparticles due to the very low θ_w observed for these systems. While not directly investigated

by the authors, it is expected that the introduction of an external magnetic field may destabilize the stable emulsion systems. As with thermo sensitive systems, some of the primary advantages of Pickering emulsion systems controlled by magnetic field intensity are their minimal invasiveness, ease of implementation, and scalability.
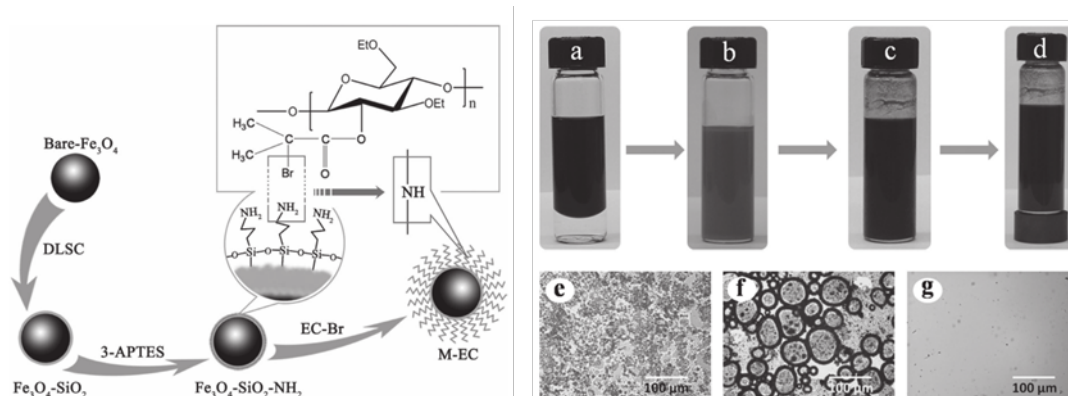
Figure 2.25 (Left) Schematic illustration demonstrating the synthetic procedure used to prepare EC grafted magnetic nanoparticles. (Right) (a-d) Digital photographs demonstrating the stabilization and destabilization process of water in asphaltene-in-toluene emulsions using EC grafted magnetic nanoparticles; (e) Microscopy image of solution (b) wherein water is dispersed within an asphaletene-in-toluene emulsion; (f) Microscopy image of solution (c) wherein EC grafted magnetic nanoparticles surround the disperse water droplets and isolate them from the oil phase; (g) Microscopy image of the oil phase of solution (d) wherein the emulsified water droplets have been removed from the oil phase by introduction of a magnetic field[169].

Zhao et al.[171] recently reported on the use of poly(4-styrenesulfonic acid-co-maleic acid) (P(SS-co-MA)) nanoaggregates as Ca^{2+}-responsive Pickering emulsifiers (Figure 2.26). Since P(SS-co-MA) is a hydrophilic polymer, containing strongly ionized SS segments and weakly ionized MA segments, it was observed to completely dissolve within the water phase. However, the addition of Ca^{2+} ions above a critical concentration (0.2 M) resulted in the aggregation of the polymer chains to form nanoparticles on the order of 10-40 nm, which proceeded to adsorb at the oil/water interface and stabilize o/w emulsions. Dilution of the system to reduce the amount of Ca^{2+} below

63

the critical concentration caused the nanoaggregates to dissociate and detach from the interface, which ultimately led to oil droplet coalescence and macrophase separation. While this method of stimulating emulsion stabilization and destabilization may be suitable for certain circumstances, the continuous dilution of the system does limit its applicability. Continuous cycling would eventually result in appreciable reductions in the oil to water ratio, altering the physical properties of the system.
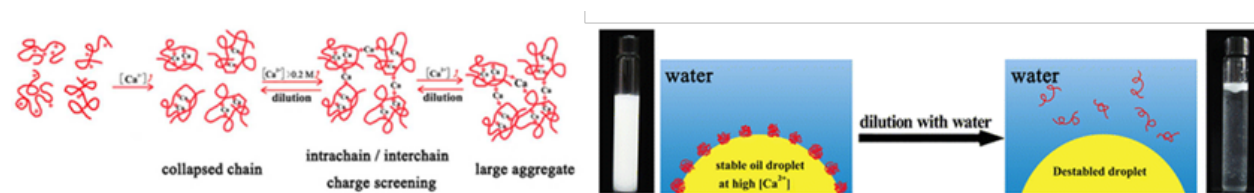
Figure 2.26 (Left) Schematic illustration demonstrating the Ca^{2+} induced formation of P(SS-co-MA) nanoparticles. (Right) Schematic illustration and digital photographs demonstrating the Ca^{2+} concentration responsiveness of o/w emulsions stabilized by P(SS-co-MA) nanoparticles[171].

Light intensity (controlled at different wavelength-near infrared and UV) is another stimulus that has been investigated for the control of Pickering emulsion systems. While not having attracted as much attention as the more conventional stimuli, namely pH, temperature, and CO_2 concentration, it can be fairly advantageous as it is generally non-destructive, precise, and easy to implement. Chen and coworkers[173] demonstrated a conceptually novel system using interfacially active upconversion nanophosphors as colloidal emulsifiers for biocatalytic applications (Figure 2.27). The surface chemistry of the particles was tuned by conjugating with photochromic sipropyrans, which undergo a hydrophilic-lipophilic conformational change in response to UV and visible light. Upon the introduction of NIR light into the system, the upconversion nanophosphors were observed to become excited and emit UV photons. The emitted UV light triggered the conformational change in the surface grafted photochromic sipropyrans. This caused the surface

of the particles to become more hydrophilic, which allowed for the Pickering stabilization of o/w emulsions. Exposure to visible light reversed the conformational change on the surface of the particles and resulted in emulsion phase inversion to w/o. The authors used the Pickering emulsion system to facilitate the enantiocelective hydrolysis of mandelonitirile (oil soluble) to (R)-(-)-mandelic acid (water soluble) using a model bacterium, Alcaligenes faecalic ATCC 8750, which
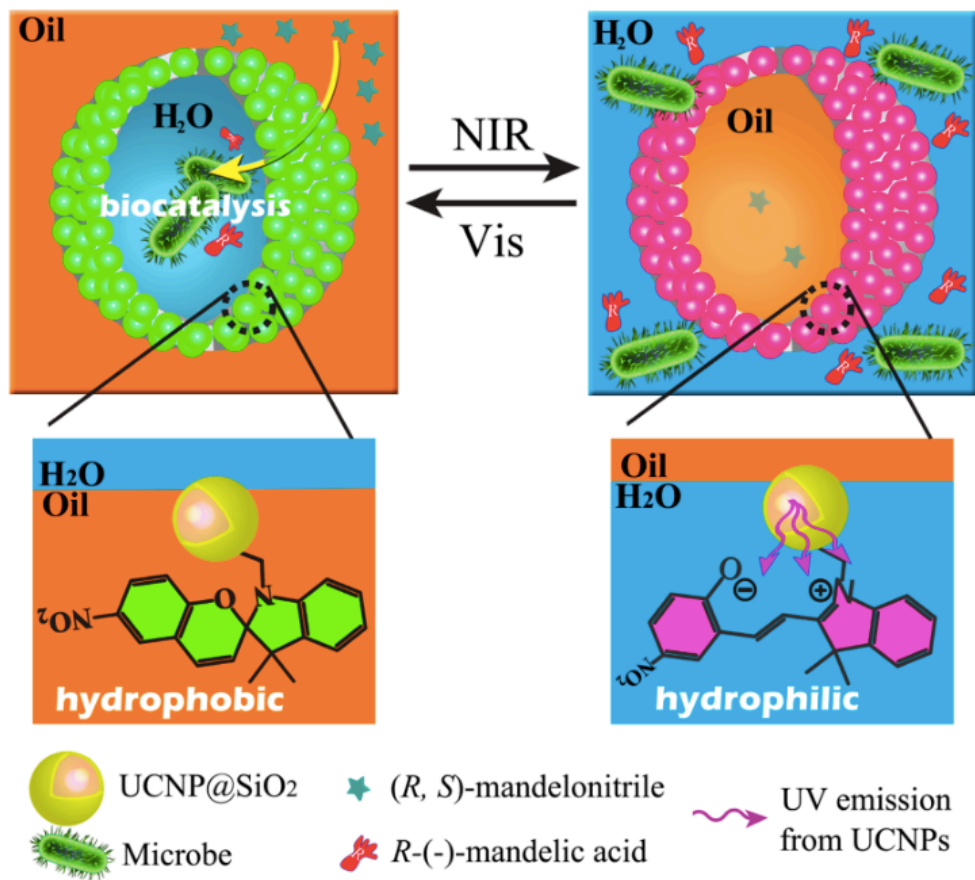
Figure 2.27 Schematic illustration demonstrating the NIR/Vis light-responsive phase inversion of emulsions stabilized by photochromic sipropyran conjugated upconversion nanophosphors for more efficient biocatalysis[173].

resided in the water phase. They observed a significant improvement in catalytic efficiency, even after cycling. This they attributed in part to reduced substrate inhibition. The phase inversion of the system also improved product, emulsifier, and biocatalyst recovery. Further, the use of light as

a stimulus, without any variation in temperature or chemical composition, proved to be gentle, showing little damage toward the biocatalysts. However, the use of light as a stimulus is limited to systems wherein light may pass easily through the entire solution so that it may interact with the entire contents. For turbid systems, wherein light is scattered in all directions by large particles, this may not be possible.

Table 2.9 Multi-responsive Pickering emulsion systems

Stimuli	Particles	Modifiers	References
Thermo, pH	P(SMA-co-NIPAM) random copolymer		[174]
Thermo, pH	P(NIPAM-MAA) microgel		[175–179]
Thermo, magnetic	Fe_3O_4-P(NIPAM-MAA) microgel		[180]
Thermo, ionic strength	Core crosslinked star (CCS) polymers poly(MEAx-co-PEGAy) *		[181]
pH, magnetic	Fe_3O_4 nanoparticle	PAA-PBA coating *	[182]
Thermo, magnetic	Fe_3O_4 nanoparticle	PNIPAM	[183]

* Poly(MEAx-co-PEGAy): poly(2-methoxyethyl acrylate)-co-poly(ethylene glycol) acrylate; PAA-PBA: poly(acrylic acid-b-butylacrylate)

2.3.2.5 Multi-responsive Pickering emulsion systems

Over the past decade, much attention has been devoted to Pickering emulsion systems that respond to more than one stimulus[9,174–183]. The combination of multiple stimuli is particularly advantageous because it can widen the controllable range or improve the degree of precision of a given system. Presented in Table 2.9 are a number of multi-responsive Pickering emulsion systems recently reported in the literature.

Given the wide range of stimuli-responsive small molecules and polymers that exist and the unique processing and modification routes available to researchers, a multitude of different multi-responsive systems may be explored. For combined pH and thermo-responsive systems, the most common material investigated has been poly(N-isopropylacrylamide)-co-poly(acrylic acid) (P(NIPAM-co-MAA)) microgels, which possess both thermo and pH-responsive blocks[175–179]. Early studies by Ngai et al. in 2005[176] showed that P(NIPAM-co-MAA) microgel stabilized o/w Pickering emulsions could be destabilized in response to either pH or temperature. Acidification of the system below pH 6 induced the protonation of carboxylate moieties on the PMAA blocks, making the particles more hydrophobic. This caused the microgels to desorb from the interface and diffuse into the oil phase, eventually resulting in droplet coalescence. Similarly, increasing the temperature of the system at pH 6 beyond 60 ºC induced the coil to globule conformation of PNIPAM segments, making the microgels more hydrophobic and destabilizing the particles at the interface. Interestingly though, the particles remained stable at the interface after an increase in temperature for mildly basic systems, i.e. pH > 8. The authors attributed this observation to the high negative charge density of PMAA blocks in alkaline conditions, which allowed the particles to remain sufficiently hydrophilic and persist at the interface, regardless of molecular conformation. By incorporating Fe_3O_4 magnetic nanoparticles into the P(NIPAM-co-MAA) microgel system, Brugger and Richtering[180] were able to stabilize o/w emulsion of both polar and nonpolar oils. Application of a static magnetic field to the emulsion caused the stable oil droplets to be separated from the continuous water phase without any observed coalescence. The application of a high frequency magnetic field caused an increase in the temperature of the Pickering emulsion, causing the emulsifier to become unstable and detach from the interface, resulting in macrophase separation. In both cases, the dual responsiveness allowed for precise remote control of the

Pickering emulsion dynamics. By manipulating the temperature and pH of the system in combination, the stabilization/destabilization window could be broadened or narrowed or even shifted as desired[158,176,180]. Depending on the application, the ability to do so may be advantageous to the operator. A thermo and salt-responsive system was recently reported by Chen et al.[181], wherein a series of core crosslinked poly(2-methoxyethyl acrylate-co-poly(ethylene glycol)acrylate) (P(MEAx-co-PEGAy)) were used to stabilize dodecane-in-water high internal phase emulsions (HIPEs). The HIPEs could be thermally triggered to rapidly and completely demulsify at mild temperatures. They also found that addition of kosmotropes, such as Na_2SO_4, led to more efficient demulsication, while addition of chaotropes, such as NaSCN, resulted in the opposite effect. Chen and coworkers[183] have recently developed a smart Pickering emulsion system for oil harvesting applications with the ability to respond to temperature and magnetic field intensity (Figure 2.28). They demonstrated that PNIPAM grafted magnetic composite particles allowed for efficient oil droplet transport within aqueous media. Application of an external magnetic field resulted in separation of the emulsified oil droplets from the water phase and increasing the temperature of the system to 50 ºC caused the droplets to coalesce.
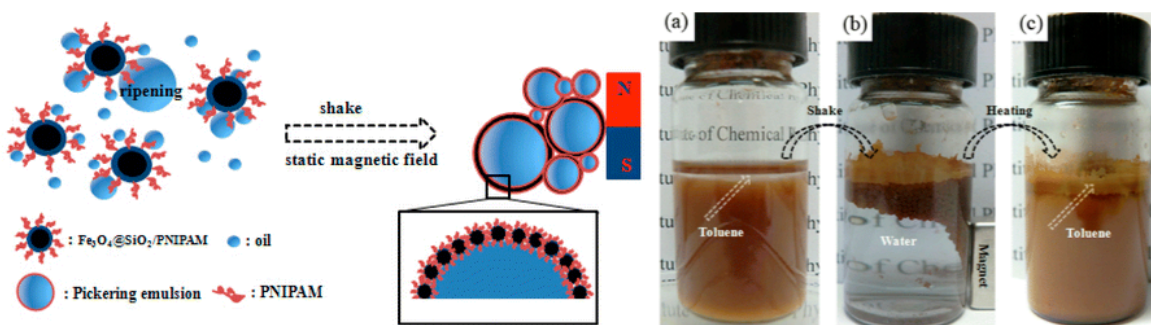
Figure 2.28 (Left) Schematic illustration demonstrating the destabilization of an o/w emulsion stabilized by PNIPAM grafted magnetic nanoparticles. (Right) (a-c) Digital photographs demonstrating the two-stage destabilization of a toluene-in-water emulsion responsive to magnetic field intensity and temperature[183].

2.4   Conclusions

There is a renewed impetus to develop nanomaterials from renewable sources due to the negative impact of using raw materials from traditional carbon sources, such as crude oil. New opportunities in the use of sustainable and renewable cellulose nanocrystal (CNC) for various advanced engineering applications offers a new route to product development and formulations in various industrial sectors. This review chapters covers the specific research topics on cellulose nanocrystals, and could be generally divided into four important aspects, including preparation, modification, properties and applications.

Studies on the modification of cellulose nanocrystals offer fundamental understanding, which is a prerequisite and foundation for designing novel functional systems for potential applications. Through modifications, functional groups or molecules can be introduced onto cellulose nanocrystals to achieve the desired properties for a specific application. However, while carrying out these exploratory research, consideration on simplicity, cost as well as the potential practical product development should be taken into account. Cellulose nanocrystals have potentials in many disciplines, but it is still a rather new material and the revolution will continue to unravel.

Chapter 3 Dual responsive pickering emulsion stabilized by poly(dimethylaminoethyl methacrylate) grafted cellulose nanocrystals

In this chapter, a weak polyelectrolyte, poly[2-(dimethylamino)ethyl methacrylate] (PDMAEMA), was grafted onto the surface of cellulose nanocrystals. The abilities of stabilizing the oil-in-water emulsions using modified CNC or pristine CNC were compared. Various factors, such as polarity of solvents, concentration of particles, electrolytes, and pH, on the properties of the emulsions were discussed. Using Nile Red as a florescence probe, the stability of the emulsions as a function of pH and temperature was elucidated. It was deduced that PDMAEMA chains promoted the stability of emulsion droplets and their chain conformation varied with pH and temperature to trigger the emulsification and demulsification of oil droplets. Interestingly, for heptane system, the macroscopic colors varied depending on the pH condition, while the colour of the toluene system remained the same.
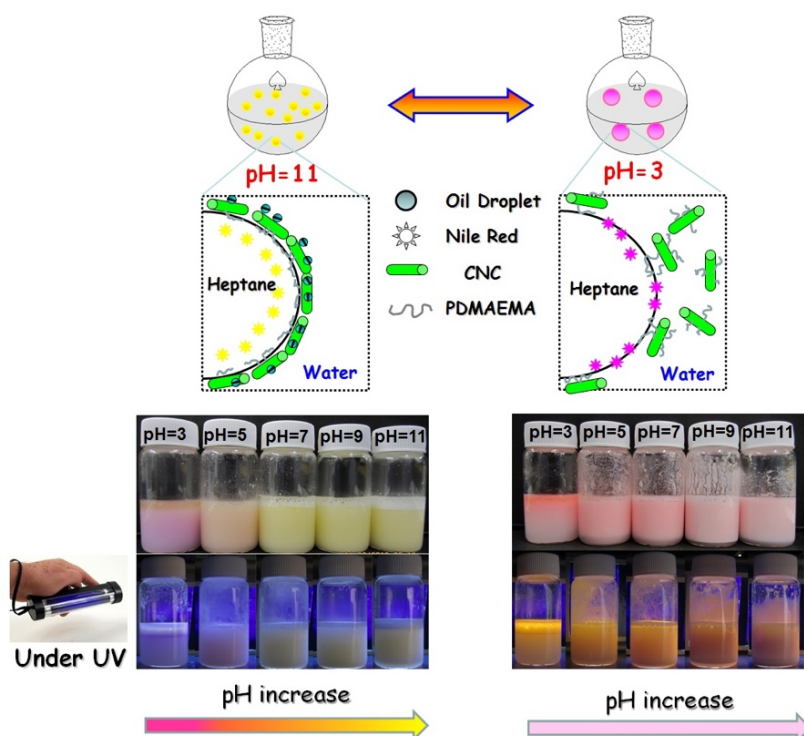
3.1   Introduction

Pickering emulsions are types of emulsions that are stabilized by solid particles instead of surfactants[93]. The solid particles with intermediate hydrophobicity adsorb strongly at the interface between two immiscible liquids forming an effective steric/electrostatic shield for the emulsified droplets. Therefore, the stabilization of emulsions by solid particles offers attractive performance, such as high resistance to coalescence. In addition, the 'surfactant-free' character makes them attractive to some applications, in particular cosmetic and pharmaceutical formulations, where surfactants often display adverse effects (irritancy, hemolytic behavior etc.)[92]. In some cases, such as fossil fuel production, oil transport, and emulsion polymerization, the emulsions need to be temporarily stabilized and then subsequently demulsified. Hence, nanoparticles with switchable interfacial properties are desirable, and this can be achieved by designing nanoparticles that are responsive to external stimuli. Currently, there is a growing interest in developing stimuli-responsive or switchable emulsion systems since they possess many attractive features[131,140,145,169,171]. pH[128,134,143,149,166,184] and thermo-responsive systems[156,158,159,174,176,185] are the most common examples, where stimuli-responsive polymers were grafted on the nanoparticle surface. These polymers undergo phase transition when triggered by different external stimuli and multi-stimuli responsive properties have also been demonstrated[136,141,147]. One of the popular polymer systems is poly[2-(dimethylamino)ethyl methacrylate] (PDMAEMA) that displays both pH- and thermo-responsive properties[158,186], and the property is preserved when the polymers are attached to surfaces. PDMAEMA undergoes phase change above its lower critical solution temperature (LCST) when it is fully deprotonated, and it possesses charge by changing the pH

values. Hence, this polymer is an ideal model system for the study on the reversibility of nanoparticles in emulsion systems.

Cellulose nanocrystals (CNC) has gained increasing attention as a sustainable nanoparticle from renewable sources[49,52,53,187–189]. Due to the sulfuric acid hydrolysis, the CNC possesses negative surface charge (OSO_3^-) which renders the surface hydrophilic. In previous studies, emulsions stabilized by pristine CNC were reported[19,21], followed by studies on the influence of CNC from different acid treatment processes[20], cellulose sources[55], and hydrophobic modifications[190] on the stability of emulsion system. However, to the best of our knowledge, there are no reported studies on the mechanism of stimuli-responsive CNC particles used in Pickering emulsions. Modifications of other inorganic nanoparticles (e.g. silica) have been extensively studied. These studies have illustrated the responsiveness of modified nanoparticles in emulsion systems. However, modified CNC (MCNC) can be considered to be a superior candidate to reversibly stabilize emulsions because of their rod like geometry and their environmental friendly. In this chapter, a dual stimuli-responsive polyelectrolyte PDMAEMA was grafted onto the surface of CNC via free radical polymerization and the ability of PDMAEMA-g-CNC to stabilize the Pickering emulsion was investigated systematically. The surface and interfacial properties of modified particles were characterized by surface tensiometer. Various factors such as polarity of solvents, concentration of particles, electrolytes, and pH were investigated. Nile red was used as a probe to identify the phase separation or the formation of emulsions. The change in the color of Nile red provides insight into the solubility of PDMAEMA chains in different oil phases. It was deduced that PDMAEMA chains can be used to trigger the stability of emulsion droplets via the manipulation of pH and temperature to produce a dual-responsive emulsion system.

3.2   Experimental section

3.2.1   Materials

Cellulose nanocrystals hydrolyzed from wood with an average charge density of 0.26 mmol/g was provided by CelluForce Canada. All the reagents were purchased from Sigma-Aldrich unless otherwise stated. N, N-(dimethylamino)ethyl methacrylate (DMAEMA, Aldrich, 99%) was passed through a column of neutral aluminum oxide prior to use. All the other chemicals were used as received: potassium bromide (KBr), sodium chloride (NaCl), ammoniun persulfate (APS), Nile Red, heptane (99%), and toluene (99%). Hydrochloric acid (HCl 1M) solution and sodium hydroxide (NaOH 1M) solution were diluted from standard solutions.

3.2.2   PDMAEMA grafting on CNC by free radical polymerization

CNC (2 g) was dissolved in 200 mL distilled water in a 500 mL 3-necked flask equipped with a magnetic stirrer and purged with N_2 for 1 h. The initiator (APS, 300 mg) was charged to the flask under continuous stirring and kept at 60 $^{\circ}$C for 10 min. The temperature was reduced to 50 $^{\circ}$C and a degassed solution of DMAEMA (2 g) was introduced. The temperature of the solution was slowly raised to 70 $^{\circ}$C and kept at this temperature for 3 h. The reaction mixture was concentrated via centrifugation and washed 3 times with Millipore water, and the solution was dialyzed (M_W cutoff of 12,000 Da) against Millipore water for 2 days with constant change of water. The solution was concentrated and freeze dried.

3.2.3 Preparation of Pickering emulsions

All emulsions (volume of 10 mL) were prepared using an oil-to-water ratio of 1:4, each containing a fixed PDMAEMA-g-CNC content in the aqueous phase and emulsified with an Ultraturrax T25 homogenizer (IKA, Germany) at 6000 rpm for 2 min at 25 $^{\circ}$C. Except for specific illustrations, an aqueous phase containing 0.5 wt. % of nanoparticles and at pH 12 was used throughout the studies. For labelling the oil phase, 2 mg of Nile Red was dissolved in 250 mL heptane and toluene respectively. The type of emulsion was determined by the drop test, where a drop of emulsion was added to pure water and heptane, and their dispersibility was evaluated. The fluorescence was observed under a hand-held UV lamp in a dark room (UVP$^{®}$ 95-0017-09 model UVGL-15).

3.2.4 Characterization of the PDMAEMA-CNC nanoparticles and stabilized emulsions

Potentiometric titration was performed using a Metrohm 809 autotitrator equipped with a water bath to control the temperature. The titrator was controlled by a Tiamo software that dosed μL of titrants. Measurements were performed in triplicate in a closed jacketed vessel at 25ºC while stirring at a medium rate. The pH of 50 mL samples with 0.15 wt. % was adjusted to ~ 3 by adding 1 M HCl and the suspensions were titrated using 0.01 M NaOH under nitrogen and constant stirring. The conductivity and pH of the suspensions were recorded simultaneously until the pH of the samples reached 11. Finally, the pH and conductivity values were plotted against the volume of NaOH (in mL), which were used to determine the amount of tertiary amines on PDMAEMA-g-CNC.

FTIR spectra were acquired at room temperature using a Bruker Tensor 27 spectrometer FT-IR spectrometer with a resolution of 4 cm^{-1} and a scanning number of 32 from 400 to 4,000 cm^{-1}. Test pellets were prepared by grinding and compressing approximately 2% of the samples in KBr.

Zeta potential measurements of the samples at different pH values were measured using a Malvern Zetasizer nano ZS instrument equipped with a dip cell. The concentration of the samples was maintained at ~0.1 wt. % and the experiments were conducted at room temperature with 10 repeated measurements.

Thermogravimetric analysis was performed using TGA Q600 of TA Instruments (Lukens Drive, Delaware, USA). The experiments were carried out under dry nitrogen purge at a flow rate of 10 mL/min from room temperature to 500 ºC at 15 ºC /min.

Elementary analysis (Vario Micro cube, Elementar Americas, Inc) was used to determine the atomic composition (carbon, hydrogen, nitrogen, and sulfur content) for freeze-dried CNC and PDMAEMA-g-CNC particles. Each sample was measured several times, and the average values were reported.

The emulsion droplets were visualized using an inverted optical microscope (Carl Zeiss Axio Observer. Z1m) equipped with a CCD camera (Carl Zeiss Axio Cam 1Cm1). Emulsion droplets were placed directly onto a glass slide and captured under 5~50x magnification.

The tensiometer Data Physics DCAT 21 system was employed to perform the surface and interfacial tension measurement. Before doing the measurement, several purification processes (e.g. centrifugation, dialysis and ultrafiltration) were utilized to remove the free homopolymers to ensure that the observed properties were attributed to polymers grafted on the CNC surface. Samples for measurement were prepared by dissolving the freeze-dried powders (PDMAEMA-g-CNC) in water to form dispersions.

3.3 Results and discussion

3.3.1 Basic characterizations of PDMAEMA-g-CNC

PDMAEMA-g-CNC were prepared using the free radical polymerization process (Figure 3.1A), performed in an aqueous environment that is simple and practical to implement. It is known that the water-soluble initiators, e.g. ammonium persulfate will decompose thermally at elevated temperature to produce a pair of initiating radicals $(SO_4^-\cdot)$[191]. These primary radicals are consumed by fast reacting scavengers, and they can also abstract H atoms attached to accessible carbinol groups generating active sites where vinyl monomers can be covalently bonded to the specific substrate, such as the backbone of cellulosic polymers or nanoparticles[191]. Several purification methods (e.g. centrifugation, dialysis and ultrafiltration) were used to remove free homopolymers to ensure that the observed properties were attributed to polymers grafted on the CNC surface.

The FTIR spectroscopy was first used to confirm the presence of PDMAEMA on the CNC surface. Figure 3.1C provides a comparison between pristine CNC and PDMAEMA-g-CNC samples; it confirmed the grafting of PDMAEMA onto the CNC surface. Compared with the spectra of pristine CNC, the PDMAEMA-g-CNC displayed new small shoulders at 2761 and 2819 cm^{-1} corresponding to the symmetric and asymmetric stretching of methyl groups as well as another obvious new peak at 1727 cm^{-1} that is related to the stretching of the C=O bond on PDMAEMA chains. These bands are characteristic peaks of PDMAEMA[192-].

Further confirmation of the grafting was supported by TGA measurements. As shown in Figure 3.1D, unmodified CNCs displayed the typical degradation behavior of CNCs obtained from sulfuric acid hydrolysis with an onset temperature of about 270 °C[51,52]. The initial weight loss from 30 to 100 °C (4.1%) was attributed to the loss of moisture on cellulose nanocrystals. For modified

cellulose nanocrystals (MCNC), the TGA curve exhibited a 3-stage degradation process; significant decomposition of PDMAEMA on the surface from around 250 °C, and followed by a sharp decrease at 320 °C due to the onset of weight loss of cellulose nanocrystals. Further confirmation of the grafting was supported by potentiometric titration and elemental analyses.
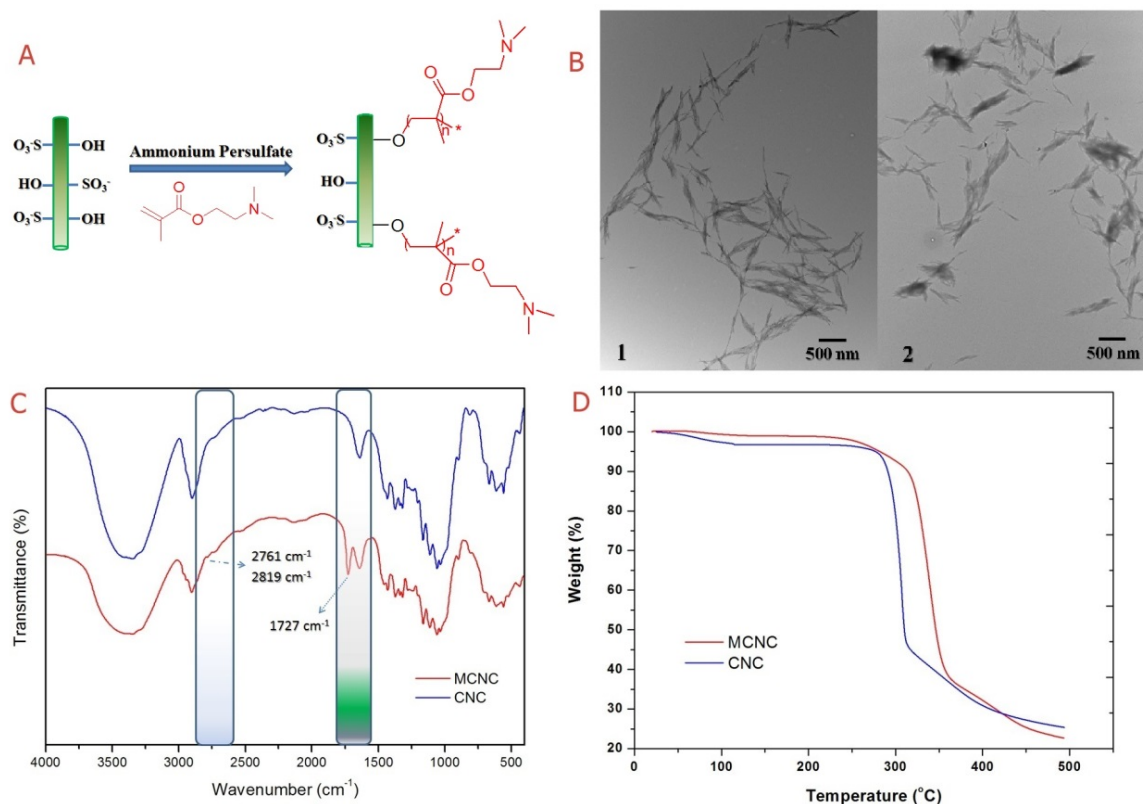
Figure 3.1 (A) Schematic illustrating the polymerization of PDMAEMA from the surface of sulfuric acid-hydrolyzed CNC; (B) TEM images of pristine CNC (1) and PDMAEMA-g-CNC (2); (C) FTIR Spectra of cellulose nanocrystals (CNC) and after modification with PDMAEMA (MCNC); (D) Thermogravimetric curves of cellulose nanocrystals (CNC) and modified CNC (MCNC).

Table 3.1 summarizes the elementary analyses on the amount of polymer chains grafted onto the CNC surface. Successful grafting was demonstrated by the increase in the overall nitrogen content from 0.023 to 0.981%. The approximate amount of tertiary amines (~0.8 mmol/g CNC) was

determined based on the difference in the nitrogen content before and after grafting. The carbon and sulphur content of the grafting CNC samples were checked and compared, and they agreed with the values determined from elemental analyses. The small reduction in %S for PDMAEMA-g-CNC compared with pristine CNCs was related to the desulfation during the grafting process. The calculated weight ratio of polymer chain on PDMAEMA-g-CNC of 11.17% agreed with the result from TGA.

Table 3.1 Atomic composition determined by elementary analyses

	% N	% C	% H	% S
CNC	0.023	41.106	5.619	0.844
PDMAEMA-g-CNC	0.981	43.336	5.924	0.694

Potentiometric titration was used to determine the composition of the functional groups (tertiary amine groups) on the CNCs. The suspension was first treated with hydrochloric acid to adjust the pH to 3.2, and titrated with 0.01 M NaOH at 25 ºC. As shown in Figure 3.2, the titration curve of PDMAEMA-g-CNC exhibited three regions, which correlated to (1) strong acid, (2) weak acid and (3) strong base behavior respectively. In the first stage, excess HCl will be neutralized by NaOH resulting in the initial linear decrease in the conductivity up to the first equivalence point. In the third stage, due to the complete deprotonation of tertiary amines, the second equivalence point corresponded to the onset of excess ions (Na^+ and OH^-) titrated to the system. PDMAEMA chains were deprotonated between these two equivalence points, where the amounts of tertiary amines on the CNC surface were calculated to be approximately 0.8 mmol of $-N(CH_3)_2$ per gram of PDMAEMA-g-CNC (Figure 3.2 - ~0.06 mmol per 75 mg sample).

TEM images of CNC and PDMAEMA-g-CNC dispersions are shown in Figure 3.1B, where the particles possessed identical size and shape in agreement with literature observations[3]. Some

"bundle-like" aggregates of PDMAEMA-g-CNC samples were observed, and this point will be discussed later.
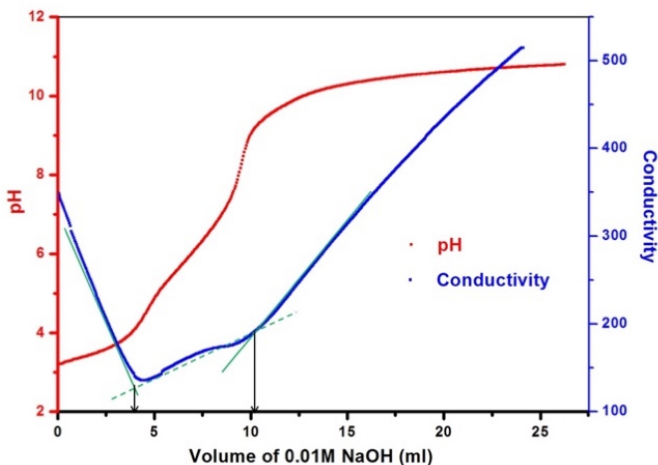
Figure 3.2 pH and conductivity titration curve of 0.15 wt. % PDMAEMA-*g*-CNC

3.3.2 pH-responsive behavior of PDMAEMA-g-CNC

PDMAEMA is a weak polyelectrolyte with pKa of around 7.4 at room temperature[194–196]. Previous studies indicated that the conformation of the polymer chain undergoes stretch-to-collapse transition due to the deprotonation of amine functional groups with increasing pH.. The samples were cloudy with a transmittance of ~8% when the pH values were less than 10. A possible explanation is as follows: before the point of complete deprotonation of amino groups (the deprotonation of the amino groups was incomplete as indicated from the zeta potential), PDMAEMA chains are hydrophilic and positively charged (below its pKa) due to the protonation of dimethylamino groups while the sulfate ester groups on the CNC surface are negatively charged. Under this condition, electrostatic interactions between PDMAEMA chains and OSO_3^- groups on the CNC surface induced aggregation resulting in the lowering of the transmittance (wavelength of 600 nm). When the pH was increased beyond the pKa (pH 10, 11), complete neutralized

dimethylamino groups occurred, and the modified CNC possessed only negatively charged sulfate ester groups, and the stability of the CNC is sterically enhanced by PDMAEMA chains. This was further confirmed by zeta potential and particle size analyses as shown in Figure 3.3. The zeta potential of PDMAEMA-g-CNC at pH 3.0 was +40 mV, and it decreased continuously to -38 mV when pH was increased to 11 due to the progressive deprotonation of PDMAEMA chains. The Z-average size of PDMAEMA-g-CNC were approximately 350 nm at pH less than 9.0, and it then dropped dramatically to 60 nm, which is slightly larger than unmodified CNC particles.
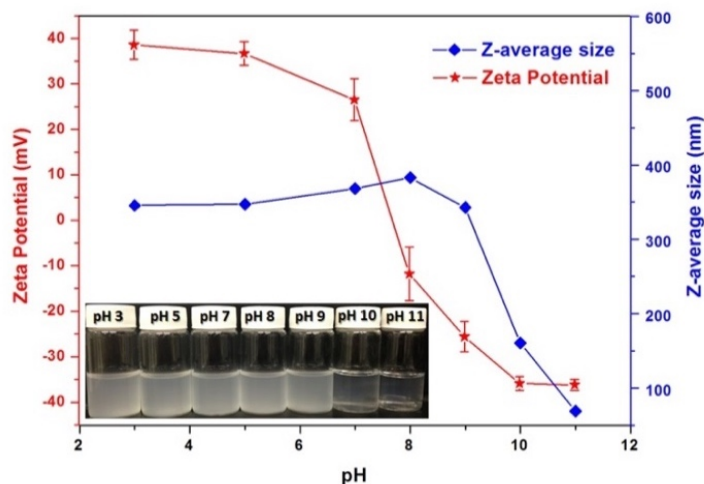
Figure 3.3 Effect of pH on the zeta potential and z-average size of PDMAEMA-g-CNC (0.1 wt. %); Inserted picture shows the PDMAEMA- g-CNC suspensions (0.1wt. %) at different pHs.

3.3.3 Emulsification with PDMAEMA-g-CNC

Surface and interfacial properties of PDMAEMA-g-CNC

Cellulose nanocrystals are an attractive Pickering emulsifier for cosmetic and pharmaceutical formulations because of its sustainability, biodegradability, and good toxicity profile. The ability of CNC to emulsify oil/water is highly correlated to its surface properties, such as charge density,

hydrophobicity and aspect ratio. Thus, it is valuable to investigate the impact of surface modification of CNC on its performance as a Pickering emulsifier.
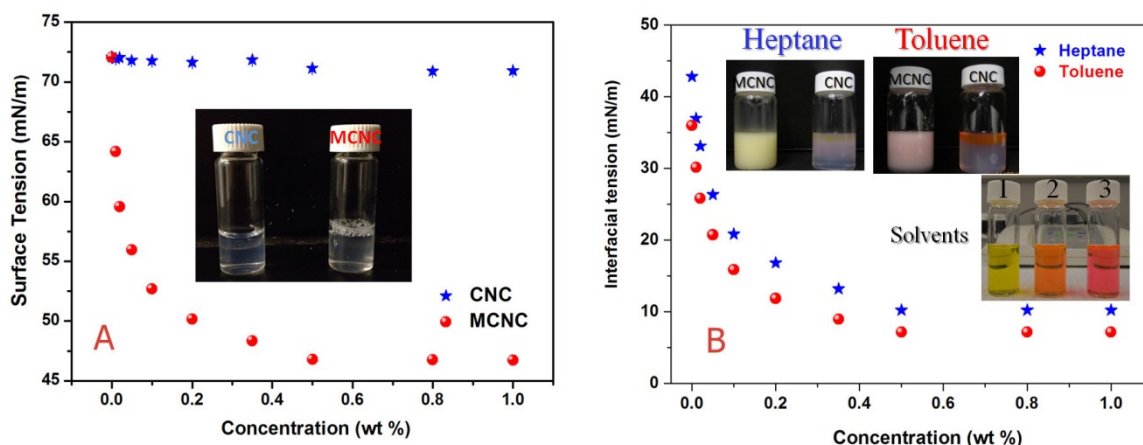
Figure 3.4 (A) Surface tension as a function of concentration of CNC (blue stars) and PDMAEMA-g-CNC (red circles) (pH 12). Inserted is the photograph of suspensions (0.1 wt. %, at pH 12) right after hand shaking; (B) variation of interfacial tensions (heptane/water; toluene/water) with varying concentrations of PDMAEMA-g-CNC (pH 12), inserts are emulsions (heptane and toluene as oil phase with Nile Red inside) prepared with CNC (0.5 wt. %) and PDMAEMA-g-CNC (MCNC, 0.5 wt. %, pH 12) as well as photograph showing colors of different organic solvents probed with Nile Red: (1) heptane, (2) mixture of heptane and toluene with volume ratio of 1 and (3) toluene.

Dynamic surface tension measurements were performed, with standard errors of less than 0.03 mN/m (Figure 3.4A). The steady surface tension curve of pristine CNC displayed a concentration independent value of 72 mN/m, suggesting that pristine CNC did not possess surface active characteristics. However, in the case of 1.0 wt. % PDMAEMA-g-CNC, the surface tension (SFT) decreased continuously from 72 to 47 mN/m in accordance with other nanoparticles investigated previously[145]. The significant difference in the surface tension of PDMAEMA-g-CNC dispersion would indicate that these nanoparticles exhibited a higher affinity for the air-water interface that is associated to the amphiphilic characteristics of PDMAEMA chains. The foaming tendency of

PDMAEMA-g-CNC dispersions as shown in Figure 3.4 A would suggest that the modified CNC was surface active. Firas et al. also observed similar behavior with thermo-responsive Jeffamine-decorated CNCs[49]. Usually, the adsorption of solid particles at the oil-water interface requires the wettability of the particles at oil-water interface. The surface activities of solid particles are not a necessary requirement as reported for surfactant molecules[93], however more stable emulsions are produced by modified nanoparticles that display surface active properties.

The solubility of polymer grafted CNC in different organic phase will impact the degree of partitioning of the polymer chains to the oil-water interface, which is controlled by the particle adsorption energy and interfacial tension. Heptane (polarity: 0.2) and toluene (polarity: 2.4) were used to represent a poor and good solvent for PDMAEMA-g-CNC respectively. The grafted PDMAEMA chains on adsorbed CNC particles could penetrate further into a good solvent than a poor solvent. Interfacial tension (IFT) measurements were performed to gain more understanding and insight into the behavior of modified CNC at the oil-water interface. The interfacial tensions of heptane and toluene against water were measured with PDMAEMA-g-CNC dispersed in the aqueous phase at room temperature.

Figure 3.4B shows the interfacial tension of heptane-water and toluene-water for modified CNC ranging from 0.01 to 1.0 wt%. The results confirmed that PDMAEMA-g-CNC possessed favorable interfacial property. The heptane/water interfacial tension for 1.0 wt. % PDMAEMA-g-CNC was approximately 12 mN/m, which is a significant reduction from the heptane/water interfacial tension of 44 mN/m (value consistent with literature data[197]). Similarly, the toluene/water interfacial tension decreased from 38 to 8 mN/m. However, the reduction in the IFT for toluene-water-MCNC was larger than heptane-water-MCNC, which was attributed to the better compatibility of PDMAEMA chains in toluene than in heptane. These measurements confirmed

that PDMAEMA-grafted nanoparticles significantly reduced the interfacial tension of oil/water emulsion as was reported for PDMAEMA homopolymer[198]. From these studies, we concluded that oil-in-water (o/w) emulsion were produced using both modified or unmodified CNC, however a more stable o/w emulsion in modified CNC was observed as shown in Figure 3.4B.
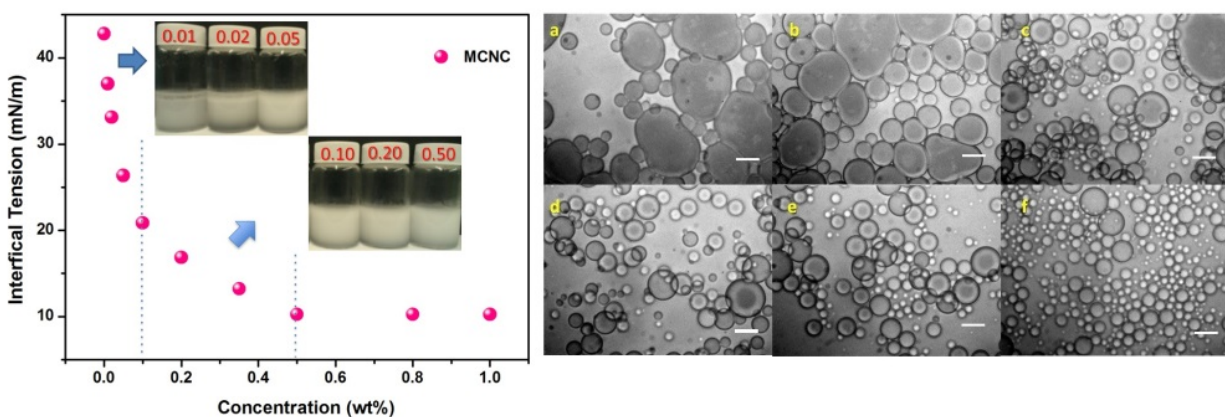
Figure 3.5 Interfacial tension profile of heptane-water as a function PDMAEMA-g-CNC concentrations, inserted photographs are the emulsions prepared using heptane as oil phase and PDMAEMA-g-CNC as aqueous phase (pH 12); On the right hand side are the optical micrographs of emulsions with different PDMAEMA-g-CNC concentrations (a. 0.01 wt. %; b. 0.02 wt. %; c. 0.05 wt. %; d. 0.10 wt. %; e. 0.20 wt. %; f. 0.50 wt. %), the length of the scale bar inside is 15 μm.

Effect of different concentration of PDMAEMA-g-CNC on emulsification.

Heptane-in-water emulsions stabilized by different amounts of modified CNC are shown in Figure 3.5. Three different regions delineated by the particle concentration at 0.1, and 0.5 wt% (shown by dotted lines) are indicated together with micrographs of the oil droplets. Emulsification to produce stable heptane droplets failed in the first regime at a concentration of less than 0.1 wt.% of PDMAEMA-g-CNC as the smaller droplets coalesced to produce large ones. Beyond 0.1 wt%, coalescence was suppressed as the heptane emulsions were coated with sufficient PDMAEMA-g-CNC to stabilize heptane droplets. However, creaming was still evident due to size and density

effects. The average emulsion droplet sizes are controlled by the solid particle to oil mass ratio, which decreased from around 20 to 8 μm (see Figure 3.5). Finally, a third regime was reached beyond 0.5 wt. %, where stable emulsions were produced due to the sufficient coverage of the oil-water interface by the modified CNCs.

Effect of ionic strength on the stability of emulsions with modified CNC

A previous study by Irina et al. showed that it was not possible to produce stable emulsions with CNC that possessed surface charge density greater 0.03 charge/nm[19,20]. However, by adding electrolytes such as NaCl or KCl to screen the electrostatic forces, stable emulsions were obtained with highly charged cellulose nanocrystals. We have investigated the stabilization of heptane-water emulsions using pristine CNC. The emulsions with 0.5 wt. % pristine CNC yielded emulsions that were stable for 2 h and obvious creaming occurred after 24 h resulting in macroscopic phase separation (data not shown here). Addition of NaCl to the emulsions produced more stable emulsions due to the reduced coalescence and creaming of the oil-water droplets. The influence of electrolyte on the stability of oil droplets in the 0.5 wt. % PDMAEMA-g-CNC system was investigated in the presence of various NaCl concentrations at pH of 12. The influence of Na^+ on the colloidal stability of modified CNC is presented in Figure 3.6. As NaCl concentration increased, the zeta potential of modified CNC became less negative due to the electrostatic screening by counter ions. At low NaCl concentrations, the absolute value of zeta potential was greater than 30 mV, where the dominant electrostatic repulsion inhibited aggregation of the nanoparticles. At higher NaCl concentrations, the absolute value of zeta potential decreased dramatically, and the attractive van der Waals force dominated, which induced the aggregation of CNC nanorods (see Figure 3.6a). Furthermore, the influence of ionic strength on the emulsion

properties was examined, and salt addition reduced and inhibited creaming. Adding salt to the system can lead to charge shielding that weakens the repulsive force, and promotes the aggregation of CNC nanoparticles. Therefore, the modified CNC network in the continuous phase is strengthened, resulting in further stabilization of the emulsions. The dispersion rheology of CNC particles at similar particle and salt concentrations was measured to confirm the observed phenomenon (Figure 3.7). As the salt concentration was increased, repulsion forces were screened inducing aggregation giving rise to gelation and a corresponding viscosity increase. The emulsions displayed a yield stress and shear thinning behavior, which are common features of aggregated systems. When sheared, large droplets or a distinct layer of oil was evident indicating the disruption of the droplet-particle networks, as reported previously for silica nanoparticles[199,200] or chitin nanocrystals[122].
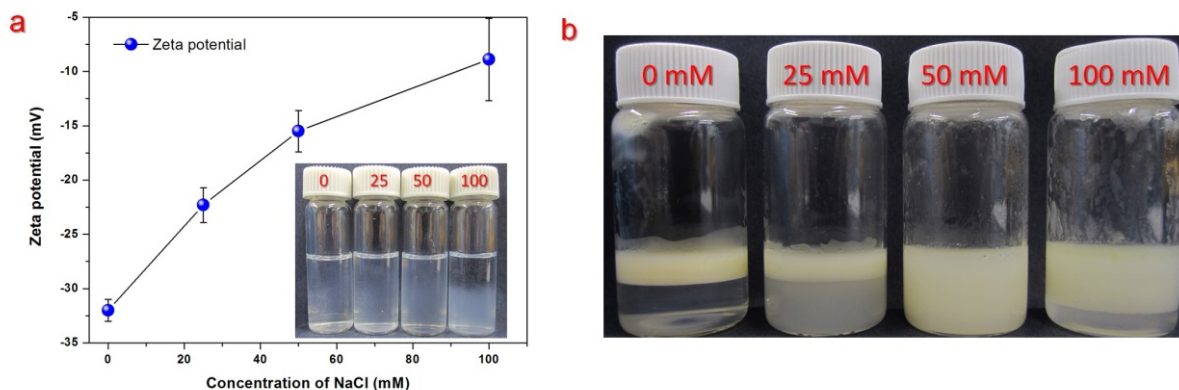
Figure 3.6 (a) Effect of the ionic strength on the zeta potential of PDMAEMA-g-CNC suspensions (0.1 wt. %, pH 12), insert is the photograph showing the colloidal stability of suspensions with different concentrations of NaCl (0, 25, 50, 100 mM) after 24 h; (b) emulsions with heptane as oil phase (probed with Nile Red) and PDMAEMA-g-CNC suspensions (0.5 wt. %, pH 12) with NaCl as aqueous phase kept at room temperature for 1 month.
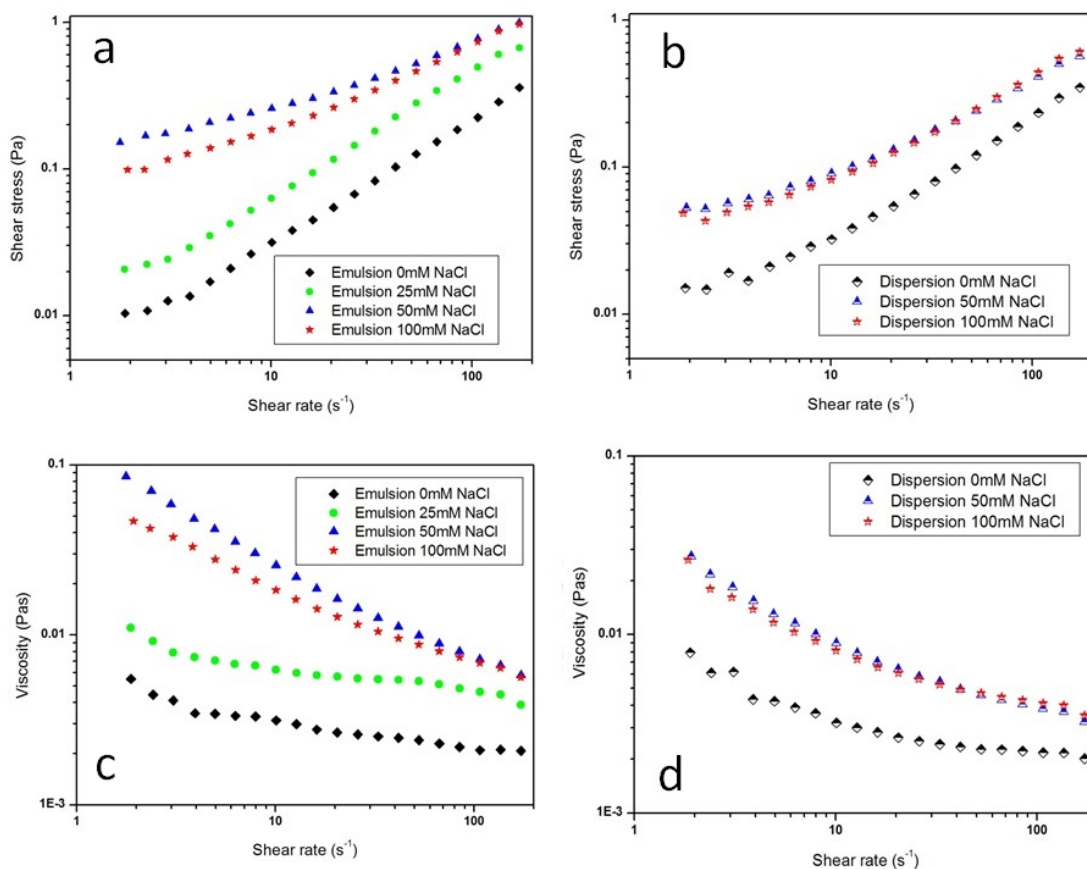
Figure 3.7 Shear rate dependence of shear stress of heptane-water emulsion (a) stabilized with PDMAEMA-*g*-CNC with different concentration of NaCl and PDMAEMA-*g*-CNC dispersions (b) with NaCl; Viscosity profile of heptane-water emulsion (c) stabilized with PDMAEMA-*g*-CNC with different concentration of NaCl and PDMAEMA-*g*-CNC dispersions (d) with NaCl vs shear rate.

Pickering emulsion with pH-responsive behaviors

It has been discussed that the surface charge and partial wettability of the Pickering emulsifier are key parameters that control the type and stability of emulsions (For discussing the stabilities, only coalescence that lead to phase separation is actual destabilization). Therefore, the responsive properties of modified nanoparticles were correlated to the dispersion pH, which can be exploited for stabilizing emulsions[134,143,145]. All Pickering emulsions were prepared by first sonication 0.5

wt. % PDMAEMA-g-CNC in 8 ml water followed by the addition of 2 ml of organic phase (heptane or toluene). Then the pH of the aqueous phase was adjusted to the desired value by adding 1M HCl or 1M NaOH. Emulsions were prepared by mechanically shearing the mixture using a homogenizer. Figure 3.8 shows the appearance of emulsions prepared in different pH solutions 2h after the emulsification procedure. By discounting the solvent effects and colors from Nile red, emulsions at high pH were more stable. PDMAEMA chains are highly deprotonated under alkaline conditions and they are more compatible with the oil phase due to the increased hydrophobicity while the CNC nanoparticles are preferentially wetted by water. The partially wetted PDMAEMA-g-CNC yielded a more stable emulsion. When the aqueous dispersions were acidified, PDMAEMA-g-CNC particles became more hydrophilic and were incompatible with the oil phase and they detached from the oil-water interface resulting in phase separation (see Figure 3.8, at pH 3).

Nile Red (9-(diethylamino)-5H-benzo[α]phenoxazin-5-one) was used to further confirm the pH responsive properties of PDMAEMA or more specifically, the phase transition of PDMAEMA from hydrophilic to hydrophobic. Nile Red is a solvatochromic dye in which the wavelength of its visible adsorption maximum shifts from longer to shorter wavelength when the polarity of its corresponding solvent decreases, and thus displaying varied colors ranging from strong yellow-gold to deep red[201]. Nile Red has been extensively used to study biological membranes[202], micelles[203,204], cyclodextrins[205], and surfactant emulsions[184]. It has also been employed for probing the phase transition of poly(N-isopropyl acrylamine) (PNIPAM)[206] and polypyrene (PPy)[207]. For the systems investigated here, Nile Red displayed pale green and yellow fluorescence under UV light for heptane and toluene respectively (see Figure 3.8c-bottom). By using Nile red as the probe for an indication of oil phase, unstable emulsions at low pH were confirmed, as the oil phase on
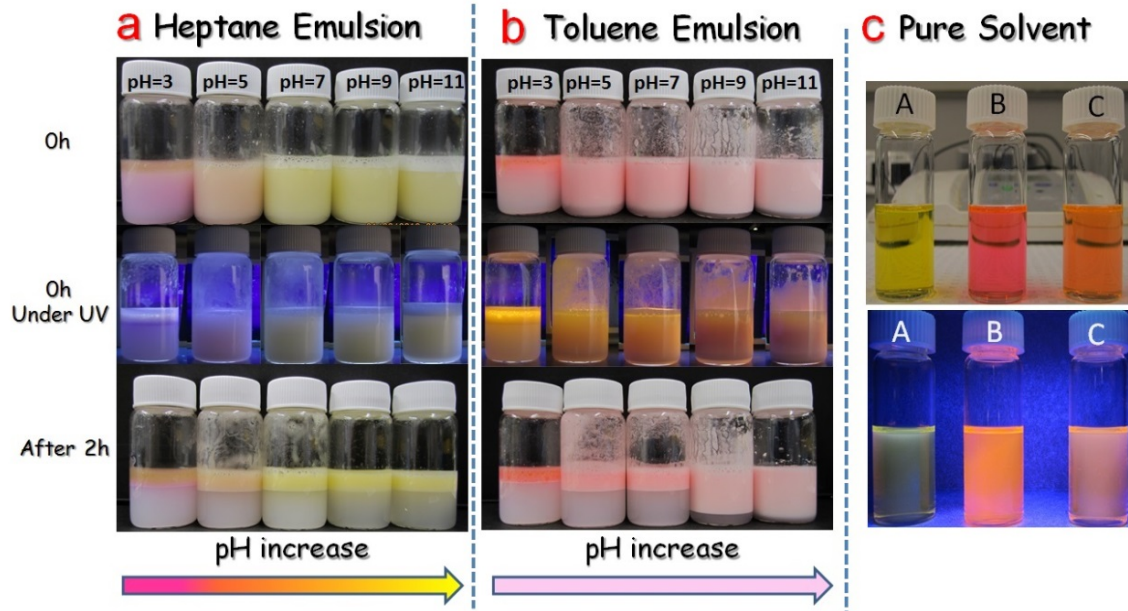
Figure 3.8 Photographs of emulsions (Heptane-**a**; Toluene-**b**, oil-water ratio 1:4) stabilized with PDMAEMA-g-CNC (0.5 wt. %) under different pH conditions (from top down: right after emulsification without UV light; right after emulsification with UV light in dark room and after emulsification for 2 hr without UV light); (**c**) pictures showing different colors (upper part) and florescence (bottom part) lights with UV when placed in a dark room (A-heptane; B-toluene; C-mixture of heptane and toluene with volume ratio 1:1)

the upper part of emulsion displayed fluorescence (See Figure 3.8a-0h-under UV). However, at high pH conditions, the emulsions did not display any fluorescence since all the oil droplets were encapsulated by PDMAEMA-g-CNC nanoparticles and the emulsions were reasonably stable. Further agreement has been shown in the emulsion system of heptane-water stabilized by pristine CNC in which no color change was observed at different pH (Figure 3.9a). Therefore, the PDMAEMA was deprotonated at high pH which imparted particles with partial hydrophobicity for a stable adsorption at the heptane-water interface. Notably the colors displayed by the heptane-water emulsions (Figure 3.8a) with PDMAEMA-g-CNC varied across different pH, while they remained unchanged for the toluene-water emulsions (Figure 3.8b). To explain this difference,

pristine CNC in different oil-water systems were studied, and no color change was observed as shown in Figures 3.9 and 3.10. Nile red has been used in the study of emulsion stability at different pH previously and shows independent maximum emission to pH as well[146]. Comparing the conditions above (two Pickering emulsifiers: pristine CNC and PDMAEMA-g-CNC as well as two organic solvents: heptane and toluene), color variation was only observed in the heptane-water emulsion systems with PDMAEMA-g-CNC as emulsifier at different pH. Further discussion of this observation will be based on PDMAEMA and heptane since there are the variables among the emulsion systems observed.
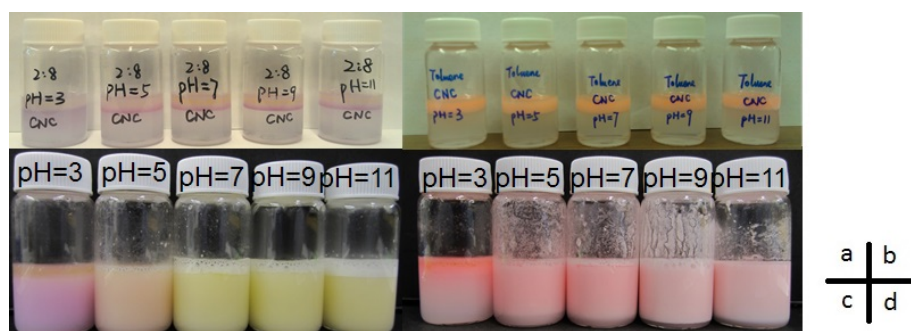
Figure 3.9 (a) Emulsions (heptane system) stabilized with CNC at different pHs; (b) Emulsions (toluene system) stabilized with CNC at different pHs; (c) Emulsions (heptane system) stabilized with PDMAEMA-*g*-CNC at different pHs; (d) Emulsions (toluene system) stabilized with PDMAEMA-*g*-CNC at different pHs.

Figure 3.10 Emulsification of heptane-water system with CNC (top layer) and PDMAEMA-*g*-CNC (bottom layer) (0.5 wt. %) under different pH conditions

In the heptane/water emulsion with PDMAEMA-g-CNC as emulsifier, color changes at different pH were observed (Figure 3.8a); whereas no color change was observed for the toluene/water emulsion (Figure 3.8b). There are only three phases in the emulsion systems, - water phase, oil phase and oil-water interface. But only the latter two are compatible with Nile Red. During emulsification at pH 3(Figure 3.8a-pH 3), Nile Red migrated to the heptane/water interface at where the polarity of the environment gradually increased, the color displayed by Nile red changed from yellow to fuchsia. This observation is in agreement with Figure 3.9. The heptane-water emulsion was de-emulsified, and the Nile red displayed a fuchsia color at the interface, signifying a more polar environment. Some Nile red molecules were partitioned to the heptane phase yielding a slight yellowish color. In pristine CNC dispersions, only the fuchsia color was observed at all pH conditions as the Nile red molecules migrated to the heptane-water interface (Figure 3.10). However, by increasing the pH, PDMAEMA-g-CNC became more hydrophobic, and had a higher affinity for the heptane phase; the polymer chains penetrate into the heptane phase and further stabilized the heptane-water emulsion. The yellow color was originated from the Nile Red molecules within the heptane droplets (see Figure 3.8a - pH 7, 9, 11). Meanwhile, for the toluene/water systems, only pink color was observed at different pH conditions (Figure 3.8b). We attribute this to the difference of solvent polarities. Toluene has a polarity of 2.4, which is 12 times greater than heptane (polarity of 0.2), thus the range of visible color change is limited and therefore no variations can be detected by the naked eye.

The reversibility of emulsions in response to changes in pH is shown in Figure 3.11. Emulsion containing heptane stabilized by PDMAEMA-g-CNC possessed a yellow color at an alkaline pH of 11. Immediately after the addition of acid (1M HCl), the color changed from orange (pH 5), and finally to fuchsia at pH 3. Large oil droplets in the upper section of the liquid mixture were evident

indicating that the emulsions droplets demulsified at low pH. When a base (1M NaOH) was added and the emulsion was homogenized, the color changed from fuchsia to orange and then to yellow, confirming the reversibility of the emulsion by manipulating the pH. Such a system could be used in applications like switchable Pickering emulsion polymerizations. However, due to the increasing amounts of salt generated from the acid/base reaction, the reversibility is only limited to several cycles. Improvement can be made by triggering the pH changes with CO_2.

Pickering emulsion with thermo-responsive behaviors

PDMAEMA is a thermo-responsive polymer exhibiting a pH dependent lower critical solution temperature (LCST) of between 40-45 °C[158,208]. The emulsions with thermo-responsive properties are demonstrated here. At pH greater than 7, emulsions comprising toluene as the oil phase and modified CNC dispersion as the aqueous phase were stable for more than 4 months (Figure 3.12A); however, when it was placed in a water bath at 50 °C for 5 min, the emulsions at pH 11 destabilized and phase separated. For emulsions at pH 7 or 9, phase separation was not obvious under the UV light as shown in Figure 3.12D. Since PDMAEMA chains are fully deprotonated above its pKa of 7.5, it possessed a LCST of 40-45 °C. Reducing the pH leads to an increase in the LCST of the polymer solution.[208,209]
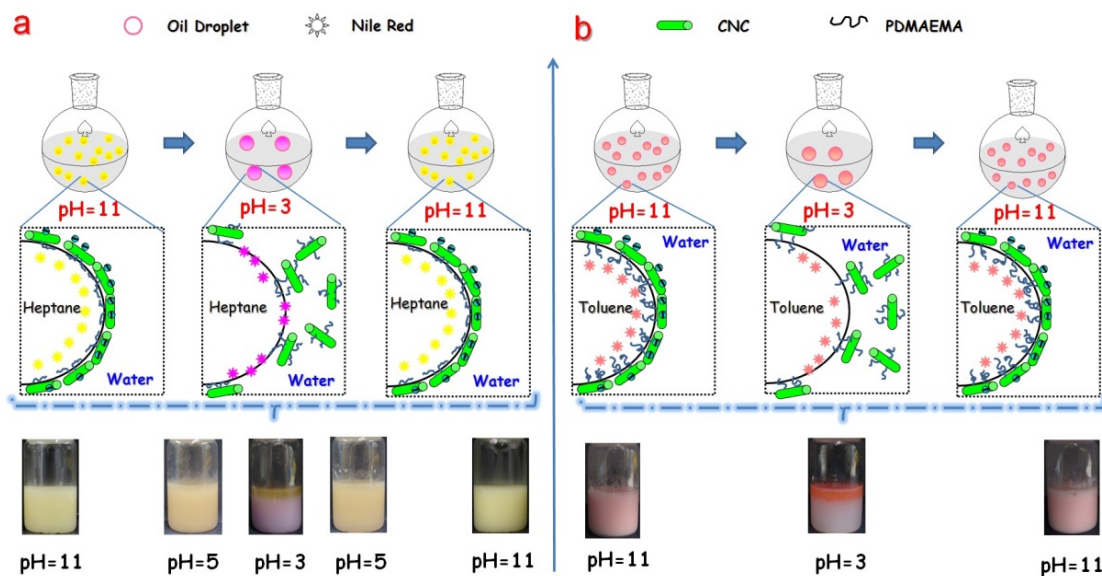
Figure 3.11 Responsive behavior of emulsions (PDMAEMA-g-CNC, 0.5 wt. %) by adjusting the pH values of the continuous phase (a, heptane; b, toluene); upper section is the schematic representation of possible mechanisms for emulsification and demulsification as well as color changes.
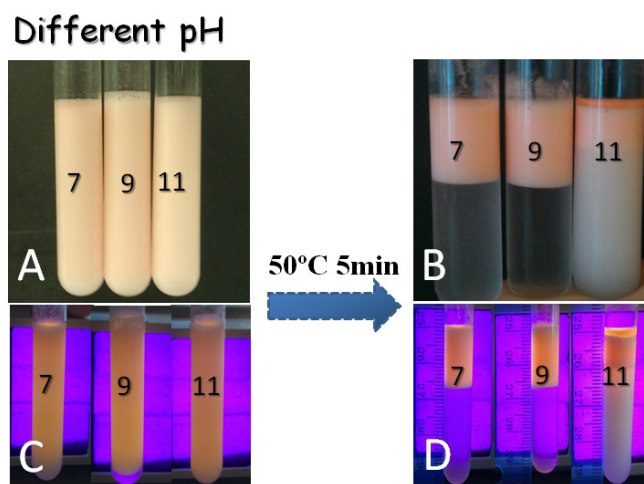
Figure 3.12 Photographs of toluene-water emulsions stabilized by PDMAEMA-g-CNC in different pHs: without UV (A); with UV lights (C); Photographs of emulsions taken after equilibration in a water bath for 5 min (without UV (B) and with UV light (D))

3.4   Conclusions

Novel dual responsive Pickering emulsifiers based on sustainable and bio-renewable cellulose nanocrystals were successfully synthesized by grafting PDMAEMA onto CNC via a free radical polymerization process. The modified nanoparticles displayed good surface and interfacial properties when the amino groups on PDMAEMA were highly deprotonated. The air-water surface tension decreased from 72 to 47 mN/m depending on the concentrations of PDMAEMA-g-CNC. Compare to pristine CNC, oil-in-water emulsions prepared with modified CNC displayed improved stability against coalescence over a 4 months' period. Creaming behavior was reduced or inhibited by adding electrolytes up to 50 mM due to the screening of charges on the CNC surface (from sulfate ester and amino groups) that induced the aggregation of the particles. Using Nile Red as an indicator in heptane-water emulsions, the color changed from fuchsia to yellow when the pH was increased, and this is correlated to changes in the polarity of the oil phase probed by Nile Red molecules that is influenced by the extent of PDMAEMA chain penetration to the oil phase that depended on the degree of protonation of amine groups. However, this behavior was not observed for toluene-water systems due to the polarity of toluene, which is less hydrophobic. Stimuli responsive Pickering emulsions utilizing polysaccharide nanocrystals with controllable stability suitable for cosmetic and pharmaceutical applications are demonstrated.

Chapter 4 Stimuli-responsive cellulose nanocrystals for surfactant-free oil harvesting

In this chapter, cellulose nanocrystals grafted with binary polymer brushes (CNC-BPB), poly(oligoethylene glycol) methacrylate (POEGMA) and poly(methacrylic acid) (PMAA), was prepared. The physical properties of CNC-BPB can be controlled by external triggers, such as temperature and pH, which can be utilized to stabilize and destabilize oil–water emulsions. By virtue of the modifications, these bifunctionalized CNCs diffused to the oil–water interface and stabilized the oil droplets at high pHs. When the pH was lowered to 2, strong hydrogen bonding between POEGMA and PMAA chains grafted on the CNC induced the coalescence of the emulsion droplets, resulting in the phase separation of oil and water. Successive stabilization–destabilization over 5 cycles was demonstrated by modulating the pH with the addition of acid or base without any loss in efficiency. This work demonstrates that functional sustainable nanomaterials can be used for small scale oil–water separations, particularly for oil droplet transportation and harvesting of lipophilic compounds.
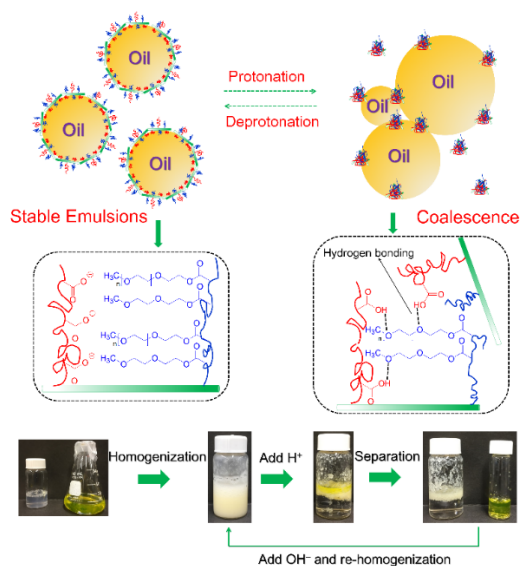
4.1   Introduction

Surfactant stabilized emulsions are commonly used in the petroleum industry, where the destabilization of emulsions is desirable prior to the separation of oil-water mixtures[210]. Examples of chemical demulsifiers presently used are: polymeric surfactant such as copolymers of polyethylene-oxide and polypropylene-oxide[211]; alkylphenol-formaldehyde resins; and blends of different surface-active compounds[212]. These surface-active agents increase the surface pressure at the oil-water interface, and induce the coalescence of the emulsions. The use of demulsifiers derived from fossil fuels poses economic and environmental challenges. These challenges have led to the development of switchable or stimuli-responsive stabilizers from sustainable materials for controlling the stability of emulsions[163,167,213–215].

Conventional surfactant based emulsion systems that are thermodynamically stable generally only work at surfactant concentrations exceeding the critical micelle concentration (CMC) which increases cost and environmental impact. Pickering emulsions, which are particle-stabilized emulsions, are more attractive as they provide extremely stable interfaces that inhibit the coalescence at relatively low concentrations. Further, the stability of the interface can be reduced considerably by altering the amphiphilic characteristics of the particle using functional moieties that possess switchable stimuli-responsive properties[92,98,216]. The pioneering work carried out by S. Fuji & S. Arms[144,217] as well as T. Saigai & R. Tilton[158] could provide suggestive ideas for this research field. A review of the literature indicated that studies on the use of functional particle with responsive properties for controlling the stability of Pickering emulsions for the separation of oil and water mixtures is limited. Chen et al. reported an efficient oil harvesting system based on poly(N-isopropylacrylamide) (PNIPAM) grafted magnetic composite particles[183]. The magnetic core offers the ease of separation using a magnetic field, and the temperature-responsive PNIPAM

allows for thermal induced destabilization of emulsion droplets for the recovery of the oil phase. Wang et al. reported on a similar core-shell poly(2-(dimethylamino)ethyl methacrylate) grafted-hybrid magnetic nanoparticle for the separation of emulsified oil droplets and the recovering of oil using pH as the trigger[218]. However, the synthetic route, the choice of nanoparticle (silica on a magnetic nanoparticle), and the polymerization method (atom transfer radical polymerization) are complicated, not sustainable and are difficult to scale-up. In addition, the efficiency of demulsification is generally low since the emulsions are not completely coalesced on the application of triggers, such as pH and temperature. As a result, we propose to address these shortcomings using an abundant and easily-modified sustainable nanoparticle, cellulose nanocrystals (CNC)[216].

Cellulose nanocrystals, derived from acid hydrolysis of biomass, have attracted increasing attention for various applications[219–221], particularly for the stabilization of Pickering emulsions. Kalashnikova and coworkers were the first to report on the use of cellulose nanocrystals to stabilize oil-in-water emulsions[19,20,55]. Since then, surfactant and surface active polymers (such as surfactant adsorption[222], periodate oxidation and amination[223], esterification[190], as well as PNIPAM[56] and long alkyl chain grafting[224]) have been incorporated onto the CNC surface to further demonstrate its function in Pickering emulsions. Various strategies were used to manipulate the surface functionalities of CNC in controlling the physical properties of Pickering emulsions. Our research group has recently reported on a dual-responsive Pickering emulsion system based on poly[2-(dimethylamino)ethyl methacrylate] grafted cellulose nanocrystals[9]. However, when the triggers (pH and temperature) were applied, the destabilization of the emulsion was not sufficient for the recovery of the oil phase, thus limiting their use in industrial applications. To address this limitation, we adopted a new strategy by introducing a binary polymer brush consisting of

poly(oligoethylene glycol) methacrylate (POEGMA) and poly(methacrylic acid) (PMAA) on the surface of CNC nanoparticles using water as the reaction medium. The choice of the polymers allows for the control of the system using two types of triggers, i.e. POEGMA for temperature and PMAA for pH trigger. To the best of our knowledge, this is the first trial that using of a binary brush nanoparticle with tailorable interactions (hydrogen bonding) between POEGMA and PMAA chains to control the stability of particle-stabilized emulsions. Pickering emulsions based on the proposed modified CNC particles were investigated in detail in this chapter. By taking advantage of the functional groups on the surface of cellulose nanocrystals, polymer modifications can offer greater flexibility in the design and development of Pickering emulsifier. A reversible process of emulsification-demulsification could be controlled by manipulating pH. This chapter demonstrates that sustainable functional nanomaterials can be used for small scale oil-water separations, particularly in viscous oil transportation and harvesting of lipophilic compounds.

4.2   Experimental Section

4.2.1   Materials

Cellulose nanocrystals were supplied by CelluForce Inc. with an average charge density of 0.26 mmol/g. Di(ethylene glycol) methyl ether methacrylate (MEO$_2$MA, 95%), poly(ethylene glycol) methyl ether methacrylate (average M_n 300, OEGMA$_{300}$) and methacrylic acid (99%) were purchased from Sigma-Aldrich and passed through columns of neutral aluminum oxide prior to use. Cerium (IV) ammonium nitrate (CAN), ammonium persulfate (APS), heptane (99%), Nile red, poly(methacrylic acid, sodium salt) solution (average M_w 4000~6000, 40 wt.% in water) were used as received from Sigma-Aldrich. Standard solutions of hydrochloric acid and sodium hydroxide were used to prepare 1 M solutions.

4.2.2 Preparation of CNC-POEGMA

For grafting POEGMA to the surface of CNC, the typical experimental procedure was as follows: CNC (1.0 g) and 0.5 mL 70 wt% HNO_3 were dispersed in 150 mL of deionized water in a 250 mL one-neck flask equipped with magnetic stirrer first. MEO_2MA (9 mmol, 1.692 g) and $OEGMA_{300}$ (3 mmol, 0.9 g) (ratio of 3:1) were mixed in 5 mL ethanol and added dropwise into the reaction flask. The mixture was stirred for 15 mins and purged with high purity Argon for 1 h. Then the degassed initiator solution (CAN, 200 mg in 2 mL water) were added drop-wise into the reaction flask to initiate the polymerization. The reaction mixture was kept at room temperature overnight and the final product was concentrated via centrifugation and washed 3 times with Millipore water. The product was purified 2 times via ultrafiltration and dialyzed against Millipore water for 3 days with constant changes of water. The CNC-POEGMA dispersion with a measured solid content was recovered and stored in the refrigerator for future use.

4.2.3 Preparation of CNC-POEGMA-PMAA

To prepare the binary polymer brush grafted nanoparticles, 80 mL of CNC-POEGMA (1.0 g) aqueous dispersion was first mixed with 40 mL ethanol and dispersed using a sonication bath for 15 mins. The mixture was purged with high purity Argon for 1 h under constant stirring. The initiator (APS, 200 mg) was charged to the reaction flask and the temperature was kept at 50 $^\circ$C for 10 mins. After the degassed MAA (0.7 mL) was introduced, the temperature of the reaction mixture was slowly increased to 60 ^{0}C, which was maintained for 6 hours. By adding 1 ml of 1 M NaOH solution to the mixture, the modified nanoparticles were recovered by centrifugation and washed 3 times with deionized water. The mixture was then dialyzed against Millipore water for

3 days until the conductivity remained constant. The dispersion was finally concentrated and freeze-dried.

4.2.4 Preparation of Pickering emulsions

All emulsions were prepared using an UltraTurrax T25 homogenizer (IKA, Germany) at 6000 rpm for 2 min at room temperature. Except for specific illustrations, the ratio of oil and water was 3:7 and the aqueous phase with 0.3 wt% of nanoparticles was used in this study. To distinguish the oil and water phases and to facilitate the visualization of the emulsion droplets, 2 mg of Nile Red was dissolved in 250 mL of toluene or heptane, respectively.

4.2.5 Characterization Techniques

Conductometric and potentiometric titrations, performed on a Metrohm titrator, were used to quantify the surface functional groups. Typically, 40 mL of the 0.1 wt% nanoparticle dispersion was charged into the vessel and the pH was adjusted to 2.5. The dispersion was then titrated with 0.01 M NaOH solution under continuous stirring. Freeze-dried samples were homogenously mixed with KBr powder to yield a transparent pellet for FT-IR characterization. The spectra were acquired using a Bruker Tensor 27 FT-IR spectrometer with a resolution of 4 cm^{-1} and a scanning number of 32 from 400 to 4000 cm^{-1} at room temperature. The thermal responsive measurement was performed on a Varian (Cary 100 Bio) UV-Vis spectrometer equipped with a temperature controller. All the measurements were performed at a heating rate of 0.5 °C/min and a wavelength of 500 nm. Dynamic light scattering and ζ-potential experiments were acquired on a Malvern Instrument Zetasizer Nanoseries and thermal analyses were performed on a TGA Q600 TA Instrument (Lukens Drive, Delaware, U.S.A.) (Temperature program: 10 °C/min until 100 °C,

maintained at 100 °C for 5 min then 10 °C/min until 700 °C). Samples for TEM characterizations (Philips CM10) was prepared by spraying a 0.5 wt% aqueous dispersion onto copper grids (200 mesh coated with copper) and allowed to dry. In order to clarify the morphology of the nanoparticles, all samples were stained using 3 drops of 1.0 M ferric ion solution. Elemental analysis was carried out using a Vario Micro cube, Elementar Americas, Inc. Carbon, hydrogen, nitrogen, and sulphur content of the samples were determined by repeated measurements and the average values were reported. Surface tension measurements were conducted on the tensiometer Data Physics DCAT 21 system. Aqueous suspensions with a nanoparticle concentration of 1.0 wt% were analyzed using a Bohlin CS rheometer, where the steady shear viscosities versus shear rate curves were determined.

The emulsion droplets were captured at 200x magnification by an inverted optical microscope (Nikon Elipse Ti-S) equipped with a CCD camera (QImaging ReTIGA 2000R) by placing the emulsion droplets on a glass slide.
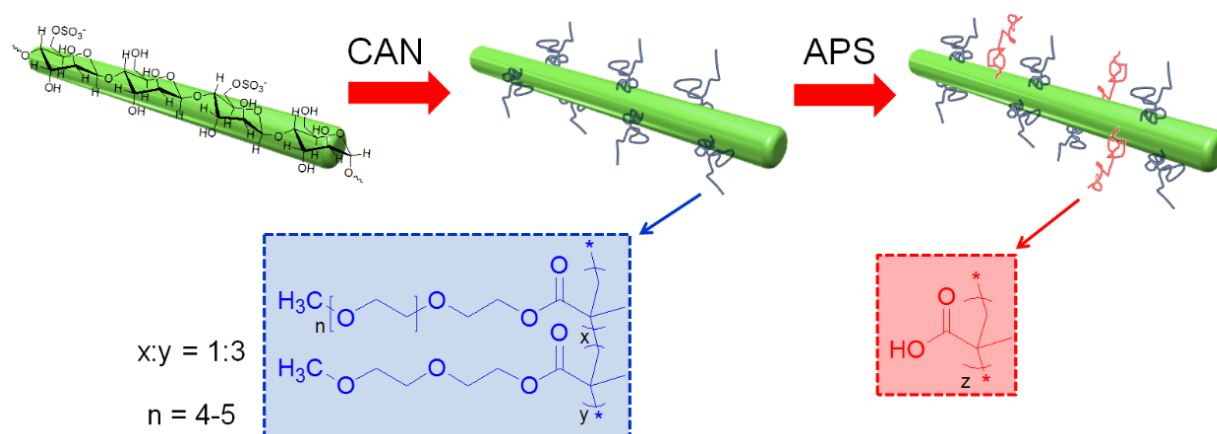
Figure 4.1 Schematic illustrating the synthesis of binary polymer brushes consisting of poly(oligoethylene glycol) methacrylate (POEGMA) and poly(methacrylic acid) (PMAA), on cellulose nanocrystals.

4.3   Results and discussion

4.3.1   Basic characterization of stimuli-responsive nanoparticles

Dual-responsive cellulose nanocrystals were synthesized by grafting stimuli-responsive polymer brushes, poly(oligo(ethylene glycol) methyl ether methacrylates (POEGMA) and poly(methacrylic acid) (PMAA) via a two-step polymerization process from the surface of CNC (Figure 4.1). POEGMA is a thermo-responsive and nontoxic polymer suitable for applications in injectable hydrogels, cell culture substrates as well as bio-separations by virtue of its biocompatibility and sharp thermal transition chracteristics[225–228]. By varying the number of ether groups using MEO$_2$MA, OEGMA$_{300}$, or OEGMA$_{475}$ or by changing the molar proportion of different types of monomers, the lower critical solution temperature (LCST) can be tuned accordingly. On the other hand, PMAA is a well-known polyelectrolyte with a mild hydrophobic character due to the repeating methyl groups that possesses a pH-dependent behavior that is correlated to the protonation and deprotonation of the carboxyl groups[129].

In the first step, the POEGMA copolymer was randomly grafted on the CNC surface (CNC-POEGMA) via a redox initiated free radical polymerization using cerium ammonium nitrate (CAN). It should be noted that the cerium ion is a strong oxidant for an alcohol containing 1, 2-glycol groups. The mechanism of the reaction involves the formation of a chelating complex that decomposes to generate free radicals on the cellulose backbone[53]. The free radicals can further react with the monomers that propagate until chain termination. In a second step, PMAA was grafted onto CNC-POEGMA nanoparticles via a persulfate initiator, ammonium persulfate (APS). The sulfate radical anion $SO_4^-\bullet$ extracts a hydrogen from a primary hydroxyl group resulting in a RO$\bullet$ radical that serves as a macro-initiator. The detailed mechanism can be found in the literatures[9,229].
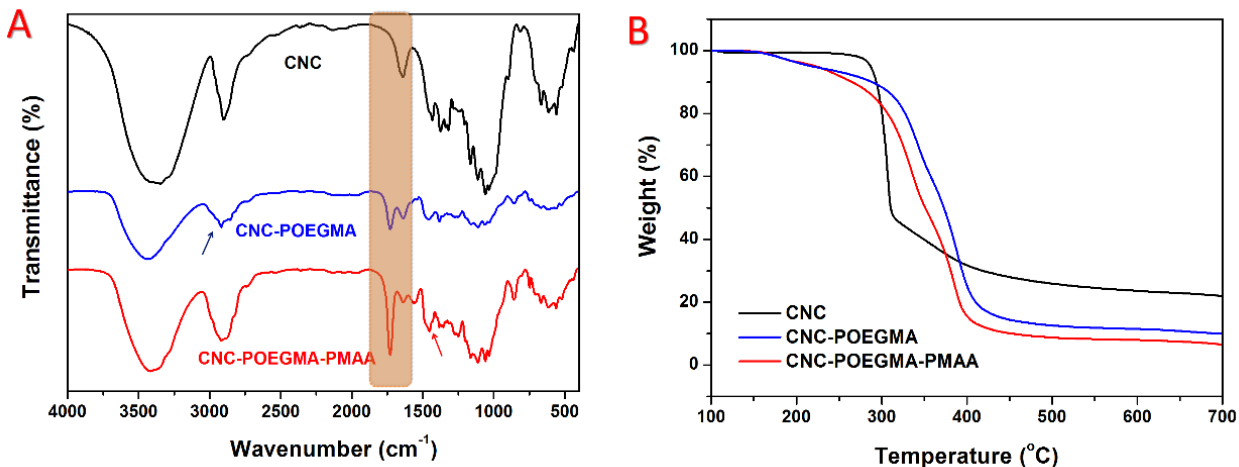
Figure 4.2 (A) FTIR spectral of pristine cellulose nanocrystals (CNC), CNC-POEGMA and CNC-POEGMA-PMAA. (B) Thermogravimetric curves of CNC (black), CNC-POEGMA (blue) and CNC-POEGMA-PMAA (red) samples.

Successful grafting of POEGMA and PMAA on the CNC nanoparticles was confirmed by FT-IR spectroscopy (Figure 4.2A). In addition to the characteristic stretching vibrations of hydroxyl groups at 3400 cm^{-1} and 1058 cm^{-1} on cellulose nanocrystals, a new peak corresponding to carbonyl stretching was observed at 1729 cm^{-1} for CNC-POEGMA. In addition, the obvious change of the spectra in the region near 2900 cm^{-1} is a consequence of the methylene moieties of POEGMA chains, as reported previously[226,230]. When the CNC-POEGMA system was further grafted with PMAA, the absorption ratio between 1730 and 1640 cm^{-1} was increased due to the increase in the specific absorption of C=O bonds on the MAA repeating units. Another apparent sharp peak around 1550 cm^{-1} was observed in the spectrum of CNC-POEGMA-PMAA, indicating the presence of carboxylate groups[231,232].
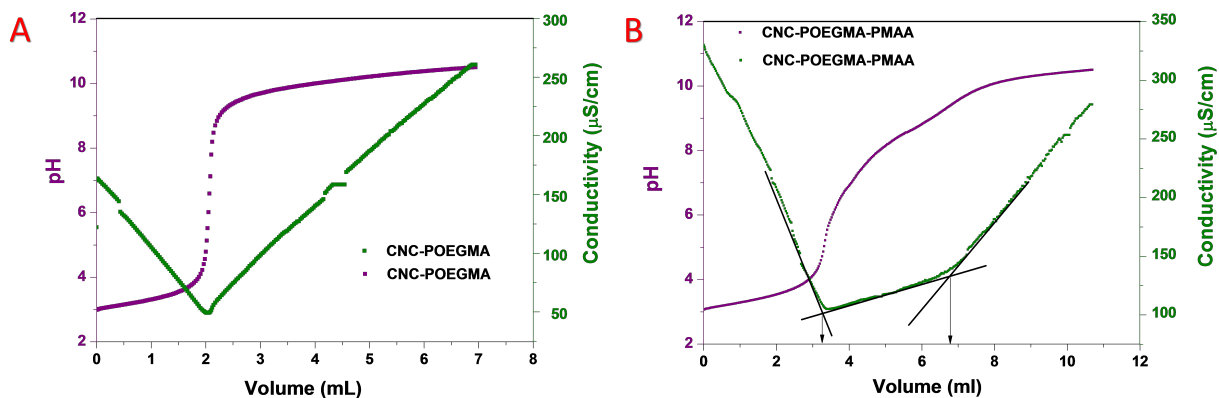
Figure 4.3 pH and conductivity titration curves of 0.1 wt.% CNC-POEGMA(A) and CNC-POEGMA-PMAA(B) dispersions.

In addition, the as-prepared nanoparticles were characterized by potentiometric titration, and the results for different nanoparticles, CNC-POEGMA and CNC-POEGMA-PMAA, are shown in Figure 4.3. CNC-POEGMA displays a classic profile of strong base titration into strong acid, while the CNC-POEGMA-MAA sample exhibited a three-stage process, correlating to strong acid, weak acid and strong base behavior, respectively[9,233,234]. The weak acid region is associated to the deprotonation of carboxylate groups. Depending on the titration curves, the amount of MAA repeating units was calculated to be approximately ~0.850 mmol per gram of CNC-POEGMA-PMAA nanoparticles.

TGA measurements were used to elucidate the thermal stability of CNC after modifications (Figure 4.2B). It was observed that the polymer grafting lowered the thermal stability of the nanoparticle. Polymer grafted CNC started to decompose at temperatures around 180 ^{o}C, which is substantially lower than that of pristine CNC samples (270 ^{o}C). The reduction in thermal stability after the polymer grafting may also result from the oxidation process as CAN initiator will oxidize the backbone of the cellulose to produce aldehyde functional groups that are less thermal stable. Compared to CNC-POEGMA, CNC-POEGMA-PMAA displayed a faster degradation rate

between 200 °C and 300 °C as well as a lower residual mass at high temperature. The TGA analyses provided an indirect confirmation of successful grafting on CNC.

The possible changes in the morphologies of the nanoparticles were characterized by TEM. As shown in Figure 4.4, all the nanoparticles were well-dispersed with fairly identical rod structure. With the grafting of hydrophilic polymers, the nanoparticles present higher polydispersity as well as a more homogenous dispersion. The TEM images of CNC and CNC-POEGMA contains several bundle-like structure due to van der Waals interactions and hydrogen bonding, rendering it to somewhat different from the CNC-POEGMA-PMAA system. This is probably due to the strong electrostatic repulsions between CNC-POEGMA-PMAA nanoparticles. We used the zeta-sizer to check the size change of the nanoparticles after each modification steps, and only slightly change was observed.
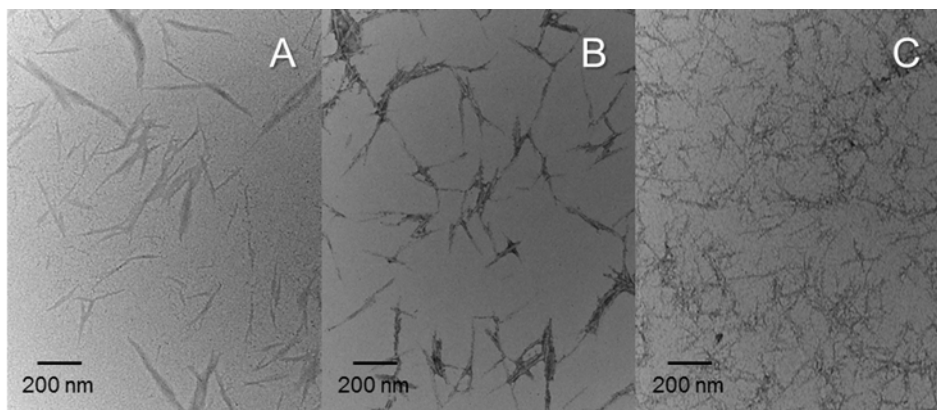
Figure 4.4 TEM images showing the morphologies of pristine CNC (A), CNC-POEGMA (B) and CNC-POEGMA-PMAA (C).

Elemental analysis (Table 4.1) was used to further confirm the presence of polymer grafting. From the knowledge of the elemental weight of both the glucose unit and the monomer used, it is possible to determine the change in the amounts of each element. In the second modification step, regardless of the molecular weight and grafting density, the PMAA weight ratio on CNC-POEGMA-PMAA

nanoparticles was determined to be 11.5 wt%, which is in agreement with the result obtained from potentiometric titration. The weight ratio of PMAA to mixed brush modified cellulose nanocrystals was determined from the analysis of the compositional change of carbon and oxygen. The detail description is included in the supporting information.

Table 4.1 Atomic composition of different nanoparticles determined by elemental analyses

Sample	N%	C%	H%	S%
CNC	0.02	41.11	5.62	0.84
CNC-POEGMA	0.01	49.25	6.43	0.34
CNC-POEGMA-PMAA	0.00	50.01	6.68	0.22
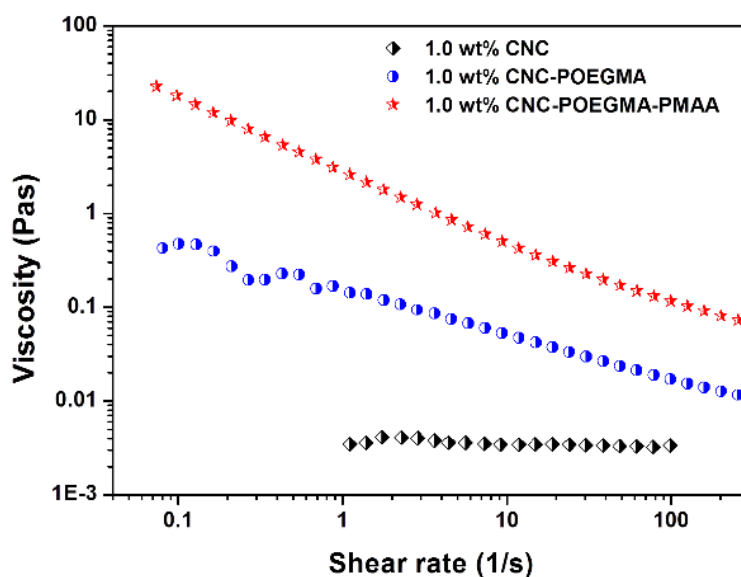
Figure 4.5 Viscosity profiles of 1.0 wt% nanoparticle dispersions (CNC in black, CNC-POEGMA in blue and CNC-POEGMA-PMAA in red).

Figure 4.5 shows the viscosity-shear rate relationship of the polymer grafted CNC suspensions under steady shear flow. The viscosity profile of the 1.0 wt% CNC dispersion is independent of

shear rate since the concentration of the nanoparticle is in the dilute solution regime, and significant particle-particle interaction is absent. However, shear thinning behavior was clearly evident for CNC-POEGMA, which is attributed to the network structures produced by the grafted polymer chains induced by hydrogen bonding. For the CNC-POEGMA-PMAA system, the viscosity increased by 20 times due to more hydrogen bonds and the ionization of carboxyl groups that induce electrostatic repulsions between the nanostructures.
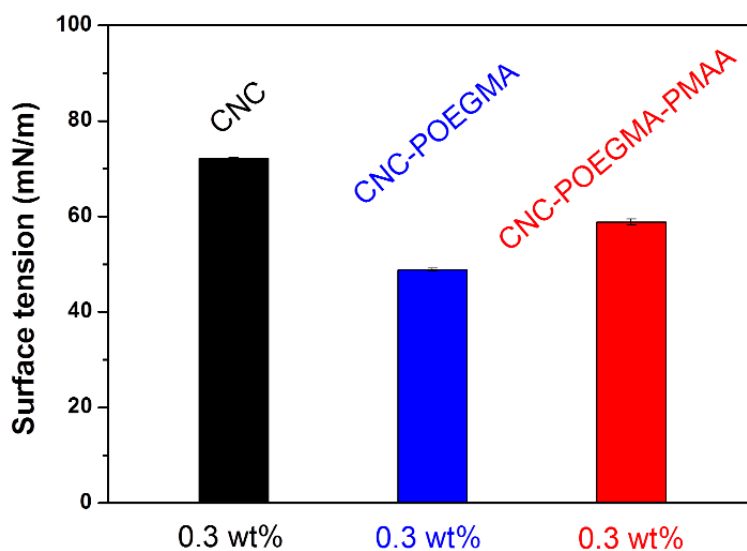
Figure 4.6 Surface tension values of 0.3 wt% CNC (black), CNC-POEGMA (blue) and CNC-POEGMA-PMAA (red) dispersions.

The surface tensions of the three nanoparticle dispersions (0.3 wt%) are shown in Figure 4.6. It should be noted that the dispersion of polymer grafted CNC displayed a lower surface tension than pristine CNC due to the amphiphilic characteristics of the polymer chains, which is consistent with previous reports[9,49].

4.3.2　Stimuli-responses of the nanoparticles to pH and temperature

The impact of pH on the surface properties of the nanoparticles was determined by zeta-potential measurements. As shown in Figure 4.7A, the zeta-potentials of CNC-POEGMA samples in water were between -12 to -16mV, which is independent of pH due to the absence of pH-responsive functional groups. CNC-POEGMA-PMAA however possessed a pH-dependent zeta-potential due to the presence of the weak polyelectrolyte (PMAA), which undergoes subtle molecular rearrangements close to the pK_a of MAA. Below the pH of 4.5, all the COOH groups are protonated, and the hydrogen bonding between POEGMA and PMAA may lead to the formation of CNC-POEGMA-PMAA aggregates and precipitates, causing a hazy dispersion. Above the pH of 4.5, the COOH groups become deprotonated, where repulsive carboxylate anions disrupt the hydrophobic association and hydrogen bonding to yield a stable dispersion[235,236]. The zeta-potential decreased from -25 to -40mV when the pH was increased from 4.5 to 8.0 due to the progressive deprotonation of carboxylic acid groups. Based on previous reported studies on polyethylene glycol and PMAA[231,237–245], we infer that the hydrogen bonding between POEGMA and PMAA contributed to the instability of the nanoparticles at low pH, and this will be discussed later.

Temperature-dependent UV-Vis transmittance measurements at a wavelength of 500 nm were performed on 0.2 wt% samples as shown in Figure 4.7B. Both CNC-POEGMA and CNC-POEGMA-MAA dispersions were translucent at low temperature (25 °C, see inserts), and the transmittance was around 90 % due to the limited scattering by nanoparticles. Upon heating, the transmittance decreased dramatically to around 10% for CNC-POEGMA due to the dehydration of ethylene-oxide side chains distributed along the backbone, producing a compact globular structure induced by the intra- and intermolecular aggregations. A transition temperature of around

37ºC was observed, which is in agreement with polymers prepared using controlled polymerization techniques[228]. This result indicates that the thermo-responsive behavior of co-polymers prepared by free radical polymerization (FRP) is similar to those prepared by controlled polymerization. Our study is in agreement with previous studies and supported by the molecular characteristics of the polymers (only a small impact of the polymer tacticity on the thermo-responsiveness was observed[225,227]. For CNC-POEGMA-MAA samples, the transition temperature increased slightly and the transition region broadened maybe due to the change in the hydrophilicity of the nanoparticles.
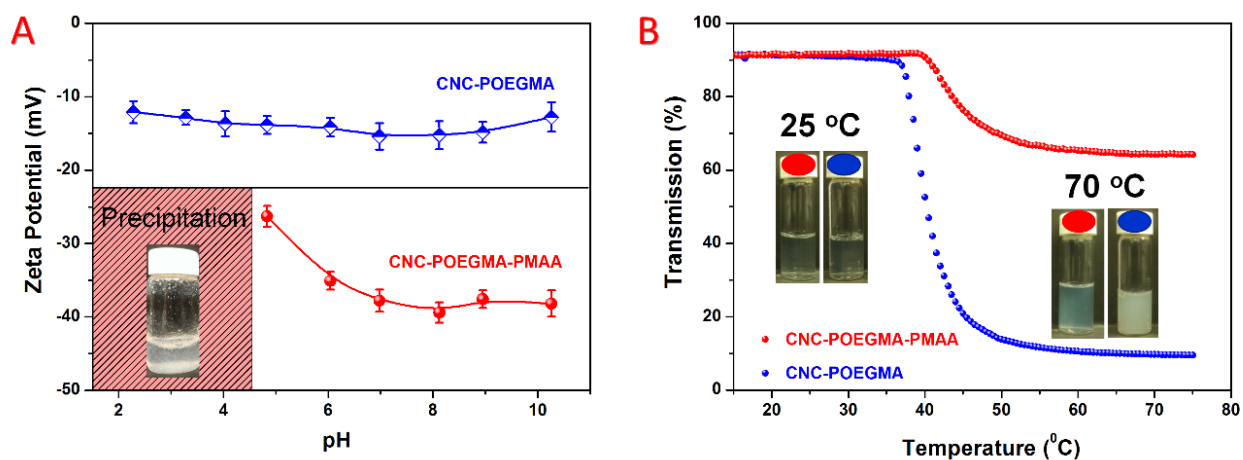
Figure 4.7 (A) Effect of pH values on Zeta-potential profile of CNC-POEGMA and CNC-POEGMA-PMAA in aqueous suspension; (B) Transmittance versus temperature of 0.2 wt% CNC-POEGMA (blue) and CNC-POEGMA-PMAA (red) aqueous suspensions at a heating rate of 0.5 °C/min and a wavelength of 500 nm.

4.3.3   Emulsion stability

Evaluation of Coverage

Surface coverage is an important parameter to understand the organization of nanoparticles at the oil-water interface. Heptane-in-water emulsions stabilized by different concentrations of CNC-POEGMA-PMAA were investigated. It shows that the emulsion droplet size decreased from 43.7

to 10 µm with increasing concentration from 0.08 to 0.6 wt % (see Figure 4.8A). From the calculation of the surface coverage described in the supporting information, the values of surface coverage determined and plotted against the mass of nanoparticle in the aqueous phase. The results show that a minimum of approximately 85% of covered surface is sufficient to stabilize an emulsion with CNC-POEGMA-PMAA nanoparticles (see Figure 4.8B). This value is in accordance with the data reported in the literature for Pickering emulsion system stabilized by cellulose nanocrystals[18, 19]. Also noted from the previous report, for cellulose nanocrystals with a low aspect ratio, it may need a higher surface coverage to stabilize the emulsion[55]. As the aspect ratio and the flexibility of the nanoparticles may vary, carrying out experiment to compare their packing status at the interface would be quite interesting in future work.

Thermo-responsive behavior

Heptane-in-water-emulsion systems prepared using a 0.3 wt% nanoparticle concentration were used to study the effect of temperatures on the stability of the emulsions. As shown in Figure 4.9, CNC-POEGMA-PMAA systems phase separated when incubated at 70 $^{\circ}$C for 1 hour. Beyond the transition temperature of between 37 and 40 $^{\circ}$C, the hydrophobicity of the polymer was increased by the disruption of hydrogen bonds between water and ether groups resulting in the hydrophobic association of the polymer chains and nanoparticles. As a consequence, the oil droplets became unstable as the polymer grafted CNC began to associate resulting in the coalescence of oil droplets to form larger droplets. (~20% coalescence based on the volume ratio of oil collected to the emulsified oil before emulsification) When the temperature was increased, the droplet collision frequency was enhanced, while the interfacial viscosity and film-drainage rate were reduced leading to greater droplet coalescence[57].
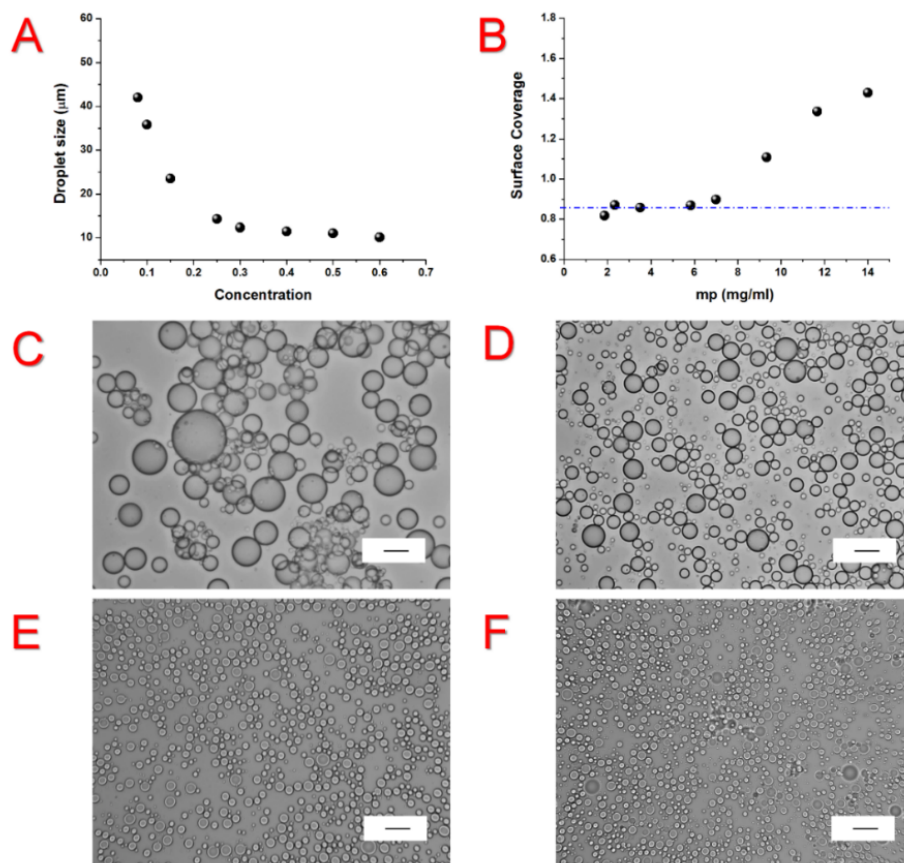
Figure 4.8 (A) Heptane in water emulsion droplet size profile as a function of CNC-POEGMA-PMAA concentrations; (B) Evolution of surface coverage vs the amount of CNC-POEGMA-PMAA included in the water phase per ml of heptane; (C-F) Optical micrographs of heptane emulsions stabilized by different concentration of CNC-POEGMA-PMAA (C: 0.1 wt%; D 0.15 wt%; E: 0.3 wt%; F: 0.5 wt%), the oil to water ratio is 30:70.
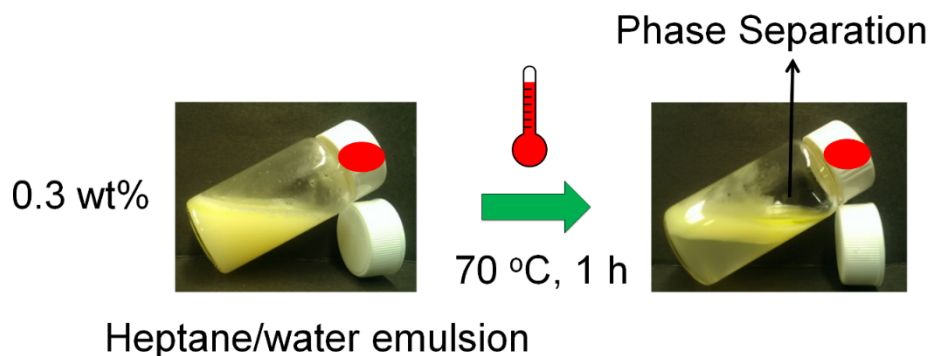
Figure 4.9 Photographs of heptane-in-water emulsions stabilized by CNC-POEGMA-MAA (0.3 wt%) and its response to being placed in a 70 $^{\circ}$C water bath for 1 hour.

pH-responsive behavior

The stability of Pickering emulsions with nanoparticles grafted with pH-responsive polyelectrolyte brushes is expected to depend on pH. Heptane was used as the organic phase and a 0.3 wt% aqueous dispersion of nanoparticle was used as the aqueous phase. The pH values of the aqueous dispersions were tuned to the targeted values by adding 1M NaOH or HCl. As discussed earlier, CNC-POEGMA did not possess pH-dependent characteristics; hence changing pH did not impact the emulsion, which remained stable against coalescence for more than 6 months (Figure 4.10A). A slight creaming was evident due to the density difference between water and heptane. However, for CNC-POEGMA-PMAA, the stability of the Pickering emulsion is dependent on pH. Above pH 6, the emulsions were stable, and negligible coalescence or creaming of the emulsions was evident. The sizes of emulsion droplets at different pHs were fairly uniform because the emulsions are reasonably stable (average oil droplet diameter of 12.3 μm) at pH 10. The fluorescence micrographs of heptane-in-water emulsions stabilized by 0.3 wt % CNC-POEGMA-PMAA at pH 10 are shown in Figure 4.10C. When the pH was decreased to 4, incomplete coalescence of emulsions and formation of particulate flocs were observed (Figure 4.10B and 4.10C), along with a dramatic increase in the viscosity. We infer that by lowering the pH, the carboxyl groups on PMAA chains become protonated and complex with $-CH_2-CH_2-O-$ groups on the POEGMA chains via hydrogen bonding (Figure 4.11). As a result, the polymer brushes undergo conformational change forming hydrophobic associations and globular domains that lead to inter- or intra-nanoparticle aggregation. The aggregation will result in incomplete coverage of the oil-water interface, promoting the coalescence of oil droplets to compensate for the reduced surface coverage of the droplet interfaces (Figure 4.11). Further reducing the pH to 2 resulted in the formation of two distinctive layers soon after emulsification and large aggregates were evident.

These results reflect a strong correlation between emulsion stability and interactions between modified nanoparticles, where the emulsion stability increases with the introduction of electrostatic repulsions by manipulating the pH values.
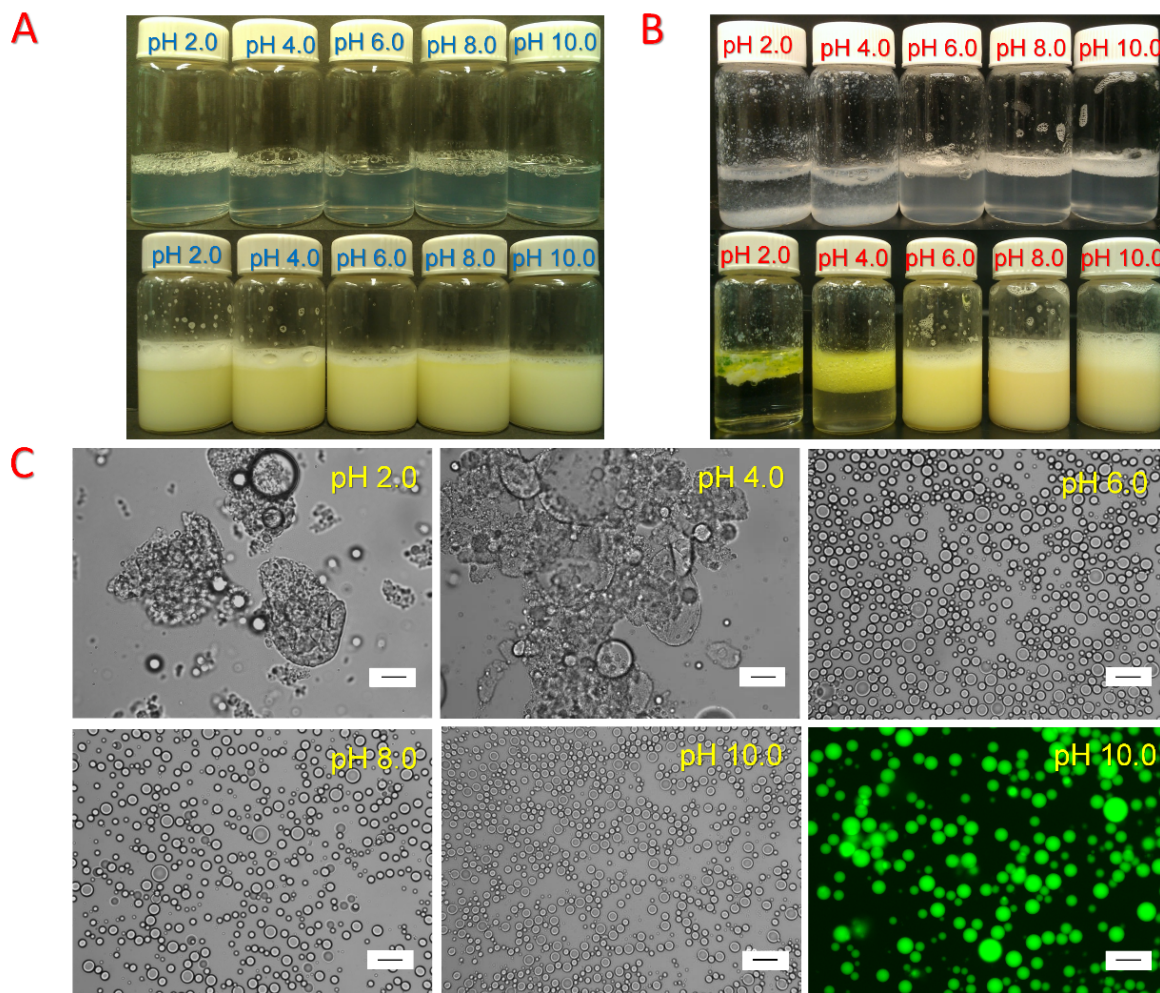
Figure 4.10 (A) Photographs of CNC-POEGMA (0.3 wt%) suspensions as well as emulsions (heptane water ratio 3:7) stabilized by them under different pH values; (B) Photographs of CNC-POEGMA-PMAA (0.3 wt%) suspensions as well as emulsions (heptane water ratio 3:7) stabilized by them under different pH values; (C) Optical micrographs of emulsions stabilized by CNC-POEGMA-PMAA at different pHs; fluorescence micrographs of heptane in water emulsion stabilized by CNC-POEGMA-PMAA (0.3 wt%) at pH 10, the oil phase is dyed with Nile red. The scale bars shown in all pictures are 50 μm.
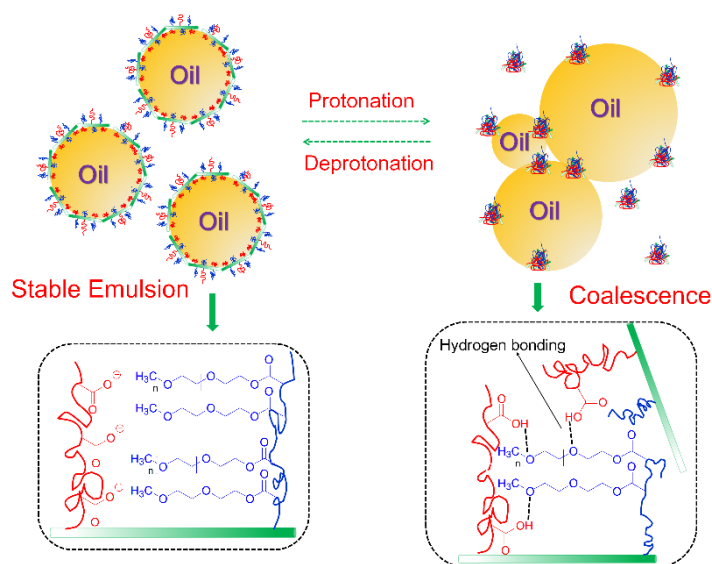
Figure 4.11 Schematic illustrating the pH-responsive behavior of Pickering emulsions stabilized by CNC-POEGMA-PMAA.

In order to demonstrate the importance of both grafted polymer chains on controlling the stability of the emulsions, other systems stabilized by CNC-PMAA or PMAA and CNC-POEGMA mixtures were investigated. It should be noted that the results differ significantly from the CNC-POEGMA-PMAA systems. As shown in Figure 4.12, the emulsion droplets using CNC-PMAA as stabilizer possessed pH-dependent stability characteristics, displaying an opposite trend to the CNC-POEGMA-PMAA system. The emulsions readily coalesced without agitation after 24 hours at high pH conditions (pH = 8 or 10), while they were stable at low pH conditions (pH =2, 4 or 6) because the carboxylate groups are protonated at low pH and the hydrophobic PMAA chains will partition to the oil phase to cover the oil-water interface.[235,236] The modified nanoparticles can further stabilize the oil droplets compared to pristine CNC nanoparticles, which is in agreement with our previous studies[9]. However, at high pH, the charged polymeric chains induced strong electrostatic repulsions between nanoparticles, which decreased the affinity of the nanoparticles to

the oil/water interface resulting in the destabilization of the oil droplets. Although the pH-responsive behaviors were achieved with the grafting of polyelectrolyte chains, CNC-PMAA is still not an ideal oil harvesting stabilizer as the demulsification efficiency at high pH values is not very effective.
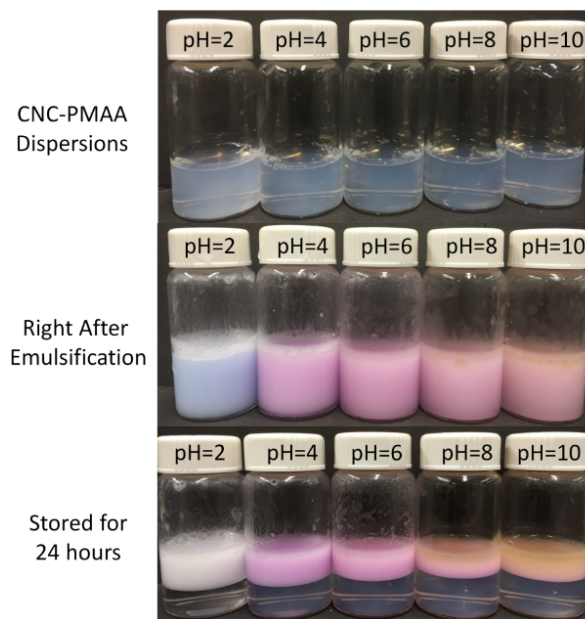
Figure 4.12 Photographs of 0.3 wt% CNC-PMAA dispersions under different pH conditions; Emulsions (heptane used as oil phase; oil to water ratio of 3:7) stabilized by 0.3 wt% CNC-PMAA right after emulsification and stored for 24 hours.
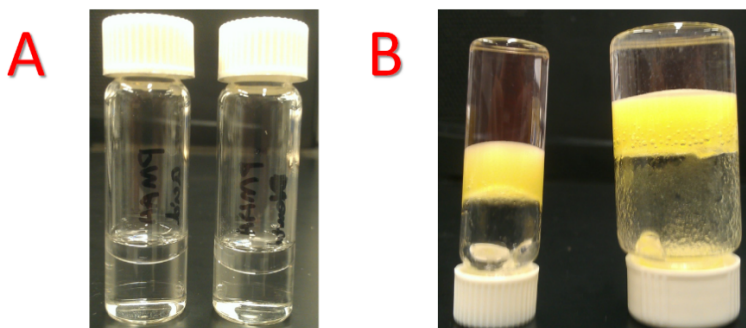
Figure 4.13 (A) Phase separation after homogenization showing heptane droplets cannot be stabilized by PMAA neither at protonate (left) or deprotonate (right) state; (B) Dense and viscose emulsion phases shown by upside down of the glass vials.
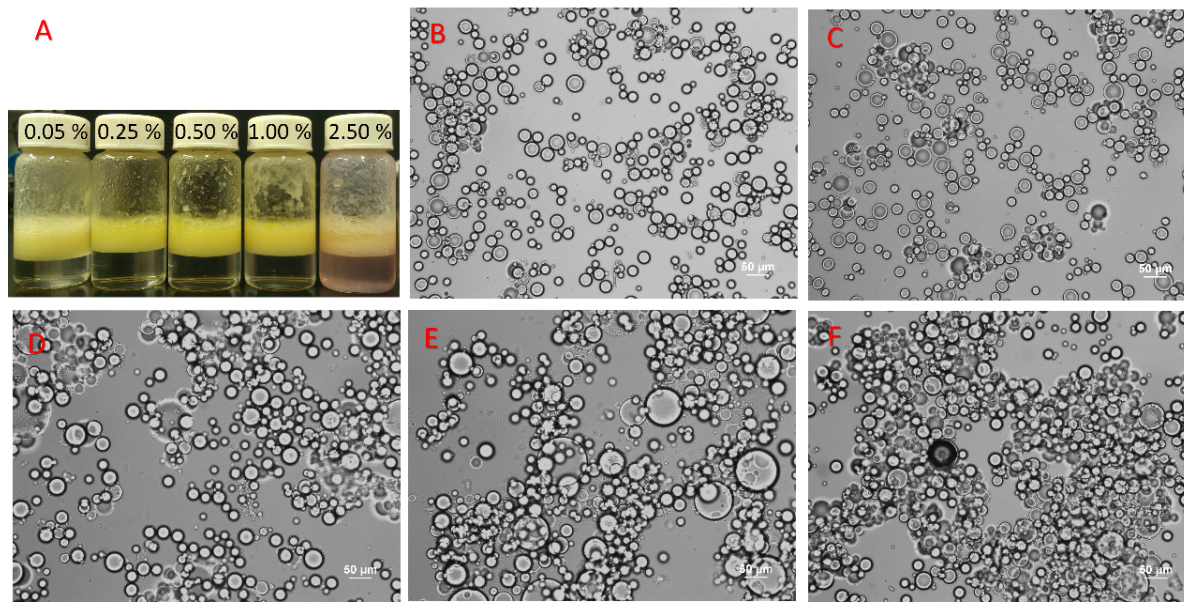
Figure 4.14 (A) Emulsions (heptane used as oil phase; oil-to-water ratio 3:7) stabilized by mixture of CNC-POEGMA and different concentrations PMAA at pH 2 after storing for 1day. (B-F) Microscopy images of oil droplets from emulsions shown in picture A [B (0.05 wt%), C (0.25 wt%) D (0.50 wt%) E (1.00 wt%) F (2.50 wt%)], the scale bar is 50μm.

Ungrafted PMAA chains are unable to stabilize emulsion droplets in its protonated or deprotonated state as shown in Figure 4.13A. To systems stabilized by CNC-POEGMA (0.3 wt%), various amounts of free PMAA chains were introduced. At pH 2, a viscous emulsion phase was observed in the supernatant in all the samples (see in Figure 4.13B and 4.14), which suggests the presence of hydrogen bond interactions between the ether and carboxylic groups on the POEGMA and PMAA respectively. We observed that neither of them instantaneously destabilized the emulsions, even in excess of PMAA chains. (Note: at low concentrations (Figure 4.14A-0.05 %, 0.25%, 0.5 %), free PMAA chains were prone to interact with CNC-POEGMA resulting in a clear dispersion. At high polymer concentration (2.5 %), excess free PMAA chains will adopt a collapsed structure in water, producing hydrophobic domains that partition hydrophobic florescence dye molecules, such as Nile Red resulting in a pink solution (Figure 4.14A-2.50 %)).

The stability of the emulsions was monitored, and Figure 4.15 shows the changes in the size of emulsion droplets as a function of time, where the size increased dramatically due to the coalescence of the emulsion droplets (Figure 4.15A). We hypothesize that chain flexibility and the molecular weight of PMAA may play important roles in destabilizing the emulsions. At pH 2, adding free PMAA polymer into the CNC-POEGMA Pickering emulsion may lead to bridging of oil droplets driven by hydrogen bonding between PMAA and POEGMA chains on the surface of CNC. The nanoparticles at the oil-water phase may form large hydrophobic aggregates with time that reduce the total surface coverage of CNC-POEGMA on the emulsion droplets. This induces the oil droplet to "ripen" or coalesce to compensate for the reduced surface coverage of the emulsion droplets. More studies are in progress to elucidate the observed phenomenon.
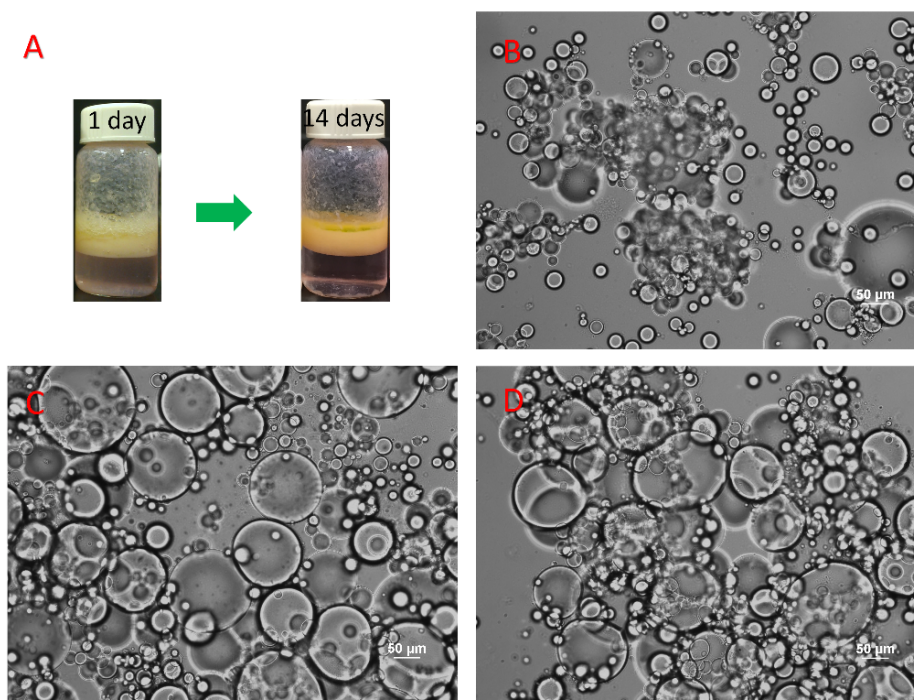
Figure 4.15 (A) Emulsions (heptane used as oil phase; oil-to-water ratio 3:7) stabilized by mixture of CNC-POEGMA and PMAA (2.5 wt%) at pH 2 after storing for 1day and 14 days. (B-D) Microscopy images of oil droplets from emulsions storing for 1 day (B), 7 days (C) and 14 days (D).

116

4.3.4 Reversibility and Recycling

It is vital to demonstrate the reversibility of the stimuli-responsive nanoparticles by manipulating the external environmental conditions. Two short videos illustrating this phenomenon were recorded and can be viewed in the Supporting information. The demulsification occurred immediately when several drops of 1 M HCl were added to the vial containing the stable Pickering emulsions (pH 6.8), resulting in the formation of two separate layers (Figure 4.16A). When a similar amount of 1 M NaOH was added to reverse the pH, stable emulsions were restored with
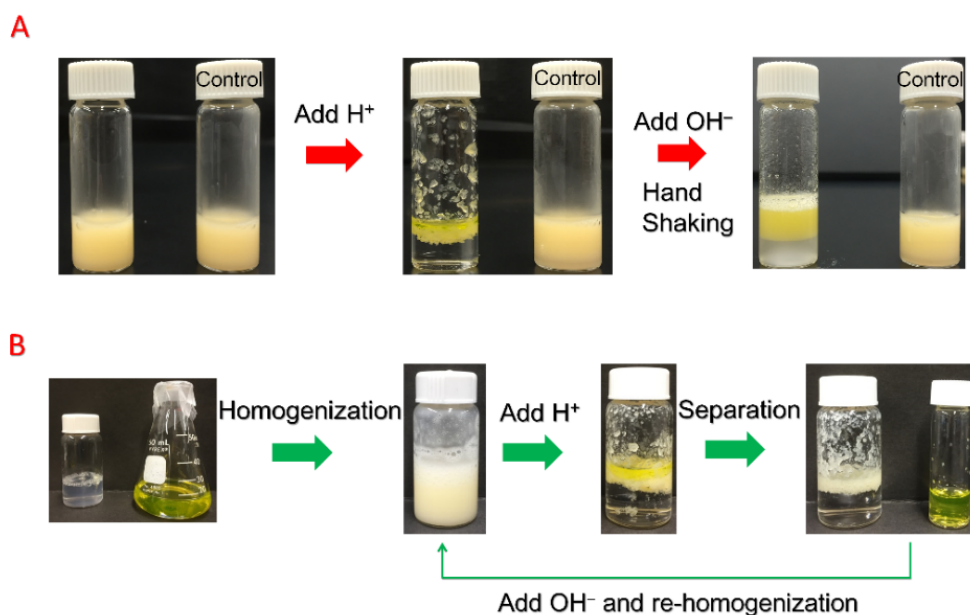
Figure 4.16 (A) Flowchart showing the reversible stabilization-destabilization by alternate addition of acid or base and (B) a demonstration of oil harvesting by manipulating the pH.

a slight creaming effect due to the presence of salts. Successive stabilization-destabilization cycles were possible by alternate addition of acid or base, demonstrating the reversibility of the emulsification and oil-water separation protocols. As shown in Figure 4.16B, a stable heptane-in-water emulsion could be stabilized by 0.3 wt% CNC-POEGMA-PMAA nanoparticles. Tuning the pH to an acidic condition leads to strong hydrogen bonding between the nanoparticles, resulting

in the coalescence and phase separation of the emulsion droplets. The oil phase could be recovered by gravity separation with up to 92% capture efficiency (by volume ratio). The aggregated flocs can be re-dispersed by changing the dispersion pH to 7, and the oil phase can be emulsified to form stable emulsions. This process can be repeated 5 times without any loss in efficiency.

4.4   Conclusions

Binary polymer brushes, poly(oligoethylene glycol) methacrylate (POEGMA) and poly(methacrylic acid) (PMAA), grafted cellulose nanocrystals were synthesized using a straightforward synthetic protocols. The modified nanoparticles can respond to specific triggers, such as temperature (CNC-POEGMA), pH (CNC-PMAA) or temperature/pH (CNC-POEGMA-PMAA). Destabilization of the emulsion was achieved by increasing the temperature caused by the conformational change of POEGMA chains. By incorporating PMAA chains, the emulsions stabilized by CNC-POEGMA-PMAA displayed pH-responsive stability caused by the tunable interaction between the nanoparticles. Bifunctionalized CNCs diffused to the oil-water interface and stabilized the oil droplets at high pHs. When the pH was reduced to 2, strong hydrogen bonding between POEGMA and PMAA chains grafted on the CNC induced instant coalescence of emulsions, resulting in the phase separation of oil and water. However, for emulsions stabilized by CNC-POEGMA and free PMAA mixtures, instant coalescence was not observed at low pHs. We hypothesized that the chain flexibility and molecular weight of PMAA may play important roles in destabilizing the emulsions. Furthermore, we demonstrated a reversible emulsification-demulsification process controlled by pH, where the emulsification and oil-water separation can be repeated 5 times without any loss in efficiency. A new approach to prepare surface-tailorable sustainable nanomaterials for oil-water separations, especially for oil droplet transportation and lipophilic substances harvesting was developed.

Chapter 5 Polyrhodanine coated cellulose nanocrystals as optical pH indicators

In this chapter, a simple and green approach to produce cellulose nanocrystal@polyrhodanine (CNC@PR) core-shell nanoparticles via *in-situ* polymerization is proposed. The core-shell nanoparticles displayed reversible colour change in response to pH, confirming their utility as optical pH indicator. This property was retained when the nanoparticles were configured into other shapes, such as flat films or hydrogel beads.
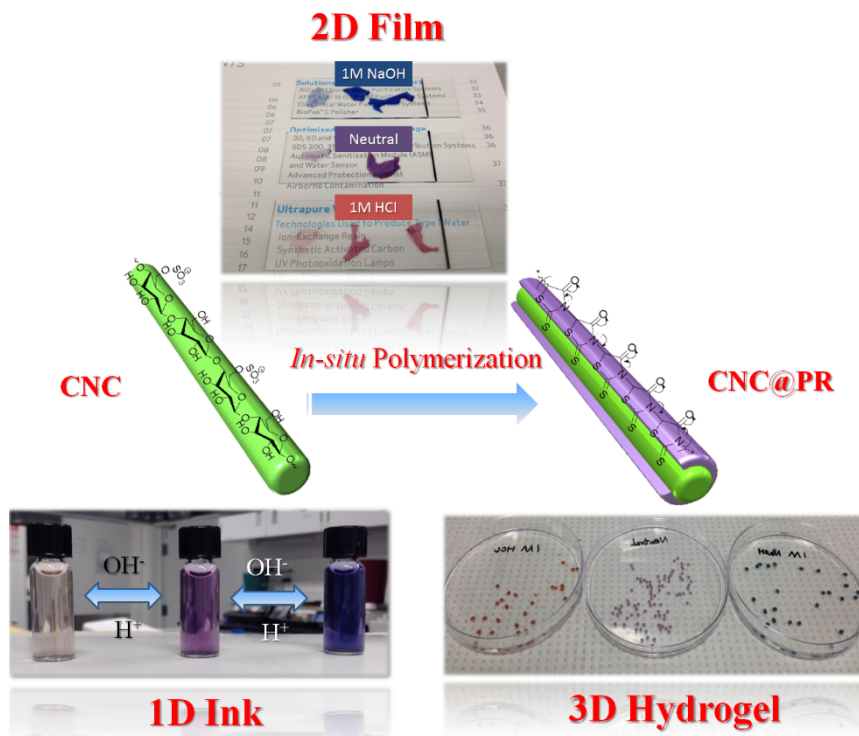
5.1 Introduction

Fabrication of core-shell nanoparticles with unique and tunable properties for various applications has been actively researched in recent years. The structure of these nanoparticles often consists of an inner core encapsulated by a shell layer composed of another material. Compared to conventional single-component nanoparticles, the core-shell structure facilitates the incorporation of diverse functionalities and processibilities starting from the shell material into the core, thereby providing synergistic effects. Among all the research topics, rendering the nanoparticles with electric or optical responsive properties are the most fascinating, because the surface of the nanoparticles can be easily tailored to accommodate specific electronic, optical, catalytic or fluorescence properties[246].

Cellulose nanocrystals (CNC), prepared and isolated from natural cellulosic materials by acid hydrolysis, has driven many of the innovations in science and engineering by virtue of its good water dispersity and eco-sustainable features[3,9,12]. Due of their attractive mechanical properties, CNC and its modified forms have been extensively used as reinforcing agent in nanocomposites[2]. Moreover, harnessing the chiral nematic phase of rod-like particle and high surface area, CNC represents an interesting potential template system for producing porous inorganic nanomaterials[18,247]. It is anticipated that these nanoparticles can be used for various applications, ranging from drilling fluids, paints, industrial coatings, automotive components, building and packaging materials. Intrinsically conductive polymers (ICPs) such as polypyrrole (PPy), polyaniline (PANI) and poly(3,4-ethylene-dioxythiophene)(PEDOT) have gained increasing attention due to their low cost, unique redox behavior, ease of synthesis, environmental and chemical stability, and relatively high conductivity[248–255]. Polyrhodanine (PR) as a conductive

polymer is receiving some attention for application as antimicrobial agent and water purification for the removal of toxic metallic ion[256–260]. However, to the best of our knowledge, there are no reports on the reversibility of color in response to the pH.

In this chapter, a simple and green approach was developed to produce cellulose nanocrystal@polyrhodanine (CNC@PR) core-shell nanoparticles. The polyrhodanine shell was prepared by *in-situ* polymerization of rhodanine monomer using Fe(III) ions as both initiator, oxidant and counter-ion for doping the synthesized PR. The polymerization proceeded preferentially on the surface of cellulose nanocrystals, where Fe(III) ions were deposited on the CNC surface via electrostatic interactions. This process is simple and environmentally benign since the aqueous solution was used. Our protocol satisfies most of the requirement for CNC modifications, such as retaining the morphologies and crystalline properties as well as preventing the aggregation of nanoparticles when dispersed in other polar solvents. CNC serves as an ideal substrate to support the polymer coating and the resulting nanocomposite possesses excellent colloidal stability against flocculation or aggregation, thereby addressing a critical issue with the poor solubility of the PR in water. Due to the excellent mechanical strength and film-formation property of CNC, the composite nanoparticles can be assembled onto flat membrane substrate with good transparency, or it could be incorporated into stable hydrogel beads. To the best of our knowledge, this is the first reported study on the reversible color-change of polyrhodanine in response to oxidative or reductive environment. Thus, novel color sensitive core-shell nanomaterial that responds to external stimuli, such as pH can be configured into solution based ink, flat films or stable hydrogel beads that possess properties comparable to dye conjugated nanocellulose[261].

5.2 Experiment part

5.2.1 Materials and reagents

Cellulose nanocrystals (CNCs) were produced and provided by CelluForce Inc. with an average charge density of 0.26 mmol/g. Other reagents or chemicals were purchased from Sigma-Aldrich and used without further purification. Hydrochloric acid (HCl 1M) solution and sodium hydroxide (NaOH 1M) solution were diluted from standard solutions.

5.2.2 Instruments and characterizations

FTIR spectra were acquired at room temperature using a Bruker Tensor 27 FT-IR spectrometer with a resolution of 4 cm^{-1} and a scanning number of 32 from 400 to 4000 cm^{-1}. UV-Vis spectra were acquired a Cary 100 Scan Varian. Dynamic light scattering and ζ-potential experiments were conducted on a Malvern Instrument Zetasizer Nanoseries. Thermal analyses were performed on a TGA Q600 TA Instrument (Lukens Drive, Delaware, U.S.A.) (Temperature program: 10 °C/min until 100 °C, maintained at 100 °C for 5 mins then 10 °C/min until 500 °C, maintained at 500 °C for 2 mins). Elemental analysis was carried out using a Vario Micro cube, Elementar Americas, Inc. Carbon, hydrogen, nitrogen, and sulphur content of the samples were determined by repeated measurement and the average values reported.

5.2.3 Preparation of CNC@PR nanoparticles

$FeCl_3$ (22.5mM) was added into a well-dispersed 20mL CNC solution (0.2 wt %), and the mixture vigorously magnetic stirred for 6h. The resulting CNC-Fe(III) complexes were quite viscous and had a lemon yellow color. Rhodanine monomers (22.5mM) were dissolved in 20mL deionized water (DI water) and heated up to 85ºC with vigorous stirring to ensure that the monomers dissolved completely. The CNC-Fe(III) complexes were introduced dropwise into the dissolved

rhodanine monomer solution. Vigorous magnetic stirring was applied and the temperature was maintained at 85 °C during the whole polymerization process. After 24 h, cellulose nanocrystal@polyrhodanine (CNC@PR) core-shell nanoparticles were obtained after ultrafiltration with 100 nm pore size filter-paper membranes and rinsed several times using millipore-Q water until the filtered solution became colorless and transparent. For further characterizations, CNC@PR powders were produced by freeze drying.

5.2.4 Preparation of CNC@PR reinforced chitosan beads

A mixed solution was prepared by dissolving 300mg chitosan powder and 30mg CNC@PR in 40 mL of a 1% (v/v) acetic acid solution. The solution was dropped into a precipitation bath containing 250 ml of 0.50 M NaOH, which neutralized the acetic acid within the chitosan gel and caused the coagulation of spherical uniform chitosan gel beads. The aqueous NaOH solution was stirred using a magnetic stirrer. The wet chitosan gel beads were extensively rinsed with distilled water to remove any NaOH, filtered and collected in a vial.
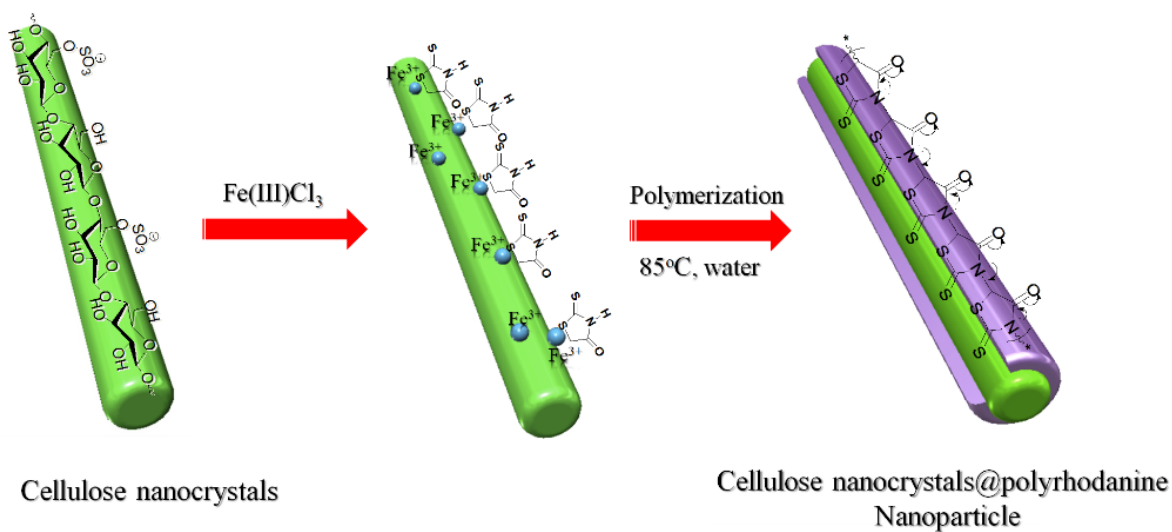
Figure 5.1 Schematic illustration of fabricating CNC@PR nanoparticles.

5.3   Results and discussion

Development of simple and versatile strategies for surface coating (polypyrrole etc.) has proven challenging, especially to achieve a homogenous coverage of the surface[262]. The surface coating phenomenon depends on the coating material and many process related parameters, such as solvent types, pH, temperature etc. Due to the limited solubility of rhodanine monomer, a relatively high temperature of 85 $^{\circ}$C was used for the polymerization so as to ensure that a homogeneous reaction mixture was maintained. Figure 5.1 illustrates the typically process to prepare core-shell CNC@PR nanoparticles. FeCl$_3$ (22.5 mM) was added to 20 ml well-dispersed CNC (supplied by Celluforce Inc.) dispersion (0.2 wt. %), followed by vigorous magnetic stirring for 6h. Then CNC-Fe(III) complexes were introduced dropwise into the prepared rhodanine monomer solution (22.5 mM). Upon the addition, the coordinative bond was formed between ferric ions and oxygen, sulfur, and nitrogen atoms on rhodanine monomers. Consequently, the chemical oxidation polymerization of rhodanine proceeded for 24 hrs and the final products were recovered.

The polymerization of rhodanine was investigated by Fourier transform infrared spectroscopy (FTIR). Figure 5.2A presents the results for polyrhodanine, pristine CNC and CNC@PR samples, where the specific peaks for polyrhodanine were observed for CNC@PR. The split peaks, between the 3000 and 2850 cm^{-1}, were assigned to C-H stretching vibration of methylene group and the O=C-H structure in the heterocyclic ring. The peak around 1710 cm^{-1} is associated to the stretching vibration of C=O and the peaks around 1637 and 1390 cm^{-1} corresponded to the C=C group stretching vibration and the C=N$^+$ bond stretching.

To further confirm the coating of CNC by polyrhodanine, ζ-potential (Table 5.1) of the nanoparticles in MiliQ water were performed at pH 7. The pristine CNC nanoparticles possessed a negative value of -54.1 mV due to the abundance of sulfuric ester groups on the surface. For

CNC@PR nanoparticles, the absolute value of ζ-potential decreased to -30.3 mV (still negative), indicating that some of the negatively charged sites on the surface were shielded by polyrhodanine coating.
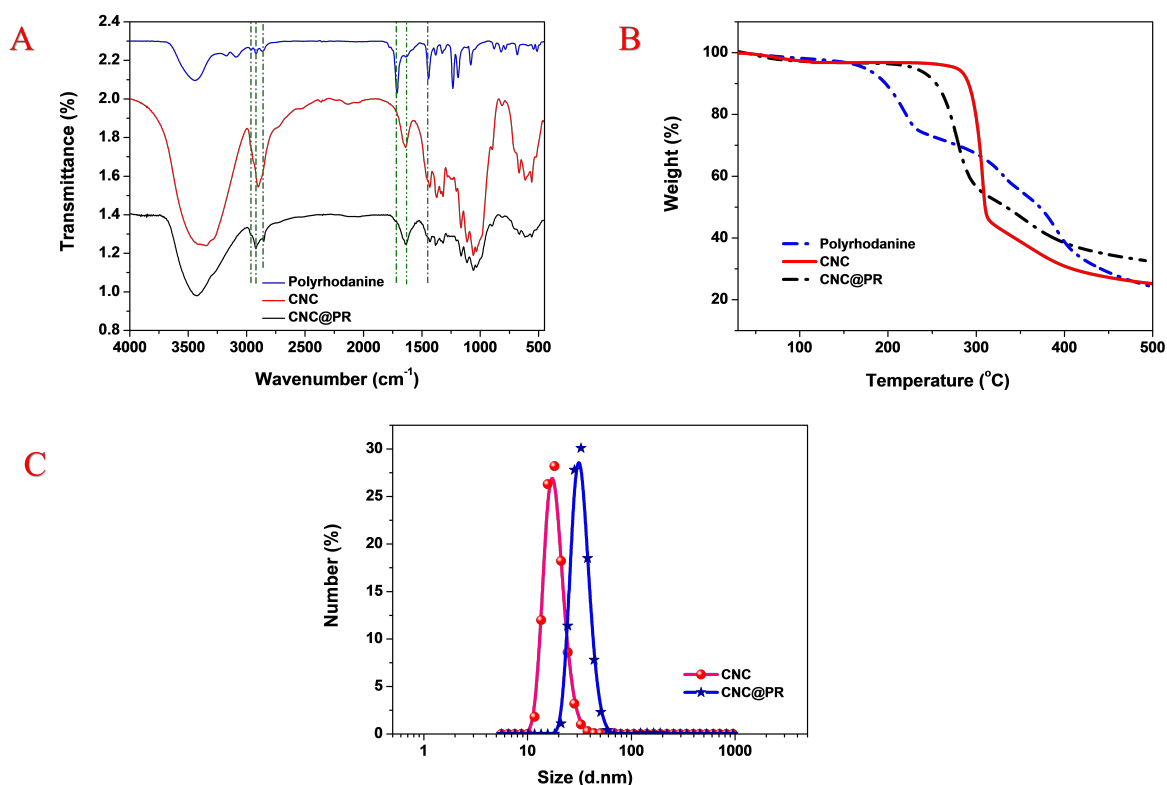
Figure 5.2 (A) FTIR spectra of polyrodanine, pristine CNC and CNC@PR nanoparticles (B) Thermogravimetric analysis (TGA) of polyrodanine, pristine CNC and CNC@PR nanoparticles (C) Particle size distribution curves of CNC and CNC@PR in a colloidal solution, determined by DLS at 90°

Table 5.1 also summarized the elemental analysis of the polyrhodanine coated nanoparticles and pristine CNC. Compared to pristine CNC, CNC@PR displayed a large increase in the sulfur and nitrogen and a small reduction in the carbon and hydrogen contents. The observed increase in the sulfur content on the core-shell nanoparticle confirmed the successful coating of PR on CNC. The

125

thermal analyses of core-shell CNC@PR was characterized and compared to the behavior of pure polymer and pristine CNC (Figure 5.2B). Pure polyrhodanine displayed a three-stage degradation process, in agreement to the literature[256,259]. Core-shell nanoparticles possessed a lower onset degradation temperature (210 ^{o}C) than pristine CNC, indicating the coating of polyrhodanine on the surface.

Table 5.1 Summary of the results from elemental analysis and ζ-Potential measurement

	N%	C%	H%	S%	ζ-Potential (mV)
CNC	0.023	41.106	5.619	0.844	-54.1
CNC@PR	0.812	38.564	5.306	5.873	-30.3

The particle-size distribution for the nanoparticles was determined by dynamic light-scattering measurements (Figure 5.2C). The CNC nanoparticles exhibited a particle size distribution of 18.2 nm in mean diameter. After coated with polyrhodanine, the mean diameter of the particle size distribution moved to 29.6 nm.

pH is commonly used to monitor the solution conditions in various fields, ranging from food, clinical diagnostics, bio-processing, and waste water treatment. Optical sensing based on changes of spectroscopic properties in response to pH provides a useful platform to simplify the analysis. UV-Vis absorption analysis was performed to characterize the dispersion of CNC@PR nanoparticles. Figure 5.4A shows the UV-Vis absorption spectra of core-shell nanoparticle with increasing pH values. By extracting the data of maximum absorption, the intensity or wavelength *vs.* pH values are summarized in Figure 5.4B. The intensity at the maximum absorption wavelength displayed a typical "S" shape, increasing continuously from 0.207 to 0.512 with increasing pH values from 2.04 to 12.04. The maximum absorption wavelength was blue-shifted from 453 to 578 nm showing the same trend as the intensity. At pH 12.04, the PR on the surface existed in a doped state as reflected by the presence of the polaron band transition at about 492 and 578 nm, which is

attributed to the π-π* transition of conjugated polymer backbone. As the pH of the solution decreased to 2.04, the polaron bands gradually red-shifted to 453 nm, indicating the decrease in the conductivity. The inserted picture in Figure 5.4B shows the macroscopic color change of composite nanoparticle against the pH of the solution. The color changed from pale red to blue violet when the pH was increased from 2.04 to 12.04, and the results were consistent with the UV-Vis spectral shift shown in Figure 5.4A, indicating that polyrhodanine has been fully doped producing a more conductive coating. The state of the coating could be reversed by decreasing the pH and a reversible color change from blue violet to pale red was observed. This pH-induced redox reversibility confirmed the formation of PR coating on the CNC surface and the core–shell nanoparticles could potentially be utilized into pH sensing devices.
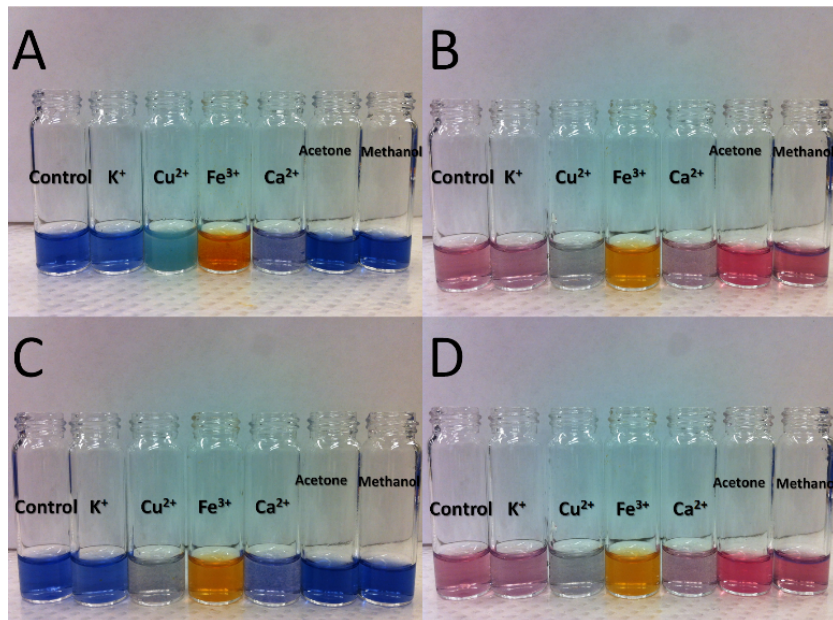
Figure 5.3 Color presented in different systems when tuning the pH for 2 times (CNC@PR samples with concentration of 0.01 wt% were used. A: adding 1M NaOH; B: adding 1M HCl after A; C: adding 1M NaOH after C; D: adding 1M HCl after C)
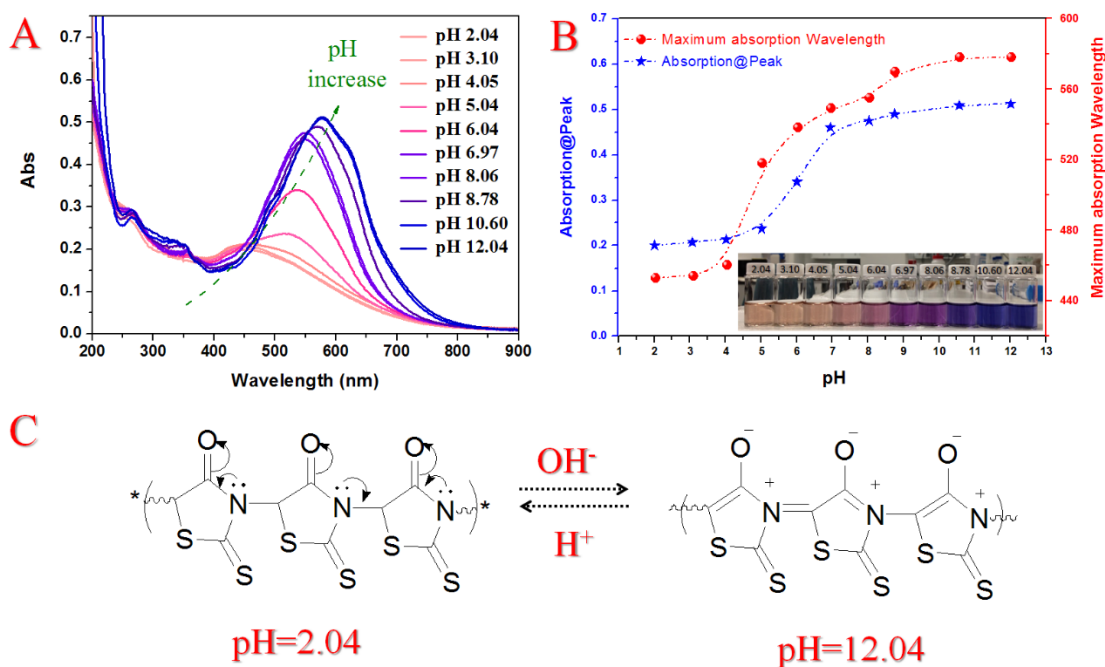
Figure 5.4 (A) Summary of the UV-Vis spectra of 0.01wt% CNC@PR suspension in pH ranging from 2.04 to 12.04 (B) Sigmoidal fittings of maximum absorption wavelength and absorbance@peak versus pH values. Inserted picture showed the macroscopic color of CNC@PR dispersions at different pH (C) Structure change of polyrhodanine during protonation and deprotonation.

The versatility of this novel hybrid nanomaterial is such that it can be shaped into a variety of configurations. Owing to the film-formation properties of CNC nanoparticles, an aqueous suspension of 1wt% was cast onto a glass slide and allowed to dry at room temperature for 2 days to produce a film. Then the UV-Vis absorption spectra of the film with minute amounts of 1 M NaOH or 1 M HCl were measured. The results showed that the maximum absorption peaks at acidic and alkaline conditions were in agreement with the spectra for the nanoparticle in aqueous solutions, as shown in Figure 5.5. The maximum absorption wavelength for the films upon adding 1 M NaOH, neutral pH water as well as 1 M NaOH was 524, 549, and 649 nm, respectively. The

change of transparency could make this flat film as a smart window material in the future. Incorporating the core-shell nanoparticle into chitosan hydrogel beads to produce color beads that respond to the pH of the surroundings were also demonstrated (see Figure 5.6). Thus the core-shell nanoparticle could be integrated into different forms to fabricate chemical sensors for direct visualization.
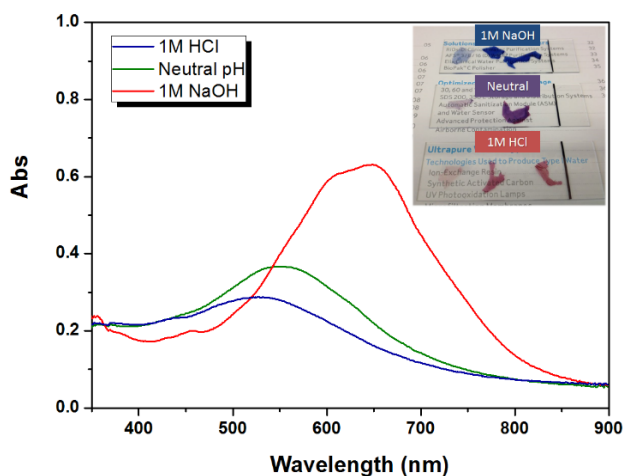
Figure 5.5 Summary of the UV-Vis spectrum of CNC@PR films upon adding 1M HCl, 1M NaOH or neutral pH water. Inserted pictures show the colors of piled-off films attached on the glass slides.
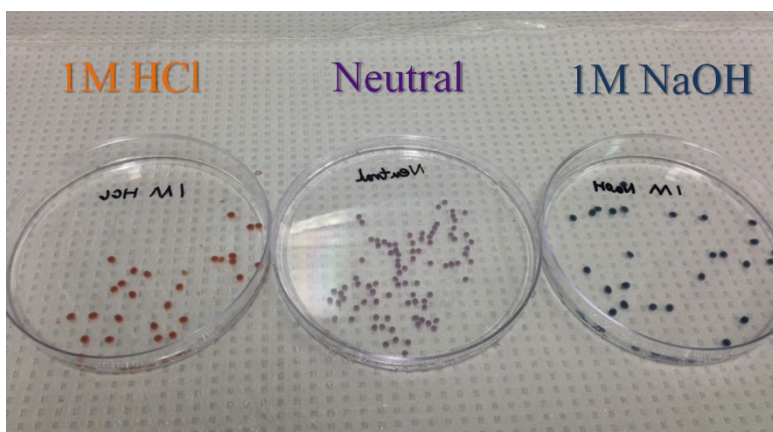
Figure 5.6 Visible color change of CNC@PR reinforced chitosan beads in solutions with different pH values presented by photograph.

5.4   Conclusions

In summary, we have demonstrated a simple and green approach to fabricate the cellulose nanocrystal@polyrhodanine (CNC@PR) core-shell nanoparticles by *in-situ* polymerization in aqueous solutions. These CNC@PR core–shell nanoparticles possessed redox reversibility in response to changes in pH. The color gradually changed from pale red to blue violet when the pH was increased from 2.04 to 12.04. The redox reversibility of the hybrid nanomaterial in response to pH was retained when shaped into different forms, such as 1D printable inks, 2D flat film, membranes, and 3D hydrogel beads. Templating of CNC with PR yielded pH-responsive core-shell nanostructures that possess colloid stability, high surface area and good mechanical strength. Such system could hold promise for the development of cheap and environmentally friendly pH sensing devices.

Chapter 6 Polyrhodanine coated cellulose nanocrystals for sustainable antimicrobial application

In this chapter, the coating conditions were optimized by varying the ratio of CNC and monomer as well as the concentration of oxidant. Antimicrobial tests were performed using *Escherichia coli* (Gram negative) and *Bacillus subtilis* (Gram positive) as model bacteria and the minimum inhibitory concentrations were determined by plate colony counting methods. By taking advantage of the nano-size effects, the core-sheath materials can be a potential candidate for antimicrobial applications, such as food-packaging, antimicrobial additives and antimicrobial surfaces or coatings.
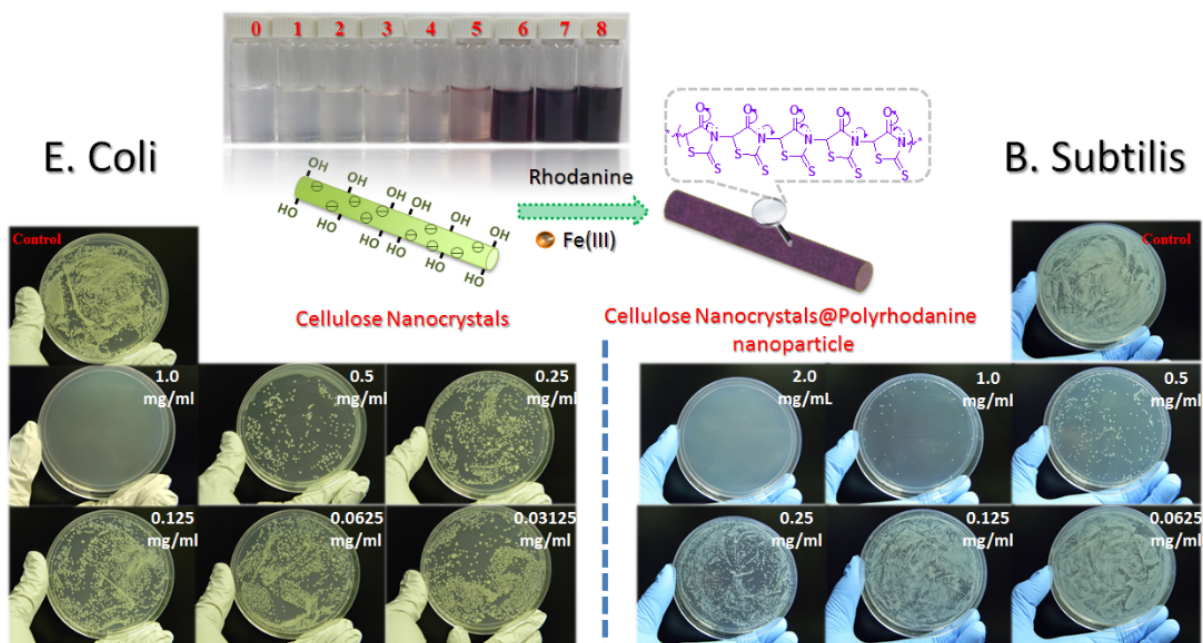
6.1   Introduction

The extensive use of antibiotics has contributed to the serious and global concerns surrounding the development of bacterial strains that are resistant to these antibiotics. Thus, a new generation of antimicrobial agents with low susceptibility to the development of resistance by bacteria or pathogens are being research and explored[263–265]. The common antimicrobial agents used are diverse, ranging from metals or metal oxides (Ag, CuO), small organic molecules (CTAB) to large molecular-weight cationic polymers[266–272]. Among them, silver and silver-based materials are among the most popular system studied since they exhibited high killing efficiency with a low propensity to induce resistance[273–277]. With the growing interest in the environment and sustainability, however, silver is no longer the most desirable choice for antimicrobial applications, and there is an overwhelming demand to develop materials that are biocompatible, bio-renewable and non-toxic.

Cellulose nanocrystals (CNC) are known to be one of the most abundant natural biopolymers on earth since they can be acid-hydrolyzed from different kinds of cellulosic resources[1,3,4,278].It represents an interesting class of nanomaterials that could be used to fabricate antimicrobial agents due to their bioavailability, biorenewability, biocompatibility and biodegradability. Also the higher surface area to volume ratio compared to spherical particles can contribute to their specific functions even at low concentration. There are limited studies on the development of CNC nanoparticle-based antimicrobial systems, thus rendering cellulose nanocrystals with antimicrobial properties seems promising and necessary. To the best of our knowledge, the antimicrobial properties of polyrhodanine-functionalized cellulose or cellulose derivatives have not been reported. Inspired by versatile polymerization methods, polyrhodanine (PR) was coated onto the surface of CNC in a green approach and several critical conditions for coating were optimized in

the present study. CNC serves as an ideal substrate for the polymer coating and the resulting composite possesses excellent colloidal stability against flocculation or aggregation for up to several months. Furthermore, these CNC@PR nanoparticles have been investigated for their antimicrobial properties against strains of *Escherichia coli* (Gram negative) and *Bacillus subtilis* (Gram positive). Compared to PR coated inorganic spherical materials, the rod-like nanoparticles possessed lower minimum inhibition concentrations (MIC) due to a lower percolation concentration relating to their geometry[257]. In addition, the cytotoxicity of CNC and CNC@PR toward human cells was also assessed using cell culture arrays.

6.2   Experimental Section

6.2.1   Materials

Cellulose nanocrystals (CNC) were produced and provided by CelluForce Inc., and it possesses an average charge density of 0.26 mmol/g. Ferric chloride and rhodanine monomers were purchased from Sigma-Aldrich. To perform anti-bacterial tests, *E. coli* (ATCC 8739) and *B. subtilis* (ATCC 23059) bacteria were purchased from Cedarlane Laboratories, in Burlington, Ontario. Plate Count Agar (DifcoTM) was acquired from the Becton Dickinson Company. Nutrient broth powders (OptiGrow™ Preweighed LB Broth, Lennox) were purchased from Thermo Fisher Scientific Inc. The HeLa cell line (ATCC CCL-2) was purchased from the American Type Culture Collection (ATCC, MD, USA). The cells were cultured in Dulbecco's Modified Eagle Medium/Nutrient Mixture F-12 (DMEM/F12) medium, supplemented with 10% fetal bovine serum (FBS), 100 U/mL penicillin, and 100 μg/mL streptomycin at 37 $^{\circ}$C. All the chemicals were used without further purification. Hydrochloric acid (HCl 1 M) solution and sodium hydroxide (NaOH 1 M) solution were diluted from standard solutions.

6.2.2 In-situ polymerization of polyrhodanine on cellulose nanocrystals

In a typical procedure, $FeCl_3$ (22.5 mM) was added into a well-dispersed 20 mL CNC dispersion (0.2 wt.%), followed by vigorous magnetic stirring for 6 h. The obtained CNC-Fe(III) complexes were fairly viscous, displaying a yellow color. Rhodanine monomers (22.5 mM) were dissolved in 20 mL deionized water (DI water) and heated to 85 ^oC under vigorous stirring to ensure the monomers dissolved completely. The CNC-Fe(III) complexes were introduced dropwise into the prepared rhodanine monomer solution. Vigorous magnetic stirring was applied and the temperature was maintained at 85 ^oC during the whole polymerization process. After 24 h, CNC@PR core-shell nanoparticles were obtained through an ultrafiltration process using a 100 nm membrane filter and the sample was rinsed several times with Millipore-Q water until the filtrate turned colorless. For further characterization, CNC@PR powders were collected via freeze-drying.

6.2.3 Evaluation of Anti-bacterial Property

Bacterial culture: E. coli and *B. subtilis* were chosen as model bacteria, both of which were isolated from the Luria-Bertani (LB) agar plate, added into fresh LB broth separately for incubation at 37 °C in a shaking incubator at a speed of 60 rpm (revolutions per minutes) overnight. For future use, the bacterial stocks were diluted to attain an absorbance of 0.08 at 600 nm.

Antibacterial test: 2 mL of nanoparticle dispersions (CNC and CNC@PR mixed with 2 g/L nutrient broth) with different concentrations (ranging from 0.031 to 2 mg/mL) were prepared by half-dilution method and inoculated with 10 μL bacterial (*E. coli* or *B. subtilis*) stock suspension. The bacteria-inoculated solutions were incubated at 37 ^oC in a shaking incubator with a shaking speed of 90 rpm. After 3 hours (the bacterial growth located in the exponential phase), 100 μL

aliquots were removed from each tube and distributed homogeneously on LB agar plates (3 parallel plates for each sample). The LB agar plates were kept in an incubator at 37 $^{\circ}$C for 24 h and the number of bacterial colonies was observed and counted to evaluate antibacterial performance. The MIC values are defined as the lowest concentration of nanoparticles where there was no visible bacterial growth.

For the control, the nanoparticle suspensions were substituted with DI water with the other conditions kept constant. In order to precisely count the colony units, we also prepared a 1000-times-diluted bacterial stock (bacterial stock x1000) and a 10000-times-diluted bacterial stock (bacterial stock x10000). The above two stocks were used in the inoculated process for a control sample with 1000 times dilution (control x1000) and 10000 times dilution (control x10000), respectively. All experiments were conducted in duplicate and the MIC was reported as the lowest concentration to completely inhibit the growth of each bacterial strain being tested.

Cell growth inhibition assay: HeLa cells were seeded in 96-well plates at 5000 cells per well in 100 μL of cell medium, and incubated at 37 $^{\circ}$C for 24 hr. The culture medium was then replaced with 100 μL of freshly prepared culture medium containing CNC or CNC@PR at different concentrations. The cells were further incubated for 72 h, and then 25 μL of 3-(4,5-dimethylthiazol-2-yl)-2,5-diphenyltetrazolium bromide (MTT) stock solution (5 mg/mL in phosphate buffered saline (PBS)) was added to each well to achieve a final concentration of 1 mg/mL, with the exception of the wells (acting as blank) to which 25 μL of PBS was added. After incubation for another 2 h, 100 μL of extraction buffer (20% SDS in 50% DMF, pH 4.7, prepared at 37 $^{\circ}$C) was added to the wells and incubated for another 4 h at 37 $^{\circ}$C. The absorbance was measured at 570 nm using a SpectraMax M3 microplate reader. Cell viability was normalized to

that of HeLa cells cultured in the normal cell media. The cell viability experiments were conducted in duplicate (n = 6 for each sample) and average values were reported.

Antimicrobial kinetic test: CNC@PR 8 nanoparticles dispersion (8 mg/mL) was inoculated with 50 μL of *B. subtilis* suspension (10^6-10^7 CFU/mL). After certain contact time, 50 μL aliquots were removed from each tube and cultured on LB agar plates. The LB agar plates were kept at 37 °C for 24 h and the number of bacterial colonies was observed and counted to evaluate antibacterial performance. The same experiments were also carried out for *E. coli*.

6.2.4 Instrumentation

Zeta-Sizer (Malvern, Nano ZS90) was used to measure the size and ζ-potential of CNC@PR dispersions. Detection was carried out at room temperature and the averaged number of scan data was 10. FTIR measurements were acquired at room temperature using a Bruker Tensor 27 spectrometer FT-IR spectrometer with a resolution of 4 cm^{-1} and a scanning number of 32 from 400 to 4000 cm^{-1}. All the samples were ground with potassium bromide and the pellets were used for characterization. UV-visible Spectroscopy System (Cary 100 Scan Varian) was employed to analyze the CNC@PR dispersions. All samples with a concentration of 0.02 wt% were prepared. Thermogravimetric analysis (TGA) was attained using the TGA Q600 of TA Instruments (Lukens Drive, Delaware, USA) (Temperature program: 10 °C/min until 100 °C, maintained at 100 °C for 5 mins then increased the temperature to 500 °C at 10 °C/min, maintained at 500 °C for 2 mins). Elemental analysis was carried out by employing Vario Micro cube, Elementar Americas, Inc. Results were determined by repeating the experiments several times, and the average values were reported. X-ray diffraction analysis: The crystalline phases of the samples were obtained by X-ray diffraction analyzer (XRD, D8 Discover, Bruker) equipped with Cu-Kα radiation, with a scan

136

speed of 4° per minute ranging from 10° to 90°. Transmission electron microscope (TEM) images were obtained using a Philips CM10 electron microscopy with an acceleration voltage of 60 kV. In preparing samples for TEM characterization, freeze-dried CNC@PR powders were re-dissolved into DI water to form aqueous dispersions (0.05 wt.%) and sprayed onto carbon-coated copper grids.
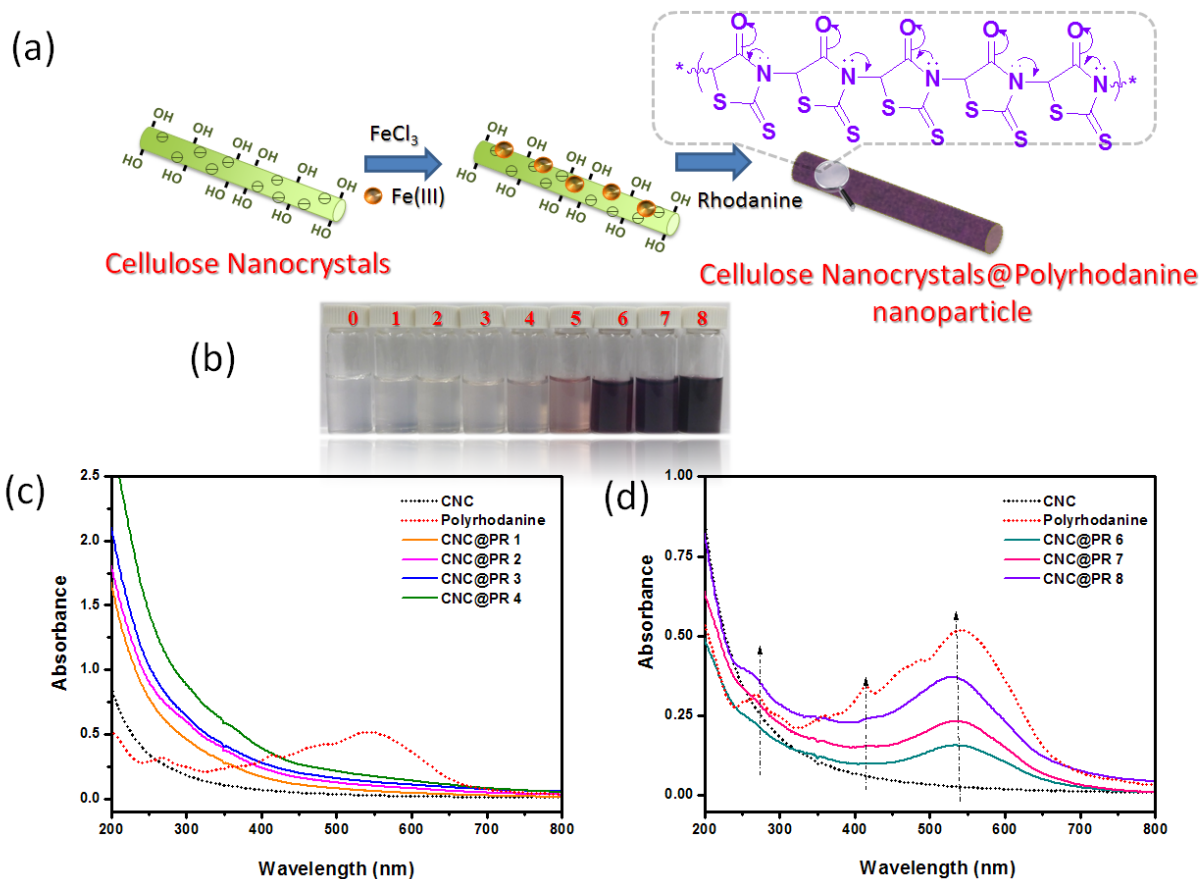
Figure 6.1 (a) Schematic illustration of in situ polymerization of CNC@PR nanoparticles; (b) Digital camera pictures showing color change of 0.1 wt% CNC@PR suspensions under different reaction conditions; (c) and (d) UV absorption spectrum of polyrhodanine solution, pristine CNC dispersion as well as CNC@PR suspensions from different reaction conditions.

6.3 Results and Discussion

6.3.1 In-situ polymerization of polyrhodanine on cellulose nanocrystals

Coating the cellulose nanocrystals surface with a functional layer is a popular approach for depositing polymers on CNC surfaces. To date, metal oxide (TiO_2)[279], inorganic materials (SiO_2)[18,247] as well as polymers like polypyrrole (PPy)[280] and polydopamine (PDA)[281] have been introduce onto rod-like 1D nanoparticles. However, it has been shown that the coating process can be quite challenging, particularly in developing a simple and versatile strategy to produce a homogenous coating[262]. The coating process not only correlated to the material used but it is also influenced by many uncertain physiochemical conditions when performing the synthesis.

The typical procedure in the formation of CNC@PR is illustrated in Figure 6.1a. When injecting ferric chloride into the CNC solution, the cationic ions Fe(III) adsorbed onto the surface of negatively charged CNCs (sulfate ester groups) driven by electrostatic interactions. When the mixture was added to the rhodanine solution, interactions between Fe(III) ions and monomers and in-situ oxidative polymerization process proceeded on the CNC surface, where Fe(III) acted as initiator (in activating the polymerization) and oxidant (in accepting an electron from the electron donor nitrogen atom in the ring structure). The bond structure between nitrogen and the methylene group of the two rhodanine molecules led to the formation of polymer backbone (propagation and termination).

In this study, optimization of the coating process was performed by changing the ratio of CNC and monomer (Rp: monomer/CNC) as well as the concentration of oxidant. Initially, when increasing the Rp values, the color of the product remained the same as pristine CNC with the concentration of oxidant fixed at 3 mM (see Figure 6.1b). The results could be attributed to insufficient amounts of Fe(III) introduced to the system since CNC is a rod-shape nanoparticle having a large surface

area for the adsorption of Fe^{3+} on its surface. By fixing the Rp value and increasing the concentration of ferric ion, the color of the CNC@PR products turned to dark purple (see Figure 6.1b), indicating a higher amount of polymer polymerized on the surface of CNC. Sample 8 has a molar ratio of oxidant/monomer of 1 that yielded the best coating representing the optimal oxidation polymerization condition.

Table 6.1 Summary of the reaction conditions and ζ-potential of 0.01% nanoparticle suspensions.

No.	CNC (wt %)	Rhodanine (mM)	Fe^{3+} (mM)	ζ-Potential (mV)
0	0.2	0	0	-54.0
1	0.2	7.5	3	-43.3
2	0.2	15	3	-46.7
3	0.2	22.5	3	-44.6
4	0.2	22.5	4.5	-44.8
5	0.2	22.5	6	-33.5
6	0.2	22.5	12	-38.2
7	0.2	22.5	15	-37.6
8	0.2	22.5	22.5	-30.3

6.3.2 Basic Characterizations

Table 6.1 shows the comparisons of ζ-potential as a function of conditions used to produce the CNC@PR dispersions. As Fe(III) concentration increased, the color of CNC@PR solution gradually turned darker, from colorless to dark purple. Meanwhile, the absolute value of ζ-potential decreased to around -30mV. Compared to pristine CNC dispersion (Sample 0), whose ζ-potential was -55mV, the differences suggested that the surface of CNC had been substantially covered with PR.

The surface coating was further clarified by UV-Vis spectra, which is summarized in Figure 6.1c and 6.1d. Pristine CNC exhibits strong scattering signals without any specific absorption peaks. In the case of pure PR samples, the absorption peaks of around 270 and 410 nm were presented. The

wide absorption peak at around 550 nm is assigned to polaronic transitions[282,283]. As for Sample 1 to 4, the concentration of Fe(III) was kept constant while the concentration of monomers was progressively increased. There were no characteristic peaks in the UV-Vis spectra of Sample 1 to 4, correspondingly. Since the coating amount was insufficient, the conditions were optimized by increasing the Fe(III) concentration, which corresponds to Sample 5 to 8. When the concentration of Fe(III) approached 12 mM, the adsorption peaks between 550 and 270 nm began to appear in the UV-Vis spectra. Further increases in the Fe(III) amount, to the same level as the rhodanine monomers, yielded another characteristic peak near 410 nm.
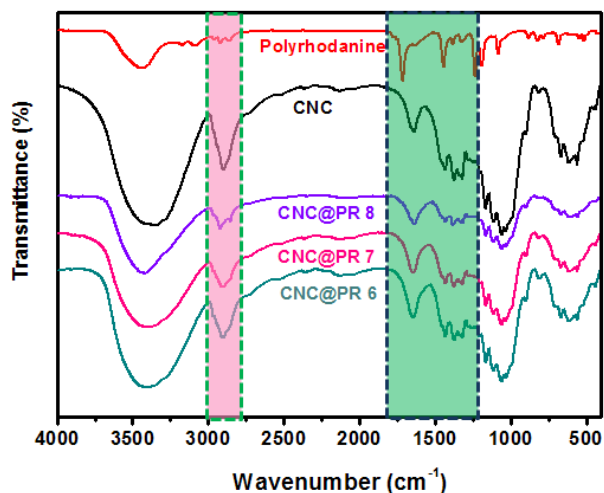
Figure 6.2 FTIR spectra of pristine CNC, polyrhodanine and CNC@PR from Samples 6, 7 and 8

The CNC@PR was further characterized by FT-IR spectroscopy (Figure 6.2). According to the results from UV-Vis spectroscopy, the coating amounts were insufficient to analyze Sample 1 to 4. Hence, only Samples 6 to 8 were subjected to FT-IR analyses. For pure polyrhodanine, peaks around 1637 cm^{-1} and 1390 cm^{-1} were observed due to the C=C group stretching vibration and the C=N$^+$ bond stretching in the polymer chains. The peaks between 3000 cm^{-1} and 2850 cm^{-1} were assigned to C-H stretching vibration of the methylene group and the O=C-H structure in the

140

heterocyclic ring. The absorption around 1710 cm^{-1} was associated with stretching vibrations of C=O. These peaks became more significant in the CNC@PR samples with increasing concentrations of Fe(III), especially for Sample 8 (Figure 6.2).

The atomic composition of the coating products was measured by elemental analysis. Table 6.2 summarizes the results of the CNC@PR samples from Sample 5 to 8. The surface coating was confirmed by the gains in weight percentage of nitrogen and sulfur, which also offers information on the coating efficiency of the shell material on the CNC surface, e.g. the weight ratio of polyrhodanine to CNC calculated to be 3.2% and 7.3% for sample CNC@PR 7 and 8, respectively. The coating amounts of polyrhodanine increased with increasing concentration of Fe(III). In contrast to pure CNC, the weight percentages of sulfur and nitrogen approached 5.87% and 0.81%, respectively, while the atomic content of carbon and hydrogen decreased to 38.56% and 5.306%, accordingly. In addition, the trend of particle size distributions also indicated that the size of coated particles was increased due to the coated polymer layer, which was comparable to the results of rod-like particles reported using DLS[284,285] (Figure 6.3).

Table 6.2 Atomic composition as determined by elemental analysis

Sample	N%	C%	H%	S%
CNC	0.002	41.106	5.619	0.844
CNC@PR 5	0.050	39.383	5.539	1.534
CNC@PR 6	0.181	39.021	5.527	1.977
CNC@PR 7	0.321	38.774	5.495	3.338
CNC@PR 8	0.813	38.563	5.306	5.873
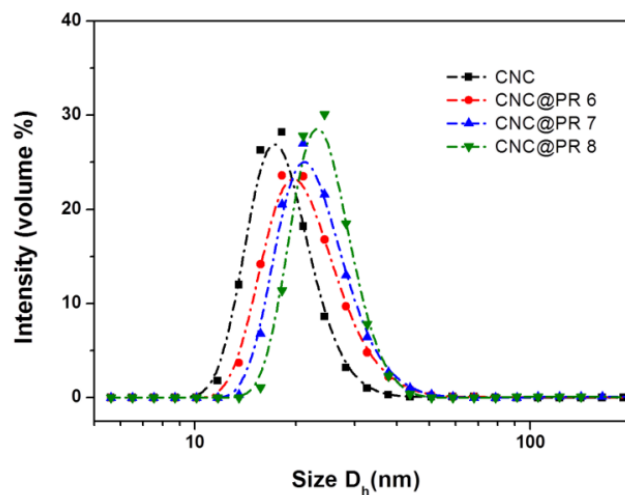
Figure 6.3 DLS results comparing the volume-averaged size distribution profile of pristine CNC and CNC@PR from conditions 6, 7 and 8.
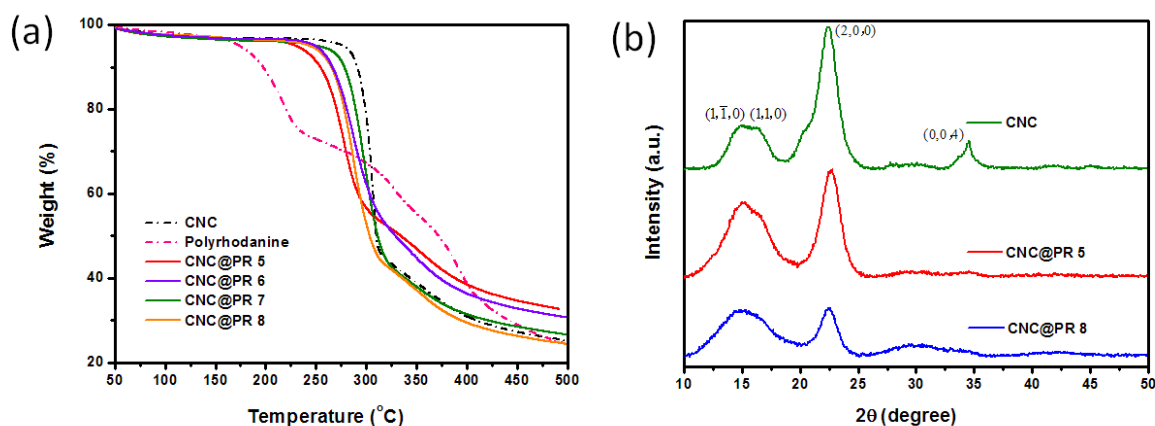
Figure 6.4 Thermal degradation behaviors of pristine CNC, polyrhodanine as well as CNC@PR under different conditions; (b) XRD spectra of pristine CNC, Sample 5 and 8.

The TGA curves in Figure 6.4a show the thermal degradation behaviors of pure CNC, pure PR and Sample 5 to 8. It can be seen from Figure 6.4a that the weight loss of pristine CNC and pure PR commenced at 270 and 200 °C, respectively. Pristine CNC displayed a typical degradation profile of nanoparticles containing sulfate groups that originated from sulfuric acid hydrolysis[52].

142

The pure polymer exhibited a three-stage degradation process, which is comparable to previously reported data[256,259]. In all the CNC@PR samples, the results showed a lower onset degradation temperature (240 ^{o}C) than pristine CNC, indicating that the coating of polyrhodanine was on the surface of CNC. The differential thermogravimetry (DTG) curves revealed characteristic differences in the coating of polyrhodanine, it is clear that shifts in DTG peaks were observed for pristine CNC and CNC@PR nanoparticles. The enhancement in the coating amount with increasing Fe(III) content was also confirmed from the TGA curves.

The effect of surface coating on the crystal structure of CNC was further investigated by XRD. Figure 6.4b presents the diffraction patterns for pristine CNC and CNC@PR (Sample 5 and 8). Analysis of the nanoparticles before and after modification confirmed that the coating process retained the crystal structure of native cellulose. CNC@PR still displayed peaks similar to the typical reflection planes of cellulose I, which is labeled in the diffraction pattern of pristine CNC, indicating that the chemical modification did not significantly alter the crystal lattice. However, the degree of crystallinity of the particles decreased, which can be attributed to the coating of amorphous polyrhodanine on the surface (The degree of crystallinity was determined to be 0.93, 0.65 and 0.58 for CNC, CNC@PR 5 and CNC@PR 8, respectively using the Buschle-Diller and Zeronian Equation[223,286], see supporting information). Higher amounts of PR may lead to a lower degree of apparent crystallinity. The XRD results show that the coating process caused the crystalline domains within the nanoparticles to become slightly longer and more rectangular in cross-section, which is comparable to results reported previously[286].

The morphologies of CNC@PR and pristine CNC can be observed from the TEM images shown in Figure 6.5. These images revealed that the length dimension of individual pristine CNC was approximately 250~300 nm, confirming the rod-like shape with smooth surfaces. For CNC@PR,

the rod-like shape was preserved and they exhibited an improved dispersibility in aqueous solutions. The modified nanoparticles had a rougher surface due to the coating of polymer and the diameter of the rods increased. Also the thickness of the coating layer increased slightly with increasing amounts of Fe(III).

6.3.3 Assessment of the CNC@PR Antimicrobial Activity

The anti-bacterial properties of CNC@PR from Sample 8 were assessed using the Gram-negative bacterium *E. coli* and Gram-positive bacterium *B. subtilis* as model organisms. During this evaluation, pristine CNC was used as the control. From Figure 6.6a and 6.6b, it is
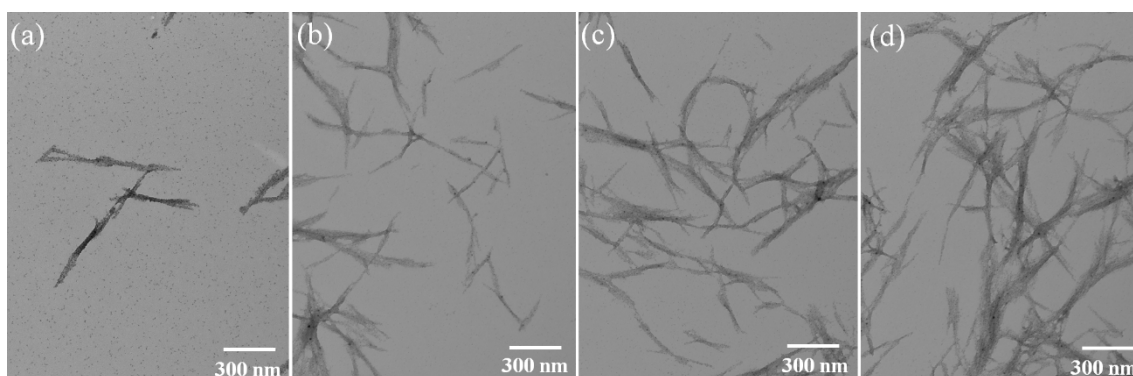
Figure 6.5 TEM images showing the morphologies of pristine CNC (a) and CNC@PR nanoparticles from conditions 6(b), 7(c) and 8(d). In order to highlight the contrast, CNC sample (a) was stained with ferric ions.

clear that the pristine CNC dispersion displayed no anti-bacterial effects towards either *E. coli* or *B. subtilis*. However, the CNC@PR dispersion showed an excellent anti-bacterial effect on both *E. coli* (Figure 6.6c) and *B. subtilis* (Figure 6.6d). As presented in Figure 6.6c, within the experiments with *E. coli*, the density of the bacterial colonies decreased as the concentration of CNC@PR increased, resulting in the complete elimination when the concentration approached 1 mg/mL. Similarly, the results for *B. subtilis* exhibited the same trend of eliminating colonies as the

144

concentration of solution increased. In brief, the MIC values towards *E. coli* and *B. subtilis* were 0.5~1.0 mg/mL and 1.0~2.0 mg/mL, respectively, for the CNC@PR nanoparticles from Sample 8. The backbone of polyrhodanine contains tertiary amide groups that acquire positive charges when they are partially protonated. Once the polymer was coated onto CNC, these nanoparticles could interact with negatively charged lipid membrane structures and induce damage to the bacterial cell wall leading to cell lysis. As proposed by Jang and coworkers, the sulfur and oxygen groups in the polyrhodanine contain unshared electron pairs, which can play a role in the bactericidal process[257]. The CNC@PR nanoparticle also exhibited some differences in the killing efficacy towards different kinds of bacteria (more effective against *E. coli*). These results are comparable to previous studies on different bacteria, where rod-like particles exhibited lower minimum inhibition concentration (MIC) than spherical silica-polyrhodanine nanoparticles, which could be attributed to a lower percolation concentration[257]. Brunauer-Emmett-Teller (BET) absorption experiment was conducted to determine the surface area, and the nanofibrous structure (124 m^2/g) provided a higher contact area compared to other structures (108, and 75 m^2/g for spherical nanoparticles with a diameter of 27 and 56 nm respectively)[257].

In order to further confirm the antimicrobial properties of CNC@PR 8, kinetic studies were conducted and the results are shown in Figure 6.7. The killing efficiency increased with increasing contact time for both types of the bacteria due to the contact probabilities between nanoparticles and bacteria. Systematic studies on the antimicrobial mechanism of CNC@PR will be the subject of future study. It is important to note that the present system can also be shaped into different geometries, such as 1-D ink, 2-D films or 3-D gels. As this report is just focusing on the 1-D aqueous inks system, further experiment will be carried out to investigate the effectiveness toward the other 2-D and 3-D systems.
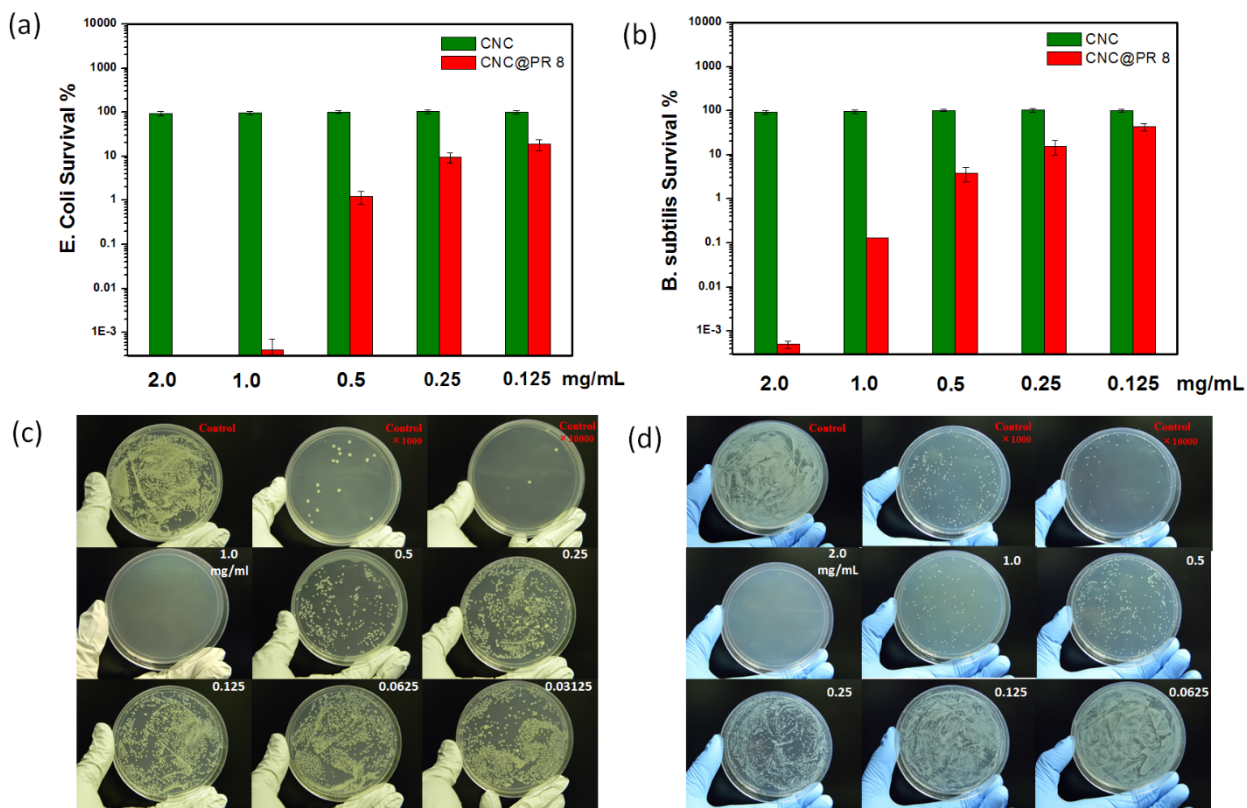
Figure 6.6 Antimicrobial assessments of pristine CNC and CNC@PR 8 suspensions toward (a) *E. coli* and (b) *B. subtilis*; Photographs of (c) *E. coli* and (d) *B. subtilis* colonies grown on LB agar plates after incubation with CNC@PR.

6.3.4   In Vitro Cytotoxicity with HeLa Cells

The biological effects of CNC@PR toward human cells can be assessed using cell culture based assays as a prescreening tool. As the improved antibacterial activity of the nanoparticles presumably comes from the membrane disruption mechanism, it was important to assess whether this mechanism of action is specific only to bacterial cells or could potentially be harmful to human cells as well. Even though CNC and its composites have been claimed to be a potential candidate for biomedical application, it is unfortunate that only a limited number of papers have addressed the issues of toxicology and safety[47,286–288].
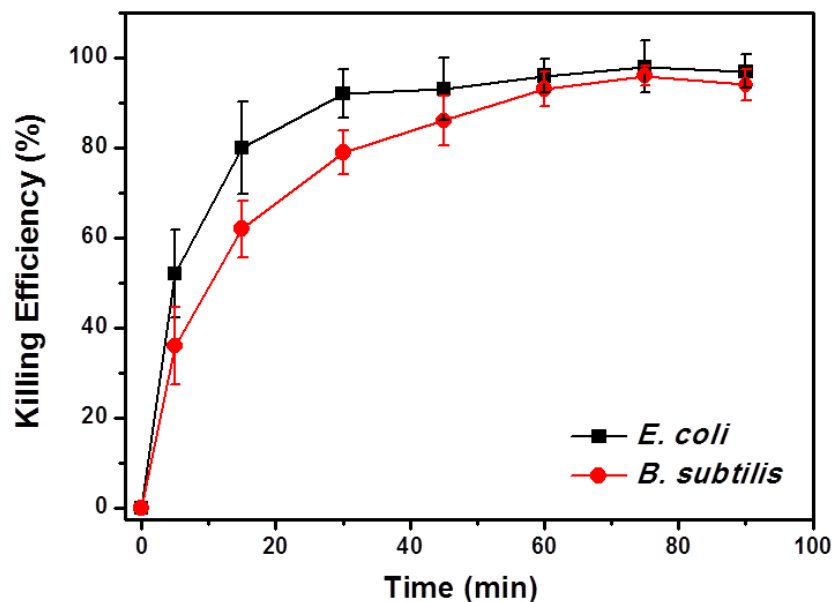
Figure 6.7 Plot of killing efficiency versus contacting time (min) against E. coli and B. subtilis for CNC@PR 8. The killing efficiency was obtained as killing efficiency = (1 - A/B) x 100 (where B is the number of surviving bacteria colonies in the control and A is that of the CNC@PR 8 sample).

Therefore, the potential cytotoxicity of CNC and CNC@PR was evaluated using HeLa cells. As presented in Figure 6.8, both CNC and CNC@PR nanoparticles displayed negligible toxicity towards HeLa cells at concentrations lower than 0.5 mg/mL. When the concentration was

increased to the levels that showed high antibacterial potential (1 mg/mL), the CNC particles induced only 6 to 7% viability reduction to HeLa cells, which is slightly different from previous studies[289] (no toxicity lower than 500 μg/mL and around 20% viability reduction at 1000 μg/mL depending on the types of cell and size of CNC). Since the type of cell and the size of nanoparticles differ significantly, it is difficult to make direct comparison with the literature, but the CNC@PR induced some toxicity with up to 50% viability reduction. The viability was statistically lower when compared to the value presented by the control sample (Student's t-test, $P < 0.05$). The toxicity can be reduced to around 10% by decreasing the concentrations of CNC@PR to a reasonable level where the nanoparticles still possess some degree of antimicrobial properties (0.5 mg/mL and 0.25 mg/mL). Previous studies have shown that amine-containing polymers induce mammalian cell toxicity due to their positive charges, which could explain the toxicity observed for CNC@PR in solution at this concentration[263,290].
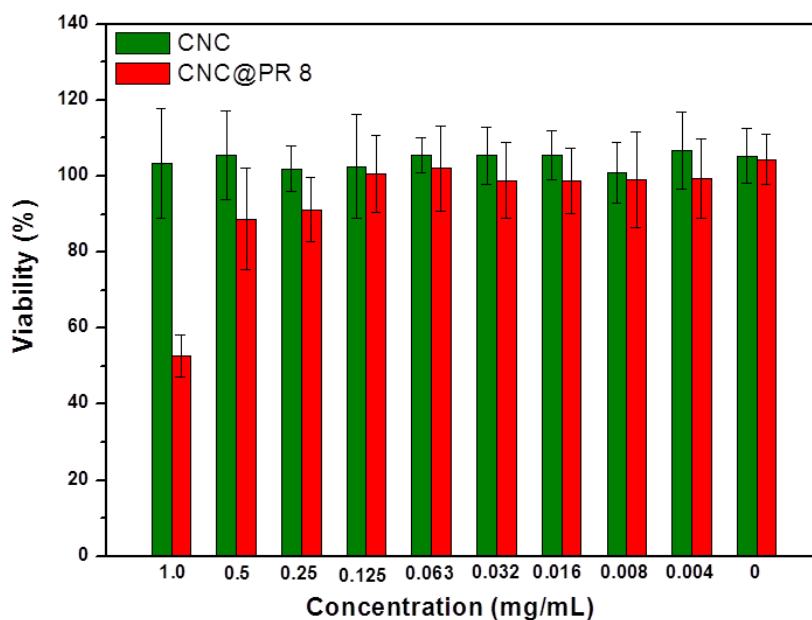
Figure 6.8 Cytotoxic assay of HeLa cells treated with cellulose nanocrystals and CNC@PR 8 nanoparticles.

6.4 Conclusions

A simple and green approach for fabricating cellulose nanocrystal@polyrhodanine (CNC@PR) core-sheath nanoparticles based in aqueous solution was reported. The coating conditions were optimized by varying the ratio of CNC and monomer as well as the concentration of oxidant (Fe(III)) in order to obtain a higher amount of polyrhodanine coating. Plate colony count methods were used to assess the antimicrobial properties of CNC@PR nanoparticles with the highest coating content. Results showed that rod-like CNC@PR nanoparticles exhibited promising antimicrobial properties towards both *Escherichia coli* (Gram negative) and *Bacillus subtilis* (Gram positive), which is comparable to spherical nano-composite particles (SiO$_2$@PR). The toxicity of CNC@PR nanoparticles against HeLa cells was evaluated using cell arrays, demonstrating that the toxicity is quite low within the concentrations that exhibit antimicrobial properties. It is anticipated that the core-sheath materials can be a potential candidate or filler for antimicrobial applications, such as food-packaging, antimicrobial additives and antimicrobial surfaces or coatings.

Chapter 7   Mussel-inspired green metallization of silver nanoparticles on Cellulose Nanocrystals and their enhanced catalytic reduction of 4-Nitrophenol in the presence of β-cyclodextrin

In this chapter, a green approach to anchor silver nanoparticles (AgNPs) onto the surface of cellulose nanocrystals (CNCs) coated with mussel-inspired polydopamine (PDA) at room temperature in the absence of a stabilizer and a reducing agent is proposed. The resulting nanohybrids possessed a core-shell structure with numerous "satellites" of silver nanoparticles decorating the CNC surface. The nanocatalyst displayed superior dispersibility over pristine AgNPs and was six times more efficient in catalyzing the reduction of 4-nitrophenol. By associating the CNC hybrid with β-cyclodextrin to promote host-guest interactions, the catalytic process was accelerated. The associated physicochemical parameters associated with the catalytic process were investigated and compared.
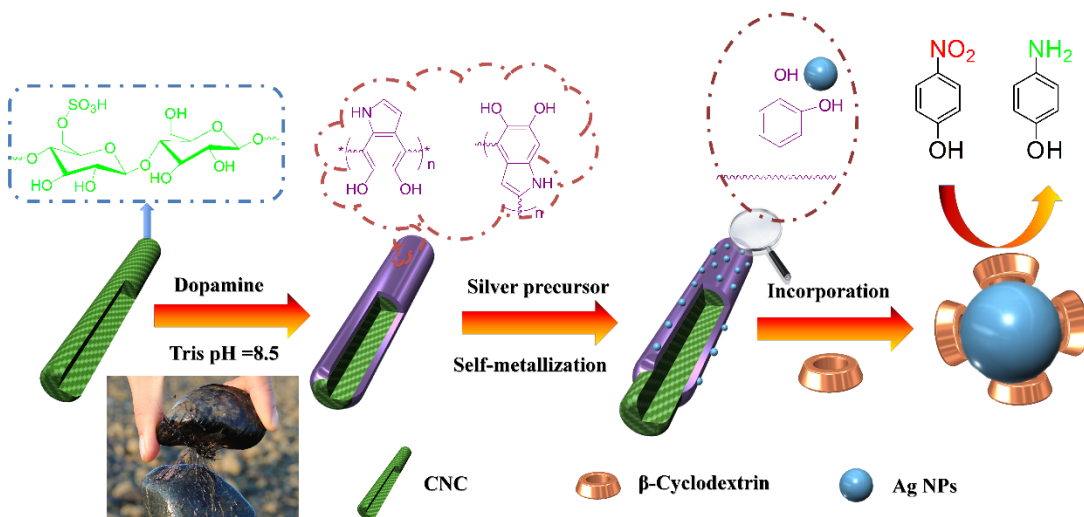
7.1 Introduction

Taking full advantages of the surface functionalities and high surface area ($\sim$250m^2/g)[291], the deposition of nanoparticles onto the surface of CNC offers a promising approach to fabricate hybrid nanomaterials for use as heterogeneous catalysts in various types of chemical reactions[63,292]. CNCs as carriers will improve the colloidal stability of metal nanoparticles and hence address issues, such as "catalyst poisoning" and deactivation of nanocatalyst.

Several studies have been performed to deposit metal, semiconducting or magnetic nanoparticles onto the surface of CNCs[5,62,63,65,293,294]. For example, Khaled and coworkers introduced Au nanoparticles onto the CNC surface to act as a support for effective enzyme immobilization[294]. Pd and Au nanoparticles were attached to the CNC surface using a hydrothermal method and the catalytic enhancement of dye degradation was investigated by Wu and coworkers[63,65]. Most recently, Marzieh and coworkers used a single step to attach Pd nanoparticles onto the surface of CNCs using supercritical CO_2[295]. The final product was reported to be an effective catalyst in the Mizoroki-Heck cross-coupling reaction. However, a detailed examination of the preparation techniques reveals some drawbacks, such as the use of reducing agents and/or the use of harsh conditions (hydrothermal treatment). In the present study, we propose a greener approach to prepare a CNC-metallic nanoparticle hybrid system that possesses properties that are similar or better than those presently available.

Inspired by the composition of adhesive proteins in mussels, catechol-based compounds such as 3, 4-dihydroxy-L-phenylalanine (dopamine), and their polymeric forms[262] have been widely exploited for antifouling[296], antibacterials[297], self-healing hydrogels[298], dye removal[299] and even lithium ion battery separators[300,301]. Polydopamine (PDA) is the polymeric form of dopamine that contains both catechol and amine functional groups that undergo spontaneous self-polymerization

151

in a defined pH range. The polymerization process is simple, green and adaptable to virtually all types of material surfaces, offering a biocompatible and highly adhesive platform for further modifications. This process offers two advantages. First, the catechol groups can form strong coordination complexes with metal surfaces through two adjacent hydroxyl groups. Secondly, the redox-active functional groups can be oxidized under mild solution conditions. Combining these two advantages, this strategy have been applied to many different systems[299,302–307]. Although recent reports do not describe or utilize PDA, catechol-based moieties are widely used[308–311].

To the best of our knowledge, the approach of using catechol groups to incorporate a nanocatalyst onto a bio-renewable nanocarrier (CNC) has not been reported. The strategy described above offers a new approach for developing hybrid nanomaterials with higher stability and adhesion for heterogeneous catalytic reactions. In this study, the PDA-coated CNC (CNC@PDA) was prepared via self-polymerization of dopamine on the surface of CNC nanoparticles. The Ag satellite nanoparticles are *in-situ* generated by reducing Ag^+ with catecholamine oxidation. This is followed by immobilizing Ag nanoparticles on the exterior surface of PDA-coated CNCs (Figure 7.1). The composite nanoparticles were employed in the catalytic reduction of 4-nitrophenol (4-NP), a common organic pollutant in wastewater, in the presence of $NaBH_4$. This reaction converts toxic 4-NP into benign 4-aminophenol (4-AP), and addresses an important environmental challenge[293,303,304,312–316]. As a further step, β-cyclodextrin (β-CD) was introduced into this biomimetic system to serve as a capping agent that binds to the surface of metal nanoparticles to provide a platform for host-guest interactions[317,318]. By combining some ideas reported previously[317,319–322], we developed a novel CNC hybrid system that displays enhanced catalytic properties; its corresponding kinetic and thermodynamic properties were measured to provide the knowledge necessary to design better systems for future applications.
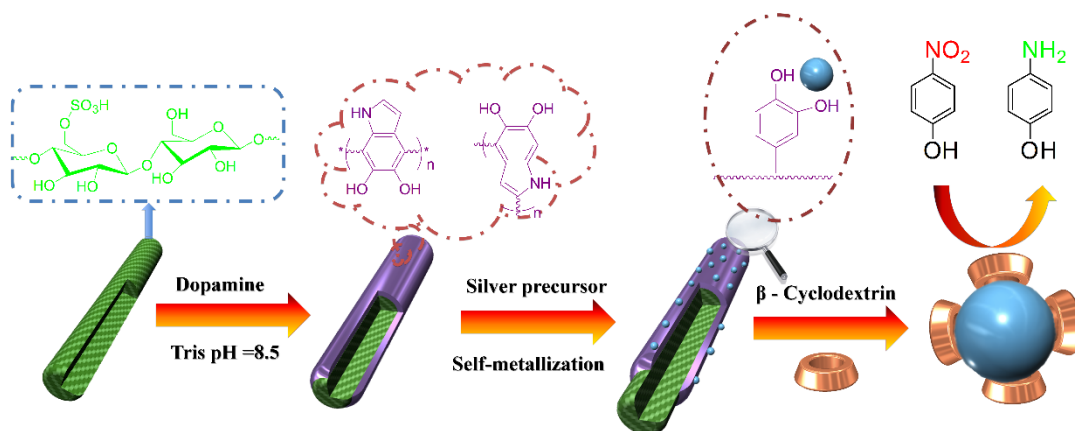
Figure 7.1 Schematic illustration of the strategy for synthesis of CNC@PDA, and the possible mechanism of metallization of Ag NPs, and binding with β-cyclodextrin.

7.2 Experimental section

7.2.1 Chemicals

Cellulose nanocrystals with surface charge density of 0.26 mmol/g were provided by Celluforce Inc. The measured surface area of CNC is approximately 250 m^2/g. Dopamine hydrochloride tris((hydroxymethyl)aminomethane (Tris), ammonium hydroxide solution, sodium borohydrate, 4-nitrophenol, and silver nitrate were purchased from Sigma-Aldrich. All the chemicals were used as received without further purification. All aqueous solutions were prepared with Milli-Q water.

7.2.2 Apparatus

Infrared spectra were collected from 400 to 4,000 cm^{-1} on a Bruker Tensor 27 spectrometer with a resolution of 4cm^{-1} and a scanning number of 32. UV-Vis spectra were obtained on an Agilent 8453 UV-visible Spectroscopy System equipped with temperature control. The crystalline phases were determined using an X-ray diffraction analyser (XRD, D8 Discover, Bruker) equipped with Cu-Kα radiation, at a scan speed of 4° per minute and with a scattering range of 10 to 90 degrees. Transmission electron microscopic (TEM) images were obtained using a Philips CM10 TEM

microscope at a 60 keV acceleration voltage. Samples for TEM characterization were prepared by placing a drop of prepared solution on copper grids (200 mesh coated with copper) and allowed to dry with no additional staining. Thermo-gravimetric analysis (TGA) of samples was performed on a TGA Q600 of TA Instruments (Lukens Drive, Delaware, USA). The sample was heated under dry nitrogen purge at a flow rate of 10 mL/min from room temperature to 800 ºC.

7.2.3   Preparation of CNC@PDA-Ag nanocatalyst

The hybrid catalyst was prepared via a two-step process adopted from previous studies with slight modifications[297,307]. In the first step, 1.0g of CNC powder was homogenously dispersed in 500 ml Milli-Q water and sonicated for 5 mins, and Tris (0.6 g) was dissolved in the CNC dispersion by adjusting the pH to 8.0. To this solution, 1.0g of dopamine hydrochloride was introduced and the coating polymerization was performed over 1 day at room temperature. The products were purified by ultrafiltration using a 0.1μm membrane filter and washed several times with DI water until the filtrate became colorless. The concentrated CNC@PDA was freeze-dried and stored for subsequent use.

A typical protocol for the second step is as follows: 50.0 mg of silver nitrate was introduced to 20 mL deionized water, and ammonia solution (3.0 wt%) was added slowly until the solution became clear confirming the formation of diammine silver (I). Then 0.5 g of CNC@PDA solution (3.0 wt%) was added to the resultant solution and stirred at room temperature for 2 h. The product was purified by centrifugation at 8000 rpm for 10 mins, and washed 3 times with deionized water. The control sample (pure AgNPs) was prepared by replacing the CNC@PDA with 4.0 mg of dopamine hydrochloride (in 1.0 mL deionized water), that served as a reducing agent for the silver ion.

154

7.2.4 The catalytic properties of the nanocomposite catalyst

The reduction of 4-nitrophenol by $NaBH_4$ was selected as a model reaction for evaluating the catalytic efficiency of the hybrid nanocatalyst. Typically, 12 mM 4-NP (Solution 1) solution was prepared by dissolving 16.7 mg 4-NP powder in 10 mL water. By diluting Solution 1 and mixing it with freshly prepared $NaBH_4$ solution, another solution (Solution 2) containing 0.12mM 4-NP and 38mM $NaBH_4$ was prepared for the experiments described here. Thereafter, 3mL of Solution 2 was pipetted into a UV cuvette and placed in a thermostated cell at 25°C. 200 μL of the catalyst dispersion (silver content of 2.0 μg/mL) was added to Solution 2 using an Eppendorf pipette and mixed for 5s. The reaction was monitored using UV-Vis spectrometry scanning from 250 to 600 nm with cycling over a 1 min interval.

For catalyst dosage experiments, catalyst stock solutions with different silver contents were diluted from concentrated CNC@PDA-Ag NPs (20 μg/mL) dispersions. The volume of catalyst introduced into the cuvette was kept constant at 200 μL.

7.2.5 Catalytic reduction with complexes of nanocatalyst with β-CD

For catalytic experiments with β-CD, stock dispersions with CNC@PDA-Ag NPs (final silver content fixed at 1.5 μg/mL) and different CD concentrations (0, 1, 2, 4*10^{-6} M respectively) were prepared from a concentrated dispersion solution. Typically, CNC@PDA-Ag NPs (silver content of 2.5 μg/mL, the weight percentage of silver on nanohybrids was determined to be 80wt% by TGA) dispersion and β-CD solution with a concentration of 0.01 mM were used as concentrated stock. Then 0, 0.2, 0.4, 0.8 mL of the β-CD stock solution were adding into 1.2mL concentrated CNC@PDA solution, respectively. The final volume of each mixture was fixed at 2.0 mL by adding the proper volume of mini-Q water. The volume of catalyst introduced into the cuvette was kept at 200 μL.

7.3   Results and discussion

7.3.1   Characterization of CNC@PDA-Ag NPs

The CNC@PDA-AgNPs were prepared by poly(dopamine)-assisted reduction of silver ions at the surface of PDA-CNC as shown in Figure 7.1. The PDA coating procedure used the optimized parameters from a previous study[281], where a dopamine**:**CNC weight ratio of 1:1 was used. During the polymerization process, the color of the dispersion rapidly turned to pink due to the oxidation of catechol groups, which then slowly turned black, indicating the successful polymerization of the monomer. However, the molecular structure of poly(dopamine) is still under debate, could have either been covalent or non-covalent interactions between dopamine molecules[323]. Metallization was achieved by introducing CNC@PDA into a diammine silver(I) solution.

The $[Ag(NH_3)_2]^+$ ions adsorbed onto the surface through interactions between the catechol and nitrogen-containing functional groups. The adsorbed Ag^+ ions were reduced to silver nanoparticles that became immobilized on the CNC surface. Figure 7.2 shows TEM micrographs comparing the morphologies of CNCs before and after the polydopamine coating. The rod-like CNCs were about 200-400 nm in length and 10-20 nm in diameter, which is in agreement with previous data[188]. When TEM was used to analyze the CNC samples, the images lacked contrast, however, with the addition of the PDA coating, the CNC contrast improved. The diameter of the nanoparticles increased by several nanometers, and the surface roughness increased significantly (Figure 7.2B). TEM was also used to directly observe the morphologies of the CNC@PDA-AgNPs. The small Ag nanoparticles (~12 nm) were densely and uniformly distributed on the CNC@PDA surface.
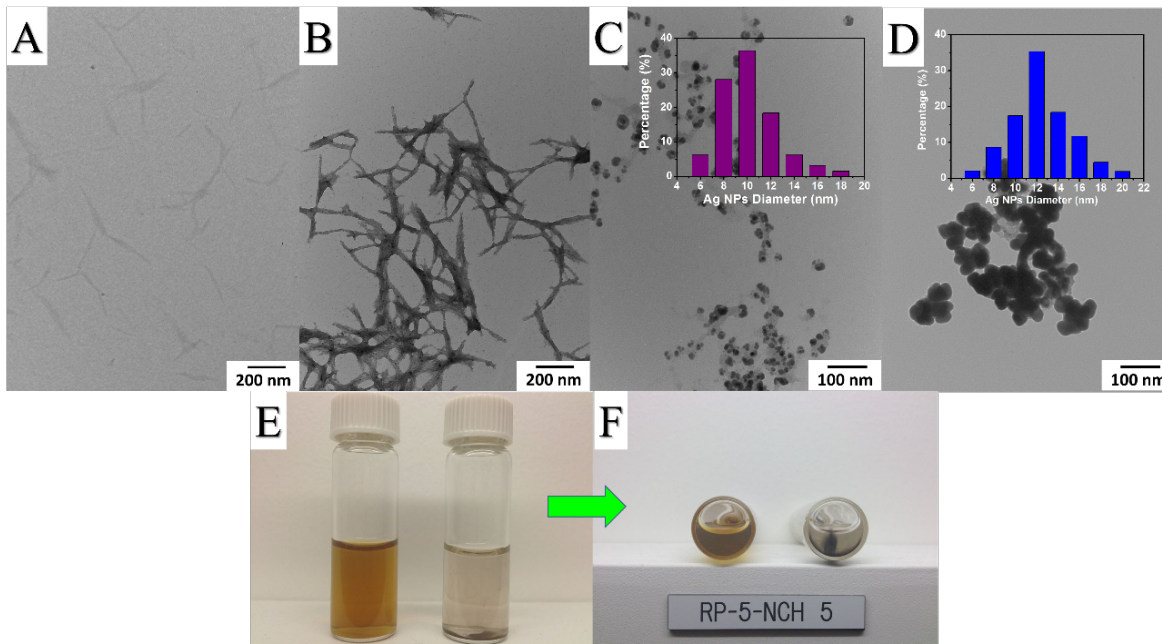
Figure 7.2 TEM images of pristine CNCs (A), core-shelled CNC@PDA (B), and weight ratio of 1:1), CNC@PDA-Ag NPs (C) and pure Ag NPs reduced by dopamine (D). Disperison stability comparison between CNC@PDA-Ag NPs and pure Ag NPs are shown in E and F (view from bottom).

UV spectroscopy was used to confirm the presence of PDA and the formation of Ag NPs, and the results are summarized in Figure 7.3A. A small peak at 281 nm, not seen with pristine CNCs, was observed for PDA-coated CNCs. This absorption band corresponds to the L_a-L_b coincident transition of dopamine structures[285]. Comparing the UV curves of CNC-PDA and CNC@PDA AgNPs dispersions, the appearance of a new peak at ~415 nm in CNC@PDA AgNPs was assigned to the surface plasmon resonance phenomena of electrons in the conduction bands of silver, confirming the formation of nanoscale silver colloids (Figure 7.3C).
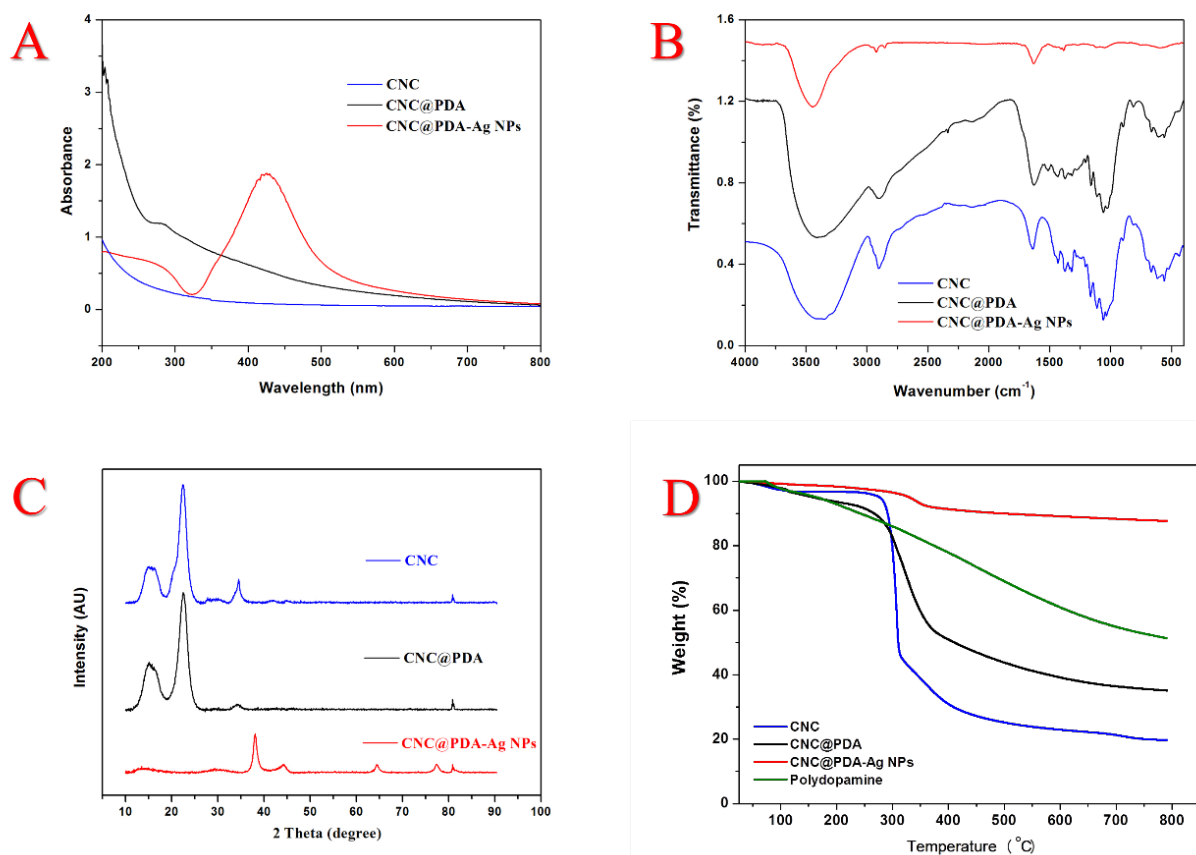
Figure 7.3 UV-Vis spectra (A), FTIR spectra (B), XRD patterns (C) and TGA results of pristine CNC (Blue), core-shell CNC@PDA (Black) and CNC@PDA-Ag NPs (Red) nanocomposites.

Figure 7.3B shows the FTIR spectra of CNCs, CNC@PDA, and CNC@PDA-AgNPs. Some of the specific peaks of CNCs are the absorption at $3417 cm^{-1}$ for hydroxyl stretching, $2903 cm^{-1}$ for symmetric C-H vibrations, and $1644 cm^{-1}$ from moisture in CNCs. After coating with PDA, significant changes in the spectra were observed within the region between 1200 and $1600 cm^{-1}$. The absorptions at $1512 cm^{-1}$ (N-H scissoring), $1350 cm^{-1}$ (phenolic O-H bending) and $1284 cm^{-1}$ (C-O stretching) are typical peaks of the polymer, indicating the successful coating of PDA on the surface of CNCs[296,303]. By further anchoring silver nanoparticles on CNCs, the intensity of these

peaks decreased dramatically together with a blue shift on the peak of around 3450 cm^{-1}. Thus, we determined that silver nanoparticles were bonded to the surface of CNC@PDA.

The surface functional nanoparticles were characterized using XRD to confirm that only the surface of CNC was modified and the crystal structure remained unchanged (Figure 7.3C). The spectra of cellulose nanocrystals displayed specific peaks at 2θ of 14.9, 16.2, 22.6 and 34.4°, corresponding to (1-10), (110), (200), and (004) crystallographic planes, respectively[63,190]. The reflections of crystalline structure from CNC@PDA exhibited nearly no differences except for a slight reduction in the intensity, confirming that coated PDA did not destroy the crystal structures of cellulose. The hybrid nanomaterial possessed peaks at 38.1, 44.3, 64.4, 77.4, and 81.5° assigned to the (111), (200), (220), (311) and (222) phase of the face-centered cubic crystal structure of silver nanoparticles respectively, which is consistent with the ASTM standard (JCPDS Card No. 04-0783)[324,325]. The results confirmed that AgNPs attached to the surface were in the zero valency state. In order to determine the content of silver nanoparticles in the nanohybrids, TGA tests were conducted and the results are presented in Figure 3D. The residual weights of pristine CNCs, PDA-coated CNCs and CNC@PDA-AgNPs were around 20%, 35.1% and 87.6% respectively, and further analyses indicated that the silver weight content was about 80%.

7.3.2   The catalytic properties of CNC@PDA-Ag NPs and Ag NPs

AgNPs have been extensively studied for catalytic reduction of nitrophenols and nitroanilines[270,326–328]. However, AgNPs are generally unstable due to their nano size and large surface area, which are prone to aggregation[275]. Introducing AgNPs onto the surface of CNCs - an ideal "green" carrier -will not only endow desirable catalytic characteristics to the nanohybrids, but it will address problems associated with the dispersion stability of AgNPs. Figures 7.2E and

7.2F compare the dispersion stability of AgNPs and CNC@PDA-AgNPs; the AgNPs were significantly agglomerated after one week while the CNC@PDA-AgNP dispersion remained stable with no evidence of sedimentation.

The model organic compound, 4-nitrophenol, was introduced to compare the catalytic properties of pristine AgNPs and CNC@PDA supported AgNPs. NaBH$_4$ was used as a reducing agent and UV-Vis was used to monitor the reaction kinetics at 1 min intervals. When 4-NP was exposed to the aqueous solution of NaBH$_4$, a strong absorption peak at 400 nm corresponding to a yellow-green color was introduced through the formation of 4-nitrophenolate ion[324,325,329].

Figures 7.4A and 7.4B show the comparison between AgNPs and CNC@PDA-AgNPs for catalyzing the reduction of 4-NP. The intensity of the absorption peak of 400 nm decreased together with the appearance of a new peak at 297 nm caused by the gradual conversion of nitrophenol to 4-aminophenol (4-AP) in the presence of AgNPs and CNC@PDA-AgNPs. There was no reduction in UV absorption over 1h when the bare substrate (CNC or CNC@PDA) was used confirming that silver nanoparticles are needed to catalyze the reduction reaction of 4-NP. Since the reduction occurred under conditions where the concentration of NaBH$_4$ greatly exceeded that of 4-NP, the reaction can be considered independent of borohydride content. Thus, the kinetic data can be fitted to a Langmuir-Hinshel-apparent first order plot[315]. The apparent rate constant (k_{app}) can be calculated using Equation7.1:

$$-\frac{dC_t}{d_t} = k_{app}C_t = k_1 SC_t$$

$$\ln(\frac{C_t}{C_0}) = \ln(\frac{A_t}{A_0}) = -k_{app}t$$

Equation 7.1

where C_t is the concentration of 4-NP at time t, k_{app} is the apparent rate constant, and k_1 is the rate constant normalized to S, the surface area of AgNPs normalized to the unit
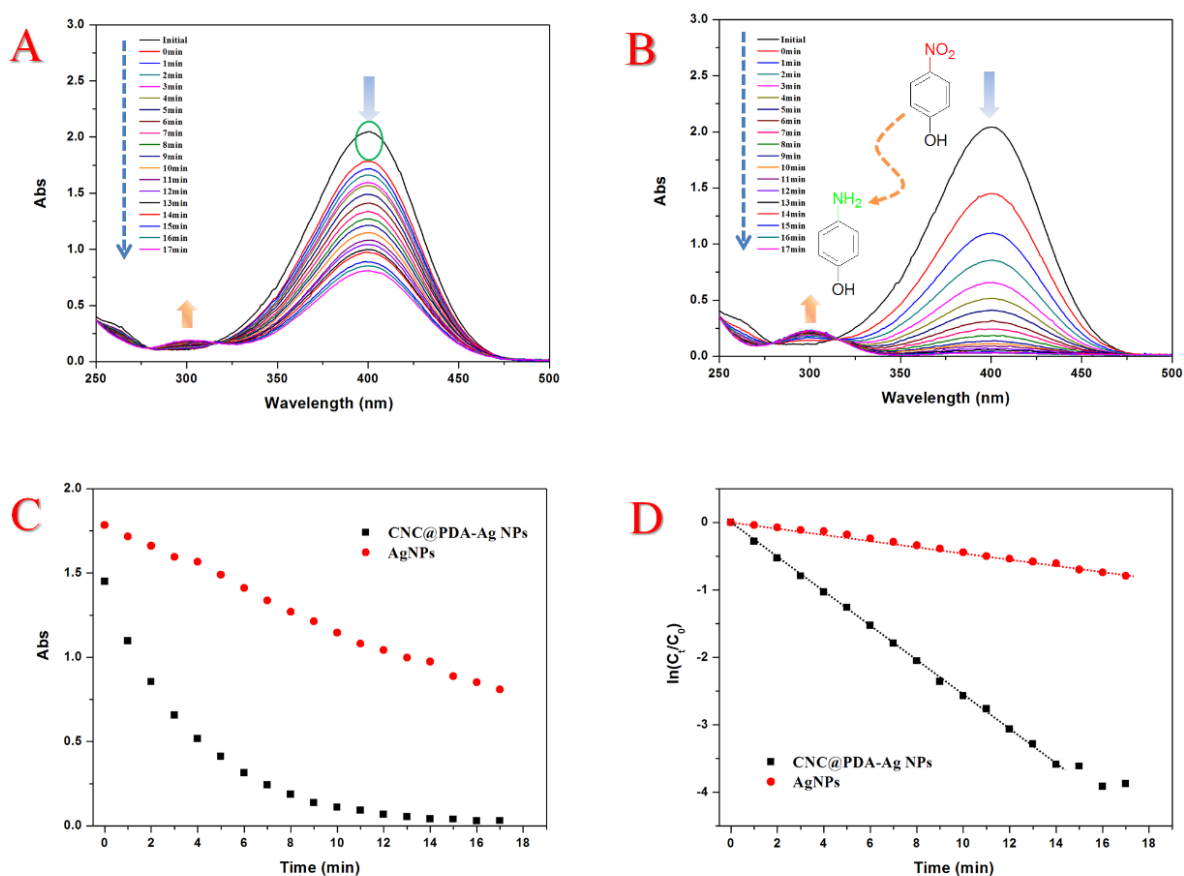
Figure 7.4 Time-dependent UV-Vis absorption spectra of 4-nitrophenol reduced by NaBH$_4$ catalyzed by pure Ag NPs (A) and CNC@PDA-Ag NPs (B). [Conditions: 200 μL of catalyst solution with a silver content of 2.0 μg/mL was introduced to a 3mL mixture of 4-NP (0.12mM) and NaBH4 (38mM), T=25°C]. Plot of absorption at 400nm (C) or ln (C$_t$/C$_0$) (D) versus time for pure Ag NPs (Red) and CNC@PDA-Ag NPs (Black).

volume of the system. The rate constant (k) was determined from the linear plot of *ln(A$_t$/A$_0$)* versus time (minutes), and found to be 0.0456 for Ag NPs and 0.2554 min^{-1} for CNC@PDA-AgNPs, (Figure 7.4D). The reaction rate for CNC@PDA-AgNPs was 6 times faster than pure AgNPs containing similar amounts of Ag. Two factors for the high catalytic activity of CNC@PDA-AgNPs are proposed: (1) the CNC@PDA hybrid nanomaterials possess a high surface area, which

161

is an important factor in catalytic reactions[315,330,331]; and (2) the readily water-dispersible carrier (CNCs) increases AgNPs dispersibility and dispersion stability to maximize the catalytic activity.

Table 7.1 Summary of the properties of different catalysts to reduce 4-NP

Catalyst supporter	Temperature (K)	Catalyst Type	TOF (h^{-1})	Ref
CNC	298	Pd	879.5	[65]
CNC	298	Au	109	[63]
CNC	298	CuO	885.7	[293]
CNC	298	Cu	1108.8	[293]
CNC@PDA	298	Ag	1077.3*	This work

* Experiments were carried out by mixing 3 mL [0.12 mM] of 4-NP (Solution 1) with 200 µL catalyst (Solution 2) containing 2 µg/m of Ag. The total volume was 3.2 mL. The molecular weight of silver of 107.87 g/mol was used for the calculation.

PDA-coated CNCs, are a versatile supporting material for anchoring and distributing metallic nanoparticles and can be used to address issues, such as catalyst "poisoning" and deactivation in heterogeneous catalytic reactions. To compare the current system with previously reported catalysts, the reaction rate and turnover frequency (TOF-defined as moles of 4-NP reduced per mole of catalyst per hour) were evaluated and are summarized in Table 7.1. Although the activity of Ag nanoparticles alone exhibited poorer catalytic performance than other metal nanoparticles[312], the TOF of Ag on PDA-coated CNCs from this study was comparable to that of other types of metal nanoparticles deposited on the surface of pristine CNC. It is anticipated that coating of mussel-inspired PDA onto CNCs will offer a simple and robust approach to fabricate novel catalyst hybrids for future applications.

The effects of CNC@PDA-AgNP catalyst dosing was investigated by varying the concentration of catalyst keeping other parameters, such as 4-NP and NaBH$_4$ constant. As shown in Figure 7.5B, the reaction rate generally increased linearly with catalyst concentration, which is consistent with a previous report[332]. This observation is consistent with the view that an increase in the total surface area and number of reaction sites enhances the catalytic activity[333].
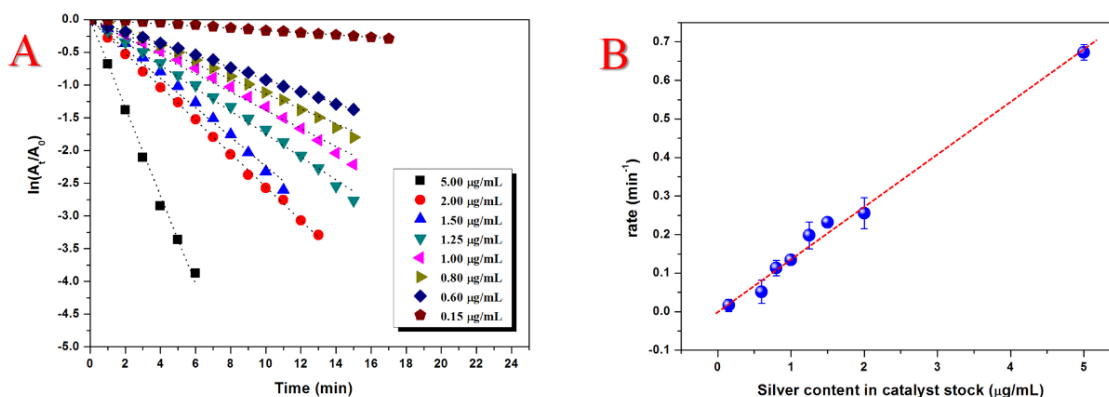
Figure 7.5 (A) Plot of $ln(C_t/C_0)$ versus time for different silver contents in CNC@PDA-Ag NP stock solutions. (B) Plot of rate constant (C_t) versus silver content for 4-NP reduction by NaBH$_4$. Conditions: 200μL of catalyst solution was introduced into a 3mL mixture of 4-NP (0.12 mM) and NaBH$_4$ (38 mM), T=25°C.

7.3.3 Temperature dependence and activation energy calculation

In reaction kinetics, the activation energy (E_a) is an empirical parameter describing the dependency of the rate constant with temperature. A larger E_a value indicates higher sensitivity of the kinetic constant k to reaction temperature. Figure 7.6B shows the corresponding linear relationship between $ln(A_t/A_0)$ and time at different temperatures.

From the linear regression, different rate constants were determined from the slopes of the linear fits shown in Figure 7.6A. The E_a were calculated using the Arrhenius equation:

$$k_{app} = Ae^{-E_a/RT}$$ Equation 7.2

$$\ln k_{app} = -\frac{E_a}{RT} + \ln A$$ Equation 7.3
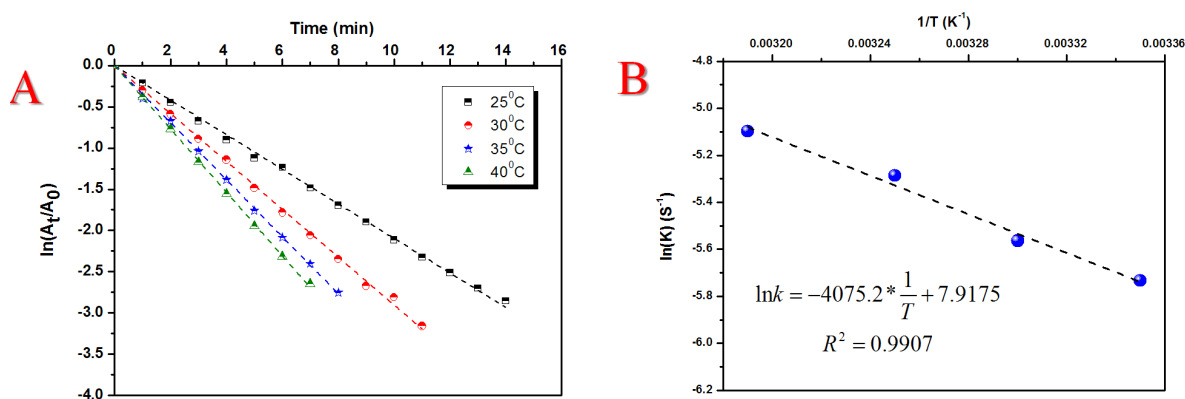
Figure 7.6 (A) Plot of *ln(C_t/C_0)* versus time for different temperatures using CNC@PDA-Ag NPs as catalyst. (B) Arrhenius plot from the slopes of the lines in 6(A). Conditions: 200 μL of catalyst solution with a silver content of 2.0 μg/mL was introduced to a 3 mL mixture of 4-NP (0.12 mM) and NaBH$_4$ (38 mM).

where A is the Arrhenius factor, k is the rate constant at temperature T (in Kelvin), and R is the universal gas constant. The experiments were conducted under the reaction conditions: total volume of the system was 3.2 mL, including 3.0 mL 4-NP stock solution (0.12mM) mixed with NaBH$_4$ (38 mM) and 0.2 mL catalyst with an Ag content of 2.0 μg/mL). From the slope of the plot of *lnK$_{app}$* against *1/T*, the activation energy E_a was determined to be 33.88 kJ/mol for the CNC@PDA-Ag nanocatalyst, which is agreement with values reported previously[313,334]. For different systems and materials, the experimentally determined E_a can vary significantly[335]. For example, Zhu reported an E$_a$ of 40.9 kJ/mol for silver nanoparticles immobilized on magnetic Fe$_3$O$_4$@C core–shell nanocomposites[336]. An activation energy of 66.8 kJ/mol was observed for

silver nanoparticles on a procyanidin-grafted eggshell membrane[311]. Usually, for surface catalyzed reactions, the activation energy lies between 8.4 to 41.9 kJ/mol[337]. Thus, the results support that the conversion of 4-NP to 4-AP occurred via surface catalysis.

7.3.4 Cooperation between CNC@PDA-Ag NPs and β-cyclodextrin

Cyclodextrins (CD) are known to readily adsorb onto nanoparticle surfaces such as Au or Ag, through their primary faces, exposing the more polar, secondary faces. This favors the binding between anchored CD hosts and guests[43, 44]. The equilibrium constant and standard enthalpy haven been measured calorimetrically for the formation of complex of β-cyclodextrin with 4-nitrophenol in aqueous solution by Gary and workers, which is certificated to be 350 L/mol and -12 kJ/mol[67]. Thus in our case, the benzene-structured 4-NP can be an ideal guest for the cavity of cyclodextrin. Plots of $ln(k_{app})$ versus $1/T$ for different concentrations of β-cyclodextrin are shown in Figure 7.7. As shown in Figure 7.7a, for the same temperature, the reaction rate increased linearly over the CD concentration range being investigated. The reason for this trend is described below. It has been suggested that the basic mechanism of 4-NP reduction is described by the following reactions:

$$2Ag + BH_4^- \leftrightarrow Ag - BH_3^- + Ag - H$$

$$6H - Ag + 4 - NP \rightarrow 4 - AP + 6Ag + 6H^+$$

$$6Ag - BH_3^- + 4 - NP \rightarrow 4 - AP + 6Ag + 6BH_3$$
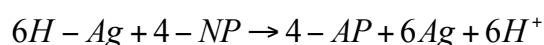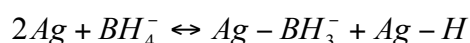
For the reaction to proceed, 6 moles of electrons are required to transform 4-NP to 4-AP at the metal surface[334]. The electron transfer rate is determined by three steps: diffusion of 4-NP to the metal surface, interfacial electron transfer and the diffusion of 4-AP from the surface. Thus, the observed rate constant can be described by Equation 7.4:

$$\frac{1}{k_{obs}} = (\frac{1}{4\pi R^2})[(\frac{1}{k_e}) + \frac{R}{D}]$$

Equation 7.4

where k_e is the rate constant of electron transfer, D is the diffusion coefficient and R is the radius of the silver nanoparticles. Introducing CD molecules to the system may increase the diffusion coefficient of 4-NP, and subsequently increase the reaction rate. The possible mechanism is illustrated in Figure 7.8.
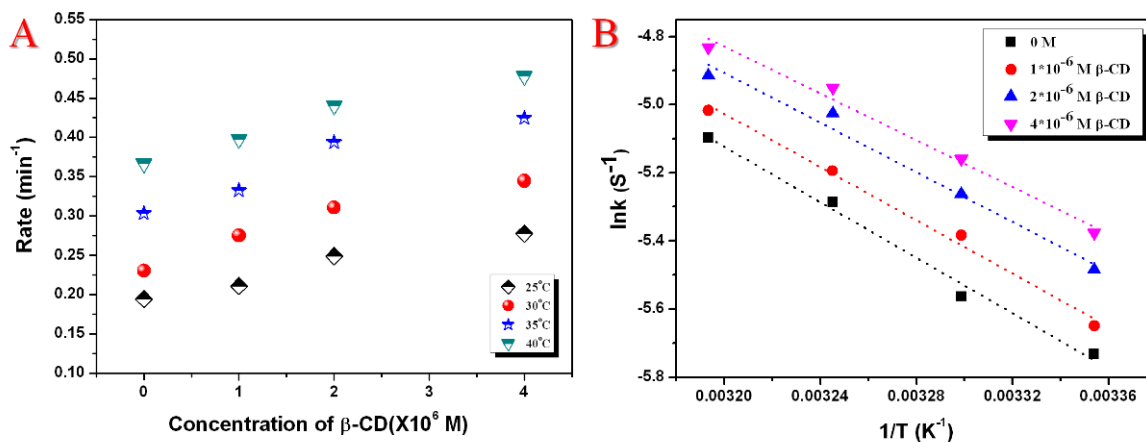
Figure 7.7 (A) Plot of rate constant versus concentration of β-CD in catalyst stock solution for 4-NP reduction by NaBH$_4$. (B) Arrhenius plots from the slopes of the lines in (A) (0, 1, 2, 4x10^{-6} were the concentrations of β-CD in the catalyst stock solution). Conditions: 200 μL of catalyst solution with a silver content of 1.5 μg/mL was introduced to a 3 mL mixture of 4-NP (0.12 mM) and NaBH$_4$ (38 mM).

The E_a of the systems with different CD concentrations was calculated by fitting Eq. 7.3 to the experimental data (Figure 7.7B) and the numerical values are summarized in Table 7.2. There was a slight decrease in the activation energy when the concentration of β-cyclodextrin was increased. These differences may be attributed to the change of hydration of 4-NP molecules anchored to CD molecules as well as the change in the mechanism at the surface of CNC-Ag nanohybrids. The E_a

data did not display a notable decrease from the results for α-CD reported by Liu and co-workers[322].
A similar trend was observed but the magnitude of the activation energy differed due to the
difference in the binding constant between 4-NP/ β-CD and 4-NP/α-CD[338].

Table 7.2 Summary on the parameters got from Arrhenius plots with different [β-CD]

CD Concentration(*10^6 M)	Slope for Arrhenius plots	Ea (kJ/mol)	R^2
0	-4075.2	33.88	0.9907
1	-3909.6	32.51	0.9927
2	-3646.3	30.32	0.9825
4	-3439.1	28.59	0.9874
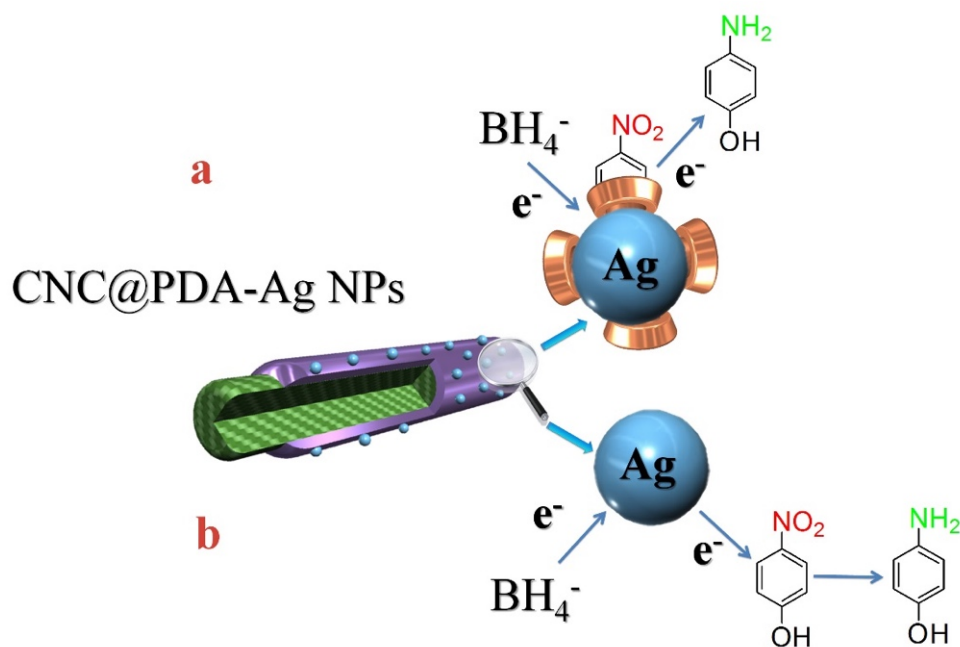
Figure 7.8 Postulated mechanism for the catalytic reduction of 4-NP with (a) or without (b) the
incorporation of β-CD.

7.4   Conclusions

A stable hybrid nanocatalyst was successfully synthesized through a mussel-inspired green method by surface coating polydopamine on cellulose nanocrystals (CNCs), followed by *in situ* reduction of silver ions. The catalytic properties of the nanohybrids were investigated through a reduction reaction of a model compound (4-nitrophenol) in the presence of $NaBH_4$ as a reducing agent. The reaction rate using CNC@PDA-AgNPs as a catalyst was 6 times faster than that of pristine AgNPs. Using the Arrhenius relationship, the activation energy (E_a) was determined to be 33.88 kJ/mol for the CNC@PDA-Ag nanocatalyst, which is consistent with other systems reported previously. With further incorporation of β-cyclodextrin (CD) into the system, the catalytic process was accelerated due to the host-guest interactions between 4-NP and CD. Therefore, CNC@PDA, a facile and green carrier, provides a versatile platform for fabricating stable nanocatalysts for industrial applications.

Chapter 8   General conclusions and perspectives for future research

8.1   Conclusions and general contributions

Replacing petroleum-based synthetic materials with green and sustainable materials is gaining increasing attention due to the challenges with green house gases and global warming. This thesis aims at modifying pristine cellulose nanocrystals, investigate the properties of functionalized CNC nanoparticles and exploring their potential applications by a combination of chemical synthesis and engineering techniques. The main contributions of the studies are summarised below:

(1) Preparation of pH and thermo-responsive cellulose nanocrystals by grafting the surface with PDMAEMA polymer chains and their capability of stabilizing the Pickering emulsions,

(2) Grafting mixed brushes (bearing pH and temperature responsive characteristics) onto CNC surfaces and explore their application for oil harvesting,

(3) Coating the CNC surface with conjugated polymer, polyrhodanine, and their potential applications in pH optical sensor, antimicrobial formulation as well as lithium sulphur battery electrode were elucidated,

(4) Anchoring silver nanoparticle (AgNPs) catalysts onto the surface of cellulose nanocrystals through a green and bio-inspired approach and an improvement of catalytic properties was achieved.

The research introduced in Chapter 3 originated from the question on whether we can prepare smart cellulose nanocrystals to stabilize Pickering emulsions and whether their stability can be manipulated by external triggers. How the surface properties will affect the nanoparticle

distribution at the oil-water interface? To address these questions, a dual responsive polymer brush, PDMAEMA, was grafted onto the CNC surface and various characterization techniques were used to confirm the successful modification. The amounts of tertiary amines on the CNC surface were determined to be approximately 0.8 mmol of $-N(CH_3)_2$ per gram of PDMAEMA-g-CNC. The modified nanoparticles displayed good surface and interfacial properties when the amino groups on PDMAEMA were highly deprotonated. The air-water surface tension decreased from 72 to 47 mN/m depending on the concentrations of PDMAEMA-g-CNC. Compared to pristine CNC, oil-in-water emulsions prepared with modified CNC displayed improved stability against coalescence over a 4 months period. Using Nile Red as an indicator in heptane-water emulsions, the colour changed from fuchsia to yellow when the pH was increased, and this was correlated to changes in the polarity of the oil phase probed by Nile Red molecules that was influenced by the extent of PDMAEMA chain penetration to the oil phase that depended on the degree of protonation of amine groups. However, this behaviour was not observed for toluene-water systems due to the more polar toluene. Stimuli responsive Pickering emulsions utilizing polysaccharide nanocrystals with controllable stability suitable for cosmetic and pharmaceutical applications were demonstrated.

Chapter 4 is an extension of the study described in Chapter 3, with the goal of improving the coalescence efficiency when triggers were applied to destabilize the emulsions. To address this issue, binary polymer brushes, POEGMA and PMAA were grafted on cellulose nanocrystals. A transition temperature of around 37ºC was observed for POEGMA modified nanoparticles. Destabilization of the emulsion was achieved by increasing the temperature caused by the conformational change of POEGMA chains. By further incorporating PMAA chains, the emulsions stabilized by CNC-POEGMA-PMAA displayed pH-responsive stability caused by the tunable interaction between the nanoparticles. Bifunctionalized CNCs diffused to the oil-water

interface and stabilized the oil droplets at high pHs. When the pH was reduced to 2, strong hydrogen bonds between POEGMA and PMAA chains grafted on the CNC induced instant coalescence of emulsions, resulting in the phase separation of oil and water. However, for emulsions stabilized by CNC-POEGMA and free PMAA mixtures, instantaneous coalescence was not observed at low pHs. We hypothesized that the chain flexibility and molecular weight of PMAA may play important roles in destabilizing the emulsions. Furthermore, we demonstrated a reversible emulsification-demulsification process controlled by pH, where the emulsification and oil-water separation could be repeated 5 times without any loss in efficiency. A new approach to prepare surface-tailorable sustainable nanomaterials for oil-water separations, especially for oil droplet transportation and lipophilic substances harvesting was proposed.

Chapter 5 and 6 describe a simple and green approach to design multi-functional materials based on cellulose nanocrystals. A conjugated polymer, polyrhodanine, were coated onto the surface of CNC by in-situ polymerization to form core-shell nanoparticles. These CNC@PR core–shell nanoparticles possessed redox reversibility in response to changes in pH. The colour gradually changed from pale red to blue violet when the pH was increased from 2.04 to 12.04. The redox reversibility of the hybrid nanomaterial in response to pH was retained when transformed into different geometries, such as 1D printable inks, 2D flat film, membranes, and 3D hydrogel beads. Results also showed that rod-like CNC@PR nanoparticles exhibited promising antimicrobial properties towards both *Escherichia coli* (Gram negative, MIC: 0.5-1.0 mg/mL) and *Bacillus subtilis* (Gram positive, MIC: 1.0-2.0 mg/mL), which is comparable to spherical nano-composite particles (SiO_2@PR). Such system could hold promise for the development of cheap and environmentally friendly pH sensing devices. They are also potential candidates for antimicrobial applications, such as food-packaging, antimicrobial additives and antimicrobial coatings.

Inspired by the composition of adhesive proteins in mussels, polydopamine assisted deposition of nanosilver catalyst on CNC was described in Chapter 7. The catalytic properties of the nanohybrids were investigated through a reduction reaction of a model compound (4-nitrophenol) in the presence of a reducing agent, NaBH$_4$. The reaction rate using CNC@PDA-AgNPs as a catalyst was 6 times faster than that of pristine AgNPs. The activation energy (E_a) was determined to be 33.88 kJ/mol for the CNC@PDA-Ag nanocatalyst. With further incorporation of β-cyclodextrin (CD) into the system, the catalytic process was accelerated due to the host-guest interactions between 4-NP and CD. CNC@PDA, a facile and green carrier, provides a versatile platform for fabricating stable nanocatalysts and shows promising potential for industrial heterogonous reactions.
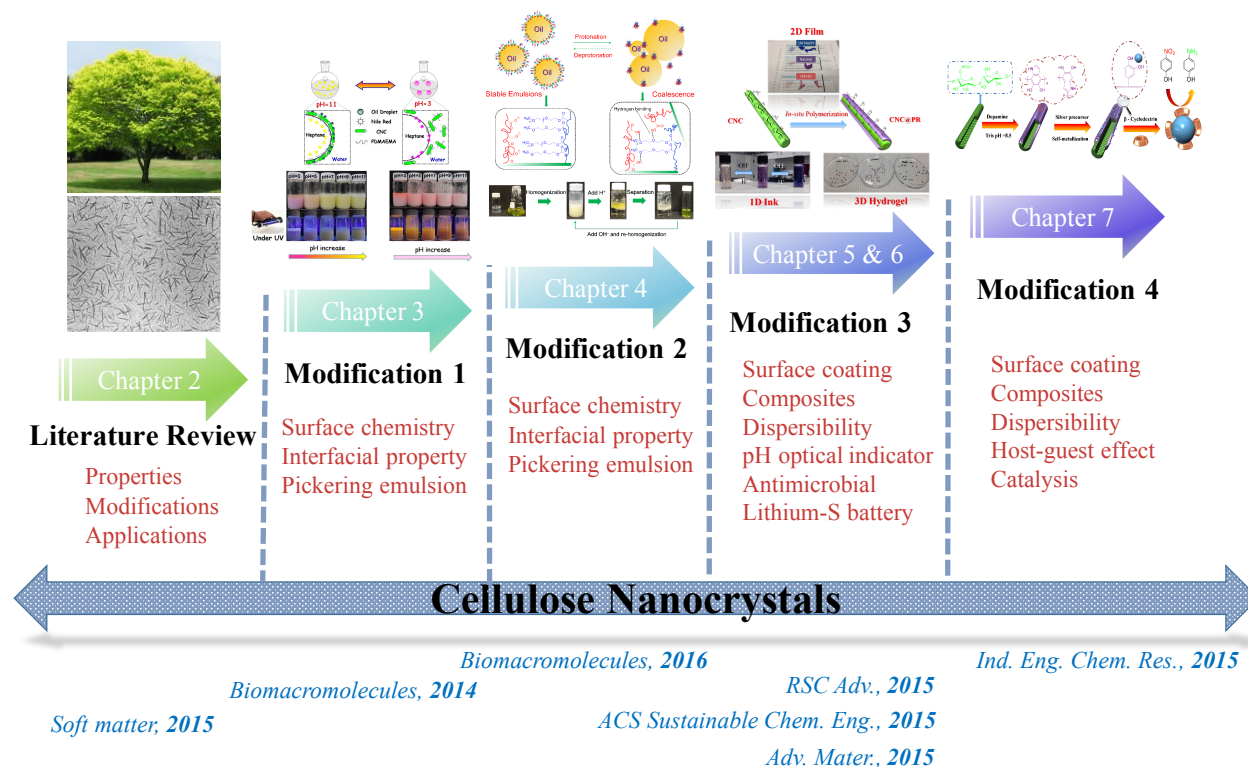
Figure 8.1 Schematic illustration of the research topics and results included in this thesis.

8.2   Recommendation for future studies

Driven by the research activity on functional nanomaterials, cellulose nanocrystal offers an opportunity to strengthen the competitiveness of the forest industry by extracting high value added sustainable nanomaterials and formulate them into green and environmentally friendly products. In summary, we anticipate that the results of the thesis not only contribute to the fundamental understanding of the properties and behaviour of cellulose nanocrystals, but also offer suggestions on novel types of application in sustainable nanomaterials beyond the classic cellulose systems. The work described in this thesis is an attempt to address some of the challenges on the development of sustainable nanomaterials for possible applications in various industrial sectors. From the research on cellulose nanocrystals described in this thesis, new challenges and opportunities have been uncovered, and several recommendations for future study are proposed:

(1) By virtue of the nanosize effect and surface grafted stimuli-responsive polymers, modified cellulose nanocrystals can function as ideal smart Pickering emulsifiers. New applications in addition to oil harvesting should be explored, for example in biocatalyst recycling, cosmetic and personal care products. It may increase the stability and shelf life of a given formulation, while permitting the rapid and controlled release of active compounds in response to external triggers. Or we may consider using stimuli-responsive CNC engineered emulsions for obesity treatment. An appropriately designed Pickering emulsion for obesity treatment should not only decrease lipid digestibility/absorbability in the upper intestine but it may also promote the feeling of "fullness" by consumer in order to reduce the amounts of food consumed. We hypothesize that the stimuli-responsive CNC-stabilized Pickering emulsion will gel in the stomach but fluidize at the upper small intestine, reducing its flow

to the ileum. By changing the environmental conditions, for example pH, the emulsion can be destabilized to release its oil cargo within the ileum to effectively trigger the "ileal brake mechanism".

(2) Other new types of triggers can also be introduced to the emulsion system, such as CO_2, light (UV or NIR) or even redox-responsive systems. In contrast to pH adjustment, the addition and removal of CO_2 is a non-accumulative process, where the acidification–neutralization cycling may be accomplished without a significant increase in the ionic strength of the system. Therefore, using CO_2 as stimuli control is a low cost, widely available, benign, biocompatible, and simple strategy in the design of novel Pickering emulsifiers.

(3) The packing characteristics as well as curvature of the functional nanoparticles at the interface need to be further investigated and elucidated. For example, controlled polymerization methods can to be implemented to control the grafting density as well as the molecular weight of the polymeric brushes. Also it would be interesting to label the stimuli-responsive CNC so that we can monitor their state at the interface or continuous phase via fluorescence microscopy.

(4) With respect to the polyrhodanine coated cellulose nanocrystals reported in Chapter 5 and 6, it will be interesting to incorporate them into polymer matrices, and develop the corresponding products with specific applications. For example, we may process them into vacuum packaging materials and the effective antimicrobial properties may provide the long-term protection for fresh meat or vegetables. The pH-dependent optical property may be used for assessing the quality of the food as the metabolism of the microorganisms may lead to pH variations. In addition, polyrhodanine is known to possess other attractive features,

such as heavy metal binding and anticorrosion properties. Based on the above, we believe that CNC@PR could provide a platform for the development of multi-functional products.

(5) Regarding the study on "improved catalytic properties using polydopamine coated CNC" reported in Chapter 7, further investigation on the effects of catalyst type and size may provide valuable insight into the design of novel nanomaterials. In order to address the recycling issue of catalysts, the CNC@PDA can also be formulated into 2D films or 3D aerogels with porous structures by post-modifying polydopamine using catechol chemistries. The resulting materials may provide the versatile substrate for catalyst deposition that significantly promote their performance in the desired applications.

In summary, the exploration of suitable approaches for modifying cellulose nanocrystals and incorporating them into various types of materials is a continuing challenge that requires more research. We are hopeful that the practical commercial applications of cellulose nanocrystals will be realised.

References:

1.   E. Lam, K. B. Male, J. H. Chong, A. C. W. Leung, and J. H. T. Luong, *Trends Biotechnol.*, 2012, **30**, 283–290.

2.   Y. Habibi, *Chem. Soc. Rev.*, 2013, **43**, 1519–1542.

3.   Y. Habibi, L. a Lucia, and O. J. Rojas, *Chem. Rev.*, 2010, **110**, 3479–500.

4.   B. L. Peng, N. Dhar, H. L. Liu, and K. C. Tam, *Can. J. Chem. Eng.*, 2011, **89**, 1191–1206.

5.   L. Chen, R. M. Berry, and K. C. Tam, *ACS Sustain. Chem. Eng.*, 2014, **2**, 951–958.

6.   S. P. Akhlaghi, R. C. Berry, and K. C. Tam, *Cellulose*, 2013, **20**, 1747–1764.

7.   B. Peng, X. Han, H. Liu, R. C. Berry, and K. C. Tam, *Colloids Surfaces A Physicochem. Eng. Asp.*, 2013, **421**, 142–149.

8.   R. Batmaz, N. Mohammed, M. Zaman, G. Minhas, R. M. Berry, and K. C. Tam, *Cellulose*, 2014, **21**, 1655–1665.

9.   J. Tang, M. F. X. Lee, W. Zhang, B. Zhao, R. M. Berry, and K. C. Tam, *Biomacromolecules*, 2014, **15**, 3052–3060.

10.   D. Klemm, B. Heublein, H.-P. Fink, and A. Bohn, *Angew. Chemie Int. Ed.*, 2005, **44**, 3358–3393.

11.   S. Eichhorn and C. Baillie, *J. Mater. Sci.*, 2001, **6**, 2107–2131.

12.   D. Klemm, F. Kramer, S. Moritz, T. Lindström, M. Ankerfors, D. Gray, and A. Dorris, *Angew. Chemie Int. Ed.*, 2011, **50**, 5438–5466.

13.   M. A. S. Azizi Samir, F. Alloin, and A. Dufresne, *Biomacromolecules*, 2005, **6**, 612–626.

14.   R. F. Nickerson and J. A. Habrle, *Ind. Eng. Chem.*, 1947, **39**, 1507–1512.

15.   B. G. Ranby, *Acta Chem. Scand.*, 1949, **3**, 649–650.

16.   J. F. Revol, H. Bradford, J. Giasson, R. H. Marchessault, and D. G. Gray, *Int. J. Biol. Macromol.*, 1992, **14**, 170–172.

17.   S. Dong and M. Roman, *J. Am. Chem. Soc.*, 2007, **129**, 13810–13811.

18.   K. E. Shopsowitz, H. Qi, W. Y. Hamad, and M. J. Maclachlan, *Nature*, 2010, **468**, 422–425.

19.   I. Kalashnikova, H. Bizot, B. Cathala, and I. Capron, *Langmuir*, 2011, **27**, 7471–7479.

20.   I. Kalashnikova, H. Bizot, B. Cathala, and I. Capron, *Biomacromolecules*, 2012, **13**, 267–275.

21.   I. Capron and B. Cathala, *Biomacromolecules*, 2013, **14**, 291–296.

22. J. Fox, J. J. Wie, B. W. Greenland, S. Burattini, W. Hayes, H. M. Colquhoun, M. E. Mackay, and S. J. Rowan, *J. Am. Chem. Soc.*, 2012, **134**, 5362–5368.

23. S. Coulibaly, A. Roulin, and S. Balog, *Macromolecules*, 2014, **47**, 152–160.

24. M. K. Khan, W. Y. Hamad, and M. J. MacLachlan, *Adv. Mater.*, 2014, **26**, 2323–2328.

25. J. a Kelly, M. Giese, K. E. Shopsowitz, W. Y. Hamad, and M. J. MacLachlan, *Acc. Chem. Res.*, 2014, **47**, 1088–1096.

26. J. a Kelly, A. M. Shukaliak, C. C. Y. Cheung, K. E. Shopsowitz, W. Y. Hamad, and M. J. MacLachlan, *Angew. Chemie Int. Ed.*, 2013, **52**, 8912–8916.

27. M. Giese, L. K. Blusch, M. K. Khan, W. Y. Hamad, and M. J. MacLachlan, *Angew. Chem. Int. Ed. Engl.*, 2014, **53**, 8880–8884.

28. K. E. Shopsowitz, A. Stahl, W. Y. Hamad, and M. J. MacLachlan, *Angew. Chem. Int. Ed. Engl.*, 2012, **51**, 6886–6890.

29. K. E. Shopsowitz, W. Y. Hamad, and M. J. MacLachlan, *J. Am. Chem. Soc.*, 2012, **134**, 867–870.

30. J. a Kelly, K. E. Shopsowitz, J. M. Ahn, W. Y. Hamad, and M. J. MacLachlan, *Langmuir*, 2012, **28**, 17256–17262.

31. K. E. Shopsowitz, J. a. Kelly, W. Y. Hamad, and M. J. MacLachlan, *Adv. Funct. Mater.*, 2014, **24**, 327–338.

32. A. C. W. Leung, S. Hrapovic, E. Lam, Y. Liu, K. B. Male, K. A. Mahmoud, and J. H. T. Luong, *Small*, 2011, **7**, 302–305.

33. L. Tang, B. Huang, Q. Lu, S. Wang, W. Ou, W. Lin, and X. Chen, *Bioresour. Technol.*, 2013, **127**, 100–105.

34. H. Zhao, J. H. Kwak, Z. Conrad Zhang, H. M. Brown, B. W. Arey, and J. E. Holladay, *Carbohydr. Polym.*, 2007, **68**, 235–241.

35. K. Schenzel, S. Fischer, and E. Brendler, *Cellulose*, 2005, **12**, 223–231.

36. P. Lu and Y. Lo Hsieh, *Carbohydr. Polym.*, 2010, **82**, 329–336.

37. M. Roman and W. T. Winter, *Biomacromolecules*, 2004, **5**, 1671–1677.

38. J. Majoinen, E. Kontturi, O. Ikkala, and D. G. Gray, *Cellulose*, 2012, **19**, 1599–1605.

39. E. E. Ureña-Benavides, G. Ao, V. A. Davis, and C. L. Kitchens, *Macromolecules*, 2011, **44**, 8990–8998.

40. S. Shafeiei-Sabet, W. Y. Hamad, and S. G. Hatzikiriakos, *Rheol. Acta*, 2013, **52**, 741–751.

41.   L. Heux, G. Chauve, and C. Bonini, *Langmuir*, 2000, **16**, 8210–8212.

42.   J. Kim and G. Montero, *Polym. Eng. Sci.*, 2009, **49**, 2054–2061.

43.   O. Rojas, G. Montero, and Y. Habibi, *J. Appl. Polym. Sci.*, 2009, **113**, 927–935.

44.   M. Salajková, L. a. Berglund, and Q. Zhou, *J. Mater. Chem.*, 2012, **22**, 19798.

45.   Q. Zhou, H. Brumer, and T. T. Teeri, *Macromolecules*, 2009, **42**, 5430–5432.

46.   J. Majoinen, J. S. Haataja, D. Appelhans, A. Lederer, A. Olszewska, J. Seitsonen, V. Aseyev, E. Kontturi, H. Rosilo, M. Österberg, N. Houbenov, and O. Ikkala, *J. Am. Chem. Soc.*, 2014, **136**, 866–869.

47.   N. Lin and A. Dufresne, *Eur. Polym. J.*, 2014, **59**, 302–325.

48.   S. Eyley, D. Vandamme, S. Lama, G. Van den Mooter, K. Muylaert, and W. Thielemans, *Nanoscale*, 2015, **7**, 14413–14421.

49.   F. Azzam, L. Heux, J.-L. Putaux, and B. Jean, *Biomacromolecules*, 2010, **11**, 3652–3659.

50.   F. Azzam, E. Siqueira, S. Fort, R. Hassaini, F. Pignon, C. Travelet, J.-L. Putaux, and B. Jean, *Biomacromolecules*, 2016, **17**, 2112–2119.

51.   J. Yi, Q. Xu, X. Zhang, and H. Zhang, *Cellulose*, 2009, **16**, 989–997.

52.   J. O. Zoppe, Y. Habibi, O. J. Rojas, R. a Venditti, L.-S. Johansson, K. Efimenko, M. Österberg, and J. Laine, *Biomacromolecules*, 2010, **11**, 2683–2691.

53.   K. H. M. Kan, J. Li, K. Wijesekera, and E. D. Cranston, *Biomacromolecules*, 2013, **14**, 3130–3139.

54.   W. Wu, F. Huang, S. Pan, W. Mu, X. Meng, H. Yang, Z. Xu, A. J. Ragauskas, and Y. Deng, *J. Mater. Chem. A*, 2015, **3**, 1995–2005.

55.   I. Kalashnikova, H. Bizot, P. Bertoncini, B. Cathala, and I. Capron, *Soft Matter*, 2013, **9**, 952–959.

56.   J. O. Zoppe, R. A. Venditti, and O. J. Rojas, *J. Colloid Interface Sci.*, 2012, **369**, 202–209.

57.   Z. Hu, T. Patten, R. Pelton, and E. D. Cranston, *ACS Sustain. Chem. Eng.*, 2015, **3**, 1023–1031.

58.   Z. Hu, H. S. Marway, H. Kasem, R. Pelton, and E. D. Cranston, *ACS Macro Lett.*, 2016, **5**, 185–189.

59.   N. Drogat, R. Granet, V. Sol, A. Memmi, N. Saad, C. Klein Koerkamp, P. Bressollier, and P. Krausz, *J. Nanoparticle Res.*, 2011, **13**, 1557–1562.

60.   E. Feese, H. Sadeghifar, H. S. Gracz, D. S. Argyropoulos, and R. A. Ghiladi,

Biomacromolecules, 2011, **12**, 3528–3539.

61.   M. Kaushik and A. Moores, *Green Chem.*, 2016, **18**, 622–637.

62.   A. R. Lokanathan, K. M. A. Uddin, O. J. Rojas, and J. Laine, *Biomacromolecules*, 2014, **15**, 373–379.

63.   X. Wu, C. Lu, Z. Zhou, G. Yuan, R. Xiong, and X. Zhang, *Environ. Sci. Nano*, 2014, **1**, 71–79.

64.   Y. Shin, I. T. Bae, B. W. Arey, and G. J. Exarhos, *Mater. Lett.*, 2007, **61**, 3215–3217.

65.   X. Wu, C. Lu, W. Zhang, G. Yuan, R. Xiong, and X. Zhang, *J. Mater. Chem. A*, 2013, **1**, 8645.

66.   Y. Zhou, E. Y. Ding, and W. D. Li, *Mater. Lett.*, 2007, **61**, 5050–5052.

67.   Y. Shin, J. M. Blackwood, I. T. Bae, B. W. Arey, and G. J. Exarhos, *Mater. Lett.*, 2007, **61**, 4297–4300.

68.   Y. Shin, I. T. Bae, B. W. Arey, and G. J. Exarhos, *J. Phys. Chem. C*, 2008, **112**, 4844–4848.

69.   C. Miao and W. Y. Hamad, *Cellulose*, 2013, **20**, 2221–2262.

70.   T. Abitbol, T. Johnstone, T. M. Quinn, and D. G. Gray, *Soft Matter*, 2011, **7**, 2373.

71.   X. Zhang, J. Huang, P. R. Chang, J. Li, Y. Chen, D. Wang, J. Yu, and J. Chen, *Polymer (Guildf).*, 2010, **51**, 4398–4407.

72.   A. Hebeish, S. Farag, S. Sharaf, and T. I. Shaheen, *Carbohydr. Polym.*, 2014, **102**, 159–166.

73.   Q. Dai and J. F. Kadla, *J. Appl. Polym. Sci.*, 2009, **114**, 1664–1669.

74.   K. J. De France, K. J. W. Chan, E. D. Cranston, and T. Hoare, *Biomacromolecules*, 2016, **17**, 649–660.

75.   R. Sanna, E. Fortunati, V. Alzari, D. Nuvoli, A. Terenzi, M. F. Casula, J. M. Kenny, and A. Mariani, *Cellulose*, 2013, **20**, 2393–2402.

76.   J. Yang, C.-R. Han, J.-F. Duan, M.-G. Ma, X.-M. Zhang, F. Xu, R.-C. Sun, and X.-M. Xie, *J. Mater. Chem.*, 2012, **22**, 22467.

77.   J. Yang, C. Han, F. Xu, and R. Sun, *Nanoscale*, 2014, **6**, 5934.

78.   J. Yang, C. R. Han, J. F. Duan, M. G. Ma, X. M. Zhang, F. Xu, and R. C. Sun, *Cellulose*, 2013, **20**, 227–237.

79.   X. Yang, E. Bakaic, T. Hoare, and E. D. Cranston, *Biomacromolecules*, 2013, **14**, 4447–

4455.

80. M. Chau, K. J. De France, B. Kopera, V. R. Machado, S. Rosenfeldt, L. Reyes, K. J. W. Chan, S. Förster, E. D. Cranston, T. Hoare, and E. Kumacheva, *Chem. Mater.*, 2016, **28**, 3406–3415.

81. A. Šturcová, G. R. Davies, and S. J. Eichhorn, *Biomacromolecules*, 2005, **6**, 1055–1061.

82. V. Favier and G. Canova, *Polym. Adv. Technol.*, 1995, **6**, 351–355.

83. L. Tang and C. Weder, *ACS Appl. Mater. Interfaces*, 2010, **2**, 1073–1080.

84. a. Saralegi, L. Rueda, L. Martin, a. Arbelaiz, a. Eceiza, and M. a. Corcuera, *Compos. Sci. Technol.*, 2013, **88**, 39–47.

85. J. R. Capadona, K. Shanmuganathan, D. J. Tyler, S. J. Rowan, and C. Weder, *Science (80-.).*, 2008, **319**, 1370–1374.

86. R. Rusli, K. Shanmuganathan, S. J. Rowan, C. Weder, and S. J. Eichhorn, *Biomacromolecules*, 2010, **11**, 762–768.

87. K. Shanmuganathan, J. R. Capadona, S. J. Rowan, and C. Weder, *ACS Appl. Mater. Interfaces*, 2010, **2**, 165–174.

88. P. K. Annamalai, K. L. Dagnon, S. Monemian, E. J. Foster, S. J. Rowan, and C. Weder, *ACS Appl. Mater. Interfaces*, 2014, **6**, 967–976.

89. A. E. Way, L. Hsu, K. Shanmuganathan, C. Weder, and S. J. Rowan, *ACS Macro Lett.*, 2012, **1**, 1001–1006.

90. M. V Biyani, E. J. Foster, and C. Weder, *ACS Macro Lett.*, 2013, **2**, 236–240.

91. B. Binks, *Curr. Opin. Colloid Interface Sci.*, 2002, **7**, 21–41.

92. A. Schrade, K. Landfester, and U. Ziener, *Chem. Soc. Rev.*, 2013, **42**, 6823.

93. Y. Chevalier and M.-A. Bolzinger, *Colloids Surfaces A Physicochem. Eng. Asp.*, 2013, **439**, 23–34.

94. S. U. Pickering, *J. Chem. Soc.*, 1907, **91**, 2001–2021.

95. W. Ramsden, *Proc. Chem. Soc.*, 1903, **72**, 156–164.

96. D. Dupin, S. P. Armes, C. Connan, P. Reeve, and S. M. Baxter, *Langmuir*, 2007, **23**, 6903–6910.

97. E. Dickinson, *J. Sci. Food Agric.*, 2013, **93**, 710–721.

98. T. N. Hunter, R. J. Pugh, G. V Franks, and G. J. Jameson, *Adv. Colloid Interface Sci.*, 2008, **137**, 57–81.

99. M. Rayner, D. Marku, M. Eriksson, M. Sjöö, P. Dejmek, and M. Wahlgren, *Colloids Surfaces A*, 2014, **458**, 48–62.

100. E. Dickinson, *Curr. Opin. Colloid Interface Sci.*, 2010, **15**, 40–49.

101. M. S. Silverstein, *Prog. Polym. Sci.*, 2014, **39**, 199–234.

102. S. Melle, M. Lask, and G. Fuller, *Langmuir*, 2005, 2158–2162.

103. J. Zhou, X. Qiao, B. P. Binks, K. Sun, M. Bai, Y. Li, and Y. Liu, *Langmuir*, 2011, **27**, 3308–3316.

104. G. Sun, Z. Li, and T. Ngai, *Angew. Chemie*, 2010, **122**, 2209–2212.

105. H. Katepalli, V. T. John, and A. Bose, *Langmuir*, 2013, **29**, 6790–6797.

106. A. Saha, A. Nikova, P. Venkataraman, V. T. John, and A. Bose, *ACS Appl. Mater. Interfaces*, 2013, **5**, 3094–3100.

107. J. Dong, A. J. Worthen, L. M. Foster, Y. Chen, K. A. Cornell, S. L. Bryant, T. M. Truskett, C. W. Bielawski, and K. P. Johnston, *ACS Appl. Mater. Interfaces*, 2014, **6**, 11502–11513.

108. I. Fuchs and D. Avnir, *Langmuir*, 2013, **29**, 2835–2842.

109. G. Kaptay, *Colloids Surfaces A Physicochem. Eng. Asp.*, 2006, **282-283**, 387–401.

110. J. Masliyah, Z. Zhou, and Z. Xu, *Can. J. Chem. Eng.*, 2004, **82**, 628–654.

111. S. Wiese, A. C. Spiess, and W. Richtering, *Angew. Chemie Int. Ed.*, 2013, **52**, 576–579.

112. Y. Liu, P. Jessop, M. Cunningham, C. Eckert, and C. Liotta, *Science*, 2006, **313**, 958–960.

113. H. Duan, D. Wang, N. S. Sobal, M. Giersig, D. G. Kurth, and H. Möhwald, *Nano Lett.*, 2005, **5**, 949–952.

114. T. Chen, P. J. Colver, and S. A. F. Bon, *Adv. Mater.*, 2007, **19**, 2286–2289.

115. D. Li, Y. He, and S. Wang, *J. Phys. Chem. C*, 2009, **113**, 12927–12929.

116. D. J. Voorn, W. Ming, and A. M. van Herk, *Macromolecules*, 2006, **39**, 2137–2143.

117. W. Li, L. Yu, G. Liu, J. Tan, S. Liu, and D. Sun, *Colloids Surfaces A Physicochem. Eng. Asp.*, 2012, **400**, 44–51.

118. F. Yang, Q. Niu, Q. Lan, and D. Sun, *J. Colloid Interface Sci.*, 2007, **306**, 285–295.

119. A. Menner, R. Verdejo, M. Shaffer, and A. Bismarck, *Langmuir*, 2007, **23**, 2398–2403.

120. J. Kim, L. J. Cote, F. Kim, W. Yuan, K. R. Shull, and J. Huang, *J. Am. Chem. Soc.*, 2010, **132**, 8180–8186.

121. X. Huang, M. Li, D. C. Green, D. S. Williams, A. J. Patil, and S. Mann, *Nat. Commun.*,

2013, **4**, 2239.

122. M. V. Tzoumaki, T. Moschakis, V. Kiosseoglou, and C. G. Biliaderis, *Food Hydrocoll.*, 2011, **25**, 1521–1529.

123. C. Li, P. Sun, and C. Yang, *Starch - Stärke*, 2012, **64**, 497–502.

124. Z. Nie, J. Il Park, W. Li, S. A. F. Bon, and E. Kumacheva, *J. Am. Chem. Soc.*, 2008, **130**, 16508–16509.

125. A. Dinsmore, M. Hsu, and M. Nikolaides, *Science*, 2002, **298**, 1006–1010.

126. Y. Chenglin, Y. Yiqun, Z. Ye, L. Na, L. Xiaoya, L. Jing, and J. Ming, *Langmuir*, 2012, **28**, 9211–9222.

127. W. Zhai, G. Li, P. Yu, L. Yang, and L. Mao, *J. Phys. Chem. C*, 2013, **117**, 15183–15191.

128. S. Fujii, S. P. Armes, B. P. Binks, and R. Murakami, *Langmuir*, 2006, **22**, 6818–6825.

129. S. Dai, P. Ravi, and K. C. Tam, *Soft Matter*, 2008, **4**, 435.

130. J. W. J. de Folter, M. W. M. van Ruijven, and K. P. Velikov, *Soft Matter*, 2012, **8**, 6807.

131. H. Liu, C. Wang, S. Zou, Z. Wei, and Z. Tong, *Langmuir*, 2012, **28**, 11017–11024.

132. S. Fujii, M. Okada, and T. Furuzono, *J. Colloid Interface Sci.*, 2007, **315**, 287–296.

133. D. Yu, Z. Lin, and Y. Li, *Colloids Surfaces A Physicochem. Eng. Asp.*, 2013, **422**, 100–109.

134. J. Li and H. D. H. Stöver, *Langmuir*, 2008, **24**, 13237–13240.

135. J. I. Amalvy, G. F. Unali, Y. Li, S. Granger-Bevan, S. P. Armes, B. P. Binks, J. a Rodrigues, and C. P. Whitby, *Langmuir*, 2004, **20**, 4345–4354.

136. E. S. Read, S. Fujii, J. I. Amalvy, D. P. Randall, and S. P. Armes, *Langmuir*, 2004, **20**, 7422–7429.

137. M. F. Haase, D. Grigoriev, H. Moehwald, B. Tiersch, and D. G. Shchukin, *Langmuir*, 2011, **27**, 74–82.

138. M. F. Haase, D. O. Grigoriev, H. Möhwald, and D. G. Shchukin, *Adv. Mater.*, 2012, **24**, 2429–2435.

139. M. F. Haase, D. Grigoriev, H. Moehwald, B. Tiersch, and D. G. Shchukin, *J. Phys. Chem. C*, 2010, **114**, 17304–17310.

140. H. Yang, T. Zhou, and W. Zhang, *Angew. Chemie Int. Ed.*, 2013, **52**, 7455–7459.

141. M. Motornov, R. Sheparovych, R. Lupitskyy, E. MacWilliams, O. Hoy, I. Luzinov, and S. Minko, *Adv. Funct. Mater.*, 2007, **17**, 2307–2314.

142. A. J. Morse, J. Madsen, D. J. Growney, S. P. Armes, P. Mills, and R. Swart, *Langmuir*, 2014, **30**, 12509–12519.

143. a J. Morse, D. Dupin, K. L. Thompson, S. P. Armes, K. Ouzineb, P. Mills, and R. Swart, *Langmuir*, 2012, **28**, 11733–11744.

144. S. Fujii, Y. Cai, J. V. M. Weaver, and S. P. Armes, *J. Am. Chem. Soc.*, 2005, **127**, 7304–7305.

145. C. Ma, X. Bi, T. Ngai, and G. Zhang, *J. Mater. Chem. A*, 2013, **1**, 5353–5360.

146. F. Tu and D. Lee, *J. Am. Chem. Soc.*, 2014, **136**, 9999–10006.

147. N. Saleh, T. Sarbu, K. Sirk, G. V Lowry, K. Matyjaszewski, and R. D. Tilton, *Langmuir*, 2005, **21**, 9873–9878.

148. T. Liu, S. Seiffert, J. Thiele, A. R. Abate, D. a Weitz, and W. Richtering, *Proc. Natl. Acad. Sci.*, 2012, **109**, 384–389.

149. Z. Wei, Y. Yang, R. Yang, and C. Wang, *Green Chem.*, 2012, **14**, 3230–3236.

150. A. K. F. Dyab, *Colloids Surfaces A Physicochem. Eng. Asp.*, 2012, **402**, 2–12.

151. J. Tan, J. Wang, L. Wang, J. Xu, and D. Sun, *J. Colloid Interface Sci.*, 2011, **359**, 155–162.

152. X. Liu, C. Yi, Y. Zhu, Y. Yang, J. Jiang, Z. Cui, and M. Jiang, *J. Colloid Interface Sci.*, 2010, **351**, 315–322.

153. Q. Lan, C. Liu, F. Yang, S. Liu, J. Xu, and D. Sun, *J. Colloid Interface Sci.*, 2007, **310**, 260–269.

154. F. Nan, J. Wu, F. Qi, Y. Liu, T. Ngai, and G. Ma, *Colloids Surfaces A Physicochem. Eng. Asp.*, 2014, **456**, 246–252.

155. H. Liu, Z. Zhang, H. Yang, F. Cheng, and Z. Du, *ChemSusChem*, 2014, **7**, 1888–1900.

156. B. P. Binks, R. Murakami, S. P. Armes, and S. Fujii, *Angew. Chem. Int. Ed. Engl.*, 2005, **44**, 4795–4798.

157. C. Monteux, C. Marlière, P. Paris, N. Pantoustier, N. Sanson, and P. Perrin, *Langmuir*, 2010, **26**, 13839–13846.

158. T. Saigal, H. Dong, K. Matyjaszewski, and R. D. Tilton, *Langmuir*, 2010, **26**, 15200–15209.

159. S. Tsuji and H. Kawaguchi, *Langmuir*, 2008, **24**, 3300–3305.

160. M. Destribats, V. Lapeyre, M. Wolfs, E. Sellier, F. Leal-Calderon, V. Ravaine, and V.

Schmitt, *Soft Matter*, 2011, **7**, 7689.

161. M. Destribats, V. Lapeyre, E. Sellier, F. Leal-Calderon, V. Ravaine, and V. Schmitt, *Langmuir*, 2012, **28**, 3744–3755.

162. J. Niskanen, C. Wu, M. Ostrowski, G. G. Fuller, S. Hietala, and H. Tenhu, *Macromolecules*, 2013, **46**, 2331–2340.

163. J. Jiang, Y. Zhu, Z. Cui, and B. P. Binks, *Angew. Chemie*, 2013, **125**, 12599–12602.

164. C. Liang, Q. Liu, and Z. Xu, *ACS Appl. Mater. Interfaces*, 2014, **6**, 6898–6904.

165. Y. Qian, Q. Zhang, X. Qiu, and S. Zhu, *Green Chem.*, 2014, **16**, 4963–4968.

166. a J. Morse, S. P. Armes, K. L. Thompson, D. Dupin, L. a Fielding, P. Mills, and R. Swart, *Langmuir*, 2013, **29**, 5466–5475.

167. P. Liu, W. Lu, W.-J. Wang, B.-G. Li, and S. Zhu, *Langmuir*, 2014, **30**, 10248–10255.

168. S. Lin and P. Theato, *Macromol. Rapid Commun.*, 2013, **34**, 1118–1133.

169. J. Peng, Q. Liu, Z. Xu, and J. Masliyah, *Adv. Funct. Mater.*, 2012, **22**, 1732–1740.

170. T. Nypelö, C. Rodriguez-Abreu, Y. V. Kolen'ko, J. Rivas, and O. J. Rojas, *ACS Appl. Mater. Interfaces*, 2014, **6**, 16851–16858.

171. C. Zhao, J. Tan, W. Li, K. Tong, J. Xu, and D. Sun, *Langmuir*, 2013, **29**, 14421–14428.

172. K. Y. Tan, J. E. Gautrot, and W. T. S. Huck, *Langmuir*, 2011, **27**, 1251–1259.

173. Z. Chen, L. Zhou, W. Bing, Z. Zhang, Z. Li, J. Ren, and X. Qu, *J. Am. Chem. Soc.*, 2014, **136**, 7498–7504.

174. C. Yi, N. Liu, J. Zheng, J. Jiang, and X. Liu, *J. Colloid Interface Sci.*, 2012, **380**, 90–98.

175. S. Schmidt, T. Liu, S. Rütten, K.-H. Phan, M. Möller, and W. Richtering, *Langmuir*, 2011, **27**, 9801–9806.

176. T. Ngai, S. H. Behrens, and H. Auweter, *Chem. Commun.*, 2005, 331.

177. B. Brugger and W. Richtering, *Langmuir*, 2008, **24**, 7769–7777.

178. B. Brugger, B. a Rosen, and W. Richtering, *Langmuir*, 2008, **24**, 12202–12208.

179. W. Richtering, *Langmuir*, 2012, **28**, 17218–17229.

180. B. Brugger and W. Richtering, *Adv. Mater.*, 2007, **19**, 2973–2978.

181. Q. Chen, Y. Xu, X. Cao, L. Qin, and Z. An, *Polym. Chem.*, 2014, **5**, 175–185.

182. K. Y. Yoon, Z. Li, B. M. Neilson, W. Lee, C. Huh, S. L. Bryant, C. W. Bielawski, and K. P. Johnston, *Macromolecules*, 2012, **45**, 5157–5166.

183. Y. Chen, Y. Bai, S. Chen, J. Ju, Y. Li, T. Wang, and Q. Wang, *ACS Appl. Mater.*

Interfaces, 2014, **6**, 13334–13338.

184. A. R. Patel, E. Drost, J. Seijen ten Hoorn, and K. P. Velikov, *Soft Matter*, 2013, **9**, 6747–6751.

185. T. Saigal, A. Yoshikawa, D. Kloss, M. Kato, P. L. Golas, K. Matyjaszewski, and R. D. Tilton, *J. Colloid Interface Sci.*, 2013, **394**, 284–292.

186. Z. L. Yao and K. C. Tam, *Langmuir*, 2011, **27**, 6668–6673.

187. N. Lin and A. Dufresne, *Biomacromolecules*, 2013, **14**, 871–880.

188. S. Beck, J. Bouchard, and R. Berry, *Biomacromolecules*, 2012, **13**, 1486–1494.

189. S. Beck, J. Bouchard, and R. Berry, *Biomacromolecules*, 2011, **12**, 167–172.

190. G. Sèbe, F. Ham-Pichavant, and G. Pecastaings, *Biomacromolecules*, 2013, **14**, 2937–2944.

191. A. A. Naim, A. Umar, M. Sanagi, and N. Basaruddin, *Carbohydr. Polym.*, 2013, **98**, 1618–1623.

192. X. Zhang, C. Gao, M. Liu, Y. Huang, X. Yu, and E. Ding, *Appl. Surf. Sci.*, 2013, **264**, 636–643.

193. E. Larsson, C. C. Sanchez, C. Porsch, E. Karabulut, L. Wågberg, and A. Carlmark, *Eur. Polym. J.*, 2013, **49**, 2689–2696.

194. A. C. Rinkenauer, A. Schallon, U. Günther, M. Wagner, E. Betthausen, U. S. Schubert, and F. H. Schacher, *ACS Nano*, 2013, **7**, 9621–9631.

195. J.-F. Gohy, S. Antoun, and R. Jérôme, *Macromolecules*, 2001, **34**, 7435–7440.

196. A. P. Majewski, U. Stahlschmidt, V. Jérôme, R. Freitag, A. H. E. Müller, and H. Schmalz, *Biomacromolecules*, 2013, **14**, 3081–3090.

197. S. Zeppieri, J. Rodríguez, and A. L. López de Ramos, *J. Chem. Eng. Data*, 2001, **46**, 1086–1088.

198. F. Baines, N. Billingham, and S. Armes, *Macromolecules*, 1996, **29**, 3416–3420.

199. C. P. Whitby, D. Fornasiero, and J. Ralston, *J. Colloid Interface Sci.*, 2009, **329**, 173–181.

200. C. P. Whitby, F. E. Fischer, D. Fornasiero, and J. Ralston, *J. Colloid Interface Sci.*, 2011, **361**, 170–177.

201. P. Greenspan, E. P. Mayer, and S. D. Fowler, *J. Cell Biol.*, 1985, **100**, 965–973.

202. E. Prifti, L. Reymond, M. Umebayashi, R. Hovius, H. Riezman, and K. Johnsson, *ACS Chem. Biol.*, 2014, **9**, 606–612.

203. J. Rao and A. Khan, *J. Am. Chem. Soc.*, 2013, **135**, 14056–14059.

204. T. Felbeck, T. Behnke, K. Hoffmann, M. Grabolle, M. M. Lezhnina, U. H. Kynast, and U. Resch-Genger, *Langmuir*, 2013, **29**, 11489–11497.

205. Z.-Q. Dong, Y. Cao, X.-J. Han, M.-M. Fan, Q.-J. Yuan, Y.-F. Wang, B.-J. Li, and S. Zhang, *Langmuir*, 2013, **29**, 3188–3194.

206. C. Locatelli-Champagne and M. Cloitre, *Colloid Polym. Sci.*, 2013, **291**, 2911–2916.

207. J. Jiang, X. Tong, and Y. Zhao, *J. Am. Chem. Soc.*, 2005, **127**, 8290–8291.

208. D. Fournier and R. Hoogenboom, *Macromolecules*, 2007, **40**, 915–920.

209. L. Besnard, F. Marchal, J. F. Paredes, J. Daillant, N. Pantoustier, P. Perrin, and P. Guenoun, *Adv. Mater.*, 2013, **25**, 2844–2848.

210. L. He, F. Lin, X. Li, H. Sui, and Z. Xu, *Chem. Soc. Rev.*, 2015, **44**, 5446–5494.

211. Z. Zhang, G. Y. Xu, F. Wang, S. L. Dong, and Y. M. Li, *J. Colloid Interface Sci.*, 2004, **277**, 464–470.

212. A. a. Peña, G. J. Hirasaki, and C. a. Miller, *Ind. Eng. Chem. Res.*, 2005, **44**, 1139–1149.

213. Y. Liu, P. G. Jessop, M. Cunningham, C. a Eckert, and C. L. Liotta, *Science*, 2006, **313**, 958–960.

214. C. Liang, J. R. Harjani, T. Robert, E. Rogel, D. Kuehne, C. Ovalles, V. Sampath, and P. G. Jessop, *Energy and Fuels*, 2012, **26**, 488–494.

215. P. Brown, C. P. Butts, and J. Eastoe, *Soft Matter*, 2013, **9**, 2365.

216. J. Tang, P. J. Quinlan, and K. C. Tam, *Soft Matter*, 2015, **11**, 3512–3529.

217. S. Fujii, D. P. Randall, and S. P. Armes, *Langmuir*, 2004, **20**, 11329–11335.

218. X. Wang, Y. Shi, R. W. Graff, D. Lee, and H. Gao, *Polymer,* 2015, **72**, 361–367.

219. J. Tang, Y. Song, R. M. Berry, and K. C. Tam, *RSC Adv.*, 2014, **4**, 60249–60252.

220. J. Tang, Z. Shi, R. M. Berry, and K. C. Tam, *Ind. Eng. Chem. Res.*, 2015, **54**, 3299–3308.

221. J. Tang, Y. Song, S. Tanvir, W. a. Anderson, R. M. Berry, and K. C. Tam, *ACS Sustain. Chem. Eng.*, 2015, **3**, 1801–1809.

222. Z. Hu, S. Ballinger, R. Pelton, and E. D. Cranston, *J. Colloid Interface Sci.*, 2015, **439**, 139–148.

223. M. Visanko, H. Liimatainen, J. A. Sirviö, J. P. Heiskanen, J. Niinimäki, and O. Hormi, *Biomacromolecules*, 2014, **15**, 2769–2775.

224. A. G. Cunha, J.-B. Mougel, B. Cathala, L. a Berglund, and I. Capron, *Langmuir*, 2014, **30**,

9327–9335.

225. J.-F. Lutz, *Adv. Mater.*, 2011, **23**, 2237–2243.

226. C. Porsch, S. Hansson, N. Nordgren, and E. Malmström, *Polym. Chem.*, 2011, **2**, 1114.

227. J. F. Lutz, Ö. Akdemir, and A. Hoth, *J. Am. Chem. Soc.*, 2006, **128**, 13046–13047.

228. J.-F. J.-F. Lutz, A. Hoth, and K. Schade, *Des. Monomers Polym.*, 2009, **12**, 343–353.

229. A. Abu Naim, A. Umar, M. M. Sanagi, and N. Basaruddin, *Carbohydr. Polym.*, 2013, **98**, 1618–1623.

230. Y. Kotsuchibashi and R. Narain, *Polym. Chem.*, 2014, **5**, 3061–3070.

231. M. Ye, D. Zhang, L. Han, J. Tejada, and C. Ortiz, *Soft Matter*, 2006, **2**, 243.

232. P. Zhang and D. B. Henthorn, *AIChE J.*, 2012, **58**, 2980–2986.

233. J. T. Auletta, G. J. LeDonne, K. C. Gronborg, C. D. Ladd, H. Liu, W. W. Clark, and T. Y. Meyer, *Macromolecules*, 2015, **48**, 1736–1747.

234. T. S. Anirudhan, a R. Tharun, and S. R. Rejeena, *Ind. Eng. Chem. Res.*, 2011, **50**, 1866–1874.

235. L. Ruiz-Pérez, A. Pryke, M. Sommer, G. Battaglia, I. Soutar, L. Swanson, and M. Geoghegan, *Macromolecules*, 2008, **41**, 2203–2211.

236. X. Wang, X. Ye, and G. Zhang, *Soft Matter*, 2015, **11**, 5381–5388.

237. C. L. Lay, J. N. Kumar, C. K. Liu, X. Lu, and Y. Liu, *Macromol. Rapid Commun.*, 2013, **34**, 1563–1568.

238. Y. Wang, T. Li, S. Li, R. Guo, and J. Sun, *ACS Appl. Mater. Interfaces*, 2015, **7**, 13597–13603.

239. C. W. F. Hideko Tamaru Oyama, Wing T. Tang, *Macromolecules*, 1987, **20**, 1839–1847.

240. H. T. Oyama, D. J. Hemker, and C. W. Frank, *Macromolecules*, 1989, **22**, 1255–1260.

241. D. J. Hemker, V. Garza, and C. W. Frank, *Macromolecules*, 1990, **23**, 4411–4418.

242. D. Hemker and C. Frank, *Macromolecules*, 1990, 4404–4410.

243. A. Klierj and N. A. Peppas, *Macromolecules*, 1990, **23**, 4944–4949.

244. D. N. Robinson and N. A. Peppas, *Macromolecules*, 2002, **35**, 3668–3674.

245. O. E. Philippova, N. S. Karibyants, and S. G. Starodubtzev, *Macromolecules*, 1994, **27**, 2398–2401.

246. H. Wang, L. Chen, Y. Feng, and H. Chen, *Acc. Chem. Res.*, 2013, **46**, 1636–1646.

247. T.-D. Nguyen, W. Y. Hamad, and M. J. MacLachlan, *Chem. Commun.*, 2013, **49**, 11296–

11298.

248. N. K. Guimard, N. Gomez, and C. E. Schmidt, *Prog. Polym. Sci.*, 2007, **32**, 876–921.

249. S. Bhadra, D. Khastgir, N. K. Singha, and J. H. Lee, *Prog. Polym. Sci.*, 2009, **34**, 783–810.

250. J. Janata and M. Josowicz, *Nat. Mater.*, 2003, **2**, 19–24.

251. N. a Rakow and K. S. Suslick, *Nature*, 2000, **406**, 710–713.

252. S. Kirchmeyer and K. Reuter, *J. Mater. Chem.*, 2005, **15**, 2077–2088.

253. J. Jang and Y. Kim, *Chem. Commun.*, 2008, 4016.

254. J. Jang, J. Ha, and B. Lim, *Chem. Commun.*, 2006, 1622.

255. M. G. Han and S. H. Foulger, *Chem. Commun.* , 2004, 2154–2155.

256. H. Kong, J. Song, and J. Jang, *Chem. Commun.*, 2010, **46**, 6735.

257. J. Song, H. Song, H. Kong, J.-Y. Hong, and J. Jang, *J. Mater. Chem.*, 2011, **21**, 19317–19323.

258. H. Kong and J. Jang, *Biomacromolecules*, 2008, **9**, 2677–2681.

259. G. Kardaş and R. Solmaz, *Appl. Surf. Sci.*, 2007, **253**, 3402–3407.

260. J. Song, H. Kim, Y. Jang, and J. Jang, *ACS Appl. Mater. Interfaces*, 2013, **5**, 11563–11568.

261. P. Chauhan, C. Hadad, A. H. López, S. Silvestrini, V. La Parola, E. Frison, M. Maggini, M. Prato, and T. Carofiglio, *Chem. Commun..*, 2014, **50**, 9493–9496.

262. H. Lee, S. M. Dellatore, W. M. Miller, and P. B. Messersmith, *Science*, 2007, **318**, 426–430.

263. P. Li, Y. F. Poon, W. Li, H. Zhu, S. H. Yeap, Y. Cao, X. Qi, C. Zhou, M. Lamrani, R. W. Beuerman, E. Kang, Y. Mu, C. M. Li, M. W. Chang, S. S. J. Leong, and M. B. Chan-Park, *Nat. Mater.*, 2011, **10**, 149–156.

264. R. Zhang, K. Eggleston, V. Rotimi, and R. J. Zeckhauser, *Global. Health*, 2006, **2**, 6–20.

265. A. Muñoz-Bonilla and M. Fernández-García, *Eur. Polym. J.*, 2015, **65**, 46–62.

266. A. M. Ferraria, S. Boufi, N. Battaglini, A. M. Botelho do Rego, and M. ReiVilar, *Langmuir*, 2010, **26**, 1996–2001.

267. M. C. Moulton, L. K. Braydich-Stolle, M. N. Nadagouda, S. Kunzelman, S. M. Hussain, and R. S. Varma, *Nanoscale*, 2010, **2**, 763–770.

268. J. Song, H. Kang, C. Lee, S. H. Hwang, and J. Jang, *ACS Appl. Mater. Interfaces*, 2012, **4**,

460–465.

269. H. Liu, J. Song, S. Shang, Z. Song, and D. Wang, *ACS Appl. Mater. Interfaces*, 2012, **4**, 2413–2419.

270. R. Eising, A. M. Signori, S. Fort, and J. B. Domingos, *Langmuir*, 2011, **27**, 11860–11866.

271. A. Travan, C. Pelillo, I. Donati, E. Marsich, M. Benincasa, T. Scarpa, S. Semeraro, G. Turco, R. Gennaro, and S. Paoletti, *Biomacromolecules*, 2009, **10**, 1429–1435.

272. A. Muñoz-Bonilla and M. Fernández-García, *Prog. Polym. Sci.*, 2012, **37**, 281–339.

273. P. V AshaRani, G. Low Kah Mun, M. P. Hande, and S. Valiyaveettil, *ACS Nano*, 2009, **3**, 279–290.

274. S. Chernousova and M. Epple, *Angew. Chemie Int. Ed.*, 2013, **52**, 1636–1653.

275. V. K. Sharma, K. M. Siskova, R. Zboril, and J. L. Gardea-Torresdey, *Adv. Colloid Interface Sci.*, 2014, **204**, 15–34.

276. W. K. Jung, H. C. Koo, K. W. Kim, S. Shin, S. H. Kim, and Y. H. Park, *Appl. Environ. Microbiol.*, 2008, **74**, 2171–2178.

277. Z. Xiu, Q. Zhang, H. L. Puppala, V. L. Colvin, and P. J. J. Alvarez, *Nano Lett.*, 2012, **12**, 4271–4275.

278. S. J. Eichhorn, *Soft Matter*, 2011, **7**, 303–315.

279. A. Ivanova, D. Fattakhova-Rohlfing, B. E. Kayaalp, J. Rathouský, and T. Bein, *J. Am. Chem. Soc.*, 2014, **136**, 5930–5937.

280. X. Wu, V. L. Chabot, B. K. Kim, A. Yu, R. M. Berry, and K. C. Tam, *Electrochim. Acta*, 2014, **138**, 139–147.

281. Z. Shi, J. Tang, L. Chen, C. Yan, S. Tanvir, W. a. Anderson, R. M. Berry, and K. C. Tam, *J. Mater. Chem. B*, 2015, **3**, 603–611.

282. E. Altunbaş, R. Solmaz, and G. Kardaş, *Mater. Chem. Phys.*, 2010, **121**, 354–358.

283. H. Kong, J. Song, and J. Jang, *Macromol. Rapid Commun.*, 2009, **30**, 1350–1355.

284. H. Rosilo, J. R. McKee, E. Kontturi, T. Koho, V. P. Hytönen, O. Ikkala, and M. a. Kostiainen, *Nanoscale*, 2014, **6**, 11871–11881.

285. E. Karabulut, T. Pettersson, M. Ankerfors, and L. Wågberg, *ACS Nano*, 2012, **6**, 4731–4739.

286. S. Dong, H. J. Cho, Y. W. Lee, and M. Roman, *Biomacromolecules*, 2014, **15**, 1560–1567.

287. J. O. Zoppe, V. Ruottinen, J. Ruotsalainen, S. Rönkkö, L.-S. Johansson, A. Hinkkanen, K. Järvinen, and J. Seppälä, *Biomacromolecules*, 2014, **15**, 1534–1542.

288. H. Ni, S. Zeng, J. Wu, X. Cheng, T. Luo, W. Wang, W. Zeng, and Y. Chen, in *Bio-Medical Materials and Engineering*, 2012, vol. 22, pp. 121–127.

289. Z. Hanif, F. R. Ahmed, S. W. Shin, Y.-K. Kim, and S. H. Um, *Colloids Surfaces B Biointerfaces*, 2014, **119**, 162–165.

290. M. M. Fernandes, A. Francesko, J. Torrent-Burgués, F. J. Carrión-Fité, T. Heinze, and T. Tzanov, *Biomacromolecules*, 2014, **15**, 1365–1374.

291. L. Heath and W. Thielemans, *Green Chem.*, 2010, **12**, 1448–1453.

292. B. Xia, F. He, and L. Li, *Langmuir*, 2013, **29**, 4901–4907.

293. Z. Zhou, C. Lu, X. Wu, and X. Zhang, *RSC Adv.*, 2013, **3**, 26066–26073.

294. K. a Mahmoud, K. B. Male, S. Hrapovic, and J. H. T. Luong, *ACS Appl. Mater. Interfaces*, 2009, **1**, 1383–1386.

295. M. Rezayat, R. K. Blundell, J. E. Camp, D. a. Walsh, and W. Thielemans, *ACS Sustain. Chem. Eng.*, 2014, **2**, 1241–1250.

296. Y. Li, Y. Su, X. Zhao, X. He, R. Zhang, J. Zhao, X. Fan, and Z. Jiang, *ACS Appl. Mater. Interfaces*, 2014, **6**, 5548–5557.

297. Z. Zhang, J. Zhang, B. Zhang, and J. Tang, *Nanoscale*, 2013, **5**, 118–123.

298. M. Krogsgaard, M. a Behrens, J. S. Pedersen, and H. Birkedal, *Biomacromolecules*, 2013, **14**, 297–301.

299. Y. Xie, B. Yan, H. Xu, J. Chen, Q. Liu, Y. Deng, and H. Zeng, *ACS Appl. Mater. Interfaces*, 2014, **6**, 8845–8852.

300. M.-H. Ryou, D. J. Lee, J.-N. Lee, Y. M. Lee, J.-K. Park, and J. W. Choi, *Adv. Energy Mater.*, 2012, **2**, 645–650.

301. M.-H. Ryou, Y. M. Lee, J.-K. Park, and J. W. Choi, *Adv. Mater.*, 2011, **23**, 3066–3070.

302. J. Zhou, B. Duan, Z. Fang, J. Song, C. Wang, P. B. Messersmith, and H. Duan, *Adv. Mater.*, 2014, **26**, 701–705.

303. T. Zeng, X. Zhang, H. Niu, Y. Ma, W. Li, and Y. Cai, *Appl. Catal. B Environ.*, 2013, **134-135**, 26–33.

304. Z. Ma, X. Jia, J. Hu, F. Zhou, and B. Dai, *RSC Adv.*, 2014, **4**, 1853–1856.

305. M. Sureshkumar, P.-N. Lee, and C.-K. Lee, *J. Mater. Chem.*, 2011, **21**, 12316–12320.

306. R. Liu, Y. Guo, G. Odusote, F. Qu, and R. D. Priestley, *ACS Appl. Mater. Interfaces*, 2013, **5**, 9167–9171.

307. Y. Jiang, Y. Lu, L. Zhang, L. Liu, Y. Dai, and W. Wang, *J. Nanoparticle Res.*, 2012, **14**, 938–948.

308. L. Q. Xu, B. S. M. Yap, R. Wang, K.-G. Neoh, E.-T. Kang, and G. D. Fu, *Ind. Eng. Chem. Res.*, 2014, **53**, 3116–3124.

309. G. Marcelo, a. Muñoz-Bonilla, and M. Fernández-García, *J. Phys. Chem. C*, 2012, **116**, 24717–24725.

310. H. Wu, X. Huang, M. Gao, X. Liao, and B. Shi, *Green Chem.*, 2011, **13**, 651–658.

311. M. Liang, R. Su, R. Huang, W. Qi, Y. Yu, L. Wang, and Z. He, *ACS Appl. Mater. Interfaces*, 2014, **6**, 4638–4649.

312. K. Esumi, R. Isono, and T. Yoshimura, *Langmuir*, 2004, **20**, 237–243.

313. S. Jana, S. Ghosh, S. Nath, S. Pande, S. Praharaj, S. Panigrahi, S. Basu, T. Endo, and T. Pal, *Appl. Catal. A Gen.*, 2006, **313**, 41–48.

314. H. Xu, J. Xu, Z. Zhu, H. Liu, and S. Liu, *Macromolecules*, 2006, **39**, 8451–8455.

315. Q. Geng and J. Du, *RSC Adv.*, 2014, **4**, 16425–16428.

316. A. Panáček, R. Prucek, J. Hrbáč, T. Nevečná, J. Šteffková, R. Zbořil, and L. Kvítek, *Chem. Mater.*, 2014, **26**, 1332–1339.

317. X. Chen, X. Cheng, and J. J. Gooding, *Anal. Chem.*, 2012, **84**, 8557–8563.

318. X. Chen, S. Parker, G. Zou, W. Su, and Q. Zhang, *ACS Nano*, 2010, **4**, 6387–6394.

319. T. Huang, F. Meng, and L. Qi, *J. Phys. Chem. C*, 2009, **113**, 13636–13642.

320. C. H. B. Ng, J. Yang, and W. Y. Fan, *J. Phys. Chem. C*, 2008, **112**, 4141–4145.

321. L. Devi and A. Mandal, *RSC Adv.*, 2013, **3**, 5238–5253.

322. J. Liu, J. Wang, Z. Zhu, L. Li, X. Guo, S. F. Lincoln, and R. K. Prud'homme, *AIChE J.*, 2014, **60**, 1977–1982.

323. D. R. Dreyer, D. J. Miller, B. D. Freeman, D. R. Paul, and C. W. Bielawski, *Langmuir*, 2012, **28**, 6428–6435.

324. Y. Li, Y. Wu, Y. Gao, S. Sha, J. Hao, G. Cao, and C. Yang, *RSC Adv.*, 2013, **3**, 26361–26366.

325. S. P. Dubey, A. D. Dwivedi, I.-C. Kim, M. Sillanpaa, Y.-N. Kwon, and C. Lee, *Chem. Eng. J.*, 2014, **244**, 160–167.

326. Y. Lu, Y. Mei, M. Schrinner, M. Ballauff, M. W. Moller, and J. Breu, *J. Phys. Chem. C*, 2007, **111**, 7676–7681.

327. W. Zhang, F. Tan, W. Wang, X. Qiu, X. Qiao, and J. Chen, *J. Hazard. Mater.*, 2012, **217-218**, 36–42.

328. L. Ai, H. Yue, and J. Jiang, *J. Mater. Chem.*, 2012, **22**, 23447.

329. P. Liu and M. Zhao, *Appl. Surf. Sci.*, 2009, **255**, 3989–3993.

330. X. Du, J. He, J. Zhu, L. Sun, and S. An, *Appl. Surf. Sci.*, 2012, **258**, 2717–2723.

331. E. K. Jeon, E. Seo, E. Lee, W. Lee, M.-K. Um, and B.-S. Kim, *Chem. Commun.*, 2013, **49**, 3392.

332. K. D. O. Santos, W. C. Elias, A. M. Signori, F. C. Giacomelli, H. Yang, and J. B. Domingos, *J. Phys. Chem. C*, 2012, **116**, 4594–4604.

333. B. Baruah, G. J. Gabriel, M. J. Akbashev, and M. E. Booher, *Langmuir*, 2013, **29**, 4225–4234.

334. J.-R. Chiou, B.-H. Lai, K.-C. Hsu, and D.-H. Chen, *J. Hazard. Mater.*, 2013, **248-249**, 394–400.

335. S. Wunder, F. Polzer, Y. Lu, Y. Mei, and M. Ballauff, *J. Phys. Chem. C*, 2010, **114**, 8814–8820.

336. M. Zhu, C. Wang, D. Meng, and G. Diao, *J. Mater. Chem. A*, 2013, **1**, 2118–2125.

337. S. Saha, A. Pal, S. Kundu, S. Basu, and T. Pal, *Langmuir*, 2010, **26**, 2885–2893.

338. G. L. Bertrand, J. R. Faulkner, S. M. Han, and D. W. Armstrong, *J. Phys. Chem.*, 1989, **93**, 6863–6867.